UNIVERSITY OF SOUTHAMPTON

FACULTY OF ENGINEERING, SCIENCE & MATHEMATICS

Institute of Sound & Vibration Research

Modelling Cochlear Micromechanics

by

Robert Henryk Pierzycki

Thesis for the degree of Doctor of Philosophy

September 2007

to my Parents

UNIVERSITY OF SOUTHAMPTON

ABSTRACT

FACULTY OF ENGINEERING, SCIENCE & MATHEMATICS
INSTITUTE OF SOUND & VIBRATION RESEARCH

Doctor of Philosophy

MODELLING COCHLEAR MICROMECHANICS

by Robert Henryk Pierzycki

An active mechanism, the cochlear amplifier, enhances the response of the cochlea to low-level stimuli and is assumed to be controlled by the action of the outer hair cells (OHCs) located within the organ of Corti. Because it is difficult to infer the dynamics of the organ of Corti from physiological data, a number of models have been proposed. However, the micromechanical behaviour of the organ of Corti is still not well understood.

Classical models of the cochlea use an array of isolated lumped parameter systems along its length, coupled through the cochlear fluid. These models employ active feedback loops between the basilar and tectorial membrane (TM) for the mechanism of the cochlear amplifier. Several such models are reviewed and their underlying dynamic behaviour examined, in order to compare the predicted response with recent measurements of the relative motion within the organ of Corti. Their stability is also tested to establish reliability of calculated frequency responses. The models are conditionally stable and operate close to instability to achieve high sensitivity of the cochlear amplifier. Compressive nonlinearity is also included in one of the classical models using a quasi-linear approach.

It has recently been suggested that wave motion within the organ of Corti may also play a role in the cochlear amplifier. The behaviour of two possible types of wave between the reticular lamina and the TM is examined, one in which the TM is assumed to behave as a plate in bending and another in which it is assumed to behave like an elastic half-space. The propagation speed is very low for both waves and incorporation of the losses induced by viscosity causes the waves to decay significantly within a wavelength. Feedback from the OHCs coupled into these waves overcomes the effects of viscosity and enhances waves' resonant response supporting this form of amplification in the cochlea.

Contents

List of Tables

List of Figures

Acknowledgements

Firstly, I would like to thank Professor Steve Elliott and Doctor Ben Lineton for their supervision and guidance throughout, their optimism and support. It is greatly appreciated.

I am also grateful to Doctor Oliver Baumann for his help and for sharing his experience with great enthusiasm. I thank all my colleagues and the ISVR staff for their friendship and help, and in particular Mrs. Joyce Shotter for her help and advice.

I would like to thank my beloved Laura for her heart, support and dedication. I would like to express my gratitude to Fr. Mike and Cathsoc, and to all my friends for their counsel, patience and support.

Finally, I would like to thank my family for being with me at all times. Without them this work would not have been possible.

List of Symbols

General symbols

c	wavespeed [ms^{-1}]
d	thickness of the fluid layer/duct's height [m]
$eig()$	eigenvalue of matrix in ()
f	frequency [Hz]
$\mathbf{I}$	unit matrix
$g(x)$	lever gain
$Im\{\}$	imaginary part of a complex variable in $\{\}$
j	unit imaginary, equal to $\sqrt{-1}$
k	wavenumber [m^{-1}]
$l(x)$	decay length [m]
l_{1-3}	distance of the OHC1-3 from the IHC [m]
$Re\{\}$	real part of a complex variable in $\{\}$
s	complex frequency variable, equal to $j\omega$
t	time [s]
x	longitudinal direction in the cochlea [m]
y	radial direction in the cochlea [m]
z	transverse direction in the cochlea [m]
γ	amplification factor of the active component
η	coefficient of viscosity of the subtectorial fluid [kgm^{-1}s^{-1}]
λ	wavelength [m]
ρ	density of the cochlear fluid [kgm^{-3}]

ω	radian frequency [rad s^{-1}]
ω_n	natural frequency of freely vibrating undamped system [rad s^{-1}]
ω_r	resonance frequency [rad s^{-1}]

Chapter 3

Section 3.1 and 3.2

c	damping of the CP [Nsm^{-1}]
c_0	damping constant [Nsm^{-1}]
f_p	frequency of the pole in $H_{\mathrm{T}}(x,s)$ [Hz]
f_z	frequency of the zero in $H_{\mathrm{T}}(x,s)$ [Hz]
f_{BM}	transverse force acting on the BM [N]
f_{CR}	radial force acting on the OHC cilia [N]
f_{CT}	radial reaction force acting on the OHC cilia [N]
h	height of the organ of Corti [m]
H	upper cochlear chamber's height [m]
$H_{\mathrm{T}}(x,s)$	shear transfer function
$k(x)$	stiffness of the CP [Nm^{-1}]
k_0	stiffness of the CP at the base [Nm^{-1}]
k_{C}	stiffness of the OHC cilia [Nm^{-1}]
K_{B}	stiffness of the BM [Nm^{-1}]
L	length of the CP [m]
m	mass of the CP [kg]
m_0	mass of the CP [kg]
m_{B}	mass of the BM [kg]
m_{T}	mass of the TM [kg]
p_d	pressure difference across the CP [Pa]
Q	quality factor of the BM resonance bandwidth
r_{C}	viscous damping from the fluid in the subtectorial space [Nsm^{-1}]
W	width of the CP [m]
W_1	BM width from hinge to the point of maximum transverse displacement [m]
Y_{BM}	BM mobility [mN^{-1}s^{-1}]

Z_{pass}	passive impedance of the CP [Nsm^{-1}]
Z_{act}	active impedance of the CP [Nsm^{-1}]
Z_{BM}	impedance of the BM [Nsm^{-1}]
Δ	radial shear displacement [m]
Δ_{C}	relative radial shear displacement [m]
Δ_{BM}	radial displacement of the BM [m]
Δ_{TM}	radial displacement of the TM [m]
ϵ	height of the subtectorial space [m]
ζ_0	damping factor
$\zeta(x)$	damping factor at position x along the cochlea
θ	angle of the BM and TM rotation from the resting position
ξ	transverse displacement of the BM [m]

Section 3.3

b	ratio of ξ_b to ξ_p
c_1	damping component of Z_1 [Nsm^{-3}]
c_2	damping component of Z_2 [Nsm^{-3}]
c_3	damping component of Z_3 [Nsm^{-3}]
c_4	damping component of Z_4 [Nsm^{-3}]
$f(t)$	elastic force [N]
$g(x)$	lever gain between the transverse BM and radial RL displacements
k_1	stiffness component of Z_1 [Nm^{-3}]
k_2	stiffness component of Z_2 [Nm^{-3}]
k_3	stiffness component of Z_3 [Nm^{-3}]
k_4	stiffness component of Z_4 [Nm^{-3}]
L_c	average length of a cat cochlea [m]
m_1	mass component of Z_1 [kgm^{-2}]
m_2	mass component of Z_2 [kgm^{-2}]
P_a	active pressure source in the OHC [Nm^{-2}]
P_d	pressure difference across the BM [Nm^{-2}]
Y_p	mobility of the CP [$\mathrm{m}^3\mathrm{N}^{-1}\mathrm{s}^{-1}$]
Z_1	impedance associated with ξ_b [Nsm^{-3}]
Z_2	impedance associated with ξ_t [Nsm^{-3}]

Z_3	impedance associated with ξ_c [Nsm^{-3}]
Z_4	impedance associated with P_a [Nsm^{-3}]
Z_p	impedance of the CP [Nsm^{-3}]
γ	OHC force-generation gain
ξ_b	maximum transverse BM displacement over the width of the BM [m]
ξ_c	shear displacement between the TM and RL [m]
ξ_p	average transverse CP displacement over the width of the CP [m]
ξ_t	radial displacement of the TM [m]
τ	time delay [s]

Section 3.4

a	'slope' constant in the CF/place function of Greenwood
A	constant in the CF/place function of Greenwood
$f(t)$	excitation force [N]
f_{0b}	frequency of antiresonance in Y_b [Hz]
f_1	natural frequency at the first mode of vibration [Hz]
f_2	natural frequency at the second mode of vibration [Hz]
f_{BM}	estimated resonance frequency of the BM [Hz]
f_{TM}	estimated resonance frequency of the TM [Hz]
F	complex amplitude of the excitation force $f(t)$
k	integration constant in the CF/place function of Greenwood
$\mathbf{K}$	stiffness matrix
$\mathbf{M}$	mass matrix
V_b	transverse velocity of the BM [ms^{-1}]
V_t	transverse velocity of the TM [ms^{-1}]
Y_b	point mobility of the BM [m^{3}N^{-1}s^{-1}]
Y_t	transfer mobility of the TM [m^{3}N^{-1}s^{-1}]
$\boldsymbol{\xi}$	displacement vector
$\ddot{\boldsymbol{\xi}}$	acceleration vector
$\dot{\xi}_b$	transverse velocity of the BM [ms^{-1}]
$\dot{\xi}_t$	radial velocity of the TM [ms^{-1}]
$\ddot{\xi}_b$	transverse acceleration of the BM [ms^{-2}]
$\ddot{\xi}_t$	radial acceleration of the TM [ms^{-2}]

ξ_{b1}	BM displacement at ω_1 [m]
ξ_{b2}	BM displacement at ω_2 [m]
ξ_{t1}	TM displacement at ω_1 [m]
ξ_{t2}	TM displacement at ω_2 [m]
Ξ_b	complex amplitude of ξ_b
Ξ_t	complex amplitude of ξ_t
Ξ_{b1}	complex amplitude of ξ_b at ω_1
Ξ_{b2}	complex amplitude of ξ_b at ω_2
Ξ_{t1}	complex amplitude of ξ_t at ω_1
Ξ_{t2}	complex amplitude of ξ_t at ω_2
ϕ_1	normal mode at ω_1
ϕ_2	normal mode at ω_2
ω_1	natural radian frequency at the first mode of vibration [rad s^{-1}]
ω_2	natural radian frequency at the second mode of vibration [rad s^{-1}]

Section 3.5

A_p	effective area of the CP [m^2]
b_w	effective width of the CP [m]
g_f	place-dependent forward transduction gain [mV nm^{-1}]
g_r	place-dependent reverse transduction gain [nm mV^{-1}]
H_c	OHC gain function
K_0	stiffness of the OHC hair bundles [Nm^{-1}]
K_b	stiffness of the BM [Nm^{-1}]
K_t	stiffness of the TM [Nm^{-1}]
R_0	viscous damping of the subtectorial fluid [Nsm^{-1}]
R_b	damping of the BM [Nsm^{-1}]
R_t	damping of the TM [Nsm^{-1}]
M_b	mass of the BM [kg]
M_t	mass of the TM [kg]
P_f	pressure difference across the CP [Nm^{-2}]
T_f	forward, mechanoelectric transduction function [mV nm^{-1}]
T_r	reverse, electromechanic transduction function [nm mV^{-1}]
Z_0	impedance of the BM/TM coupling [Nsm^{-3}]

Z_b	impedance of the BM [Nsm^{-3}]
Z_t	impedance of the TM [Nsm^{-3}]
δ	longitudinal thickness of the CP slice [m]
ξ_0	radial deflection of the OHC cilia [m]
ξ_c	contraction of the OHC body [m]
ξ_r	radial displacement of the RL [m]
ξ_t	radial displacement of the TM [m]
$\dot{\xi}_p$	volume velocity of the CP [$\mathrm{m}^3\mathrm{s}$]
τ_f	time constant of the forward transduction filter [s]
τ_r	time constant of the reverse transduction filter [s]

Section 3.7

T_{shear}	shear transfer function between ξ_r^{tr} and ξ_0
Y_{OC}	organ of Corti mobility [$\mathrm{mN}^{-1}\mathrm{s}^{-1}$]
Y_p^{mod}	CP mobility modifying Y_p of the original model of Neely [$\mathrm{mN}^{-1}\mathrm{s}^{-1}$]
Y_p^{N}	CP mobility derived for the original model of Neely [$\mathrm{mN}^{-1}\mathrm{s}^{-1}$]
Z_{add}	additional active impedance [Nsm^{-1}]
Z_{A}	active impedance [Nsm^{-1}]
Z_{L}	load impedance due to TM mass [Nsm^{-1}]
Z_{OC}	organ of Corti impedance [Nsm^{-1}]
Z_p^{mod}	CP impedance modifying Z_p of the original model of Neely [Nsm^{-1}]
Z_p^{N}	CP impedance derived for the original model of Neely [Nsm^{-1}]
ξ_r^{tr}	transverse displacement of the RL [m]
$\gamma_{critical}$	apparent critical value of gain for stable response

Chapter 4 and 5

A	threshold amplitude
c_{tw}	wavespeed of the travelling wave [ms^{-1}]
$\mathbf{C}$	coupling matrix
$G(j\omega)$	plant response
G_{closed}	overall gain of the nonlinear feedback controller

$H(j\omega)$	feedback gain
k_{tw}	wavenumber of the travelling wave [m^{-1}]
k_{BM}	stiffness of the BM [Nm^{-1}]
k_{TM}	stiffness of the TM [Nm^{-1}]
$\mathbf{M}$	mobility matrix
$\mathbf{p}_d$	pressure difference vector
P_d^{E}	equivalent pressure difference [Nm^{-2}]
P_a^{E}	equivalent active pressure [Nm^{-2}]
$\mathbf{q}$	input source vector
$\mathbf{T}$	tridiagonal matrix
u_{st}	stapes velocity [ms^{-1}]
u_{st}^L	stapes velocity at desired stimulus level L [ms^{-1}]
$v(t)$	output signal of the nonlinear network
$x(t)$	input signal of the positive feedback controller
x_c	characteristic place [m]
$y(t)$	output signal of the positive feedback controller
$z(t)$	output signal of the feedback path of the positive feedback controller
β	gain of the frequency-selective network in the quasi-linear model
γ_{global}	global active gain of the quasi-linear model
$\gamma_{\mathrm{local}}(x)$	active gain of the quasi-linear model at position x along the cochlea
λ_{tw}	wavelength of the travelling wave [m]
$\lvert\dot{\xi}_b\rvert_{max}$	maximum magnitude of the BM velocity [ms^{-1}]
Σ	summing point
$\Phi(t)$	nonlinear network in the quasi-linear model
$\Phi_{\mathrm{D}}(x,\omega)$	describing function in the quasi-linear model

Chapter 6

d_2	thickness of the fluid layer between the RL and TM plates [m]
E	Young's modulus of the TM plate [Pa]
f_{1-3}	electromotile forces from OHC1-3 [Nm^{-1}]

F	force acting on the TM plate per unit length [Nm^{-1}]
F	force required to overcome viscosity of the subtectorial fluid [Nm^{-3}]
G_{up}	response at the IHC to external pressure [$\mathrm{m}^3\mathrm{N}^{-1}$]
G_{uf}	response at the IHC to OHC electromotile forces [$\mathrm{m}^2\mathrm{N}^{-1}$]
G_{wp}	response at the OHC positions to external pressure [$\mathrm{m}^3\mathrm{N}^{-1}$]
G_{wf}	response at the OHC positions to OHC electromotile forces [$\mathrm{m}^2\mathrm{N}^{-1}$]
$G_{w_2f_2}$	response at the OHC2 to OHC2 electromotile force [$\mathrm{m}^2\mathrm{N}^{-1}$]
G_{total}	overall velocity response [$\mathrm{m}^3\mathrm{N}^{-1}$]
$\mathbf{G}$	matrix of the duct responses
$\mathbf{G}_{uf}$	vector of G_{uf} responses
$\mathbf{G}_{wp}$	vector of G_{wp} responses
$\mathbf{G}_{wf}$	matrix of G_{wf} responses
h	thickness of the TM plate [m]
h_s	semi-thickness of the TM plate [m]
H_{11-33}	OHC1-3 gain functions [Nm^{-2}]
$\mathbf{H}$	matrix of the OHC responses
I	moment of inertia of the TM plate [m^3]
k_v	wavenumber of the viscous 'squirting' wave [m^{-1}]
l_j	distance of the OHC from the IHC [m]
L	length of the subtectorial duct [m]
M	bending moment of the TM plate per unit length [N]
p	pressure acting on the TM plate [Pa]
$w(y,t)$	transverse displacement of the TM plate [m]
w_{1-3}	TM plate transverse displacements at OHC1-3 positions [m]
γ	feedback gain [Nm^{-1}]
δ	viscous boundary layer [m]
ν	Poisson's ratio of the TM plate
τ	time delay [s]

Chapter 7

a	effective radius of an indenter [m]
c_1	wavespeed of a compressional wave [ms^{-1}]
c_2	wavespeed of a shear wave [ms^{-1}]
E	Young's modulus of the elastic half-space [Pa]
E_0	magnitude of the complex Young's modulus [Pa]
G_{up}	response at the IHC to external pressure [$\mathrm{m}^3\mathrm{N}^{-1}$]
G_{us}	response at the IHC to OHC area displacements [m^{-1}]
G_{wp}	response at the OHC positions to external pressure [$\mathrm{m}^3\mathrm{N}^{-1}$]
G_{ws}	response at the OHC positions to OHC area displacements [m^{-1}]
$G_{w_2s_2}$	response at the OHC2 to unit area displacement at OHC2 [m^{-1}]
G_{total}	overall velocity response [$\mathrm{m}^3\mathrm{N}^{-1}$]
$\mathbf{G}$	matrix of the duct responses
$\mathbf{G}_{us}$	vector of G_{us} responses
$\mathbf{G}_{wp}$	vector of G_{wp} responses
$\mathbf{G}_{ws}$	matrix of G_{ws} responses
H_{11-33}	OHC1-3 gain functions [m]
$\mathbf{H}$	matrix of the OHC responses
k_1	wavenumber of a compressional wave [m^{-1}]
k_2	wavenumber of a shear wave [m^{-1}]
k_v	wavenumber of the viscous fluid-elastic wave [m^{-1}]
K	complex stiffness of the TM [Nm^{-1}]
K_0	magnitude of the complex stiffness [Nm^{-1}]
L	length of the subtectorial duct [m]
$p(y,t)$	subtectorial fluid's pressure [Pa]
p_{ext}	external driving pressure [Pa]
R	real part of wavenumber [m^{-1}]
S_{wall}	wall stiffness of the elastic half-space [Nm^{-3}]
s_{1-3}	internal area displacements from OHC1-3 [m^2]
$u(y,t)$	radial particle displacement of the subtectorial fluid [m]
$v(y,t)$	transverse particle displacement of the subtectorial fluid [m]

$w(y,t)$	transverse displacement of the elastic half-space [m]
w_{1-3}	elastic half-space displacements at OHC1-3 positions [m]
X	imaginary part of wavenumber [m^{-1}]
Z_{TM}	TM impedance [Nsm^{-1}]
α	imaginary part of wavenumber [m^{-1}]
β	real part of wavenumber [m^{-1}]
γ	feedback gain [m]
μ	loss factor in the elastic half-space
ν	Poisson's ratio of the elastic half-space
τ	time constant of the OHC gain filter [s]

Appendix B and D

K_{b0}	BM stiffness at the base [Nm^{-1}]
$K_{bL/2}$	BM stiffness in the middle of the CP [Nm^{-1}]
K_{bL}	BM stiffness at the apex [Nm^{-1}]
y_0	parameter value at the base
$y_{L/2}$	parameter value in the middle of CP
y_L	parameter value at the apex
$\gamma_{\mathrm{global}\,0}$	global active gain of the quasi-linear model at step 0 of iteration
$\gamma_{\mathrm{global}\,1}$	global active gain of the quasi-linear model at step 1 of iteration

Appendix E

A	complex amplitude of travelling waves in the positive direction
B	complex amplitude of travelling waves in the negative direction
C	complex amplitude of evanescent waves in the positive direction
C	complex amplitude of evanescent waves in the negative direction
A_i	complex amplitude of incident waves in the positive direction
B_r	complex amplitude of reflected waves in the positive direction

C_i	complex amplitude of incident waves in the negative direction
D_r	complex amplitude of reflected waves in the negative direction
G_{up}	response at the IHC to external pressure [m^3N^{-1}]
G_{uf_j}	response at the IHC to OHC force at position j [m^2N^{-1}]
G_{w_ip}	response at the OHC position i to external pressure [m^3N^{-1}]
$G_{w_if_j}$	response at the OHC position i to OHC force at position j [m^2N^{-1}]
i	position of the output along the subtectorial duct
j	position of the input along the subtectorial duct
k_+^p	wavenumber of the wave propagating in the positive direction [m^{-1}]
k_-^p	wavenumber of the wave propagating in the negative direction [m^{-1}]
k_+^n	wavenumber of the standing nearfield in the positive direction [m^{-1}]
k_-^n	wavenumber of the standing nearfield in the negative direction [m^{-1}]
k_0	real part of the wavenumber's travelling wave component [m^{-1}]
k_1	real part of the wavenumber's nearfield component [m^{-1}]
k_2	imaginary part of the wavenumber's nearfield component [m^{-1}]
k_{a-f}	roots of the wavenumber of the 'squirting' wave [m^{-1}]
l_i	distance of the output from the IHC [m]
l_j	distance of the input from the IHC [m]
$p_+(y)$	subtectorial fluid's pressure in the positive direction [Pa]
$p_-(y)$	subtectorial fluid's pressure in the negative direction [Pa]
R_+	reflection coefficient in the right-hand side region from input
R_-	reflection coefficient in the left-hand side region from input
$u_+(y)$	radial fluid particle displacement in the positive direction [m]
$u_-(y)$	radial fluid particle displacement in the negative direction [m]
$u_{v+}(y)$	radial viscous fluid's particle displacement in the positive direction [m]
$u_{v-}(y)$	radial viscous fluid's particle displacement in the negative direction [m]
$w_+(y)$	transverse plate displacement in the positive direction [m]
$w_-(y)$	transverse plate displacement in the negative direction [m]
$w_{v+}(y)$	transverse plate displacement for viscous waves in the positive direction [m]
$w_{v-}(y)$	transverse plate displacement for viscous waves in the negative direction [m]
$w_+^n(y)$	transverse plate displacement of the positive standing nearfield [m]
$w_-^n(y)$	transverse plate displacement of the negative standing nearfield [m]

I	integral
α	imaginary part of the complex wavenumber [m^{-1}]
α_2	imaginary part of the wavenumber's nearfield component [m^{-1}]
β	real part of the complex wavenumber [m^{-1}]
β_1	real part of the wavenumber's travelling wave component [m^{-1}]
β_2	real part of the wavenumber's nearfield component [m^{-1}]

Appendix G

G_{up}	response at the IHC to external pressure [m^3N^{-1}]
G_{us_j}	response at the IHC to OHC area displacement at position j [m^{-1}]
G_{w_ip}	response at the OHC position i to external pressure [m^3N^{-1}]
$G_{w_is_j}$	response at position i to OHC area displacement at position j [m^{-1}]
$p(y)$	subtectorial fluid's pressure [Pa]
p_+	complex amplitude of subtectorial fluid's pressure in the negative direction
p_-	complex amplitude of subtectorial fluid's pressure in the negative direction
p_L	subtectorial fluid's pressure in the left-hand side region from source [Pa]
p_R	subtectorial fluid's pressure in the right-hand side region from source [Pa]
$u(y)$	radial fluid particle displacement [m]
u_+	complex amplitude of fluid's particle displacement in the negative direction
u_-	complex amplitude of fluid's particle displacement in the negative direction
u_L	fluid particle displacement in the left-hand side region from source [m]
u_R	fluid particle displacement in the right-hand side region from source [m]
$w(y)$	transverse elastic half-space displacement [m]
w_L	elastic half-space displacement in the left-hand side region from source [m]
w_R	elastic half-space displacement in the right-hand side region from source [m]
S_{wave}	'dynamic wave stiffness' of the fluid-elastic wave [$kgm^{-2}s^{-2}$]

Comments:

1. Matrices are presented in upper case bold typeface

2. Vectors are presented in lower case bold typeface

3. $\dot{}$ and $\ddot{}$ represent the first and second derivative of a variable with respect to time

4. Some variables dependent on x may also depend on ω

List of Abbreviations

BM	basilar membrane
CF	characteristic frequency
CP	cochlear partition
DC	Deiter's cell
DOF	degree of freedom
IHC	inner hair cell
LDV	laser Doppler velocimeter
M	microscope
MET	mechano-electrical transduction
OHC	outer hair cell
OHC1	first row of outer hair cells from sulcus side
OHC2	second row of outer hair cells from sulcus side
OHC3	third row of outer hair cells from sulcus side
PD	photodiode
RL	reticular lamina
SPL	sound pressure level
TM	tectorial membrane

Chapter 1

Introduction

1.1 Why model the cochlea?

The cochlea is thought to be the main structure responsible for the processing and analysis of sound in the periphery of the hearing system. Therefore, it is of great importance to understand its underlying processes, since they determine its performance. These processes appear to be very complex however, involving mechanical, electrical and chemical interactions, and are thus difficult to analyse.

Not only is access to the cochlea, deeply embedded in the temporal bone and of a very small size, very difficult, but also the physiological processes within it are extremely vulnerable. Any interference within the cochlear environment may cause the cochlea to work in a different manner than normally. For example, to measure the cochlear response or its mechanical properties under realistic conditions, the cochlea is often excised, unsealed and artificially preserved in conditions similar to those within the body. After such a treatment the cochlea's state and physiological processes deteriorate rapidly until its behaviour resembles that of a dead cochlea. Secondly, even the most modern techniques introduce many artefacts, which may deform the cochlear response and reveal difficult to analyse or unrealistic features. Finally, since the response of a dead cochlea significantly differs from that of a live one, the measurements have to be carried out on cochleae in a very good condition, e.g. immediately after the death or under deep anaesthesia. Therefore the experiments are conducted on mammalian

or other species to find analogies with human hearing, which may itself confuse interpretation.

Cochlear models are generally built to explain and interpret the results of these difficult cochlear experiments. The models attempt to gather all information obtained experimentally into one functional representation of the real structure. Cochlear models enable analysis and interpretation of the experimental results but may also stimulate the physiological research. Since the models are built on the experimental data, the lack or inaccuracy of the data can stimulate further research. The ultimate goal of each cochlear model is to reproduce the results of the experiment, so that the behaviour of the real system could be predicted when new conditions are applied. For example, cochlear models might be helpful when predicting the impact of damage or disorders to cochlear function, and may even provide information useful to compensate for them.

The cochlea is an organ that possesses many remarkable characteristics. The astonishing filtering ability, dynamic range, and the analysis and recognition of speech signals by human hearing under very adverse conditions, are all achieved thanks to the cochlea. It seems therefore that a knowledge of cochlear physiology could be used in many engineering applications.

1.2 Aims

Cochlear models could describe some processes within the cochlea, but currently fail to give a realistic or comprehensive picture of the full cochlear function. For example, the mechanism of the cochlear response amplification, the so-called cochlear amplifier [13], is still not well understood. The literature of the subject reveals significant inconsistency between different approaches. Though some authors have postulated that some active models can be thought of as equivalent [16], they are difficult to analyse and compare [82]. Furthermore, there is a lack of common ground in describing some aspects of the cochlear micromechanics, for example there is no complete and consistent set of mechanical and geometrical parameters, due to sparse experimental data. Finally, some researchers argue that a high dimensional complexity (3D) of the cochlear models is necessary to

obtain a realistic model's response [50]. On the other hand, simplified 1D models are often used to explain cochlear function [68], and it can be argued that the complex models do not seem to give more insight into the dynamics of the cochlea than the one-dimensional models.

Therefore, in this thesis we aim to investigate the basic concepts of micromechanical modelling, initially concentrating on the example of a classical model of the cochlea proposed by Neely and Kim in [68]. The objective in this case is to gain insight into the model's assumptions and properties, through the analysis of its modes of vibration, parameters and active components. This model is then developed so that its predictions can be used to compare with experimental data such as that measured, for example, by Gummer *et al.* [40].

Another objective of the present work, was to investigate a distributed parameter model, i.e. the 'squirting wave' model proposed by Bell and Fletcher [9], as another mechanism for cochlear response amplification. The objective was to extend the model by introducing an active component in the form of a feedback loop from the outer hair cells, in order to examine whether this could overcome the very significant damping within the system.

1.3 Contributions

The main contributions of the present work are:

1. The analysis of the dynamics, modes of vibration, active mechanism and stability of the Neely and Kim [68] and Neely [66] cochlear models.

2. Comparison of the mobility responses of the above two degree of freedom models with the experimental data of the response of basilar and tectorial membrane measured by Gummer *et al.* [40] and Hemmert *et al.* [43].

3. An analysis of the active quasi-linear model of the cochlea with an investigation of stability in positive feedback models.

4. Extension of the 'squirting' wave mechanism, proposed by Bell and Fletcher [9] for the model of amplification of fluid motion in the subtectorial space, by

introducing and investigating of the effects of viscosity to the propagation of the 'squirting' waves and incorporation of an active feedback loop from the outer hair cells.

5. Development of a fluid-elastic wave model proposed by Elliott [20] for amplification of fluid motion in the subtectorial space, with incorporation of active feedback from outer hair cells.

Some of the results presented here were published and presented in:

- Elliott S.J., Pierzycki R. and Lineton B. (**2005**) "Incorporation of an active feedback loop into the squirting wave model of the cochlear amplifier," Proc. Int. Conf. Sound and Vibration (ICVS12), Lisbon.
- Pierzycki R., Elliott S.J. and Lineton B. (**2005**) "Active 'squirting wave' model of cochlear amplifier," IEEE, EMBSS, UKRI Postgrad. Conf. on Biomed. Eng. and Medical Phys. (PGBIOMED'05), Reading, UK
- Pierzycki R., Elliott S.J. and Lineton B. (**2005**) "'Squirting wave' model of the cochlear amplifier with active feedback," BSA Short Papers Meeting on Experimental Studies of Hearing and Deafness, Cardiff.
- Pierzycki R., Elliott S. J. and Lineton B. (**2006**) "Two models for fluid-structural waves in the organ of Corti," Institute of Acoustics Spring Conference, Southampton.

Chapter 2

The Cochlea

This chapter summarizes some facts about cochlear anatomy and physiology, and briefly describes the cochlear innervation at the hair cells. Some sections (2.1, 2.2.1 and 2.3) are presented to give the basis for general understanding of the cochlear function. However, an attempt is made to explain cochlear processes as thoroughly, and consistently with recent findings, as possible (Sections 2.2.2, 2.2.3), although without moving too much into the details beyond the scope of the thesis. It has to be remembered that many uncertainties, especially corresponding to the physiology of the cochlea, are still present and are subject of ongoing research.

Section 2.1, describes the anatomy of the cochlea, referring mainly to a human cochlea. In the following section the cochlea's mechanics, specifically, the so-called macro- and micromechanics and the outer hair cell mechanics, are characterised. The chapter concludes with a brief description of cochlear nonlinearities.

2.1 Anatomy

The cochlea is a small bony structure, coiled around a bony tube called the modiolus and embedded deep in the temporal bone [90]. Its shape is similar to the shell of a snail with a number of coils and dimensions different for particular species, e.g. the overall dimensions of a human cochlea coiled into 2 and 3/4

coils, amount to about 5 mm in height and 9 mm in diameter at the base [35].

For better visualisation, the cochlea is often presented as an uncoiled system like in Fig.2.1, or in its cross-sectional view where a single slice of the uncoiled structure is taken to describe the structures within as depicted in Fig.2.2. It can be seen from Fig.2.1 that the cochlea tapers along the whole length from its base to the apex. Two membranes, the Reissner's membrane and basilar membrane (BM), which run through almost entire length of the cochlea, divide it into three compartments: the scala vestibuli, scala media and scala tympani, as the cross-sectional view in Fig.2.2 reveals. The two outermost scalae, the scala vestibuli (upper) and scala tympani (bottom) are joined by a small opening at the apex of the cochlea called the helicotrema. The third, scala media, shown in Fig.2.2, located between scala vestibuli and tympani, creates an inner closed compartment. Furthermore, at the base of the cochlea, the upper cochlear channel, the scala vestibuli, is terminated with a membraneous oval window, which connects with the stapes of the middle ear ossicles (Fig.2.1), while the scala tympani is terminated by the membranous round window, which connects with the cavity of the middle ear.

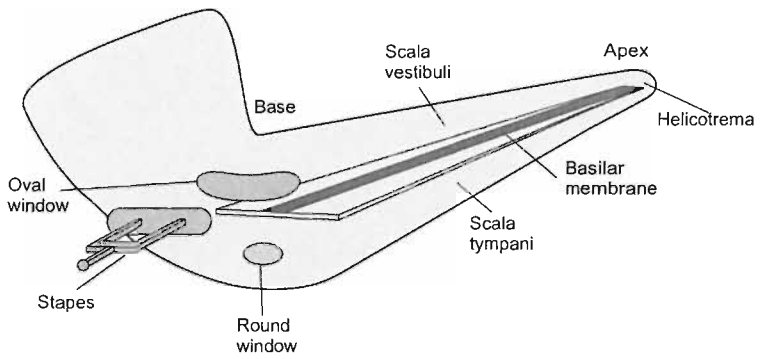

Figure 2.1: Schematic view of an uncoiled cochlea.

The scalae are filled with two kinds of fluids, which differ in the ionic composition. The scala vestibuli and scala tympani are filled with perilymph which has a high sodium ion content, whereas the scala media is filled with endolymph, a fluid with high potassium ion content [90]. The properties of the cochlear fluids are often assumed to be similar to those of the sea water because of the Na^+

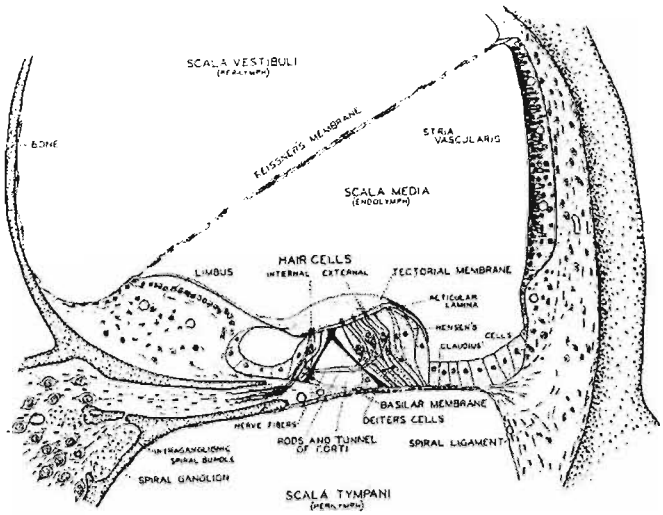

Figure 2.2: Cross-sectional view of the cochlea with indication of the cochlear channels. Reused with permission from Hallowell Davis, The Journal of the Acoustical Society of America, 34, 1377 (1962). Copyright 1962, Acoustical Society of America.

ion content[1] [35, 79, 96]. Furthermore, the endolymph exhibits a high resting potential (endocochlear potential) of about +80 mV, whereas the perilymph has a nearly zero potential, being +5 mV and +7 mV in scala vestibuli and tympani, respectively [79]. It should be also noted that the perilymph is able to diffuse beyond the BM, so that it is the tight arrangement of the apices of the sensory and supporting cells that creates the actual boundary for the perilymph-like fluids and therefore the bodies of some cells are bathed in them [90].

One of the most physiologically important structures of the cochlea is the BM, the length of which is different in different species. In the human ear the BM length is equal to approximately 35 mm. The structure of the BM differs along the length of the cochlea, so that, although the cochlea's width tapers from the base to the apex, the BM widens from its narrow base, about 0.1 mm, to the

[1] Although the cochlear fluids are assumed to have properties similar to the properties of the sea water, the fluid's density equal to 1000 kgm^{-3}, which is approximately the density of the fresh water, i.e. 998 kgm^{-3} [48], is often used in the models of the cochlea [9, 68].

wide apex end of about 0.5 mm [35]. The thickness of the BM is often represented as changing reciprocally to its width in such a way that it is thick at the base and thin at the apex of the cochlea, as can be seen e.g. for chinchilla cochlea measurements of Lim[2] [57, 58].

In the radial aspect the BM can be divided into two separate regions. The first, extending from the spiral limbus to the foot of the outer pillar cells, is called the arcuate zone (due to the arch of Corti formed by the pillar cells), while the second, extending from the foot of the outer pillar cells to spiral ligament, is called the pectinate zone. Also in the radial dimension the BM exhibits structural complexity. For instance the chinchilla cochlear measurements reveal that the proportion of the arcuate and pectinate zones' width changes along the cochlea with the arcuate zone being narrower than the pectinate zone near the base and almost equal at the apex of the cochlea [57, 58]. Furthermore, the thickness of both of these regions is thought to decrease from base to apex as presented by Lim [57, 58].

The width and thickness changes of the BM have implications for the structure's mechanical properties. Though it is hard to measure the mechanical parameters of the BM, it is widely accepted that the properties of the BM are dominated by its elasticity, such that its stiffness is highest in the basal region of the cochlea and decreases exponentially towards the apex [79]. Furthermore, the logarithmic slope of the BM's stiffness gradient along the cochlea was found to agree reasonably with the slope of the so-called place/frequency maps of a dead cochlea of e.g. human [39]. Thus, to span the frequency range of human hearing from 20 Hz–20 kHz and assuming a constant mass along the length of the BM, the stiffness must decrease a millionfold from the base to the apex. However, it has to be noted that although the mass of the BM is often assumed constant

[2]Slepecky [90] reports that the total BM thickness depends on the combination of the so-called homogeneous ground substance, the BM filaments and cells of the tympanic border (mesothelial cells). Since the population of mesothelial cells increases with the distance from the base, the total thickness of the BM increases, though the thickness of the homogeneous ground substance and the filaments decreases over the length of the cochlea. Therefore, in present considerations when referring to the thickness of the BM we refer to the thickness of the homogeneous ground substance and the filaments.

(e.g. [68]), in reality it must increase from base to apex due to the width and thickness changes along the cochlea [90].

It is often assumed that the BM stiffness changes longitudinally, and hence stiffness is a function of position along the cochlea [68]. However, because some experimental data suggests no, or insignificant, longitudinal coupling in the BM [78], and the BM fibres are spanned between the spiral limbus and the spiral ligament, each segment of the BM can be considered as an independent bar of which the point impedance could be inferred [17].

A specialised structure, called the organ of Corti, is shown in Fig.2.3. The organ of Corti rests on the BM and contains receptor cells, the hair cells, that innervate the cochlea through the connection with the synaptic ends of the auditory nerve fibres. The size of the organ of Corti is thought to change continuously along the cochlea, so that it increases from the base to the apex together with the increasing size of its cells [58, 90]. Several types of cells, of different physiological function, have been identified in the organ of Corti. The most important of them are two types of sensory cells called the hair cells due to the bundles of hair-like projections from their apical surfaces, the stereocilia.

There are about 3,500 of the first type of hair cells, the flask-shaped inner hair cells (IHCs), which are innervated mainly by the afferent (centripetal) nerve fibres and formed in one row running along the cochlea [35, 90]. The dominance of the afferent innervation in the IHC suggests that the IHCs have a predominantly sensory role in transduction [90]. The body of the IHC does not contact the BM. In the direction from the spiral limbus to the spiral ligament, the IHCs are tightly packed between the inner border and inner phalangeal cells (not indicated in figures), with their tops separated by supporting cells, but the basal parts of the cells' bodies (region of the nucleus) not separated from one another [90].

The second type of hair cells are the cylindrically shaped outer hair cells (OHCs), of which there are about 12,000 [35]. The OHCs are supported by the Deiters cells, hence not in direct contact with the BM, and innervated mainly by the efferent (centrifugal) nerve fibres. Although providing some sensory input, the OHCs are therefore rather thought to modify the mechanical response of the organ of Corti [90]. They form three to five rows along the cochlea, and their

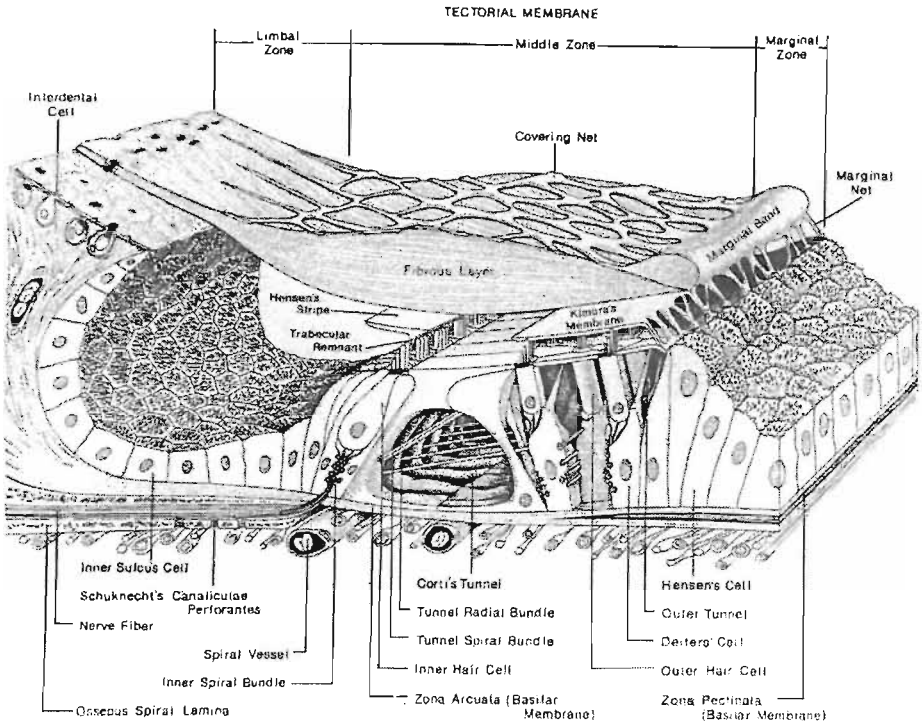

Figure 2.3: Schematic view of the organ of Corti. Reprinted from Hearing Research, 22, Lim, D. J., "Functional structure of the organ of Corti: a review," 117-146, Copyright (1986), with permission from Elsevier.

bodies are not in contact with each other due to their embedding in the Deiters cells and separation at their apices by the phalangeal processes of the Deiters cells. The OHCs are smaller in diameter than the IHCs [90]. However, the OHC cell bodies increase their length with the distance from the base of the cochlea, where no such size distribution was observed for the IHCs [58].

As in the case of the scala media fluid, the hair cells are DC-polarised (resting potentials) by about $-40\,\mathrm{mV}$ and $-70\,\mathrm{mV}$ for the IHCs and OHCs, respectively [11, 35]. Furthermore, both kinds of cells exhibit AC-receptor potentials, i.e. the responses of the hair cell after stimulation [35]. These responses are frequency and level-dependent [11].

It was said that the hair cells owe their name to the bundles of stereocilia protruding from the cuticular plates of the cells' apices. It can be seen from Fig.2.4 that the hair bundles, similar to the cells' bodies, are arranged in rows. There are three rows of the stereocilia, which differ in length, as shown in Fig.2.4, and are organised in a bundle in such a way that the shortest row is on the modiolus side, whereas the tallest row is on the lateral wall side of the organ of Corti. The bundles of both types of hair cells reveal differences in their shape and arrangement. The bundles shape a shallow 'U' on the tops of the IHCs, but form a 'W' or 'V' on the OHC's apical surfaces [35, 58, 90]. The cilia[3] are able to pivot about their rootlets, which are embedded in the cuticular plate, where the embedding of the OHC's rootlets into the shaft of the stereocilium is deeper than that of the IHC's [26, 33]. Furthermore, the cilia of the OHCs are longer and thinner than those of the IHCs [33, 90], and their length increases with the distance from the base in the OHCs but varies only slightly for the IHCs [98, 58]. It was reported by Lim [57, 58] that the number of OHC's cilia is inversely proportional to their height along the cochlea, i.e. as the height of the cilia increases, their number decreases towards the apex.

The cilia of the hair cells form tight bundles due to their cross-links on their lateral walls, connecting the adjacent cilia within and between the rows, so that the bundle moves as a single unit when the tallest row of cilia is deflected. Addi-

[3]It should be noted that the stereocilia are not true cilia [44, 79]. However, for the sake of compatibility with previous studies (e.g. [68]), they will be also referred to as cilia.

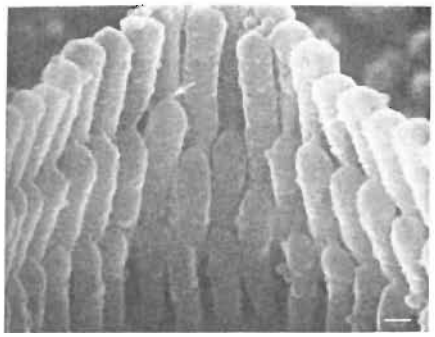

Figure 2.4: Rows of stereocilia in a hair bundle of a guinea pig outer hair cell (the arrow indicates a cilia tip link; scale bar 200 nm). Reprinted from Pickles, J. O., "An Introduction to the Physiology of Hearing," Second Edition, Copyright (1988), with permission from Elsevier.

tionally, the tip of each shorter stereocilium is connected with the wall of the taller cilia by the so-called 'tip links' as shown in Fig.2.5 [90]. Finally, the mechano-sensitive ion channels, thought to take part in the transduction process, appear to be located near the tip links in the cilia walls [90].

Figure 2.3 shows that the IHCs and the OHCs are separated by the pillar supporting cells, which together with the phalangeal processes of the Deiters cells form a close knit layer at their tops, the reticular lamina (RL) depicted in Fig.2.6. Furthermore, the RL is angled along the cochlea and the angle relative to the BM increases from the base to the apex [58]. The inner and outer pillar cells form Corti's tunnel (Fig.2.3), and the Deiters cells are assumed to provide a rigid support to counteract the mechanical stress during the organ's vibrations as well as to mediate in the transfer of vibrations from and to the BM [90]. It has been suggested that the high level of energy consumption within the Deiters cells indicates an additional role of these cells, other than just as a mechanical support [90].

The remaining supporting cells, which have a functional role that is less understood, are the Hensen cells, considered to be a part of organ of Corti, with microvilli on the apical surfaces assumed to facilitate the ion exchange [90]. The Claudius cells, resembling Hensen's cells but smaller in size, and Boettcher cells,

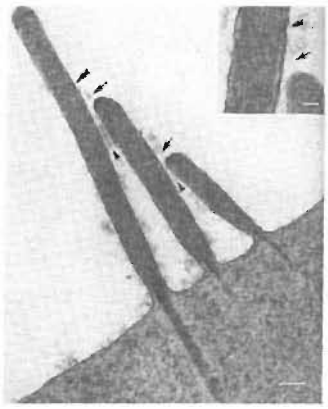

Figure 2.5: Tip links connecting the cilia of the neighbouring rows in a hair bundle (arrows). Also the cross-links between the cilia rows are visible (arrowheads; double arrowhead: upper point of the tip link attachment; scale bar 200 nm). Reprinted from [79] after Hearing Research, 35, Osborne, M. P., Comis, S. D. and Pickles, J. O., "Further observations on the fine structure of tip links between stereocilia of the guinea pig cochlea," 99-108, Copyright (1988), with permission from Elsevier.

on which the Claudius cells rest in the basal part of the cochlea, are the supporting cells on the lateral wall side of the organ of Corti, but structurally not recognised as the part of the organ [90]. The Boettcher cells are assumed to have a transport function due to their large area relative to the volume, whereas the Claudius cells (and Hensen cells) may play an important role in homeostasis as reported recently in [36]. Finally, the lateral wall and the leftmost (in Fig.2.3) boundary of the BM, are covered with the external and inner sulcus cells, respectively.

The last structure to be described here, is the tectorial membrane (TM) covering the organ of Corti as can be seen in Fig.2.3. It is a gelatinous structure with the mass increasing from the base to the apex of the cochlea, and composed of two types of fibres, A and B. The fibres, due to their distribution and packaging arrangement of the B fibres, divide the TM in the radial aspect into the limbal, middle and marginal zones [58, 90].

The first of these zones connects the TM with the spiral limbus, and hence it

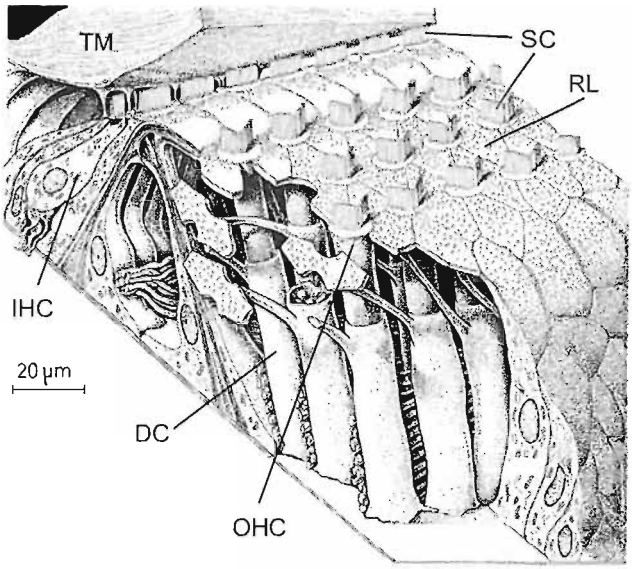

Figure 2.6: The view of the main structures of the organ of Corti after uncovering the tectorial membrane (DC-Deiters' cells, SC-stereocilia, TM-tectorial membrane, see text for others). Reprinted from "Human Microscopic Anatomy. An Atlas for Students of Medicine and Biology," 1991, p. 554, Chapter: Sensory Systems, by R. V. Krstić, Figure 1 of Plate 265, Copyright Springer-Verlag Berlin Heidelberg 1991, with kind permission of the author and Springer Science and Business Media.

is called the limbal zone (Fig.2.3). The third zone, the marginal zone, together with the marginal band covering the body of the TM, connects the membrane to the supporting cells below through the marginal net [90], but only partially closes the subtectorial space due to the holes in this outer insertion to the organ of Corti [36]. The thickest part, the middle zone, forms the main body of the TM covering the sensory cells. The tops of the tallest row of the OHC stereocilia are embedded in the TM, whereas the IHC cilia are thought to be freely projecting from the cell's body or weakly attached to the TM, although the opinion on the IHC's attachment is more controversial [58, 90, 98]. The slanted arrangement of the fibres of the amorphous under-surface of the TM, referred to as Kimura's membrane (Fig.2.3), which coincides with the slanted arrangement of the stereociliary bundle formation [58], and the imprints of the cilia in this layer, prove their strong coupling with the TM [36, 58]. It is the stereocilia's attachment to the TM that suggests the membrane's importance in the transduction process. Furthermore, the fibrous network arrangement of the TM is thought to contribute to its tensile strength and stretch resistance, which may be important when the stiffness of the membrane is to be estimated [90].

2.2 Cochlear mechanics

The mechanics of the cochlea will be described in the following sections. It is convenient to divide the functional analysis of the cochlea into two separate classes. Firstly, the so-called macromechanical vibrations, which describe the interactions of the cochlear fluids with the flexible partition (see Fig.2.1), often referred to as the cochlear partition and resembling the BM in its mechanical properties, will be discussed. Secondly, the vibrations on the 'micro' level, called the cochlear micromechanics and elucidating the interactions of the structures within the organ of Corti, will be addressed.

2.2.1 Macromechanics

The macromechanics of the cochlea describes the interactions of the cochlear fluids with the cochlear partition. Two main assumptions are posed when dealing

with the macromechanical behaviour of the cochlea. Firstly, the organ of Corti and all specialised structures, are thought to constitute a homogeneous partition, the cochlear partition (CP) [78]. Secondly, the impedance of thin Reissner's membrane [90], is assumed to be small, so that it can be neglected and the scala vestibuli and scala media will form one compartment. Therefore, the flexible CP of specified impedance, divides the cochlea into two, the upper and the lower cochlear chambers, as presented in Fig.2.1.

When the sound wave reaches our ears it is transmitted via the vibrations of the tympanic membrane to the chain of the ossicles of the middle ear, of which the last one, the stapes, connects to the oval window in the wall of the cochlea. The vibrations of the stapes cause pressure changes in its vicinity and a propagating fluid wave, which induces a propagating transverse displacement of the CP.

It is assumed that the cochlear fluids are incompressible, so that the inward displacement of the stapes results in the outward (towards the middle ear cavity) displacement of the round window. In other words, if the oval and the round windows are replaced with pistons which move inward and outward with regard to the cochlear chambers, then only the so-called 'push-pull' condition, that is the pistons' displacements in opposite directions, would cause the transverse displacement of the CP [78], known as the travelling wave. It is worth emphasising that the pressure wave does not propagate from the stapes, through the helicotrema, towards the round window, as often suggested. The pressure in the two chambers is able to equalise through the helicotrema only for low frequencies, however, mass and viscosity of the fluid have more of an effect at high frequencies [78]. At these higher frequencies the pressure is equalised through a region of the CP that has a high mobility at that frequency.

The travelling wave on the partition slows down along the length of the cochlea, until some specified point along the cochlea, where it reaches its maximum transversal displacement and after which it rapidly decays as depicted in Fig.2.7. The point for which the maximum of the travelling wave occurs is called the characteristic place and corresponds to a particular stimulus frequency. In the same manner, the frequency for which the maximum displacement at one place on the CP is observed, is called the characteristic frequency (CF). This

place-frequency dependence of the partition's maximum displacement defines the tonotopic character of the cochlear response and is derived experimentally in the form of the cochlear frequency-to-place maps, which are individual to particular species [39, 56].

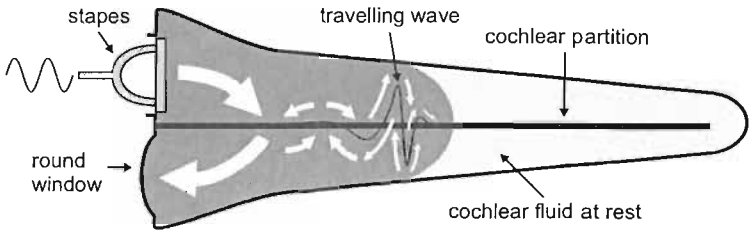

Figure 2.7: The cochlear partition's travelling wave propagating in the cochlea. The arrows indicate the local fluid flow along the cochlea. Redrawn after Trends in Neurosciences, 21, Nobili, R., Mammano, F. and Ashmore, J., "How well do we understand the cochlea?," 159-167, Copyright (1998), with permission from Elsevier.

The experiments on the cochlear response of different species show that the basal portion of the partition responds to high frequencies, whereas the apical position responds to low frequency stimuli [87]. This can be seen from the CF/place map derived for the human cochlea after [39], presented in Fig.2.8. Additionally, the response curve is more sharply tuned near the base and broadens with the distance along the cochlea [79].

Experiments of von Békésy, carried out on cadavers' ears, revealed large accumulations in the phase response [8]. This led to rejection of the theory of simple oscillators existing within the cochlea, so that the travelling wave mechanism was proposed. However, the amplitude responses observed by von Békésy for the dead cochleae were much broader than those measured more recently in live cochlea, which also have the characteristic place moved towards the apex for given tonal stimulus [87]. The difference between the response of a dead and live cochlea, presented in terms of the displacement of the BM as a function of position along the cochlea, is depicted schematically in Fig.2.9. The broad tuning of the passive response is also not consistent with the fine frequency selectivity of the human

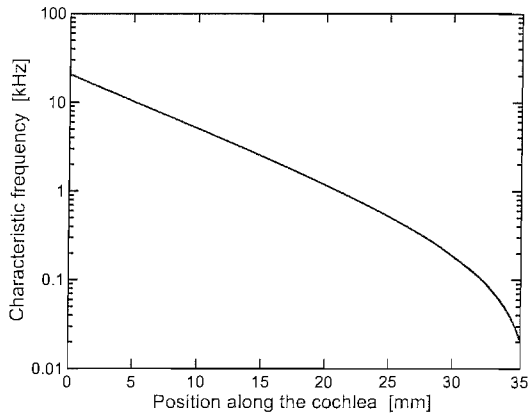

Figure 2.8: Characteristic frequency/place map for a human cochlea calculated after [39].

hearing [62].

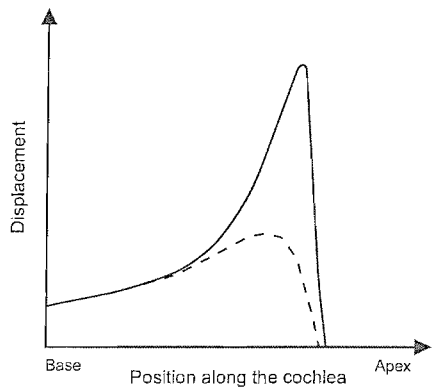

Figure 2.9: Schematic of a passive (dashed) and active (solid) basilar membrane response curve as a function of position along the cochlea.

To explain the subtleties of the cochlear response, a more complicated mechanics, often referring to as the cochlear micromechanics, must be considered. It was postulated that an active process, later named as the cochlear amplifier [13], must be present within the cochlea in order to obtain responses as sharp as those observed in the live specimens [14, 78, 79, 87]. In general, the cochlear amplifier was assumed (i) to pump energy to the system, and (ii) acting against

the viscous forces of the CP, to enhance the displacement of the travelling wave close to the characteristic place. However, only with the discovery of the OHC's electromotility was a candidate for triggering and controlling the active mechanisms within the cochlea found. Furthermore, because the OHCs are situated within the organ of Corti, the interactions of the structures within the organ are of great importance.

2.2.2 Micromechanics

The vibrations of the BM induced by the pressure difference in the fluids of the upper and lower cochlear chambers, are thought to displace the organ of Corti in the transversal direction. The geometrical and anatomical analysis suggests that the organ of Corti is pivoting at the feet of the inner pillar cells, where it is thought to be fairly rigid. This is shown schematically in Fig.2.10. Because the TM is also thought to pivot around a hinge (or, in some models, to pivot and vibrate in the radial direction [1, 68]), the upward displacement of the BM causes shearing forces between the reticular lamina (RL) and the under-surface of the TM, in which the tallest row of the OHC's stereocilia is embedded.

The cilia of the hair cells thus pivot around their rootlets' anchoring in the apical surface of the cell's body, the cuticular plate. The shearing forces between the RL and the TM lead to the deflection of the OHC's stereocilia, and during the upward displacement of the BM, they are displaced towards the lateral wall of the cochlea [35, 79]. The tight arrangement of the OHC's stereocilia within the bundle enables the deflection of the whole hair bundle and is thought to open the mechano-sensitive ion channels (transduction channels) due to the tip links connections of the neighbouring stereocilia. Although the total excursion of the bundle is estimated to be smaller than the radius of the stereocilium itself [28], it is sufficient to open the ion channels, so that the potassium ions flow into the cell body, causing depolarisation, and in turn its shortening. The shortening of the OHC's soma is thought to exert forces, which pull the BM towards the scala vestibuli, and therefore its displacement becomes bigger than just due to the pressure difference from the cochlear fluids. Thus, the OHCs are thought to enhance the mechanical response of the cochlea during their electromotile

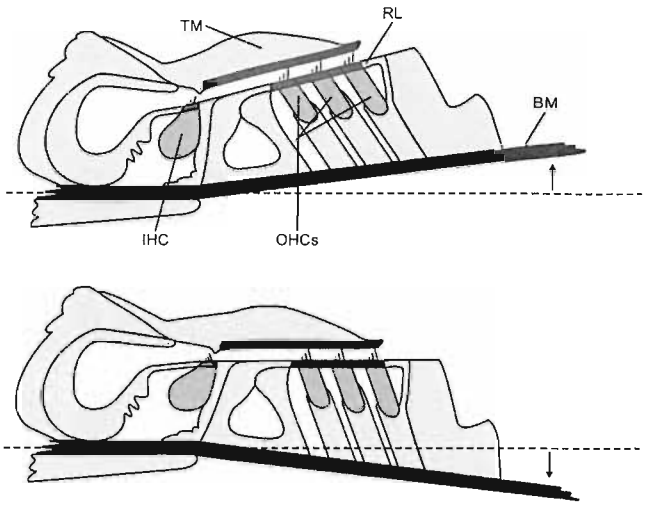

Figure 2.10: Schematic of the basilar membrane positions during the displacement towards the scala vestibuli (top) and scala tympani (bottom). The dashed line indicates the position of the basilar membrane at rest (acronyms as in the text).

action. Furthermore, due to the contractile forces from the OHCs, the fluid in the subtectorial space between the TM and the RL is thought to move towards the cavity of the spiral limbus side of the cochlea, the internal spiral sulcus, deflecting the cilia of the IHCs on its way. The deflection of the IHC's ciliary bundle leads to the closing of the ion channels, which after changing the electrochemical potential of the cell causes ions of calcium to flow into the basal, synaptic pole of the cell initiating release of the neurotransmitters, so that the information about the sound is sent via the afferent nerves to the higher auditory pathways coded in the neural impulses [35].

When the BM is displaced downward, the shearing force between the TM and the RL causes the cilia of the hair cells to move towards the modiolus. In this case the tip links of the stereocilia are thought to be compressed, and hence the transduction channels closed. This leads to the hyperpolarisation of the hair cell. For the OHCs, which were shown to possess the electromotile properties *in vitro* [87], the hyperpolarisation leads to the elongation of the cell's body, during which the BM is thought to be displaced even more towards the scala tympani. Figure 2.11 shows schematically the stereociliary deflection during the excitation

and inhibition of the hair cells.

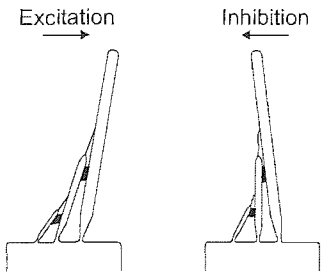

Figure 2.11: Deflections of the outer hair cell's stereocilia. Deflections towards the lateral cochlear wall cause the excitation, whereas deflections towards the modiolus, cause inhibition. The tip links are stretched in the first case and compressed in the latter. Reprinted and adapted from Hearing Research, 15, Pickles, J. O., Comis, S. D. and Osborne, M. P., "Cross-links between stereocilia in the guinea pig organ of Corti, and their possible relation to sensory transduction," 103-112, Copyright (1984), with permission from Elsevier.

The processes described above only outline the complex micromechanics of the cochlea. For instance, some recent data on the mechanics of the organ of Corti exhibit two positions about which the organ pivots. The first of them was found to be located below the feet of the inner pillar cells, as shown in Fig.2.10, or beneath the fibres of the IHCs, while the second one, being the pivot point of the RL, was localised inside the IHC or on the line extrapolating the RL's long axis [31]. Furthermore, the OHCs undergo deformations during the BM motion, i.e. the basal part of the cell's body exhibits displacements in directions different from the apical part, implying that there is no single point of rotation, as observed by Fridberger and de Monvel [31]. Such compound motion of the organ of Corti, in which the BM and the RL are capable of independent rotations, suggests that the rigidity of the organ may be questioned.

An even more complicated picture of the micromechanics of a live cochlea was shown by Nilsen and Russell [71, 72]. These authors reported a complex pattern of the BM displacements in the radial dimension. For the *in vivo* guinea pig preparations, the largest displacements of the BM to characteristic frequency

tones were observed under the Deiters cells, and were thought to be amplified by the action of the OHCs. The displacements under the Deiters cells led in phase, by about 90°, the regions under the outer pillar cells and those adjacent to spiral ligament [72]. Furthermore, Nilsen and Russell argued that the OHCs' amplification is highest when the velocity of the BM vibrations reaches its maximum [71, 72]. With sinusoidal stimulation, the velocity of the BM vibration is maximal when the membrane passes through the resting position and thus has zero displacement, which also implies that the action of the OHCs must be delayed in time with respect to the BM upward deflection. This delay time must therefore correspond to the time in which the cell undergoes the electrochemical processes described before.

The *post mortem* responses measured by Nilsen and Russell lack the OHC's amplification, being reduced by more than 50 dB in comparison with the *in vivo* responses [71]. Furthermore, the regions of the BM width vibrate in phase in response to the characteristic tones exhibiting a flat radial profile, and exceeded the noise floor after the sound level was increased by more than 65 dB SPL [72]. This resembles the situation of von Békésy's experiments on dead cochleae [8].

Studies on the TM's mechanical properties also suggest a more advanced role of this structure in the micromechanics of the cochlea. If the TM is a resonant structure with its own inertia and stiffness, its vibrations may well contribute to the response of the cochlea. The primary function of the TM, in the light of the active processes, is to provide shearing forces to the RL/cilia complex to activate the electromotility of the OHCs. However, some researchers suggest that a secondary resonance is needed within the organ of Corti to explain the shape of the cochlear tuning curve [1, 68]. This resonance, suggested to be half an octave below the resonance of the BM [61], would constitute a second vibrational degree of freedom, as proposed in various cochlear models [1, 68], and would contribute to the response of the CP.

2.2.3 Outer hair cell's mechanics

Recent experiments on the dynamics of the cochlea put emphasis on explaining the mechanism of the cochlear amplifier, so that explaining the OHC's be-

haviour becomes of great importance. One of the unknowns is the behaviour of the hair cell *in vivo*, since its motile response was mainly described *in vitro* under external electrical stimulation [97].

The so-called motor forces, responsible for producing the electromotile forces fed back to the vibrations of the BM, are connected with the OHC's lateral plasma membrane [6, 45]. The OHC's basolateral membrane contains a high density of particles, occupying over 40% of the membrane's area, which were identified as a motor protein and named prestin [4, 5]. The prestin molecules are integral membrane proteins and act as a motor, which extracts the electrical field's energy to generate lateral forces in the plane of the OHC's basolateral membrane. Tight packing of the prestin molecules ensures the force generation along the longitudinal OHC axis after molecular conformational changes occur [5]. In other words, the membrane's potential changes cause the molecules to contract (depolarisation) or expand (hyperpolarisation) within the plane of the membrane, resulting in the OHC's length changes [45]. This is called somatic motility. However, the tight coupling of the motor forces to the plasma membrane and their independence of the underlying cytoskeleton, suggests that the dynamical response of the motor seems to be affected when it is isolated mechanically from the cell (patch recordings) and may behave in a different manner than in the intact cell [6].

The character of the interactions between the radially adjacent OHCs is also not well understood. For instance, in the experiments of Reuter and Zenner, where the half-turn explants of the guinea pig cochlea (*in situ* preparation) were exposed to an electrical field, the excitation normally resulted in the synchronous radial and transversal motile responses of the three rows of the OHCs [84]. However, in some cases an antiparallel movement of the neighbouring OHCs was observed. If the antiphase motion of the adjacent OHCs occurred *in vivo*, it would be consistent with a recently proposed cochlear amplifier model, in which the out of phase motility between the second and neighbouring first and third rows of the OHCs, was suggested to facilitate the RL and TM's oscillations and sustain the motion of the subtectorial fluid towards the IHC's cilia in the form of so-called 'squirting' waves [9].

Ashmore and Géléoc also point out that the OHCs are situated in the matrix

of cells of the organ of Corti so that the length changes could be limited in the intact cochlea, and they argue that, although there is sufficient force generated to distort the neighbouring portions of the organ, the behaviour of its individual components is not clear [6]. These authors propose a secondary loop of OHC's feedback, and suggest that its forces oppose the BM vibration (see Fig.2 in [6]). This secondary loop represents the interactions between cells with an indication of how the potential and displacements of the OHC's of one section may be affected by the displacements in the adjacent section, due to the mechanical coupling between them [6]. It was shown by Zhao and Santos-Sacchi [102] that the electrical motility stimulated in one OHC can induce a change in potential of the adjoining hair cell. This interaction appears to act to oppose the changes in the contiguous cell [102]. Because Zhao and Santos-Sacchi report that the potential in the cell adjacent to the stimulated one is opposite, which may indicate lateral inhibition, the phase difference between these cells would amount to 180° [102]. However, the phase difference under the OHCs (Deiters' cells) in the experiments of Nilsen and Russell, does not reach such a value in any of the measured cases [71, 72]. On the other hand, it has to be noted that in the experiment of Zhao and Santos-Sacchi the interactions of only a pair of the clamped OHCs were investigated, whereas Nilsen and Russell measured the acoustically-evoked response of the BM in the whole organ of Corti where the OHCs were arranged in three rows across the BM width [71, 72].

The interactions between the OHCs in the secondary loop of the overall OHCs' feedback proposed in [6] are thought to generate forces to oppose the BM motion. However, the first loop of the feedback mechanism refers to the mechano-electrical transduction (MET) of the cell leading to a change of the OHC's length and enhancing the response of the BM [6]. Recent results suggest that the amplification, and thus the active processes might be controlled by the MET channels themselves, so that the cochlear amplifier would reside within the hair bundles of the hair cells [5, 28, 52, 97] via so-called 'bundle motility'.

It has been shown that the OHCs can be driven to high frequencies with the somatic motility producing constant force up to 50 kHz under *in vitro* experimental conditions [29]. However, in the real cochlea, the electrical time constant

of the cell's membrane may reduce any potential changes such that they become insufficient to drive the motor [5]. In other words, although prestin is a quick reacting protein, the membrane's potential changes *in vivo* may not be fast enough over the period of a sound wave[4] [52].

One possible mechanism for the active forces from the hair cell bundle is that the tension on the tip links during the deflection of stereocilia, is the source of the force, which is transmitted to the mechanoelectrical transducer (MET) channel through elastic elements, the so-called gating springs [28]. The tension of the tip links is thought to be increased due to the contraction of the myosin molecules with which the tip links are associated [45]. However, this motor protein is thought to have too slow kinetics in order for the proposed 'myosin motor' to work at acoustic rates [5].

Another potential mechanism of transduction assumes binding of the Ca^{2+} ions near the ion channel's interior aspect [45]. Entering of the calcium ions into the ion channels is thought to cause the channels' reclosure and increase in the tip link's tension, thus controlling the forces which act on the bundle and deflect it in the negative (inhibitory) direction [5, 45]. The forces of this fast acting mechanism were proposed to contribute to the mechanics of the cochlea [5].

The mechanisms of adaptation within the OHCs, manifested by a decline of the probability of opening of the MET during maintained hair bundle's displacement, correlate with the two types of the bundle motility [28]. Although not found to exist in one cell at the same time, the slow and fast adaptation processes (the latter being most conspicuous in the mammalian hair cells), having different time constants but both having effect on the intracellular concentration of the Ca^{2+} ions by reducing their influx, seem to connect with the described types of bundle motion, i.e. the slow myosin motor and fast Ca^{2+} direct interactions with the transduction channels (calcium binding mechanism) [28].

Finally, it should be noted that if the fast mechanism observed in the mammalian cell [28], is sufficient to drive the cochlear amplifier, the somatic motility

[4]Ashmore argues that the flow of current around the cells is different *in vivo*, so that it cannot be precluded that in this situation the potentials across the molecule of prestin could still be maintained in the hearing range [5].

which is mediated by prestin and seems to be necessary to supply energy for amplification processes [28, 52], may refer to a slow mechanism which controls the noise of transduction and shifts the hair bundle's operating point [52]. On the other hand the fast, calcium binding mechanism could provide tuning on the MET channels together with mediating the cochlear frequency selectivity and generating forces sufficient to drive the cochlear amplifier [28, 52]. Further experimental evidence is still needed, however, to support the above hypotheses [52].

2.3 Cochlear nonlinearities

In the theory of cochlear mechanics discussed so far, the system described was tacitly assumed to be linear. Specifically, the macromechanical response of the cochlea can be described using the mechanical impedance of the CP, assuming the system is linear. Many studies of models of the cochlea suggest that a linear model is a good starting point [34, 64, 65, 67, 68]. However, the real cochlea, in a pristine physiological condition, exhibits a nonlinear nature of its response [46, 85, 86, 87].

Only a few nonlinear phenomena, being the ones mostly referred to in the literature, will be described in the following section. Among these are: the nonlinear growth of the BM response, the two-tone suppression and generation of distortion products, where the last two are connected with the so-called intermodulation processes. Patuzzi identifies five separate stages of transduction, which, to some extent, exhibit nonlinearity and therefore may contribute to the 'overall' nonlinear behaviour of the cochlear mechanics [78]. These stages include: transformation from the macromechanical vibration to displacement of the hair bundle (1), transformation to current (2), to voltage (3), to the OHCs length changes (4), and finally, to forces exerted in the CP. Since the OHCs are involved in all mentioned stages, the nonlinear processes combined with the OHC action will be also briefly characterised.

The nonlinear BM response to tones of different levels, as shown by the changing frequency response as a function of stimulus level in Fig.2.12 [46, 79], were

first discovered from the measurements of Rhode and confirmed by results of experiments using modern techniques [85, 86, 87]. It can be seen from the figure that the BM displacement becomes broader with the increase of the stimulus level, i.e. the tip-to-tail ratio of the response curve becomes smaller as the level increases from 20 to 60 dB SPL. For the stimulus level of 80 dB it is hard to distinguish the tip from the tail of the observed response curve. Although it is hard to indicate a distinctive peak of the broadly tuned displacement response to a 80 dB stimulus level, it can be seen that the maximum of the curve shifts to the region of lower frequencies, which is another characteristic of the BM's response nonlinearity. Thus, not only is the frequency selectivity in this case poorer but also the CF of the response at a particular BM location is lowered.

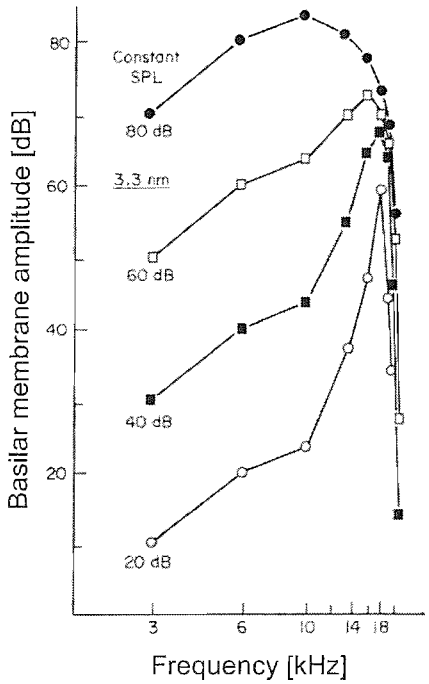

Figure 2.12: Basilar membrane amplitude responses as a function of frequency, observed in the basal end of the cochlea of the guinea pig (18 kHz site) at four different stimulus levels. Reprinted from [79] after Hearing Research, 22, Johnstone, B.M., Patuzzi, R. and Yates, G.K., "Basilar membrane measurements and the travelling wave," 147-153, Copyright (1986), with permission from Elsevier.

Another way of presenting the nonlinearity of the BM response is to show input-output curves for characteristic frequency tones, as shown schematically in Fig.2.13. The stimulus of frequency below or above the CF gives a nearly linear response of the BM [87], however, for CF stimuli the response increases linearly at low levels, to about 30 dB SPL and grows, on average, as 0.2 dB/dB (measured for 40-90 dB) at higher levels [87] as can be seen in the figure. For the levels above 90 dB the displacement response becomes linear again, which can be compared to the dashed line corresponding to a linear response [87].

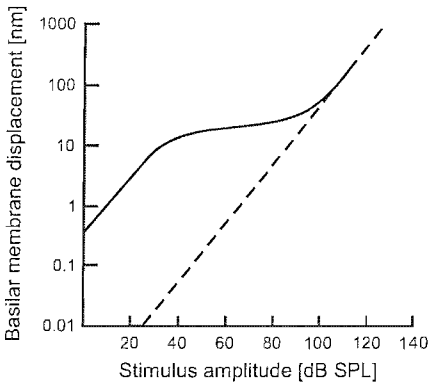

Figure 2.13: The input-output curve revealing the compressive nonlinearity in the live cochlea. The dashed line denotes the linear input-output function as observed in the dead cochleae. Reprinted and adapted from [79] after Hearing Research, 22, Johnstone, B.M., Patuzzi, R. and Yates, G.K., "Basilar membrane measurements and the travelling wave," 147-153, Copyright (1986), with permission from Elsevier.

Changes of the BM amplitude response relative to the changes of the input stimulus level, are also accompanied by changes in the phase responses of the BM. The dependence of the BM phase responses on the intensity of the stimulus measured e.g. for chinchilla and guinea pig, and normalised to a stimuli of moderate intensity reveal three different regions of specific phase behaviour [87]. For the stimuli of frequencies just below the CF increasing phase lags can be observed with an increase of the stimulus intensity. On the other hand, a phase lead, increasing with an increase of the stimulus intensity, can be observed for

frequencies little above the CF. At the CF, however, phase remains relatively constant [87]. This is indicative of a changing phase slope with the stimulus level, so that the group delays decrease with the level increase around the CF, and at the base of the chinchilla cochlea for instance, they amount to a drop of about 380 μs (990-610 μs) with the increase of the stimulus level from 10 to 90 dB SPL despite the phase lag accumulation remains almost constant at the CF [87].

Nonlinearity of the BM response is often thought to be connected with the active mechanisms of the cochlea, the cochlear amplifier. If the compression of the BM displacement is to result from the action of the cochlear amplifier, it will deteriorate not only with the increase of the stimulus level, but also with the deterioration of the cochlea's condition. Thus, the linearisation of the input-output relationship may be indicative of the damage to the cochlea [87].

The OHC's action displays its nonlinear behaviour by four main relationships [78]. The first two of these nonlinearities represent relationships between the displacement (angle of deflection) of the bundle and its stiffness as well as with the electrical conductance of the hair cell's apical membrane [78]. Firstly, the transfer curve, defined by the sigmoidal *Boltzmann function*, characterises the OHC's receptor current correlated with the number of the opened MET channels and dependent on the cilia deflection[5] [78]. Secondly, cilia of the hair cells change their compliance during their deflection, which is connected with the opening and closing of the MET channels, and hence distorted to give rise to a nonlinear process termed as the gating stiffness [78]. The adaptation of the hair bundle stiffness may be indicative of the bundle's contribution to the nonlinear nature of transduction [78]. The mechanism of adaptation refers to the bundle's displacement, which causes only a transient increase (excitory deflection towards the lateral wall of the cochlea) or decrease (inhibitory deflection towards modiolus) in the receptor potential of the hair cell, and adapts to an intermediate level after tens of milliseconds [78]. This process is suggested to be connected with the migration of the tip links through the cell membranes, due to their attachment

[5]Opening of the MET channels is described in a statistical sense, because cilia deflection modulates the probability of channel's opening [28], i.e. displacement of the cilia induces rapid changes between opening and closing states of the MET channels [78].

to the slow myosin motor, which appears to be capable of shifting the operating point of the Boltzmann function and thus contributes to mechanical nonlinearity [78].

Thirdly, the OHC's basolateral wall exhibits a nonlinear current-voltage (I/V) relationship at low frequencies, due to the nonlinear flux of the K^+ ions through the voltage-dependent membrane channels [78]. However, although nonlinear at low frequencies, above approximately 1 kHz the relation between the injected current and the potential changes is dominated by a current charging and discharging the membrane capacitance on a cycle-by-cycle basis, and the nonlinearity in the I/V curve appears to be irrelevant [78]. Finally, the fourth of the nonlinear processes associated with the OHCs refers to the length changes of the OHC's body, which are not proportional to the voltage changes across the cell's membrane [78]. Although to observe significant nonlinearity in this case tens of millivolts potential changes are required (which cannot occur for frequencies above 1 kHz as described above), this type of nonlinearity may be capable of modifying the sensitivity of force generation at low frequencies [78].

Evidence for cochlear nonlinearity can be also found in the so-called two-tone suppression or generation of the distortion tones, which are both products of the process within the cochlea called intermodulation [78]. For the compressive nonlinearity, illustrated in Fig.2.13, two stimuli of different frequencies observed at the characteristic place will be compressed in a way depending on their proximity to the CF in the frequency domain, frequency difference between them or levels. This can be observed for tones at relatively high frequencies in the phenomenon of two-tone suppression, where two tones presented to the ear may mutually or one-sidedly suppress each other [78]. The distortion products, often referred to as the combination tones, occur when frequency components, which were not present in the input stimulus, are generated and present in the response [78]. One of the distortion products, which can be mostly obtained from the expansion of the nonlinear transfer function, is the cubic intermodulation frequency $2f_1-f_2$, where f_1 and f_2 are the stimulus frequencies [101].

Chapter 3

Lumped parameter micromechanical models

Recent literature on cochlear modelling shows that there are two different approaches to the modelling of the cochlear micromechanics. In most cases a lumped parameter model is used [34, 68], whereas in the other, a distributed parameter model is proposed [3, 50]. This chapter reviews the formulation of most widely-used lumped parameter models, whereas the distributed parameter micromechanical models are discussed in Chapters 6 and 7.

In the lumped parameter models all components of the system are treated as moving as rigid bodies, when vibrating due to the cochlear fluid pressure difference excitation. For example, the BM and the organ of Corti are moving in unison and their mechanical parameters are lumped into mass, spring and damper components. The mechanical parameters are chosen to represent the distribution along the real cochlea as obtained empirically, although in the literature they often appear to be chosen and adjusted to give best model results [64, 66, 68].

The passive lumped parameter models exhibit a broad response that is characteristic to the response of a dead cochlea. It has been suggested therefore [14, 34, 65, 67, 68] that, in order to model a realistic response like that of a live cochlea, the models must include active components. These active models also involve more complicated mechanics because it is postulated that the outer hair cells within the organ of Corti are responsible for the amplification processes in

the cochlea. Lumped parameter micromechanical models investigate the interactions of the structures within the active organ of Corti. Although they employ similar modelling techniques, many of them show substantial differences in the approach.

In this chapter a brief overview of the lumped parameter models of cochlear mechanics, with the explanation of the basic physical concepts, is presented. This includes the classical models proposed by Allen in 1980 [1], Neely and Kim in 1986 [68], and the model of Neely of 1993 [66] with their original assumptions and notation. Furthermore, the analysis of the modes of vibration of the Neely and Kim [68] and Neely's [66] model are investigated in detail. We also propose a modified model of Neely [66], to investigate the effects of the TM inertial load on the model's dynamics.

3.1 Background macromechanics

The macromechanical behaviour of the cochlea has been thoroughly described theoretically, as reviewed, for example, by de Boer [14], so that the propagation of the travelling waves can be simulated using the wave equation solved for the pressure difference between the pressures in the lower and upper chamber of the cochlea. In a number of cochlear models, the wavelength is assumed to be much greater then the typical height of the cochlear chamber (long-wave assumption), H. Thus, all variables become a function of only the longitudinal position from the base to the apex of the cochlea [14, 17, 78].

The long-wave assumption is respected through almost the entire length of the cochlea, apart from the point of the maximum partition displacement [14, 17, 55, 68]. The shape of the cochlear partition (CP) transverse vibrations across the width of the CP is often assumed to be sinusoidal and constant along the cochlea, where the peak magnitude occurs in the centre of the CP's width. Thus the vertical displacement of the CP used in the theory, is averaged over its width [65, 68]. Finally, the geometry of the cochlea is generally simplified and presented as a rectangular box, divided by the CP and terminated by the oval and round windows, as presented schematically in Fig.3.1.

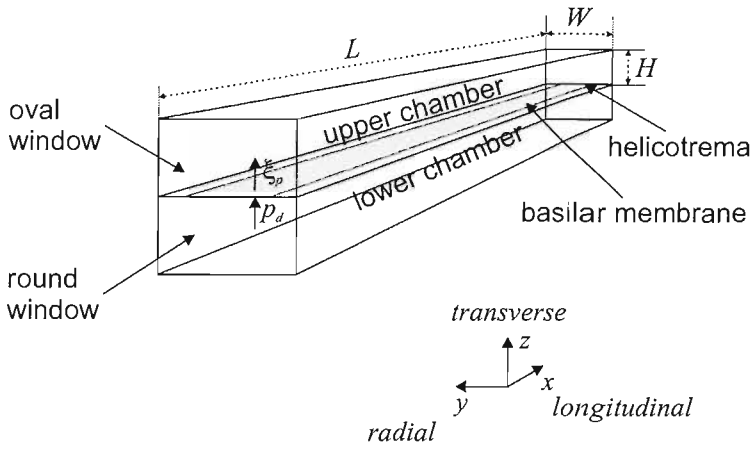

Figure 3.1: Schematic of the simplified geometry of the cochlea, with the indication of the dimensions, cochlear partition displacement, $\xi_p(x)$, and pressure difference, $p_d(x)$ (L, W denote the cochlear partition length and width, respectively, and H the height of the cochlear chambers). Redrawn after Neely and Kim [68].

The CP is generally discretised into a number of independent mass-spring-damper systems like the one shown schematically in Fig.3.2. It represents a slice of the CP, which is thought to be physically independent of its neighbours but coupled via the cochlear fluid in which they are immersed [17, 78]. The evidence to support this assumption comes from the measurements on the longitudinal coupling in the BM. It was shown by Voldřich [95], that probing of the BM produces only a local deformation with the adjacent regions relatively unmoved, suggesting that there is no significant coupling of the neighbouring sites of the BM in the longitudinal direction. Recent BM stiffness measurements have also shown relatively little longitudinal coupling within the BM [25]. However, the issue of the longitudinal BM coupling remains controversial [63].

The mechanical system shown in Fig.3.2, possesses specific mass, $m(x)$, stiffness, $k(x)$, and damping, $c(x)$, usually defined per unit area and depending only on the distance from the stapes, x. The mass is usually assumed to be constant over the length of the cochlea, whereas the stiffness and damping are assumed to have an exponential form [17]. Spanning the length of the cochlea to cover the

distribution of the mechanical impedance parameters in the real CP (BM), each system is assumed to have its natural frequency tuned to a particular stimulus frequency and thus maximally excited at this frequency.

The mechanical impedance is coupled into the homogeneous wave equation for the macromechanical behaviour of the cochlea, which in the long wavelength limit can be written as

$$\frac{\partial^2 p_d(x,\omega)}{\partial x^2} - \frac{2j\omega\rho}{Z_p(x,\omega)H}\, p_d(x,\omega) = 0, \tag{3.1.1}$$

where $p_d(x,\omega)$ denotes the pressure difference, $Z_p(x,\omega)$ the partition impedance at position x and frequency ω, ρ the density of the cochlear fluid, and H is the height of the upper cochlear chamber [14, 17, 55, 59, 82].

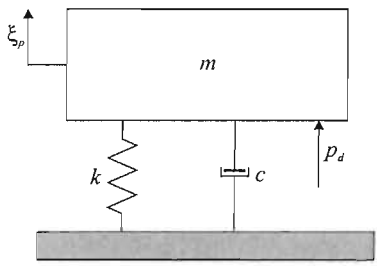

Figure 3.2: A single degree of freedom system representing a single cross-section of the cochlear partition with its mass, m, stiffness, k, and resistance, c, lumped into a mass, spring and dashpot component. The partition is displaced, due to the pressure difference p_d, by ξ_p.

For a place below the characteristic place, that is where the stimulus frequency, ω, is lower than the resonance frequencies ω_r (CFs), i.e. $\omega<\omega_r$, the partition impedance is stiffness controlled, so that $Z_p(x,\omega)\approx k(x)/j\omega$, thus the wave equation takes the form

$$\frac{\partial^2 p_d(x,\omega)}{\partial x^2} + \frac{2\omega^2\rho}{Hk(x)}\, p_d(x,\omega) = 0, \tag{3.1.2}$$

with the corresponding propagating solution of the form, for slowly varying $k(x)$,

$$p_d(x,\omega) = p_0 e^{-j\omega x/c(x)}, \tag{3.1.3}$$

where $c(x)=\sqrt{Hk(x)/2\rho}$ denotes the wavespeed which drops to zero approaching the characteristic place. It should be noted that a more complex solution is required to account for the dependency of the stiffness k on x since the wavespeed, c, (or the wavenumber $\omega/c(x)$) is also dependent on x [17].

Above the characteristic place, where $\omega>\omega_r$, the partition impedance, Z_p is mass controlled, so that $Z_p(x,\omega)\approx j\omega m(x)$, and the homogeneous wave equation can be expressed as

$$\frac{\partial^2 p_d(x,\omega)}{\partial x^2} - \frac{2\rho}{Hm(x)} p_d(x,\omega) = 0, \tag{3.1.4}$$

and the solution has the form

$$p_d(x,\omega) = p_0 e^{-x/l(x)}, \tag{3.1.5}$$

where $l(x)=\sqrt{Hm(x)/2\rho}$ is the decay length, being almost constant due to little variation of the partition's mass, $m(x)$, along the cochlea and the cochlear upper chamber height assumed constant [21].

A complete solution of the one-dimensional, frequency-domain cochlear model, requires a general expression for the mechanical impedance of the partition, $Z_p(x,\omega)$. To define Z_p, the longitudinal distribution of its stiffness, inertial and resistive components must be known, though these are hard to estimate theoretically or obtain experimentally [78].

The CP can be represented by a number of single (Fig.3.2) or two degree of freedom (DOF) independent, mechanical systems, which are coupled and excited by the cochlear fluid to give rise to the travelling wave in the cochlea [11, 14, 17, 64, 78, 79]. In the cochlear models which represent the CP as a single unit, with lumped mass, stiffness and damping, only one set of mechanical parameters is needed to define the impedance Z_p. For the micromechanical models that employ two DOF mechanical systems for the CP, where two of the constitutive components are usually resonant systems with their own masses, stiffnesses and damping, and are connected to each other by spring or spring and damper components, the x-distribution of all the components' mechanical parameters must be derived to define Z_p.

In a single DOF model, the CP is often functionally identified with the BM [17] in a sense that the CP behaves as a flexible partition vibrating in the transverse direction. However, when estimating the BM mass, which might be insignificant in comparison with the mass of the overlying organ of Corti, the structures and inertia of the fluid within the organ are often included [17, 78]. Furthermore, knowing the mass of the BM, its stiffness can be estimated from the characteristic frequency (CF)/place maps formulated from physiological experiments on the cochlea (see Fig.2.8 in Section 2.2.1) [39, 56]. Direct stiffness measurements prove to be dependent on the methodology of the measurement [78]. For example, the stiffness measurements with small actuated probes that indent just a small area of the BM, give only localised information about its stiffness, whereas in reality the pressure acting on the BM is distributed across its width [78, 88]. It is thus difficult to compare the stiffness values inferred from the CF place maps with direct measurement.

The response of the BM has a tonotopic characteristic, which means that a particular place along the cochlea is 'tuned' to a particular stimulus frequency at which the maximum of the response occurs [79, 87]. Therefore, the condition for the natural frequency of an undamped, freely vibrating system, $\omega_n^2{=}k/m$, can be used to specify the stiffness when the mass and natural frequency are known.

The remaining parameter of the impedance is the BM's resistance, assumed to be the only factor that generates losses if the cochlear fluids are incompressible and inviscid. It is hard to estimate the damping of the BM, and it is often assumed to be of an exponential form varying with the distance from the stapes [17], so that the single DOF system has a constant damping ratio.

In reality it is generally difficult to obtain a complete and consistent set of mechanical parameters from the physiological experiments. Hence many models use data extracted for various species, often extrapolated to resemble the human cochlea characteristics (or other species) because the shape of the corresponding CF/place map functions do not differ significantly [39, 56, 82].

The stiffness, $k_1(x)$ [Nm^{-3}], and resistance, $c_1(x)$ [Nsm^{-3}] are assumed to decrease exponentially from base to apex as $e^{-\alpha x}$ and $e^{-\alpha x/2}$, respectively [14,

17, 55]. Therefore, assuming a one DOF model, the mechanical impedance[1] representing the partition impedance, $Z_p(x,\omega)$ will take the form

$$Z_p(x,\omega) = c_0\, e^{-\alpha x/2} + \frac{k_0\, e^{-\alpha x}}{j\omega} + j\omega m_0, \tag{3.1.6}$$

where m_0 is the constant BM mass. The value of k_0 specifies the stiffness for x=0 (stapes). The radian resonance frequency of an undamped system, with the mass m_0 and stiffness $k_0 e^{-\alpha x}$, as described above, thus takes the form

$$\omega_r(x) = \sqrt{\frac{k_0}{m_0}}\, e^{-\alpha x/2}, \tag{3.1.7}$$

and depends on the longitudinal position in the cochlea [17].

The damping constant in Eq.3.1.6, c_0, is defined as $2\zeta_0\sqrt{m_0 k_0}$, where ζ_0 denotes the damping ratio equal to the reciprocal of twice the Q-factor of the BM resonance bandwidth [17, 55]. Thus

$$\zeta(x) = \frac{c(x)}{2\sqrt{m(x)k(x)}} = \frac{c_0 e^{-\alpha x/2}}{2\sqrt{m_0 k_0} e^{-\alpha x/2}} = \zeta_0, \tag{3.1.8}$$

and ζ_0 is independent of position along the cochlea in this model.

The above expression for the partition impedance (Eq.3.1.6), characterises a single DOF system (Fig.3.2), an array of which models the CP and gives response similar to the passive response of the cochlea. However, the cochlear tuning curves measured *in vivo* show a much sharper response at the place of the maximum partition displacement [87] than the calculated response in this simplified case. Hence it was postulated that, in order to model a realistic response of the cochlea, cochlear models require an active component, referred to as the cochlear amplifier, which is thought to enhance the model's response. The active cochlear models involve more complicated mechanics, describing vibrations on a 'micro' level i.e. of the structures within the organ of Corti [34, 66, 67, 68].

In a passive mechanical system the magnitude of the impedance at the resonance frequency, $\omega_r/2\pi$, is controlled by the amount of damping [78, 94]. To reduce the passive damping in the CP, the cochlear amplifier can be assumed

[1]The CP impedance is often referred to as the mechanical impedance, but because its components are usually defined per unit area, it has the dimension of a specific acoustic impedance.

to have a form of negative damping, acting locally at the site of (or near) the partition's resonance. Practically, the active element in the lumped parameter cochlear model is implemented by introducing into each mechanical system a feedback loop that senses the motion of the CP and introduces an active force that serves to overcome the frictional forces within the system [78].

The mechanism of activity appears to depend on the motility of the OHCs being controlled by the secondary resonator, widely assumed to be associated with the TM [1, 34, 68]. Since, the BM and the TM resonators are coupled by the stereocilia of the OHC and the cilia deflection triggers the motile action of the OHCs, the electromotile forces in the system are assumed to arise due to the relative shearing displacement between the reticular lamina (RL) and the TM [68]. The cochlear amplifier is also often assumed to possess an internal phase shift [34, 68]. This frequency dependent phase shift can result from the low-pass filtering of the OHC's membrane caused by its resistance and capacitance, and is often assumed to result in about 90 degrees phase delay between the deflection of the hair bundle cilia and the cell's motile force in the high frequency range [2].

The active component may be formulated in the form of impedance function and the assumed geometrical arrangement or the motion of the structures within the organ of Corti may be defined in various ways. Thus, it is convenient to formulate the partition impedance of a micromechanical model in the more generic form

$$Z_p(x,\omega) = Z_{pass}(x,\omega) - \gamma Z_{act}(x,\omega), \tag{3.1.9}$$

where Z_{pass} denotes the passive impedance and gathers all components contributing to the overall impedance of the two DOF system, and Z_{act} corresponds to the impedance containing the impedance components of the assumed active element of the model [47, 55]. The constant γ is specific to the active element and can be thought as an amplification factor [55] that controls the gain of the force generated by the cochlear amplifier. This cochlear amplification constant usually takes the values from 0 to 1, where setting it to zero reduces the partition impedance to the passive term, so that the model gives a response like that of a dead cochlea, and setting to one is meant to give an active response like that observed

in the live cochlea [17, 55, 68]. Some authors show also that setting the value of the gain factor higher than one leads to instability within the system giving an unstable solution of the model, and thus predicting self-oscillations, which may correspond to the mechanism of generation of the spontaneous otoacoustic emissions [68].

3.2 Review of the 1980 model of Allen

A classical lumped parameter micromechanical model of the cochlea, which includes both the BM and TM, was proposed in 1980 by Allen [1]. Although it is a passive model, it introduces some key ideas which were used and further developed in the later model of Neely and Kim [68].

The model was developed to provide a connection between the experimental and neural data and to provide a framework for better understanding of cochlear mechanics [1]. As pointed out by Allen, the crucial point to bridge the gap between the experimental and neural data appears to correspond to the processes involving the hair cells, i.e. during the mechanical to neural transduction. Thus, the model assumes a radial shearing motion between the RL and the TM of the organ of Corti, which induces deflection of the OHC cilia. Furthermore, the author reports that the neural phase response and the phase response of a spectral zero model reveal a positive, π radians phase shift relative to the input phase when the CF is above the frequency of the stimulus, so that a second order transduction filter, the zeros of which could be adjusted to fit the neural and model curve, is required in the cochlear model [1]. Finally, taking into account the microstructure of the organ of Corti, Allen extends the single DOF model by introducing a fully resonant TM as the second DOF.

A schematic of a simplified geometry of the organ of Corti, as proposed by Allen [1], is shown in Fig.3.3. The BM of width W is displaced transversally by ξ towards the TM, which is presented as a rigid bar in the first instance. Assuming that the separation between the RL and the TM is constant[2], and

[2]This would imply that the transverse stiffness of the OHC's cilia is high enough to preserve a constant height of the subtectorial space.

amounts to ϵ, the upward displacement of the BM will cause a proportional radial shearing displacement between the RL and TM, Δ. The constant ϵ was assumed to correspond to the height of the tallest OHC stereocilia row, which are also embedded in the TM, thus enabling a parallel motion of the BM and TM. Furthermore, the BM and TM are pivoting around some hinge connections, so that the distance between these structures remains constant and equal to $h+\epsilon$, where h is the height of the overlying organ of Corti.

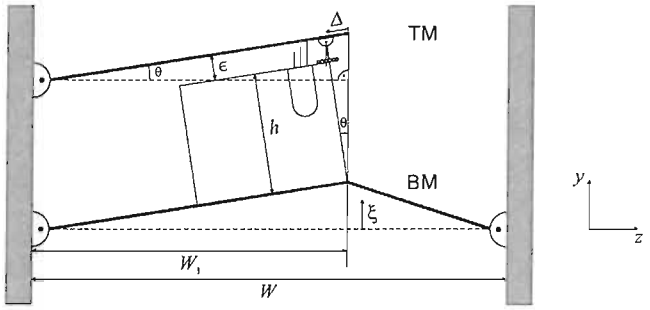

Figure 3.3: Schematic of a cross-sectional view of the organ of Corti, where the basilar membrane (BM) is displaced by ξ around two hinges, causing a proportional, radial shear displacement, Δ. TM tectorial membrane, W basilar membrane width, W_1 basilar membrane width to the point of maximum vertical displacement, h height of the organ of Corti, ϵ height of the subtectorial space, θ angle of deflection from the resting position, y and z transverse and radial direction, respectively. Redrawn after Fig.6 in [1].

The geometry of such a simplified system implies that the two right-angled triangles indicated in Fig.3.3 are similar, and for the angle θ indicated in the figure

$$\tan\theta = \frac{\xi}{W_1}, \tag{3.2.1}$$

and also

$$\tan\theta = \frac{\Delta}{\epsilon + h}, \tag{3.2.2}$$

so that

$$\frac{\xi}{W_1} = \frac{\Delta}{\epsilon + h}. \tag{3.2.3}$$

Furthermore, Allen defines a new variable, the shear gain $g(x)$[3], which depends on the position in the cochlea, x, so that

$$g(x) = \frac{\Delta(x)}{\xi(x)} = \frac{\epsilon + h}{W_1}. \tag{3.2.4}$$

Allen also assumed that $W_1 \approx W/2$, and $\epsilon \ll h$, hence

$$g(x) \approx \frac{2h(x)}{W(x)}. \tag{3.2.5}$$

It should be noted that the relation between the relative radial shear displacement Δ and the BM displacement, ξ, is linear and frequency independent [1].

The parallel transverse motion of the BM and TM, which are locked by the lever gain g defined in Eq.3.2.5, can be considered as the first DOF of the model. However, to introduce a spectral zero into the model's transfer function, a second DOF is introduced by Allen by allowing a *radial* motion of the TM. The TM's mass, m_{T}, is assumed to have an elastic connection, k_{T}, with the spiral limbus, and an internal loss within the tissue of the TM is represented by the damping element, r_{T}. The masses of the BM and TM are concentrated at the ends of the bars which represent these structures in Fig.3.4, and are denoted m_{B} and m_{T}, respectively. The BM stiffness is represented by a spring K_{B}, although Allen argues that the restoring force in this case corresponds to the bending rigidity of the membrane [1]. Finally, the BM and TM are connected by the cilia stiffness, k_{C}, which opposes the radial shear motion between the TM and RL, and the viscous damper, r_{C}, due to the viscous forces within the narrow subtectorial space. A block diagram representing this new, two DOF system is shown in Fig.3.4 [1].

The TM, represented by a mass-spring-damper system, is capable of independent vibrations, having a resonance separate from that of the BM [1]. As

[3]For better comparison the lever gain was denoted by g in the thesis.

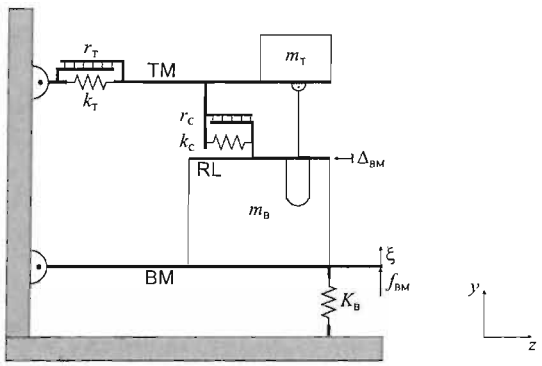

Figure 3.4: Schematic of the two degree of freedom model proposed by Allen [1]. The lower block corresponds to the basilar membrane (BM) with its mass, m_{B} and stiffness, K_{B}, whereas the upper block to the tectorial membrane (TM) with its mass, m_{T}, stiffness, k_{T}, and damping, r_{T}. These masses are connected by a spring k_{C} corresponding to the stiffness of the outer hair cell cilia. The viscous damping in the subtectorial space is represented by the dashpot r_{C}. The basilar membrane is displaced in the transverse direction by ξ and in the radial direction by Δ_{BM} due to the force f_{BM}. RL reticular lamina, y and z transverse and radial direction, respectively.

pointed out by Allen, under specific conditions the TM and RL can move in phase and with equal magnitude to produce zero relative motion, and thus introduce the spectral zero in the transfer function [1]. Furthermore, the OHC cilia are assumed to be displaced only by the radial forces, so that the neural excitation is related to the radial shear.

Assuming that a transverse force, f_{BM}, is acting on the BM due to the pressure difference across the CP, the transverse response of the system will be formulated by

$$f_{\mathrm{BM}} = \left[K_{\mathrm{B}} + s^2(m_{\mathrm{B}} + m_{\mathrm{T}})\right] \xi, \tag{3.2.6}$$

where s is equal to $j\omega$ for a stable system, and is the symbol used by Allen. The shear motion of the BM at the RL can be described using the analogy for the parallel motion, such that according to Eq.3.2.4

$$\Delta_{\mathrm{BM}} = g\xi, \tag{3.2.7}$$

where Δ_{BM} is an auxiliary variable used to denote the radial displacement of the BM, and g is the shear gain defined in Eq.3.2.5. Note that for transverse motion m_{B} and m_{T} are locked together as in the single DOF system (Fig.3.3), but that k_{C} and r_{C} are not subject to the force f_{BM}, responding only to the shearing forces between the RL and TM. The equation of motion for the second DOF, which represents the radial motion of the TM due to the radial force between the RL and TM, f_{CR}, takes the form

$$f_{\mathrm{CR}} = (k_{\mathrm{T}} + s\, r_{\mathrm{T}} + s^2 m_{\mathrm{T}})\Delta_{\mathrm{TM}}, \tag{3.2.8}$$

where Δ_{TM} denotes the radial displacement of the TM. The radial force, f_{CR}, also acts on the cilia stiffness, k_{C} and the damping r_{C}, which respond to a relative displacement $\Delta_{\mathrm{BM}} - \Delta_{\mathrm{TM}}$, so that

$$f_{\mathrm{CR}} = (k_{\mathrm{C}} + s\, r_{\mathrm{C}})(\Delta_{\mathrm{BM}} - \Delta_{\mathrm{TM}}). \tag{3.2.9}$$

Thus, using Eqs.3.2.8 and 3.2.9, the radial displacement of the TM, Δ_{TM}, can

be expressed in terms of the radial displacement of the BM, Δ_{BM}, i.e.

$$\Delta_{\mathrm{TM}} = \frac{k_{\mathrm{C}} + s\, r_{\mathrm{C}}}{(k_{\mathrm{T}} + k_{\mathrm{C}}) + s(r_{\mathrm{T}} + r_{\mathrm{C}}) + s^2 m_{\mathrm{T}}} \Delta_{\mathrm{BM}}, \tag{3.2.10}$$

so that the relative shear displacement Δ_{C}, amounts to

$$\Delta_{\mathrm{C}} = \Delta_{\mathrm{BM}} - \Delta_{\mathrm{TM}} = \frac{k_{\mathrm{T}} + s\, r_{\mathrm{T}} + s^2 m_{\mathrm{T}}}{(k_{\mathrm{T}} + k_{\mathrm{C}}) + s(r_{\mathrm{T}} + r_{\mathrm{C}}) + s^2 m_{\mathrm{T}}} \Delta_{\mathrm{BM}}, \tag{3.2.11}$$

and therefore the shear transfer function, $H_{\mathrm{T}}(x, s)$, as denoted by Allen [1], which relates the relative shear displacement Δ_{C} to the displacement of the BM, ξ, can be derived from the above equation and Eq.3.2.7, and

$$H_{\mathrm{T}}(x, s) = \frac{\Delta_{\mathrm{C}}}{\xi} = g \frac{k_{\mathrm{T}} + s\, r_{\mathrm{T}} + s^2 m_{\mathrm{T}}}{(k_{\mathrm{T}} + k_{\mathrm{C}}) + s(r_{\mathrm{T}} + r_{\mathrm{C}}) + s^2 m_{\mathrm{T}}}. \tag{3.2.12}$$

Allen refers to $H_{\mathrm{T}}(x, s)$ as the transduction filter, whose transfer function consists of a zero and a pole at frequencies, f_z and f_p, respectively, where

$$f_z = \frac{1}{2\pi} \sqrt{\frac{k_{\mathrm{T}}}{m_{\mathrm{T}}}}, \tag{3.2.13}$$

$$f_p = \frac{1}{2\pi} \sqrt{\frac{k_{\mathrm{T}} + k_{\mathrm{C}}}{m_{\mathrm{T}}}}, \tag{3.2.14}$$

and by this definition $f_p > f_z$, as it was required for the spectral zero model [1]. It is also worth noting here, that the relative displacement Δ_{C} is thought to produce deflection of the OHCs cilia, however, the velocity $s\Delta_{\mathrm{C}}$ is assumed by Allen to produce the deflection of the IHCs cilia, and thus stimulate the neural response to which the response of the present model was fitted [1].

It was shown by Elliott *et al.* [24], that in the absence of the shear motion of the TM, Fig.3.5, a transverse force, say f_{CT}, must react off f_{BM} (due to the hinge connection of the BM), and f_{CT} is related to f_{CR} by

$$f_{\mathrm{CT}} = g\, f_{\mathrm{CR}}. \tag{3.2.15}$$

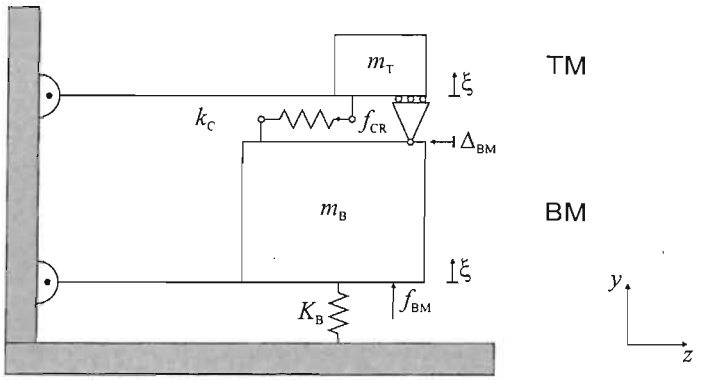

Figure 3.5: Schematic of the two degree of freedom system with the indication of the forces and displacements produced after the displacement of the basilar membrane (BM), ξ. f_{BM}, force acting on the basilar membrane, f_{CR} radial shearing force acting on the spring k_{C}, Δ_{BM} radial shearing displacement of the basilar membrane. The roller connection indicates that the subtectorial gap is of constant height, ϵ, but enabling sliding motion between the reticular lamina and tectorial membrane (TM). y and z denote transverse and radial directions (NB the second degree of freedom has been omitted).

Eq.3.2.6 can be therefore revised to give

$$f_{\mathrm{BM}} = \left[K_{\mathrm{B}} + s^2(m_{\mathrm{B}} + m_{\mathrm{T}})\right]\xi + f_{\mathrm{CT}}. \tag{3.2.16}$$

Thus, after substituting Eqs.3.2.15 and 3.2.9 for f_{CT} into Eq.3.2.16,

$$f_{\mathrm{BM}} = \left[K_{\mathrm{B}} + s^2(m_{\mathrm{B}} + m_{\mathrm{T}})\right]\xi + g(k_{\mathrm{C}} + s\,r_{\mathrm{C}})\Delta_{\mathrm{C}}, \tag{3.2.17}$$

and using the relationship between ξ and Δ_{C}, i.e. the transduction filter $H_{\mathrm{T}}(x,s)$ in Eq.3.2.12, and substituting for Δ_{C} in Eq.3.2.17, the total BM impedance can be formulated by

$$Z_{\mathrm{BM}} = \frac{f_{\mathrm{BM}}}{s\xi} = \frac{K_{\mathrm{B}}}{s} + s(m_{\mathrm{B}} + m_{\mathrm{T}}) + g^2\frac{(k_{\mathrm{C}} + s\,r_{\mathrm{C}})(k_{\mathrm{T}} + s\,r_{\mathrm{T}} + s^2 m_{\mathrm{T}})}{s[(k_{\mathrm{T}} + k_{\mathrm{C}}) + s(r_{\mathrm{T}} + r_{\mathrm{C}}) + s^2 m_{\mathrm{T}}]}, \tag{3.2.18}$$

as derived by Allen in [1]. Note that the system described by the impedance in Eq.3.2.18, has two distinctive zeros at radian frequencies of $\sqrt{K_{\mathrm{B}}/(m_{\mathrm{B}} + m_{\mathrm{T}})}$ and

$\sqrt{k_T/m_T}$, and a pole at $\sqrt{(k_T + k_C)/m_T}$. However, if the mobility, $Y_{BM}=Z_{BM}^{-1}$, of the BM is considered, as usually presented for the experimental data [40], then the system described above will be characterised by two distinctive poles, and a zero at the respective frequencies given above.

3.3 Review of the 1986 model of Neely and Kim

A micromechanical model of the cochlea, which is still widely used, was proposed in 1986 by Neely and Kim [68]. It was developed from the earlier studies of Neely [64, 65] and Neely and Kim [67] on a linear model of the cochlea. The passive model of cochlear macromechanics proposed in 1981 [64] did not refer to the micromechanics of the cochlea. However, the two later models, proposed in 1983 [67] and in 1985 [65], are active models, and discuss the organ of Corti micromechanics. The calculated response of these models was more sharply tuned and exhibited better frequency selectivity than the first model in [64].

In the first of the active models [67], Neely and Kim introduced the notion of the OHCs negative dampers acting against the damping of the CP, and suggested a secondary resonator (a mass-spring-damper system) being the cilia of the OHCs [67]. In the next model [65], the active component was presented in the form of bidirectional electromechanical transduction in the OHCs, and driven by the deflection of their cilia. Similarly to the secondary resonator in [67], a second, frequency-dependent element, with output being a low-pass filtered version of the BM's output (displacement), was added [65]. However, although this second element was defined as if it was a mechanical system, it was not physiologically identified. In addition, the secondary element was coupled into an OHC filter in the feedback model despite the fact that the character of the OHC tuning was not clear (mechanical, electrical or both) [65]. Furthermore, it was suggested in [65] that, according to the BM displacement analysis, the tuned secondary element is required for the active cochlear model to add stiffness to the impedance of the BM at each position at low frequencies, and negative damping at intermediate frequencies. At high frequencies, however, the secondary resonator was assumed to have a negligible influence.

The 1986 model [68] assumed the existence of a secondary resonance, which was identified with the TM, which possessed its own mass, stiffness, and damping. In addition, the TM was assumed, as in the model of Allen [1], to be capable of independent radial motion, which constituted the second vibrational DOF and caused shearing forces between the TM and RL leading to the deflection of the OHCs' cilia bundles [68]. Similar to previous active models [67, 65], the active sites within the cochlea, which under specific conditions supply energy to the system, were assumed in this model, and the electromotility of the OHCs, triggered by the deflection of their stereocilia, was proposed for the motor of activity [68].

Although in the first approach [64], Neely proposed that the cochlear fluid's pressure varied in two, longitudinal and vertical, dimensions, in the 1986 model [68], all dependent variables, due to the long-wave assumption, depend only on the longitudinal direction, x. The vertical displacement of the CP, averaged over its width, W, was denoted as $\xi_p(x)$. The transverse CP displacement in the radial dimension was assumed to have a uniform shape (bending mode), independent of the longitudinal position x and with the peak in the middle of the partition's width [68].

Each segment of the CP, characterised by the impedance $Z_p(x)$, is presented in the 1986 Neely and Kim model [68] as a two DOF system comprised of two subsystems with the mass, $m_1(x)$, stiffness, $k_1(x)$, and resistance, $c_1(x)$, for the BM[4], and $m_2(x)$, $k_2(x)$, $c_2(x)$ for the TM. Furthermore, both resonators are coupled by stiffness k_3 and resistance c_3, representing the coupling between the organ of Corti and the TM. A schematic of this two DOF micromechanical system, redrawn after the block diagram proposed by Neely and Kim in [68], is shown in Fig.3.6.

Although Fig.3.6 suggests that the displacements $g\xi_b$, and ξ_t, represented by the upward arrows, are vertical (transverse) displacements, in reality these are radial displacements causing a radial shearing displacement of the cilia, ξ_c, as defined by Neely and Kim [68]. The actual motion of the structures of the organ of Corti can be represented by the diagram of Fig.3.4, in which the TM's

[4]Neely and Kim refer often to $m_1(x)$ as to the mass of the organ of Corti cross-section [68].

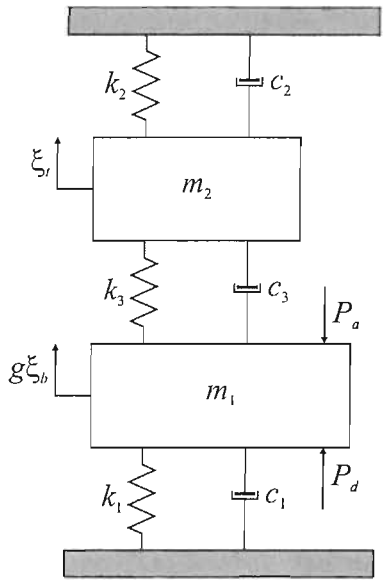

Figure 3.6: Two degree of freedom system representing the basilar membrane with its mass, m_1, stiffness, k_1, and resistance, c_1, the tectorial membrane with mass, m_2, stiffness, k_2, and resistance, c_2, coupled by the stiffness and resistance, k_3 and c_3, respectively. The cochlear fluid pressure difference, P_d, produces radial displacements of the reticular lamina, $g\xi_b$, and the tectorial membrane, ξ_t. An additional active pressure source, P_a, connected with the electromotility of the outer hair cells, acts on the basilar membrane from within the organ of Corti (block diagram redrawn after Fig.3 in [68]).

components m_T, k_T, and r_T, correspond to m_2, k_2, and c_2, whereas k_C and r_C to k_3 and c_3, respectively, in the model of Neely and Kim[5]. The BM subsystem's stiffness K_B is replaced by k_1 although m_1 is equal to m_B+m_T, and additionally the BM damping, c_1, is considered in [68]. However, the multi-axial block diagram of Fig.3.4 can be transformed into a single-axis one with entirely transverse or radial motion leaving the formulation for the BM/CP impedance unaffected, as shown by Elliott *et al.* [24]. Thus, the block diagram proposed by Neely and Kim (Fig.3.6) is a two DOF system moving in the radial direction, though confusingly shown as moving in the transverse direction.

Neely and Kim specify a ratio, b, of the CP's displacement, $\xi_p(x)$, averaged over the CP's width, to the maximum displacement over the BM, $\xi_b(x)$, so that

$$\xi_p(x) = b\,\xi_b(x) \tag{3.3.1}$$

and $b<1$ by this definition[6].

The vibrations of the CP are induced by the pressure difference, $P_d(x)$, between the pressures of the incompressible and inviscid cochlear fluid in the upper and the lower cochlear chambers. Furthermore, the pressure difference, $P_d(x)$, is coupled with the partition impedance, $Z_p(x)$, into a formulation describing the macromechanical vibrations by means of the partition's acceleration, i.e.

$$\ddot{\xi}_p(x) = \frac{j\omega P_d(x)}{Z_p(x)} \tag{3.3.2}$$

where the dots indicate the second derivative with respect to time, j, the imaginary unit and ω, the angular frequency. It has to be emphasised that, although the model's variables are explicitly shown to be dependent on x only, in fact they

[5]Strictly speaking the mechanical components of the micromechanical model of Allen, shown in Fig.3.4, have to be divided by the square of the lever gain i.e. $g^2(x)$ (Eq.3.2.7), to be equal to the mechanical components of the Neely and Kim micromechanics [24].

[6]In the 1985 model [65], Neely assumed a centered half-cosine function ζ for the shape of the CP vibration in the radial direction. This suggested a simply supported beam-like slice of the BM, although one may argue that the fixed-fixed boundary condition would be more appropriate from the anatomical point of view (Section 2.1). However, though more complicated mathematically [94], it would only slightly change the numerical value of the ratio b.

are dependent on both, x and ω. The ω was omitted remembering that the model was solved in the frequency domain.

The cochlear fluid's pressure difference, $P_d(x)$, drives the BM causing an upward displacement, $\xi_b(x)$, in the vertical direction. This vertical displacement is assumed to lead to a radial shearing motion between the RL and the TM. Neely and Kim define a lever gain, $g(x)$, between the displacement of the organ of Corti, $\xi_b(x)$, and the radial displacement of the RL (compare Eq.3.2.7), so that the relative shearing displacement between the RL and the TM, $\xi_c(x)$, takes the form

$$\xi_c(x) = g(x)\xi_b(x) - \xi_t(x), \tag{3.3.3}$$

where $\xi_t(x)$ denotes the radial displacement of the TM.

The equation of motion for the first DOF of the system presented in Fig.3.6, in the frequency domain, will take the form

$$P_d(x) - P_a(x) = g(x)Z_1(x)\dot{\xi}_b(x) + Z_3(x)\dot{\xi}_c(x), \tag{3.3.4}$$

where $Z_1(x)=k_1(x)/j\omega+c_1(x)+j\omega m_1(x)$ and $Z_3(x)=k_3(x)/j\omega+c_3(x)$, are impedances representing the mechanical impedance of the organ of Corti and coupling between the organ and the TM. P_a denotes an acoustical pressure source located within the OHC and represents the active component of the model.

The equation of motion for the second DOF is formulated by

$$0 = Z_2(x)\dot{\xi}_t(x) - Z_3(x)\dot{\xi}_c(x), \tag{3.3.5}$$

where $Z_2(x)=k_2(x)/j\omega+c_2(x)+j\omega m_2(x)$ represents the mechanical impedance of the TM.

The activity in the organ of Corti is thought to be connected with the motility of the OHCs, which contract and elongate due to the deflection of their cilia. The shearing displacement, $\xi_c(x)$, leads to the deflection of the OHC stereocilia with a positive direction towards the tallest row of the cilia. Such a deflection leads to the depolarisation of the hair cell and subsequently contraction of the cell's body. Neely and Kim assume that $\xi_c(x)$ describes the displacement of both, outer and IHC's bundle. Furthermore, the generator of the active mechanical force is

assumed to be internal to the OHC and the neural rate threshold occurs at a constant peak displacement of $\xi_c(x)$ at the IHCs [68].

The active force generator, which produces the active pressure, $P_a(x)$, acting in this model only on the BM as shown in Fig.3.6, is not an additional, independent source but is thought to be controlled by the displacement $\xi_c(x)$, and consistent with the observations of the OHCs *in vitro* [68]. Neely and Kim suggest that the pressure decrease within the OHC, transferred isometrically to the surrounding fluid, occurs when the hair cell body is contracting i.e. after being depolarised when the cilia of the OHCs are deflected towards their tallest row. Thus, according to Eq.3.3.3, decrease in $P_a(x)$ must occur when the $\xi_c(x)$ increases, so that it is formulated by

$$P_a(x) = -\gamma Z_4(x)\dot{\xi}_c(x), \tag{3.3.6}$$

where γ denotes a gain control parameter and $Z_4(x)=k_4(x)/j\omega+c_4(x)$ was introduced to provide a phase shift between the $P_a(x)$ and $\dot{\xi}_c(x)$. The stiffness k_4 and the damping c_4, are not physiologically identified[7]. Finally, the overall gain control parameter γ, independent of x and ω, is assumed to demonstrate the effects of global changes in the active components to the model, since setting γ to zero gives a passive, and one a 'fully' active response [68].

Having formulated the equations of motion and relative shear displacement, $\xi_c(x)$, for the system shown in Fig.3.6, the driving-point impedance of the CP can be derived

$$Z_p = \frac{P_d}{\dot{\xi}_p} = \frac{g}{b}\left[Z_1 + \frac{Z_2(Z_3 - \gamma Z_4)}{Z_2 + Z_3}\right], \tag{3.3.7}$$

where all quantities, excluding b and γ, depend on x and ω, and the lever gain, g, is a function of only position in the cochlea, x. The above equation can be

[7]More explanation on the origin of these components and the active impedance will be given in Sec.3.3.1.

rewritten as

$$Z_p = \frac{g}{b}\left[\underbrace{Z_1 + \frac{Z_2 Z_3}{Z_2 + Z_3}}_{Z_{pass}} - \gamma \underbrace{\frac{Z_2 Z_4}{Z_2 + Z_3}}_{Z_{act}}\right], \tag{3.3.8}$$

in which form it resembles the generic form given in Eq.3.1.9. Thus, it can be seen that setting γ to zero reduces the impedance to the passive component, the response of which is predicted to have a broad tuning.

Solving the above equation enables us to calculate the BM displacement, $\xi_b(x)$,

$$\xi_b(x) = \frac{P_d(x)}{j\omega b Z_p(x)}, \tag{3.3.9}$$

and the relative shearing displacement, $\xi_c(x)$ (cilia deflection), as

$$\xi_c(x) = g(x)\frac{Z_2(x)}{Z_2(x) + Z_3(x)}\,\xi_b(x). \tag{3.3.10}$$

The model of Neely and Kim attempts to gather the experimental (physiological) observations and their physical interpretation in the most consistent manner [68]. However, though the diagram shown in Fig.3.6 may seem to have a neat form, it has to be remembered that it is just an equivalent mechanical representation of the actual mechanics of the organ of Corti. Furthermore, Neely and Kim state that the major difference between theirs and the Allen [1] or Zwislocki and Kletsky [104] models is the introduction of the pressure source, P_a [68]. The physical interpretation of the active component in the Neely and Kim model is that the pressure source $P_a(x)$ introduces negative damping sites in the overall partition impedance, which supply energy locally to the cochlear fluid enhancing the response of the cochlea at these sites. However, this aspect of the model requires some clarifying comments.

3.3.1 Negative damping

Negative damping in the 1986 model of Neely and Kim [68], is thought to be explicitly introduced through the impedance $Z_4(x)$. $Z_4(x)$ provides a phase shift between the active pressure $P_a(x)$ and the shear velocity $\dot{\xi}_c(x)$ (Eq.3.3.6), and

thus in the time domain, a time delay between the cilia displacement and the active pressure, due to the OHCs contractions ($P_a(x)$ decrease) after their cilia undergo deflection in the tallest cilia row direction (increase in $\xi_c(x)$, Eq.3.3.6).

Considering a situation where the elastic force, $f(t)$, lags the displacement, $x(t)$, i.e.

$$f(t) = k\, x(t - \tau), \tag{3.3.11}$$

where k is a stiffness and τ a delay term, the time delay becomes the phase lag in the frequency domain [76]

$$F(j\omega) = k\, X(j\omega) e^{-j\omega\tau}, \tag{3.3.12}$$

or equivalently

$$F(j\omega) = \frac{k}{j\omega} V(j\omega) e^{-j\omega\tau}, \tag{3.3.13}$$

where $V(j\omega)$ denotes velocity.

The mechanical impedance in this situation will take the form

$$Z(j\omega) = \frac{F(j\omega)}{V(j\omega)} = \frac{k}{j\omega} e^{-j\omega\tau}, \tag{3.3.14}$$

which after expanding the right-hand side gives (for small $j\omega\tau$)[51]

$$Z(j\omega) = \frac{k}{j\omega} - k\tau. \tag{3.3.15}$$

It can be seen from the above equation that the $k\tau$ term is real and has dimension of damping, so that the mechanical impedance in the case where reactive force lags applied displacement comprises of two components, a stiffness and a negative damping. Thus, defining the stiffness and damping per unit area proves the mechanical impedance $Z(j\omega)$ to be analogous to the impedance $Z_4(x)$ in the Neely and Kim model, and that $Z_4(x)$ effectively introduces negative damping to the system. Furthermore, for high frequencies the stiffness term in $Z_4(x)$ becomes negligible and does not influence the BM impedance and the response of the cochlea, whereas for intermediate frequencies (near resonance), the negative

damping term has significant influence to the impedance Z_1, acting against the damping $c_1(x)$ and enhancing the response.

However, the signs of the damping $k\tau$ in Eq.3.3.15 and of the impedance Z_4 in the Neely and Kim model, i.e. c_4, are opposite. Thus, assuming that k in Eq.3.3.15 is equal to k_4, and knowing that Z_4=$k_4/j\omega$+c_4, then

$$c_4(x) = -k_4(x)\tau(x), \tag{3.3.16}$$

and hence the assumed distribution of the delay τ along the CP can be found from

$$\tau(x) = -\frac{c_4(x)}{k_4(x)}. \tag{3.3.17}$$

3.3.2 Calculated response

To conclude the review of the Neely and Kim model [68] the calculated mobility (velocity per unit force) of the CP is presented. The responses were calculated for the parameters shown in Table 3.1 (converted to SI units), which were selected by Neely and Kim [68] to simulate the mechanics of the cat cochlea and used to calculate the response of their model[8]. We also show the values of each parameter at x=0, $L_c/2$ and L_c, where L_c is the average length of a cat cochlea, for comparison with Table 3.2 in Section 3.5.

Note that in this model the mass of the BM and TM is constant over the length of the cochlea, where the BM mass is about one order of magnitude higher than that of the TM, since the ratio of m_1/m_2 is equal to six. Figures 3.7(a) and 3.7(b) show a comparison of the stiffness and damping components, respectively, as a function of position in the cochlea. It has to be noted that the distance from the stapes to the helicotrema was set to x=0−0.035 m (which will be referred

[8]The mass of the TM, m_2, given in Table I of [68] amounts to $0.005e^{x}$ gcm^{-2}, which in SI units equals to $0.005e^{100x}$ kgm^{-2}. The model's response, solved using this value, is significantly different from the one presented by Neely and Kim in [68]. However, the results of Neely and Kim could be reproduced using a constant value of 0.005 kgm^{-2} (see Table 3.1). Furthermore, the TM damping should exhibit an exponential decrease with the distance from the stapes, hence $c_2(x)$=10^2e^{-220x} [Nsm^{-3}] and not $10e^{2.2x}$ [dyn s cm^{-3}] as given in [68].

PARAMETER	VALUE	x=0	x=$L_c/2$	x=L_c
$k_1(x)$ [Nm^{-3}]	$1.10\times10^{10}e^{-400x}$	1.10×10^{10}	7.41×10^{7}	4.99×10^{5}
$k_2(x)$ [Nm^{-3}]	$7\times10^{7}e^{-440x}$	7×10^{7}	2.86×10^{5}	1.17×10^{3}
$k_3(x)$ [Nm^{-3}]	$10^{8}e^{-400x}$	10^{8}	6.74×10^{5}	4.54×10^{3}
$k_4(x)$ [Nm^{-3}]	$6.15\times10^{9}e^{-400x}$	6.15×10^{9}	4.14×10^{7}	2.79×10^{5}
$c_1(x)$ [Nsm^{-3}]	$200+15\times10^{3}e^{-200x}$	1.52×10^{4}	1.43×10^{3}	3.01×10^{2}
$c_2(x)$ [Nsm^{-3}]	$10^{2}e^{-220x}$	10^{2}	6.39	0.41
$c_3(x)$ [Nsm^{-3}]	$20e^{-80x}$	20	7.36	2.71
$c_4(x)$ [Nsm^{-3}]	$1.04\times10^{4}e^{-200x}$	1.04×10^{4}	8.54×10^{2}	7.01×10^{1}
$m_1(x)$ [kgm^{-2}]	3×10^{-2}	3×10^{-2}	3×10^{-2}	3×10^{-2}
$m_2(x)$ [kgm^{-2}]	5×10^{-3}	5×10^{-3}	5×10^{-3}	5×10^{-3}
g	1	1	1	1
b	0.4	0.4	0.4	0.4

Table 3.1: Mechanical parameters (SI units) proposed by Neely and Kim in [68]. The values at x=0, $L_c/2$ and L_c, where L_c=25 mm is the length of the basilar membrane, corresponding to the average length of a cat's cochlea [56], are shown for better comparison with Table 3.2.

to as the BM or cochlear length, L), whereas Neely and Kim use the average BM length measured for a cat cochlea found to be equal to L_c=25 mm (subscript 'c' refers to the cat cochlea) [56]. We use the BM length of 35 mm (average length of the BM in a human cochlea [39]), since the preliminary results of the coupled frequency response of the Neely and Kim model calculated at 1 kHz and for L=25 mm, exhibit reflections in the low frequency region due to the 'zero-pressure' apical boundary condition chosen for the coupled model (see Appendix C). Thus, by extending the length of the cochlea in our simulations, the responses to 1 kHz stimulus frequency, are sufficiently remote from the apex of the cochlea and appear to be less affected by the apical boundary condition. It should be also noted that the trend of the dependence of all mechanical parameters cochlear position, is preserved after extrapolation of the BM. Thus, the model's CF/place map does not change its slope as the BM length is extended.

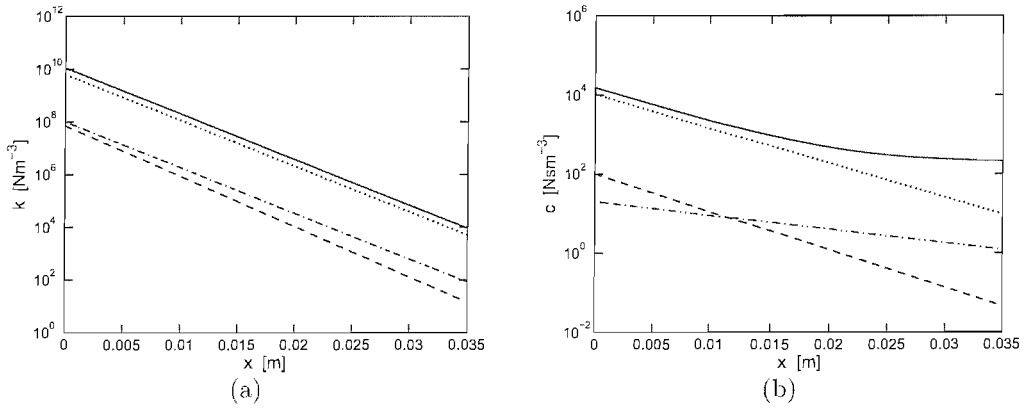

Figure 3.7: Distribution of stiffness (a) and damping (b) components along the cochlea (Table 3.1), chosen by Neely and Kim to simulate the response of a cat cochlea (**NB** the length of the cochlea is extended to 35 mm in our simulations) [68]. k_1, c_1, solid; k_2, c_2, dashed; k_3, c_3, dot-dashed; k_4, c_4, dotted lines.

The slope of the stiffness curves is the same for k_1, k_3 and k_4 and slightly steeper for the stiffness of the TM, k_2 ($\propto e^{-440x}$; Table 3.1), as shown in Fig.3.7(a). The stiffness of the BM, k_1, dominates over the entire length of the BM and is slightly higher than the stiffness of the active component, k_4. However, the stiff-

ness of the TM, k_2, and the stiffness k_3 are about two orders of magnitude lower than k_1. Despite different absolute values of the particular stiffness components, it is worth noting that the gradient of all curves amounts to about six decades per length of the cochlea.

Figure 3.7(b) shows that the damping of the TM, c_2 (dashed) and the active component's damping, c_4 (dotted) have almost the same slope (i.e. $\propto e^{-220x}$ and e^{-200x}, respectively), with the gradient of about three decades per cochlea length. The slope of the BM damping, c_1, is changing almost two decades per cochlea length, and unlike c_2 and c_4, it is approaching asymptotically a constant value of $200\,\mathrm{Nsm}^{-3}$. The damping c_3 (dot-dashed), is less steep than the remaining damping components, and has a gradient of about one decade along the length of the cochlea. Although it has the smallest value at the base, i.e. $c_3(0)=20\,\mathrm{Nsm}^{-3}$, c_3 intersects with the TM damping c_2 at $x\approx 0.0115\,\mathrm{m}$ and becomes higher than the latter one towards the apex. Like the stiffness, k_1, the damping of the BM, c_1, is the dominating damping component of the CP's impedance.

The lever gain, g, is thought to be dependent on the position in the cochlea, x, but is set equal to one and is constant along the BM length. Hence, it appears that the cilia displacement ξ_c is a difference between the transverse BM displacement ξ_b and radial displacement of the TM, ξ_t (Eq.3.3.3). The distribution along the cochlea of the angle of inclination of the RL with respect to the BM, is shown e.g. in [58] (derived for chinchilla cochlea). Knowing that the tangent of the RL's inclination angle is equal to the ratio of the RL's height to the BM width at the place of the measurement, and thus corresponds to a half of the relationship in Eq.3.2.5, distribution of $g(x)$ along the cochlea could be estimated.

The partition mobility responses ($Y_p=Z_p^{-1}$) as a function of position, calculated for the stimulus frequency of 1 kHz are shown in Fig.3.8, and the mobility as a function of frequency calculated at $x=0.0186\,\mathrm{m}$ is shown in Fig.3.9. The mobility is plotted since the velocity response per unit driving force can be directly compared with the form of the coupled responses calculated in Chapter 4, and also because it seems a more natural way of representing the micromechanical response of the CP than the force response per unit driving velocity, i.e. the mechanical impedance. The solid lines represent the active, $\gamma=1$, and the dashed

lines the passive, γ=0, mobility response of the cochlea. The frequency range in the $Y_p(f)$ plots was set from 100 Hz to 10 kHz. Although frequency range of the CF/place function for a cat cochlea obtained by Liberman spans from 90 Hz to 57 kHz [56], the range used here is sufficient for the response where the maximum is predicted at 1 kHz (predicted CF for x=0.0186 m used in the simulations).

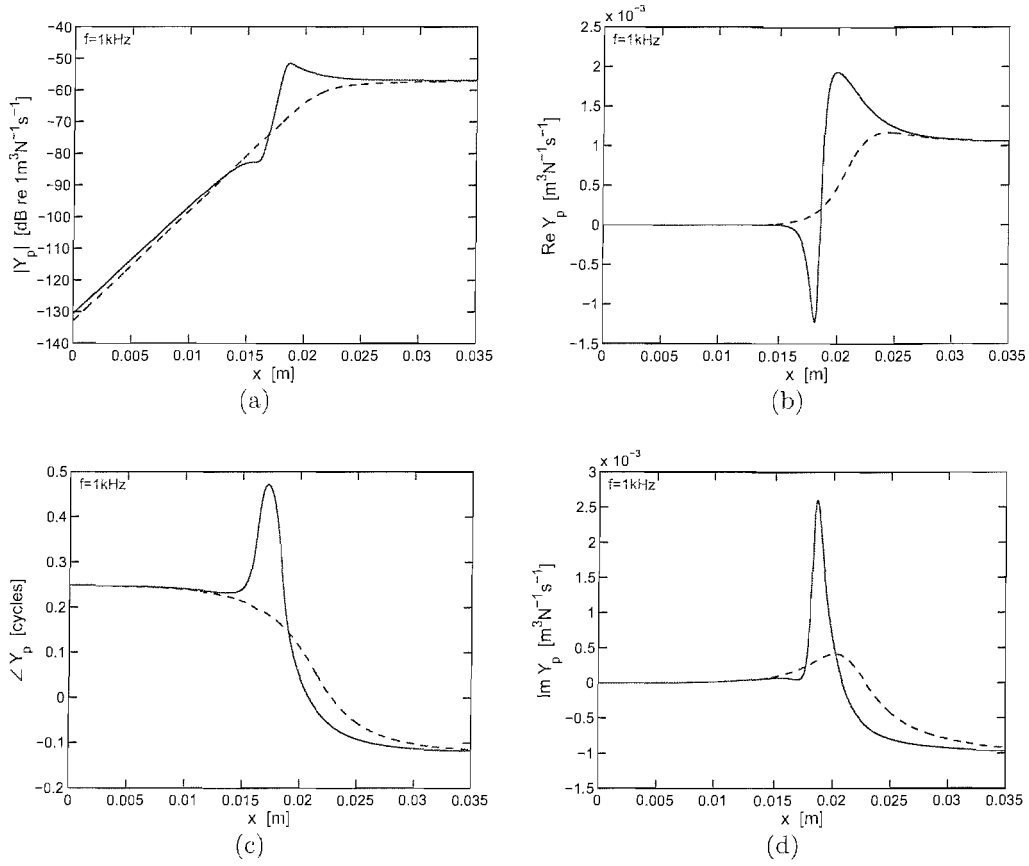

Figure 3.8: Magnitude/phase (a, c) and real/imaginary parts (b, d) of the cochlear partition mobility, Y_p, calculated for the Neely and Kim model [68], as a function of position at f=1 kHz. Solid lines represent the active, whereas dashed lines the passive response of the model, i.e. γ=1 and 0, respectively.

The magnitude of the passive partition's mobility has no specific maximum, whereas the maximum of the active mobility curve occurs at $x \approx 0.0186$ m and defines the characteristic place of the isolated micromechanical model, as shown

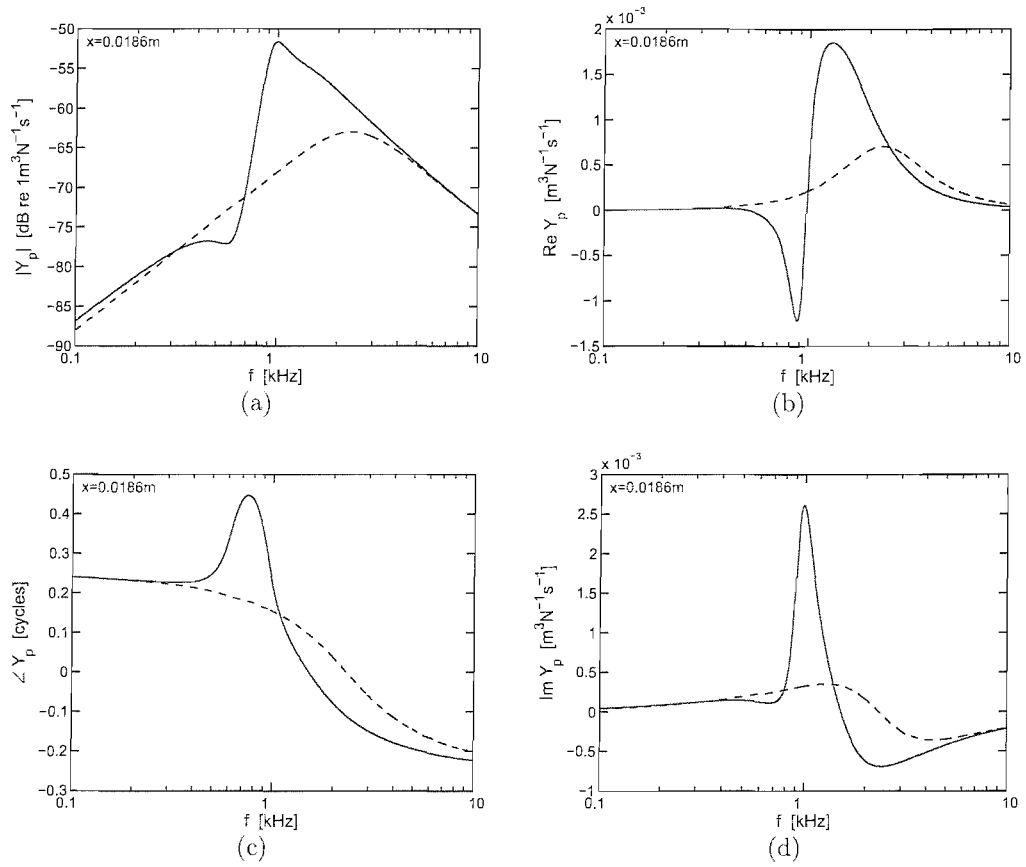

Figure 3.9: Magnitude/phase (a, c) and real/imaginary parts (b, d) of the cochlear partition mobility, Y_p, calculated for the Neely and Kim model [68], as a function of frequency at x=0.0186 m. Solid lines show the active, γ=1, and dashed lines the passive, γ=0, response of the model.

in Fig.3.8(a). The corresponding phase response of the active model, shown in Fig.3.8(c) exhibits a phase lead in the vicinity of the characteristic place, whereas the phase of the passive model exhibits only a phase lag along the length of the cochlea. Similarly, the magnitude of the frequency responses shown in Fig.3.9(a), reveals a significant enhancement of the response of the active model at the frequency of about 1 kHz in comparison with the broad tuning of the passive model's response, and the phase response of the active model exhibits a phase lead below the characteristic frequency, while no phase lead can be observed in the phase of the passive model, as depicted in Fig.3.9(c).

The magnitude peak in the active models' responses coincides with the negative real part of the active models observed in the vicinity of the characteristic place in Fig.3.8(b) and CF in Fig.3.9(b). In the region where the damping is negative the cochlear amplifier undamps the CP vibrations, which leads to the enhancement of the response of the model. The negative real part of the mobility just basal of the characteristic place, indicates that the real part of the mechanical impedance also has a negative real part at this position, as predicted from the shape of the BM response using inverse methods by Zweig [103], de Boer [15] and Talmadge *et al.* [92].

3.4 Modes of vibration in the Neely and Kim model

A dynamic system is characterised by its natural frequencies and principal modes, the number of which equals the number of the DOF [94]. To find the principal modes of vibration for the Neely and Kim model [68], an undamped free vibration of the system in Fig.3.6, will be assumed. Thus, all damping components will be removed from the equations of motion, so that the dashpots in the block diagram in Fig.3.6 are omitted to give a simplified, two degree of freedom system with stiffnesses k_{1-3} and masses $m_{1,2}$, as depicted in Fig.3.10. Furthermore, because the free vibration implies no excitation (forces/pressures) acting on the system, the pressures P_d and P_a are ignored.

The equations of motion describing the system shown in Fig.3.10 are formu-

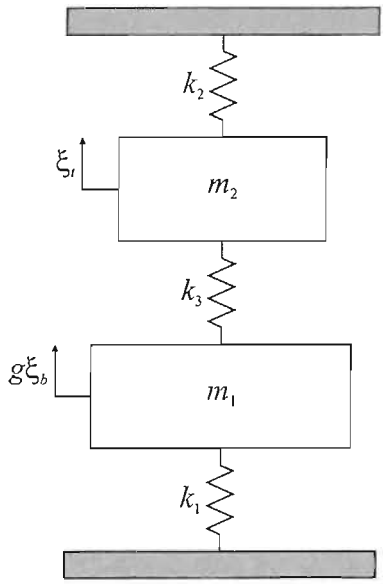

Figure 3.10: Two degree of freedom system proposed by Neely and Kim in [68], simplified to represent a freely vibrating, undamped mechanical system. All parameters same as in Fig.3.6.

lated by

$$\begin{aligned} m_1 g\ddot{\xi}_b &= -k_1 g\xi_b - k_3(g\xi_b - \xi_t), \\ m_2\ddot{\xi}_t &= -k_2\xi_t - k_3(\xi_t - g\xi_b). \end{aligned} \tag{3.4.1}$$

Since g=1 in the Neely and Kim model [68], it can be omitted, so that the equations of motion, after rearrangement, will take the form[9]

$$\begin{aligned} m_1\ddot{\xi}_b + (k_1 + k_3)\xi_b - k_3\xi_t = 0, \\ m_2\ddot{\xi}_t + (k_2 + k_3)\xi_t - k_3\xi_b = 0. \end{aligned} \tag{3.4.2}$$

[9]Note that eliminating the lever gain g in the equations of motion implies physically a multiaxis motion of the system in Fig.3.10, with ξ_b and ξ_t being a transverse and radial displacements, respectively [24]. However, since g=1 it does not influence the numerical result of the present analysis and can be adequately ignored.

Equation 3.4.2 can be rewritten in matrix notation as

$$\begin{bmatrix} m_1 & 0 \\ 0 & m_2 \end{bmatrix} \begin{Bmatrix} \ddot{\xi}_b \\ \ddot{\xi}_t \end{Bmatrix} + \begin{bmatrix} k_1 + k_3 & -k_3 \\ -k_3 & k_2 + k_3 \end{bmatrix} \begin{Bmatrix} \xi_b \\ \xi_t \end{Bmatrix} = \begin{bmatrix} 0 \\ 0 \end{bmatrix}, \tag{3.4.3}$$

or, equivalently,

$$\mathbf{M}\,\ddot{\boldsymbol{\xi}} + \mathbf{K}\,\boldsymbol{\xi} = 0, \tag{3.4.4}$$

where

$$\mathbf{M} = \begin{bmatrix} m_1 & 0 \\ 0 & m_2 \end{bmatrix}, \tag{3.4.5}$$

$$\mathbf{K} = \begin{bmatrix} k_1 + k_3 & -k_3 \\ -k_3 & k_2 + k_3 \end{bmatrix}, \tag{3.4.6}$$

$$\ddot{\boldsymbol{\xi}} = \begin{Bmatrix} \ddot{\xi}_b \\ \ddot{\xi}_t \end{Bmatrix}, \tag{3.4.7}$$

$$\boldsymbol{\xi} = \begin{Bmatrix} \xi_b \\ \xi_t \end{Bmatrix}, \tag{3.4.8}$$

where $\mathbf{M}$ and $\mathbf{K}$ are real, symmetric and positive mass and stiffness matrices, with the off-diagonal terms representing the dynamic (mass) and static (stiffness) coupling, respectively [94]. $\ddot{\boldsymbol{\xi}}$ and $\boldsymbol{\xi}$ are the acceleration and displacement vectors respectively.

Assuming time-harmonic solutions of the form $\xi_b{=}\Xi_b e^{j\omega t}$ and $\xi_t{=}\Xi_t e^{j\omega t}$, the equations of motion in Eq.3.4.2 will be formulated by (see Appendix A for details)

$$\begin{aligned} (k_1 + k_3 - \omega^2 m_1)\Xi_b - k_3\Xi_t = 0, \\ (k_2 + k_3 - \omega^2 m_2)\Xi_t - k_3\Xi_b = 0. \end{aligned} \tag{3.4.9}$$

Using the first relationship in the above equation we obtain a solution of the form

$$\Xi_t = \frac{k_1 + k_3 - \omega^2 m_1}{k_3}\,\Xi_b, \tag{3.4.10}$$

which after substitution to the second relationship gives

$$\left[\frac{(k_1+k_3-\omega^2 m_1)}{k_3}(k_2+k_3-\omega^2 m_2)-k_3\right]\Xi_b=0. \tag{3.4.11}$$

Note that setting Ξ_b=0 gives the trivial solution Ξ_b=Ξ_t=0, which implies no motion. Equating the bracketed term in Eq.3.4.11 to nought gives a quadratic in ω^2 with two real and positive values for ω^2 [94], i.e.

$$\omega^4 m_1 m_2-\omega^2[m_1(k_2+k_3)+m_2(k_1+k_3)]+k_1(k_2+k_3)+k_2k_3=0, \tag{3.4.12}$$

from which the natural (angular) frequencies, of the first and second mode, ω_1 and ω_2, respectively, can be calculated as two roots of quadratic in ω^2, i.e.

$$\omega_1^2=\frac{m_1(k_2+k_3)+m_2(k_1+k_3)-\sqrt{\Delta}}{2m_1m_2}, \tag{3.4.13}$$

and

$$\omega_2^2=\frac{m_1(k_2+k_3)+m_2(k_1+k_3)+\sqrt{\Delta}}{2m_1m_2}, \tag{3.4.14}$$

where

$$\Delta=[m_1(k_2+k_3)+m_2(k_1+k_3)]^2-4m_1m_2\left[k_1(k_2+k_3)+k_2k_3\right]. \tag{3.4.15}$$

Using the set of parameters in Table 3.1, suggested by Neely and Kim to simulate cat cochlea biomechanics [68], the natural frequencies $f_{1,2}$=$\omega_{1,2}/2\pi$ and the separation between f_2 and f_1, i.e. $\log_2(f_2/f_1)$, were calculated[10]. Furthermore, although the system in Fig.3.10 is a coupled system, we estimate the resonance frequencies of the BM, f_{BM}, and the TM, f_{TM}, as if it were two separate systems. We assume that the lower mass, m_1 and stiffness k_1 form a single DOF BM/organ of Corti mechanical system, whose resonance frequency would amount to

$$f_{\mathrm{BM}}=\frac{1}{2\pi}\sqrt{\frac{k_1}{m_1}}. \tag{3.4.16}$$

[10]We calculate $\log_2(f_2/f_1)$ according to the definition of an octave f_2/f_1=2 [48] to represent the separation between f_2 and f_1 in terms of an octave.

For the parameters selected by Neely and Kim (Table 3.1),

$$f_{\mathrm{BM}} = \frac{1}{2\pi}\sqrt{\frac{k_1(0)}{m_1}}e^{-200x}, \tag{3.4.17}$$

where $k_1(0)$ is the value of the BM stiffness at x=0. Equation 3.4.17 is analogous to Eq.3.1.7 derived for a single DOF cochlear model described in Section 3.1.

The TM mass, m_2 with its stiffness k_2 and cilia stiffness, k_3, will account for the second subsystem in Fig.3.10. According to the second relationship in Eq.3.4.2

$$m_2\ddot{\xi}_t + (k_2 + k_3)\xi_t = k_3\xi_b, \tag{3.4.18}$$

where the term on the right-hand side, $k_3\xi_b$, can be treated as a forcing term due to the displacement of the base (BM), ξ_b, acting on the spring k_3. Both separate subsystems are presented in Fig.3.11 (**NB** g=1, Table 3.1). Thus, in the absence of the forcing term, i.e. $k_3\xi_b$=0, the natural frequency of the second subsystem will take the form

$$f_{\mathrm{TM}} = \frac{1}{2\pi}\sqrt{\frac{k_2 + k_3}{m_2}}, \tag{3.4.19}$$

which for the parameters given in Table 3.1 is approximately equal to

$$f_{\mathrm{TM}} \approx \frac{1}{2\pi}\sqrt{\frac{k_2(0) + k_3(0)}{m_2}}e^{-200x}, \tag{3.4.20}$$

and will have almost the same slope as the slope of f_{BM} as a function of position x. Figure 3.12(a) depicts the comparison of frequencies $f_{1,2}$ with the estimated resonance frequencies for BM, f_{BM}, and TM, f_{TM}, whereas the comparison of $\log_2(f_2/f_1)$ and $\log_2(f_{\mathrm{BM}}/f_{\mathrm{TM}})$ ratios is shown in Fig.3.12(b).

The plots reveal that the BM natural frequency, f_2, is higher than the one of the TM, f_1, for all positions in the cochlea. The values of frequency f_2, equal to about 97 kHz at the base (x=0) and about 650 Hz at x=L_c=25 mm (cat cochlea length), and about 90 Hz at the model's apex, x=L=35 mm. The frequencies of 97 kHz and 650 Hz are significantly larger than the ones estimated for cat cochleae by Liberman [56], or as calculated from the CF/place relationship for a cat cochlea

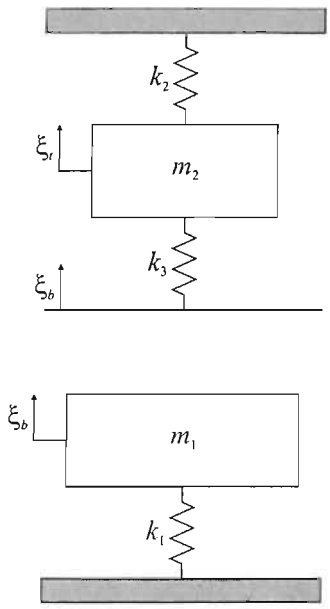

Figure 3.11: Separation of the system in Fig.3.10 into two subsystems with their resonant frequencies f_{BM} (lower) and f_{TM} (upper). NB lever gain g=1 according to Table 3.1 and the displacement for the lower subsystem is thus ξ_b.

given by Greenwood in [39] (dotted line in Fig.3.12(a)), i.e. 57 kHz and 90 Hz at the base and the apex, respectively[11]. However, it should be noted that the resonance frequencies $f_{1,2}$ are derived for isolated, two DOF systems which are not coupled longitudinally, whereas the CF/place maps given by Liberman [56] and Greenwood [39] were derived for real 'coupled' systems and hence are not expected to match the distribution of the natural frequencies along the cochlea obtained from the present model. Additionally, frequency f_2 calculated from Eq.3.4.14, is almost equal, for all positions x, to f_{BM} calculated using Eq.3.4.16 and k_1 and m_1 from Table 3.1. The natural frequency of the system, f_1 (Eq.3.4.13), ranges from about 29 kHz at the base, through about 170 Hz at x=L_c=25 mm, to about 22 Hz at the apex (x=35 mm), and is almost equal to the frequency of the TM calculated from Eq.3.4.19 and parameters in Table 3.1. Hence, the lines of f_2 and

[11] According to Greenwood [39], CF=$A(10^{ax/L}-k)$, where for a cat cochlea A=456, a=2.1, and the length of the cochlea, L, is estimated to 25mm [56], so that k=0.8. Because the CF/place map is formulated for the position from the apex to base, values of vector x were reversed to calculate CF distribution from the base to apex of the cochlea.

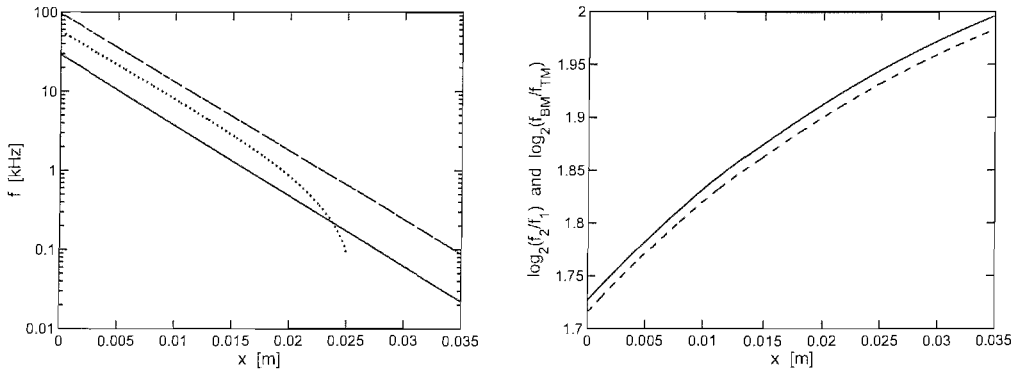

Figure 3.12: Natural frequencies of the system presented in Fig.3.10 as a function of position x (a). f_1 (solid) and f_2 (dashed), are plotted together with the estimated resonance frequencies for the basilar, $f_{\mathrm{BM}}=\frac{1}{2\pi}\sqrt{\frac{k_1}{m_1}}$ and tectorial, $f_{\mathrm{TM}}=\frac{1}{2\pi}\sqrt{\frac{k_2+k_3}{m_2}}$ membranes (dot-dashed; covered by the f_2 and f_1 line, respectively), and the CF/place map (dotted) derived according to the formula given by Greenwood in [39] for the cat cochlea length L_c=25 mm. (b) comparison of the ratios $\log_2(f_2/f_1)$ (solid) and $\log_2(f_{\mathrm{BM}}/f_{\mathrm{TM}})$ (dashed).

f_{BM} as well as of f_1 and f_{TM} in Fig.3.12(a), cover each other[12]. As predicted, the slopes of $f_{2,BM}$ and $f_{1,TM}$ are almost the same with the distance from the base.

Note that the resonance frequency f_{TM} is defined in the same way as the frequency of the pole, f_p, in the model of Allen (Eq.3.2.14), which is, by definition, greater than the frequency of the zero, f_z, (Eq.3.2.13). Allen also derives the cochlear map for his model as $\omega_{CF}=\sqrt{K_B/(m_B+m_T)}$ [1] which is slightly smaller than the BM resonance frequency, f_{BM}, estimated for the Neely and Kim model since the TM mass is not included in the f_{BM} estimate (Eq.3.4.16). The frequency of the zero, f_z, is smaller than ω_{CF} for all positions along the cochlea in the Allen model (see Fig.2 in [1]). This is also the case for the Neely and Kim model since $f_z<f_{TM}$ and f_{TM} is smaller than f_{BM}. However, it should be noted that the f_p is greater than $f_{CF}=\omega_{CF}/2\pi$ along the cochlea in the model of Allen, whereas the estimated f_{TM} ($\approx f_p$) is smaller than f_{BM} ($\approx f_{CF}$) for all positions along the cochlea in the model of Neely and Kim.

Ratios $\log_2(f_2/f_1)$ (solid) and $\log_2(f_{BM}/f_{TM})$ (dashed) are not constant but increase with position x, as shown in Fig.3.12(b), where the second ratio is slightly lower than the first one because f_2 is slightly higher than f_{BM} and f_1 is slightly lower than f_{TM}. Figure 3.12(b) shows that the ratio $\log_2(f_2/f_1)$ ranges from roughly 1.73 at the base to about 2 at the apex of the cochlea, so that the difference between the resonance frequency f_2 and f_1 is higher than one octave at the base and equals about two octaves at the apex of the cochlea. Also the second ratio, $\log_2(f_{BM}/f_{TM})$, is higher than one and increases from about 1.72 at the base to about 1.98 at the apex, and hence the difference between f_{BM} and f_{TM} is higher than one octave at the base and equals almost two octaves at the apex of the cochlea. This appears to be inconsistent with the results in e.g. [40, 61], where the lower resonance frequency (TM) was found to be about half an octave below the higher frequency (BM). However, it has to be emphasised that the distribution of the resonance frequencies is presented here as a continuum of frequencies derived for each single, independent element of the CP, whereas physiological measurements are conducted on a fully coupled

[12]Mean ratios $\overline{f_2/f_{BM}}$ and $\overline{f_1/f_{TM}}$, averaged along all positions x, are equal to 1.004 and 0.997, respectively.

(continuous) cochlear partition.

According to the relations in Eq.3.4.9 the ratio of the amplitudes is formulated by

$$\frac{\Xi_b}{\Xi_t} = \frac{k_3}{k_1 + k_3 - \omega^2 m_1} = \frac{k_2 + k_3 - \omega^2 m_2}{k_3}, \tag{3.4.21}$$

thus, for the two natural frequencies, after substituting ω_1

$$\frac{\Xi_{b1}}{\Xi_{t1}} = \frac{k_3}{k_1 + k_3 - \omega_1^2 m_1} = \frac{k_2 + k_3 - \omega_1^2 m_2}{k_3}, \tag{3.4.22}$$

and ω_2

$$\frac{\Xi_{b2}}{\Xi_{t2}} = \frac{k_3}{k_1 + k_3 - \omega_2^2 m_1} = \frac{k_2 + k_3 - \omega_2^2 m_2}{k_3}, \tag{3.4.23}$$

where the second index of Ξ denotes the natural frequency ω_1 or ω_2.

Equations 3.4.22 and 3.4.23 express the amplitude ratios, hence we choose the amplitudes of the BM displacement, ξ_b, Ξ_{b1} (at ω_1) and Ξ_{b2} (at ω_2) as equal to one, so that the amplitude ratio will be normalised to this value and the normal modes $\phi_{1,2}(\xi)$ will be obtained as

$$\begin{aligned} \phi_1 &= \begin{Bmatrix} 1 \\ \Xi_{t1} \end{Bmatrix}, \\ \phi_2 &= \begin{Bmatrix} 1 \\ \Xi_{t2} \end{Bmatrix}, \end{aligned} \tag{3.4.24}$$

where Ξ_{t1} and Ξ_{t2} can be derived from Eq.3.4.22 and 3.4.23.

Finally, because we assumed a time-harmonic motion, hence the motion at the first mode will amount to

$$\begin{Bmatrix} \xi_{b1} \\ \xi_{t1} \end{Bmatrix} = \begin{Bmatrix} 1 \\ \Xi_{t1} \end{Bmatrix} e^{j\omega_1 t}, \tag{3.4.25}$$

and at the second mode

$$\begin{Bmatrix} \xi_{b2} \\ \xi_{t2} \end{Bmatrix} = \begin{Bmatrix} 1 \\ \Xi_{t2} \end{Bmatrix} e^{j\omega_2 t}, \tag{3.4.26}$$

or, equivalently

$$\left\{ \begin{array}{c} \xi_{b1} \\ \xi_{t1} \end{array} \right\} = \left\{ \begin{array}{c} 1 \\ \Xi_{t1} \end{array} \right\} (A \sin \omega_1 t + B \cos \omega_1 t), \tag{3.4.27}$$

$$\left\{ \begin{array}{c} \xi_{b2} \\ \xi_{t2} \end{array} \right\} = \left\{ \begin{array}{c} 1 \\ \Xi_{t2} \end{array} \right\} (C \sin \omega_2 t + D \cos \omega_2 t), \tag{3.4.28}$$

where A, B, C and D are real constants of integration, determined by the initial conditions [94], and equal to

$$A = C = 0, \tag{3.4.29}$$

$$B = \frac{100\Xi_{t2}}{\Xi_{t2} - \Xi_{t1}}, \tag{3.4.30}$$

$$D = \frac{100\Xi_{t1}}{\Xi_{t1} - \Xi_{t2}}, \tag{3.4.31}$$

assuming that at t=0: ξ_b=100, ξ_t=0, $\dot{\xi}_b$=$\dot{\xi}_t$=0 and taking Ξ_{b1}=Ξ_{b2}=1 (Appendix A).

The actual motion is time-harmonic at two natural frequencies ω_1 and ω_2, and is defined as

$$\left\{ \begin{array}{c} \xi_b \\ \xi_t \end{array} \right\} = \left\{ \begin{array}{c} 1 \\ \Xi_{t1} \end{array} \right\} B \cos \omega_1 t \; + \; \left\{ \begin{array}{c} 1 \\ \Xi_{t2} \end{array} \right\} D \cos \omega_2 t, \tag{3.4.32}$$

where $B\cos(\omega_1 t)$ and $D\cos(\omega_2 t)$ are the principal coordinates at frequencies ω_1 and ω_2, respectively, where B and D are the amplitudes of the first and second mode, respectively. The terms in curly brackets on the right-hand side of Eq.3.4.32, are the eigenvectors or the mode shapes at ω_1 and ω_2, respectively (compare Eq.3.4.24) [94].

Five periods of harmonic displacements $\xi_{b1,t1}$ and $\xi_{b2,t2}$ for the first and second mode of vibration (Eq.3.4.32) were calculated for the parameters chosen by Neely and Kim [68] (Table 3.1), as shown in Fig.3.13. The amplitudes, B and D were chosen for the location of around x=0.0186 m in the cochlea, corresponding to the place where the maximum of the CP mobility magnitude in Fig.3.8(a) was

observed (derived for stimulus frequency equal to f=1 kHz). However, it should be noted that according to Fig.3.12(a) at the site of x=0.0186 m f_1≈621 Hz, whereas f_2≈2.3 kHz (1kHz occurs at about 0.0163 m for f_1 and x=0.0229 m for f_2).

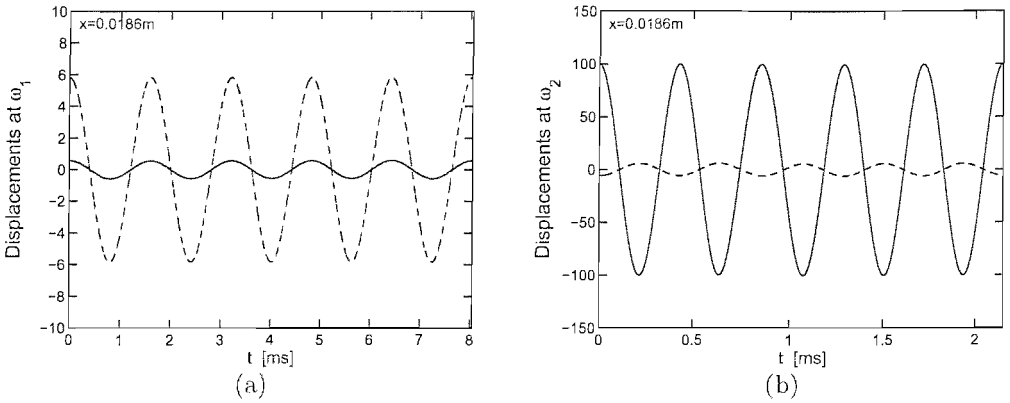

Figure 3.13: Displacements $10\xi_{b1}$ (solid) and ξ_{t1} (dashed) at the first mode of vibration, ω_1≈2π×621 Hz (a), and ξ_{b2} (solid) and ξ_{t2} (dashed) at the second mode where ω_2≈2π×2.3 kHz (b), calculated for parameters selected by Neely and Kim (Table 3.1) [68] (**NB** ξ_{b1} multiplied by a factor of ten to facilitate comparison).

Figure 3.13 reveals two separate modes of vibration of the system, where the BM and the TM are vibrating in phase and out of phase. At the first mode, Fig.3.13(a), the BM and TM are vibrating in phase and the amplitude of the BM is significantly smaller than the amplitude of the TM vibrations (maxima of ξ_{b1} to ξ_{t1} as 0.06 to 6, respectively. **NB** ξ_{b1} was multiplied by a factor of ten in Fig.3.13(a)). However, in the second mode of vibration, Fig.3.13(b), the BM and TM vibrate out of phase, and the vibration amplitude of the BM is much higher than that of the TM (maxima of ξ_{b2} to ξ_{t2} as 100 to 6, respectively). Furthermore, the period of vibrations shown in Fig.3.13(a) amounts to about 1.61 ms and in Fig.3.13(b) to about 0.43 ms, which corresponds to the frequencies of f_1≈621 kHz and f_2≈2.3 Hz, respectively, which agrees with the frequencies obtained at the site of about x=0.0186 m shown in Fig.3.12(a).

To finish the vibration analysis the point mobility of the BM and the transfer

mobility of the TM, Y_b and Y_t, respectively, being the ratio of their velocities and a unit force excitation acting upon the BM, will be derived. We assume that the lower mass of the system in Fig.3.10, m_1, is excited by a unit force f, which, like the displacements ξ_b and ξ_t, is time harmonic of the form $f{=}Fe^{j\omega t}$. Thus, equations of motion for such a forced system will be similar to those in Eq.3.4.9, but with an additional force term on the right-hand side of the first relationship, i.e.

$$\begin{aligned}(k_1 + k_3 - \omega^2 m_1)\Xi_b - k_3\Xi_t &= F,\\ (k_2 + k_3 - \omega^2 m_2)\Xi_t - k_3\Xi_b &= 0,\end{aligned} \tag{3.4.33}$$

where the amplitude of the force $F{=}1$ (the initial phase of the complex amplitude is assumed zero).

From the above equations the ratios of Ξ_b/F and Ξ_t/F (receptance) of the system can be derived, or knowing that $j\omega\Xi{=}V$, where V is the velocity (Appendix A), we have

$$\begin{aligned}Y_b = \frac{V_b}{F} &= \frac{j\omega(k_2 + k_3 - \omega^2 m_2)}{(k_1 + k_3 - \omega^2 m_1)(k_2 + k_3 - \omega^2 m_2) - k_3^2},\\ Y_t = \frac{V_t}{F} &= \frac{j\omega k_3}{(k_1 + k_3 - \omega^2 m_1)(k_2 + k_3 - \omega^2 m_2) - k_3^2},\end{aligned} \tag{3.4.34}$$

where Y_b and Y_t are the mobilities of the forced system in Fig.3.10.

The denominators of the relationships in Eq.3.4.34 have the same form as the quadratic in ω^2 in Eq.3.4.12, and here define the frequencies of the resonance peaks (poles) in the mobility functions, which are the same for both Y_b and Y_t. However, the numerators in Eq.3.4.34 define the frequencies of the antiresonances (zeros) in the mobility plots, where there is one antiresonance in Y_b at $f_{0b}{=}\frac{1}{2\pi}\sqrt{\frac{k_2+k_3}{m_2}}$, and there are no antiresonances in Y_t. The relationship for f_{0b} is the same as for f_{TM} in Eq.3.4.19, so that the antiresonance frequency can be read from the plot in Fig.3.12(a), and at $x{=}0.0186\,\mathrm{m}$ it amounts to about $f_{0b}{=}f_{\mathrm{TM}}{\approx}623\,\mathrm{Hz}$ (**NB** $f_2{\approx}621\,\mathrm{Hz}$). At this frequency the upper mass, m_2 acts as a perfect vibration absorber so that there is no motion at $\dot{\xi}_b$, whereas, since there

is no antiresonance frequency in Y_t there is some measure of $\dot{\xi}_t$ at all frequencies in this response [70].

It can be noted that all parameters in Eq.3.4.34 are defined per unit area (see Table 3.1). Hence the effective dimension of the mobility is $[\mathrm{m^3N^{-1}s^{-1}}]$, which could be treated as one for a two DOF system (Fig.3.10) with an external pressure excitation and is consistent with the one that the BM undergoes in the real cochlea, i.e. cochlear fluid's pressure difference acoustic excitation. More interestingly, taking into account the damping in the model, we could determine the mobility of the passive Neely and Kim model [68], after rewriting relationships in Eq.3.4.34. In such a case the two DOF system in Fig.3.10 will be modified to resemble the block diagram proposed by Neely and Kim (Fig.3.6), however, with no active forces acting in the model and unit force excitation upon the BM. The corresponding equations of motion for a passive, damped (acoustically driven) two DOF system will be extended by adding the respective damping components (see Appendix A)

$$\begin{aligned}(k_1 + k_3 + j\omega(c_1 + c_3) - \omega^2 m_1)\Xi_b - (k_3 + j\omega c_3)\Xi_t &= F,\\ (k_2 + k_3 + j\omega(c_2 + c_3) - \omega^2 m_2)\Xi_t - (k_3 + j\omega c_3)\Xi_b &= 0,\end{aligned} \tag{3.4.35}$$

so that the point BM and transfer TM mobility will take the form

$$\begin{aligned}Y_b = \frac{V_b}{F} &= \frac{j\omega[k_2 + k_3 + j\omega(c_2 + c_3) - \omega^2 m_2]}{\Omega},\\ Y_t = \frac{V_t}{F} &= \frac{j\omega(k_3 + j\omega c_3)}{\Omega},\end{aligned} \tag{3.4.36}$$

where

$$\Omega = [k_1 + k_3 + j\omega(c_1 + c_3) - \omega^2 m_1][k_2 + k_3 + j\omega(c_2 + c_3) - \omega^2 m_2] - (k_3 + j\omega c_3)^2. \tag{3.4.37}$$

It is noteworthy that using the formulae in Eq.3.4.36, the ratio of the TM to

BM velocity, independent of the excitation used for the model, can be determined as

$$\frac{V_t}{V_b} = \frac{k_3 + j\omega c_3}{k_2 + k_3 + j\omega(c_2 + c_3) - \omega^2 m_2}, \tag{3.4.38}$$

thus, if the velocity of the BM is known, it can be multiplied by the V_t/V_b ratio to calculate the velocity of the TM. It can be seen from Fig.3.6 that it is only m_1 that is driven by both the fluid and active pressures so the relative motion of the TM and BM is described by Eq.3.4.38 for both the passive and active Neely and Kim model.

The left panel of Fig.3.14 shows the magnitude and phase of the point, Y_b (solid), and transfer mobility, Y_t (dashed) for the undamped case. Both response curves have two resonance peaks, first at the frequency of $f_1 \approx 621\,\text{Hz}$ and the second at $f_2 \approx 2.3\,\text{kHz}$ (at $x = 0.0186\,\text{m}$), since the denominator of Eq.3.4.34 is defined in the same way as the frequency equation in Eq.3.4.12, the roots of which determined the natural frequencies of the system in Fig.3.10. There is no antiresonance in the Y_t mobility curve; however, a shallow antiresonance at the frequency of about 623 Hz occurs in the curve of Y_b as it was predicted. Furthermore, each of the resonances coincides with a phase lag of half of a cycle. However, since the magnitude of the antiresonance in Y_b is very small (and very close to the resonance peak at f_1) the predicted half of a cycle phase lead is not visible in the phase response plot (solid line in Fig.3.14(c)). Both curves have asymptotic slopes of 20 dB/decade at low frequencies. However, since Y_t is a transfer mobility of the $\dot{\xi}_t$ output to the input at the lower mass m_1, its asymptotic slope at high frequencies amounts to $-60\,\text{dB/decade}$ and not $-20\,\text{dB/decade}$ as in the case of Y_b.

The right panel of Fig.3.14 depicts the BM point mobility and transfer mobility of the TM calculated for the damped Neely and Kim model [68], using Eqs.3.4.36-3.4.37. It can be noted that the BM point mobility in Fig.3.14(b) matches the CP mobility calculated for the passive Neely and Kim model presented in Fig.3.9(a) (dashed line), with a minor difference in magnitude, which is slightly higher in Fig.3.14(b) due to the b/g factor (Eq.3.3.7) not taken into account in Eq.3.4.36. The phase response in Fig.3.14(d) has exactly the same char-

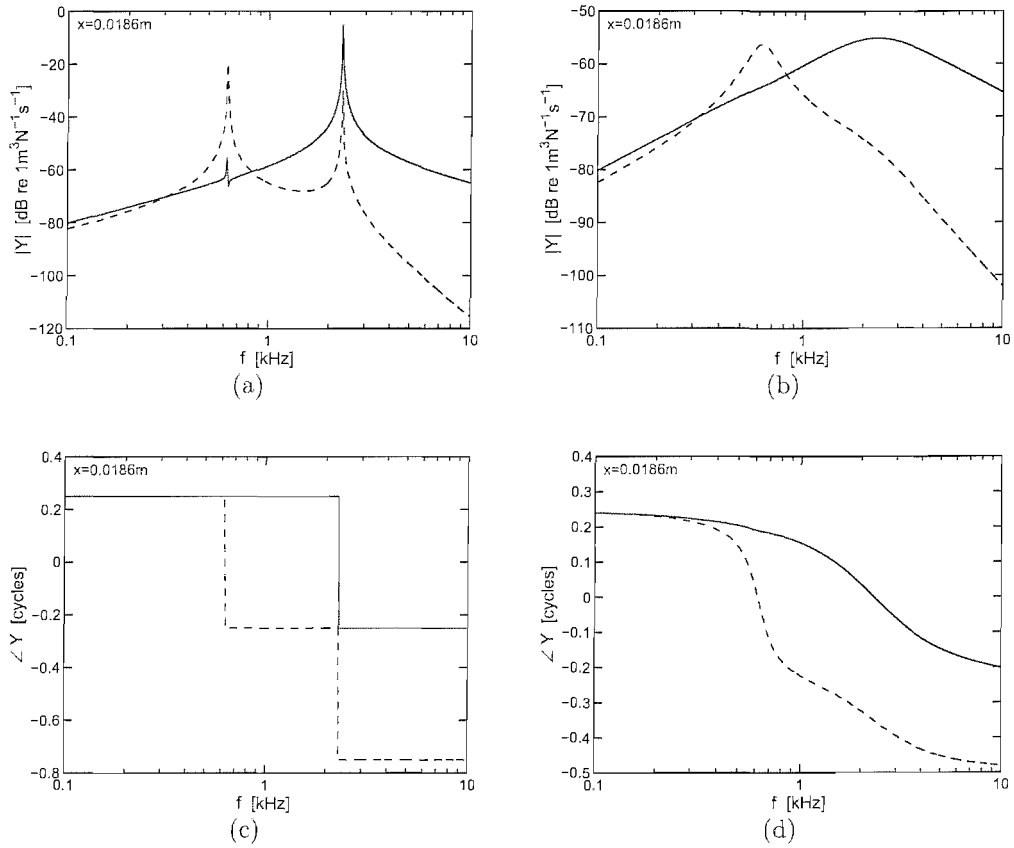

Figure 3.14: Magnitude (a, b) and phase (c, d) of the point mobility of the basilar membrane (solid), and the transfer mobility of the tectorial membrane (dashed), derived for the passive, undamped system in Fig.3.10 (left panel) and the passive, damped two degree of freedom system in Fig.3.6 (right panel), calculated at x=0.0186 m. Both systems were excited by a unit force acting upon the basilar membrane, and the parameters proposed by Neely and Kim [68] (Table 3.1) were used for calculations.

acteristic as the one of the passive model of Neely and Kim shown in Fig.3.9(c).

The magnitude and phase of the complex TM velocity to BM velocity ratio defined in Eq.3.4.38, are plotted as a function of stimulus frequency in Fig.3.15. The cochlear location was fixed to 0.0186 m, which corresponds to the maximum of the active (γ=1) CP mobility for 1 kHz stimulus frequency. The magnitude of the TM/BM velocity ratio is negative at low frequencies, up to about 300 Hz, thus the velocity of the BM is higher than the velocity of the TM in this region, as shown in Fig.3.15(a). Above 300 Hz the magnitude of V_t/V_b increases to about 8 dB (re 1) at 610 Hz (near the maximum of the TM's transfer mobility $\approx$623 Hz) beyond which it decreases rapidly and becomes negative again above about 800 Hz. The phase of the V_t/V_b ratio shown in Fig.3.15(b), is almost constant in the low frequency region and decreases rapidly above approximately 500 Hz until about 1 kHz reaching a total phase lag of about 0.38 cycles. Above 1 kHz the phase increases until the high frequency limit.

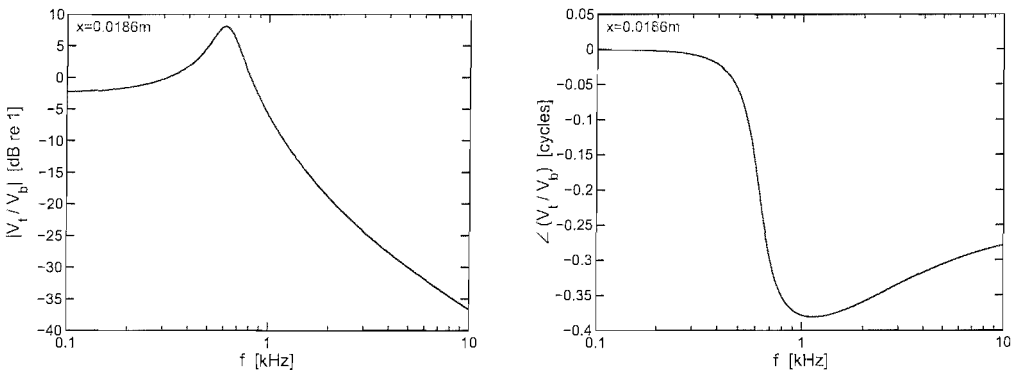

(a) (b)

Figure 3.15: The magnitude (a) and phase (b) of the ratio of the tectorial membrane to basilar membrane velocity, V_t/V_b, as a function of stimulus frequency for the Neely and Kim model [68]. The ratio was calculated using parameters in Table 3.1 evaluated at x=0.0186 m.

3.5 Review of the 1993 model of Neely

In this section the lumped parameter model proposed by Neely in 1993 [66], will be discussed. It is a model that was developed from the one of Neely and Kim proposed in 1986 [68], and described in Sections 3.3 and 3.4. The basic concepts concerning the macro- and passive micromechanics of the cochlea remain the same and are generally consistent with the earlier model [68], and the model of Allen [1] discussed in Section 3.2.

The model assumes a two DOF system for the micromechanics, in which the first DOF corresponds to the transverse motion of the BM, whereas the second DOF to the radial motion of the TM. Furthermore, the parallel motion of the BM and TM results in a relative radial shearing motion, which is thought to deflect the stereocilia of the OHC and produce the cell's depolarisation. However, the action of the OHC is not modelled as an active pressure component, P_a, as in the model of Neely and Kim, but as an *internal displacement* which causes the upward displacement of the RL. Although Neely uses an electrical analogy in his paper, here we present an equivalent mechanical system to describe model's dynamics, as shown in Fig.3.16.

The two DOF system in Fig.3.16 depicts a mechanical block diagram, in which equivalent radial motions of the BM and the organ of Corti are considered, similarly to Fig.3.6 in Section 3.3. Note that all mechanical parameters of the lower subsystem, i.e. M_b, K_b and R_b, are divided by g^2, whereas the pressure difference, P_f, is divided by g to give equivalent model with single-axis (only radial) motion [24]. Also, $g\xi_b$ and $g\xi_c$ denote now radial displacements. The figure is proposed by the present author according to Neely's electrical circuit diagram and the equations of motion for the model given in [66].

The lower block of the system in Fig.3.16, is assumed by Neely to correspond to the mass of the BM, M_b, which is connected to the bony wall of the cochlea by the spring K_b and damper R_b, corresponding to the BM stiffness and damping, respectively [66]. The upper block of the system corresponds to the mass of the TM, M_t, which is connected to the bony wall of the cochlea by the spring K_t and damper R_t, corresponding to the TM's stiffness and damping. The spring K_0 and damper R_0, in Fig.3.16 correspond to the stiffness of the OHC stereocilia

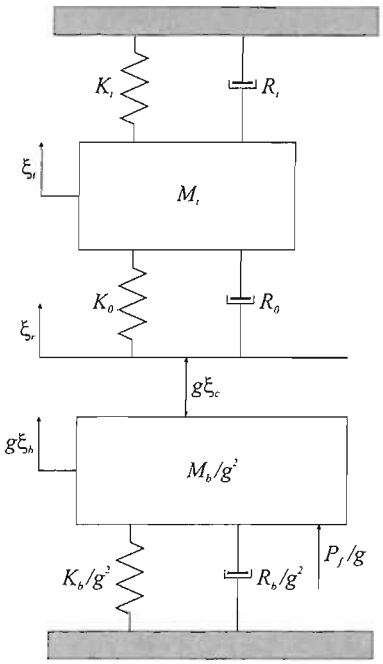

Figure 3.16: Block diagram of a two degree of freedom system proposed for the model of Neely [66]. **NB** All motion is in the radial direction.

and viscous damping of the subtectorial fluid [66].

The system is excited by the pressure difference of the cochlear fluid across the CP, P_f, which leads to the transverse displacement of the BM, ξ_b. Assuming the distance between the RL and TM is constant, the relative shearing motion between these structures leads to the deflection of the OHC's stereocilia, ξ_r, and the cell's contraction, which is depicted by an additional radial displacement $g\xi_c$ in Fig.3.16. Finally, the TM undergoes a radial displacement, ξ_t, which affects the radial RL displacement ξ_r and the active displacement $g\xi_c$.

To begin with, we consider the displacements of the particular components as defined by Neely [66]. The amount of the transverse OHC contraction, ξ_c, is related to the deflection of the hair bundle, ξ_0, in the radial direction

$$\xi_c = H_c \xi_0, \tag{3.5.1}$$

where H_c is the OHC gain function and will be described later. The radial displacement of the hair bundle, ξ_0, is defined as the difference between the

radial RL, ξ_r, and TM, ξ_t, displacements, so that

$$\xi_0 = \xi_r - \xi_t. \tag{3.5.2}$$

Furthermore, the radial displacement of the RL, ξ_r, proportional to the transverse BM displacement, ξ_b, minus the transverse OHC contraction, ξ_c, takes the form

$$\xi_r = g(\xi_b - \xi_c), \tag{3.5.3}$$

where g is a lever gain coupling the BM and TM [66], and is analogous to the lever gain g in the model of Neely and Kim (compare Eq.3.3.3) [68]. Finally, the relation between the CP's volume velocity, $\dot{\xi}_p$, and BM's velocity, $\dot{\xi}_b$, is expressed as[13]

$$\dot{\xi}_p = -A_p \dot{\xi}_b, \tag{3.5.4}$$

where A_p is the effective area of the CP, and

$$A_p = b_w \delta, \tag{3.5.5}$$

where b_w=10^{-4} m and δ=5×10^{-5} m are the effective width of the CP and the longitudinal thickness of the CP's slice, respectively, and hence A_p=5×10^{-9} m^2. It is interesting to note that Neely defines the BM displacement ξ_b as positive towards the scala vestibuli, whereas the CP displacement, ξ_p, as positive towards the scala tympani, thus the minus sign appears in Eq.3.5.4 [66].

It is clear from the above definitions, that the model of Neely proposed in [66], assumes a transverse parallel motion of the BM and TM, which produces a relative shear displacement of the cilia of the OHC. Thus, ξ_b is a transverse displacement, acting on the BM mechanical components, ξ_c is a transverse displacement corresponding to the active component of the model, which together

[13]It is rather misleading that Neely uses, $\dot{\xi}_p$, to define the CP *volume velocity* in the 1993 model [66], since it referred to the CP *velocity* in the 1986 model [68]. The $\dot{q}_p$ symbol would be more appropriate here and would avoid confusion. However, as pointed out at the beginning of this chapter, the original notation of the papers' authors will be used throughout.

with ξ_b defines the radial motion of the RL via the lever gain g (Eq.3.5.3). The second degree of freedom, however, corresponds to the radial motion of the TM. Therefore, similarly to the model of Allen and Neely and Kim, ξ_t is a radial displacement acting on the TM components, which together with the radial displacement of the RL, ξ_r, defines the radial displacement, ξ_0, i.e. deflection of the OHC stereocilia.

The expressions for the BM and TM mechanical admittance given by Neely, i.e.

$$Y_b = \left[\frac{K_b}{j\omega} + R_b + j\omega M_b\right]^{-1}, \tag{3.5.6}$$

$$Y_t = \left[\frac{K_t}{j\omega} + R_t + j\omega M_t\right]^{-1}, \tag{3.5.7}$$

can be expressed in terms of the impedance $Z{=}Y^{-1}$, so that the BM impedance takes the form

$$Z_b = \frac{K_b}{j\omega} + R_b + j\omega M_b, \tag{3.5.8}$$

and corresponds to the BM impedance Z_1 in the 1986 Neely and Kim model (see Section 3.3), and for the TM

$$Z_t = \frac{K_t}{j\omega} + R_t + j\omega M_t, \tag{3.5.9}$$

which corresponds to Z_2 in the 1986 model.

The impedance coupling the BM and TM, is formulated by Neely as

$$Z_0 = \frac{K_0}{j\omega} + R_0, \tag{3.5.10}$$

and corresponds to Z_3 in the 1986 model [68].

Having defined the impedances and displacements of the particular model's mechanical components, we derive the equation of motion for the first DOF of the system in Fig.3.16 as

$$P_f = K_b\xi_b + R_b\dot{\xi}_b + M_b\ddot{\xi}_b + g[K_0(\xi_r - \xi_t) + R_0(\dot{\xi}_r - \dot{\xi}_t)], \tag{3.5.11}$$

thus according to Eq.3.5.2

$$P_f = K_b\xi_b + R_b\dot{\xi}_b + M_b\ddot{\xi}_b + g(K_0\xi_0 + R_0\dot{\xi}_0), \tag{3.5.12}$$

or in the frequency domain

$$P_f = Z_b\dot{\xi}_b + gZ_0\dot{\xi}_0. \tag{3.5.13}$$

For the second DOF we have

$$0 = K_0(\xi_t - \xi_r) + R_0(\dot{\xi}_t - \dot{\xi}_r) + K_t\xi_t + R_t\dot{\xi}_t + M_t\ddot{\xi}_t, \tag{3.5.14}$$

so that according to Eq.3.5.2

$$0 = K_t\xi_t + R_t\dot{\xi}_t + M_t\ddot{\xi}_t - K_0\xi_0 - R_0\dot{\xi}_0, \tag{3.5.15}$$

which in the frequency domain gives

$$0 = Z_t\dot{\xi}_t - Z_0\dot{\xi}_0. \tag{3.5.16}$$

Using Eqs.3.5.1-3.5.3 it can be found that

$$\dot{\xi}_0 = \dot{\xi}_r - \dot{\xi}_t = g\dot{\xi}_b - g\dot{\xi}_c - \dot{\xi}_t = g\dot{\xi}_b - gH_c\dot{\xi}_0 - \dot{\xi}_t, \tag{3.5.17}$$

and

$$\dot{\xi}_0(1 + gH_c) = g\dot{\xi}_b - \dot{\xi}_t. \tag{3.5.18}$$

Knowing from Eq.3.5.16 that

$$\dot{\xi}_t = \frac{Z_0}{Z_t}\,\dot{\xi}_0, \tag{3.5.19}$$

and substituting for $\dot{\xi}_t$ in Eq.3.5.18, so that

$$\dot{\xi}_0\left(1 + gH_c + \frac{Z_0}{Z_t}\right) = \dot{\xi}_0\left(\frac{Z_t + gH_cZ_t + Z_0}{Z_t}\right) = g\dot{\xi}_b, \tag{3.5.20}$$

ξ_0 can be expressed solely in terms of the BM velocity $\dot{\xi}_b$, and will take the form

$$\dot{\xi}_0 = \frac{gZ_t}{Z_t + gH_cZ_t + Z_0}\,\dot{\xi}_b. \tag{3.5.21}$$

Substituting the above result into the equation of motion for the first DOF, i.e. Eq.3.5.13, gives

$$P_f = Z_b\dot{\xi}_b + gZ_0\frac{gZ_t}{Z_t + gH_cZ_t + Z_0}\dot{\xi}_b, \tag{3.5.22}$$

or

$$P_f = Z_b\dot{\xi}_b + gZ_0H_0\dot{\xi}_b, \tag{3.5.23}$$

where

$$H_0 = \frac{gZ_t}{Z_t + gH_cZ_t + Z_0}. \tag{3.5.24}$$

The transfer function, H_0, introduced by Neely relates ξ_0 to ξ_b, and after rewriting Eq.3.5.24

$$H_0 = \frac{\xi_0}{\xi_b} = \frac{gZ_t}{Z_t(1 + gH_c + Z_0Y_t)} = g(1 + gH_c + Z_0Y_t)^{-1}, \tag{3.5.25}$$

where Y_t=Z_t^{-1}, it is consistent with the definition of H_0 given in [66].

Finally, rewriting Eq.3.5.23 such that

$$P_f = Z_b\dot{\xi}_b(1 + gH_0Z_0Y_b), \tag{3.5.26}$$

where Y_b=Z_b^{-1}, and using Eq.3.5.4, gives

$$P_f = -\frac{\dot{\xi}_p}{A_p}[Z_b(1 + gH_0Z_0Y_b)], \tag{3.5.27}$$

so that the CP impedance can be defined as

$$Z_p = \frac{P_f}{\dot{\xi}_p} = -\frac{Z_b}{A_p}(1 + gH_0Z_0Y_b), \tag{3.5.28}$$

or in terms of the partition's admittance

$$Y_p = Z_p^{-1} = \frac{\dot{\xi}_p}{P_f} = -A_pY_b(1 + gH_0Z_0Y_b)^{-1}. \tag{3.5.29}$$

It should be noted that Eq.3.5.29 is not an exact form of equation (18) defining the CP admittance in the Neely's paper [66], i.e.

$$Y_p = A_p^2 Y_b (1 + gH_0 Z_0 Y_b)^{-1}. \tag{3.5.30}$$

We could not deduce unequivocally the difference in the form of the effective CP's area, i.e. $-A_p$ in Eq.3.5.29 and A_p^2 in Eq.3.5.30 as given by Neely [66]. The CP volume velocity, $\dot{\xi}_p$, is defined as [66]

$$\dot{\xi}_p = Y_p P_f, \tag{3.5.31}$$

which implies that the effective dimension of the partition admittance Y_p is $[\mathrm{m^5N^{-1}s^{-1}}]$, and is consistent with the dimension of Y_p in Eq.3.5.30, if Y_b, defined as in Eq.3.5.6, has dimension of mechanical mobility, i.e. $[\mathrm{mN^{-1}s^{-1}}]$, and the dimension of A_p is $[\mathrm{m^2}]$.

However, since each of the parameters of Y_b, i.e. K_b, R_b and M_b, is specified per unit area A_p in [66], and it appears from Eq.3.5.13 that the BM impedance is a ratio of the pressure difference P_f and linear velocity $\dot{\xi}_b$, the effective dimension of Y_b is $[\mathrm{m^3N^{-1}s^{-1}}]$. Thus, to obtain the correct dimensions for the partition admittance for the 'A_p-scaled' parameters, the square of A_p in Eq.3.5.30 has to be ignored.

Finally, the analysis of the model's macromechanics implies that the partition's volume velocity and the pressure difference must have the same direction to satisfy Eq.3.5.31 and the minus sign should be omitted in the definition of the partition's admittance Y_p. Hence, taking into account the above considerations and the results of preliminary calculations, we suggest that the CP admittance should be defined as

$$Y_p = A_p Y_b (1 + gH_0 Z_0 Y_b)^{-1}, \tag{3.5.32}$$

where the BM mechanical admittance, Y_b, has dimension of $[\mathrm{m^3N^{-1}s^{-1}}]$ and all mechanical parameters are A_p-scaled, so that the dimensions of Y_p and the CP volume velocity $\dot{\xi}_p$ are $[\mathrm{m^5N^{-1}s^{-1}}]$ and $[\mathrm{m^3s^{-1}}]$, respectively.

Note that in the absence of the OHC activity i.e. ξ_c=0 (Eq.3.5.3), the definition for the relative shearing displacement of the cilia, ξ_0 (Eq.3.5.2), is of the

same form as the corresponding displacement ξ_c in the model of Neely and Kim (see Eq.3.3.3). Furthermore, the passive partition impedance of Neely's model [66] is of exactly the same form as the passive impedance (Eq.3.3.7 for γ=0) of Neely and Kim's model proposed in 1986 [68], i.e.

$$Z_{passive} = \frac{P_f}{\dot{\xi}_p} = Z_b + \frac{Z_t Z_0}{Z_t + Z_0}, \tag{3.5.33}$$

according to Eq.3.5.22 for H_c=0 (since ξ_c=0, Eq.3.5.1), and neglecting the factors g and b, as well as g and A_p in the Neely and Kim [68] and Neely models [66], respectively. Finally, to compare the mobility of the Neely and Kim model with the mobility of the model of Neely, the A_p factor in the definition of the partition admittance in Eq.3.5.32 will be neglected, so that the expression for Y_p [$m^3N^{-1}s^{-1}$] in the model of Neely used for the numerical simulations will take the form

$$Y_p = Y_b(1 + gH_0Z_0Y_b)^{-1}, \tag{3.5.34}$$

and the mechanical parameters will be defined per area A_p, similarly to the parameters chosen by Neely and Kim shown in Table 3.1.

3.5.1 Outer hair cell gain

The active component in the Neely and Kim model was represented by the active pressure P_a [68]. In the model of Neely [66], the active component is controlled by the deflection of the hair bundle of the OHC, ξ_0, causing contraction of the cell's body, ξ_c [66]. The OHC contraction is related to the radial displacement of the cilia by OHC gain function, H_c, which was assumed to be a product of two separate transduction processes, i.e. the forward and reverse transduction, T_f and T_r, respectively [66].

The forward transduction function, also referred to as mechanoelectric transduction, refers to the ratio of the receptor potential to the displacement of the hair bundle, and is defined by Neely [66] as

$$T_f = \frac{g_f}{1 + j\omega\tau_f}, \tag{3.5.35}$$

where g_f is a place-dependent forward transduction gain expressed in mV/nm, and τ_f [s] is the forward transduction filter's time constant, also dependent on the position in the cochlea.

The reverse (electromechanic) transduction, defined at the lateral membrane of the OHC, is thought to describe the ratio between the OHC contraction and its receptor potential [66], and takes the form

$$T_r = \frac{g_r}{1 + j\omega\tau_r}, \tag{3.5.36}$$

where g_r is the reverse transduction gain expressed in nm/mV and τ_r [s] reverse transduction filter's time constant, both place-dependent.

Thus, the OHC gain function, H_c, is formulated by

$$H_c = \gamma T_f T_r, \tag{3.5.37}$$

where γ is a dimensionless factor, which was used in the same manner as in the Neely and Kim model to demonstrate the physiological condition of the OHC motility (compare Section 3.3).

Each of the OHC transduction functions is a first-order, low-pass filter, where, as pointed out by Neely, their place dependence along the CP was determined to simulate the neural tuning curves by specifying a place-dependent low-pass characteristic of the decrease in cell length relative to the deflection of the hair cell's bundle [66].

3.5.2 Calculated response

To calculate the partition mobility of the Neely model [66] the model's parameters first have to be derived. Table 3.2 presents some of the model parameters (converted to SI units), which were selected by Neely to calculate the response of the model. The parameters are specified for three locations along the cochlea, i.e. x=0, x=$L_c/2$ and x=L_c, where L_c denotes the length of the cat cochlea CP, equal to 25 mm as in the case of Neely and Kim's model (Section 3.3). The values for the remaining positions along the cochlea were interpolated after fitting a quadratic polynomial to the logarithm of the values at locations specified in

the table (see Appendix B). The BM/CP length was extended to L=35 mm in the present simulations to improve the smoothness of the coupled response in the low frequency region. Thus, the mechanical parameters were also extrapolated to find their cochlear distribution between 25 and 35 mm of the model's CP.

PARAMETER	x=0	x=$L_c/2$	x=L_c
K_b/A_p [Nm^{-3}]	1.14×10^{9}	4.19×10^{7}	5.97×10^{5}
K_t/A_p [Nm^{-3}]	1.99×10^{5}	2.21×10^{5}	3.16×10^{5}
K_0/A_p [Nm^{-3}]	1.05×10^{5}	9.23×10^{4}	1.25×10^{5}
R_b/A_p [Nsm^{-3}]	2.08×10^{-1}	2.03×10^{-1}	1.88×10^{-1}
R_t/A_p [Nsm^{-3}]	1.49×10^{3}	6.34×10^{2}	2.70×10^{2}
R_0/A_p [Nsm^{-3}]	20.37×10^{3}	2.82×10^{3}	3.80×10^{2}
M_b/A_p [kgm^{-2}]	9.14×10^{-5}	9.60×10^{-5}	1.06×10^{-4}
M_t/A_p [kgm^{-2}]	5.64×10^{-3}	1.02×10^{-2}	1.06×10^{-1}
g_f [mV nm^{-1}]	1.42×10^{5}	1.05×10^{4}	3.68×10^{2}
g_r [nm mV^{-1}]	0.1	0.1	0.1
τ_f [s]	1.40×10^{-4}	6.92×10^{-4}	5.29×10^{-3}
τ_r [s]	1.35×10^{-4}	3.61×10^{-4}	2.50×10^{-3}
A_p [m^2]	5×10^{-9}	5×10^{-9}	5×10^{-9}
g	1	1	1

Table 3.2: Mechanical parameters (SI units) proposed by Neely in [66].

Figure 3.17(a) depicts Neely's assumed variation along the CP of the BM and TM mass, whereas Fig.3.17(b) shows the stiffness of the BM, TM and the OHC's cilia and Fig.3.17(c) the BM, TM and subtectorial fluid damping. Figure 3.18(a) shows the CP-place dependence of the forward, g_f, and reverse, g_r, transduction gain, whereas Fig.3.18(b), the time constant of the forward and reverse transduction filters, τ_f and τ_r.

The BM mass, M_b, is almost constant along the cochlear length, whereas the mass of the TM, M_t, is significantly higher than that of M_b in this model, by about two orders of magnitude at the base and four orders of magnitude at the apex, as shown in Fig.3.17(a). The stiffness of the BM, K_b, dominates over the

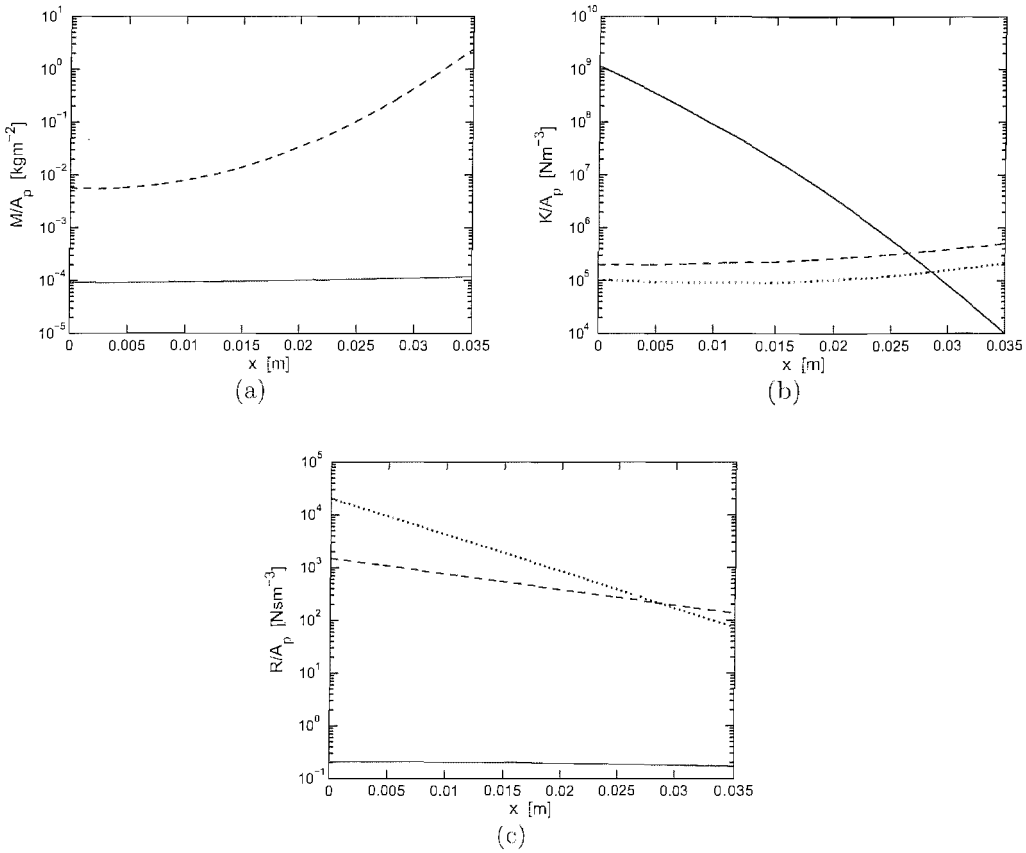

Figure 3.17: Distributions assumed in Neely's 1993 model [66] for (a) mass of the basilar membrane, M_b (solid) and tectorial membrane M_t (dashed); (b) stiffness of the basilar membrane K_b (solid), tectorial membrane, K_t (dashed) and the outer hair cell cilia K_0 (dotted); (c) damping of the basilar membrane R_b (solid), tectorial membrane, R_t (dashed) and the subtectorial fluid R_0 (dotted). Parameters were fitted by a quadratic polynomial according to values given in Table 3.2 (**NB** parameters are scaled by the A_p factor).

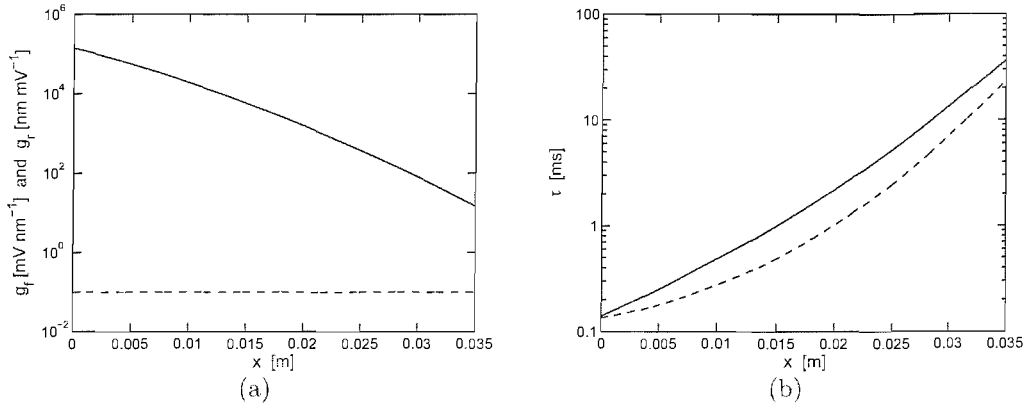

Figure 3.18: Assumed distribution along the cochlea of the forward and reverse transduction gain (a): g_f (solid) and g_r (dashed), respectively; and the time constant of forward and reverse transduction filter (b): τ_f (solid) and τ_r (dashed), in the model of Neely [66]. Parameters were fitted by a quadratic polynomial according to values given in Table 3.2.

stiffness of the TM, K_t, up to about 26 mm and the cilia K_0 up to about 28 mm, and decreases with x by about five orders of magnitude. K_t and K_0 have almost the same, constant slope with x and K_t has values almost twice that of K_0 at the base and about three times at the apex. Figure 3.17(c) shows that the damping of the BM, R_b, has the lowest value and is almost constant along the cochlea. Damping of the TM, R_t, and the subtectorial fluid, R_0, vary with the position x by about one order and more than two orders of magnitude, respectively, decreasing from the base to the apex. R_t is higher than R_b by about four and three orders of magnitude at the base and the apex respectively, whereas R_0 dominates over R_b by about five and less than three orders of magnitude at the base and the apex of the CP, respectively. Finally, the difference between R_0 and R_t is equal to about one order of magnitude at the base and decreases with the position along the cochlea up to about 28 mm, above which R_0 becomes slightly smaller than R_t.

It can be seen from Fig.3.18(a) that the reverse transduction gain, g_r (dashed), is constant and smaller than the forward transduction gain, g_f, by about six and two orders of magnitude at the base and apex of the cochlea, respectively. g_f

decreases with position along the cochlea by about four orders of magnitude. The time constants of the forward and reverse transduction filters, τ_f and τ_r, both increase with the distance from the stapes by more than two orders of magnitude, where τ_f increases faster and is higher than τ_r, as shown in Fig.3.18(b).

Once the distribution of the model's parameters along the CP is derived, the mobility of the partition, Y_p at each position, can be calculated using Eq.3.5.34. Similarly to Section 3.3.1, where the mobility of the CP was plotted for the 1986 model of Neely and Kim, the mobility of Neely's 1993 model [66], is presented as a function of position in the cochlea in Fig.3.19, and frequency in Fig.3.20. In the first case, the frequency was set to f=1 kHz, while in the latter case the position was set to x=0.0189 m, which corresponds to the site of maximum displacement for the $Y_p(x)$ plot. Furthermore, the CP mobility was plotted for a passive, γ=0 (dashed line in the plots), and a 'fully' active, γ=1 (solid lines), model. Figures 3.19(a), 3.19(c) and 3.20(a), 3.20(c) depict the magnitude and phase of Y_p, whereas the real and imaginary parts of Y_p are presented in Figs.3.19(b), 3.19(d) and 3.20(b), 3.20(d), for $Y_p(x)$ and $Y_p(f)$ plots, respectively.

A sharply tuned peak of the magnitude response of the active model of Neely [66] can be observed at about 0.0189 m in Fig.3.19(a) and about 1 kHz in Fig.3.20(a). The peak in the active magnitude response coincides with a rapid phase lag accumulation in the characteristic place or CF region, as shown in Figs.3.19(c) and 3.20(c). The real part of Y_p in the Neely model becomes negative in the vicinity of the characteristic place in Fig.3.19(b) and CF in Fig.3.20(b), which enables the cochlear amplifier to undamp the vibrations of the CP in these regions. It can be noted that all responses shown in Fig.3.19 are somewhat different from those derived for the model of Neely and Kim shown in Fig.3.8. However, both models predict a negative value of the real part of the partition mobility just basal to the characteristic place, as required for the sharp tuning of the cochlear response [15].

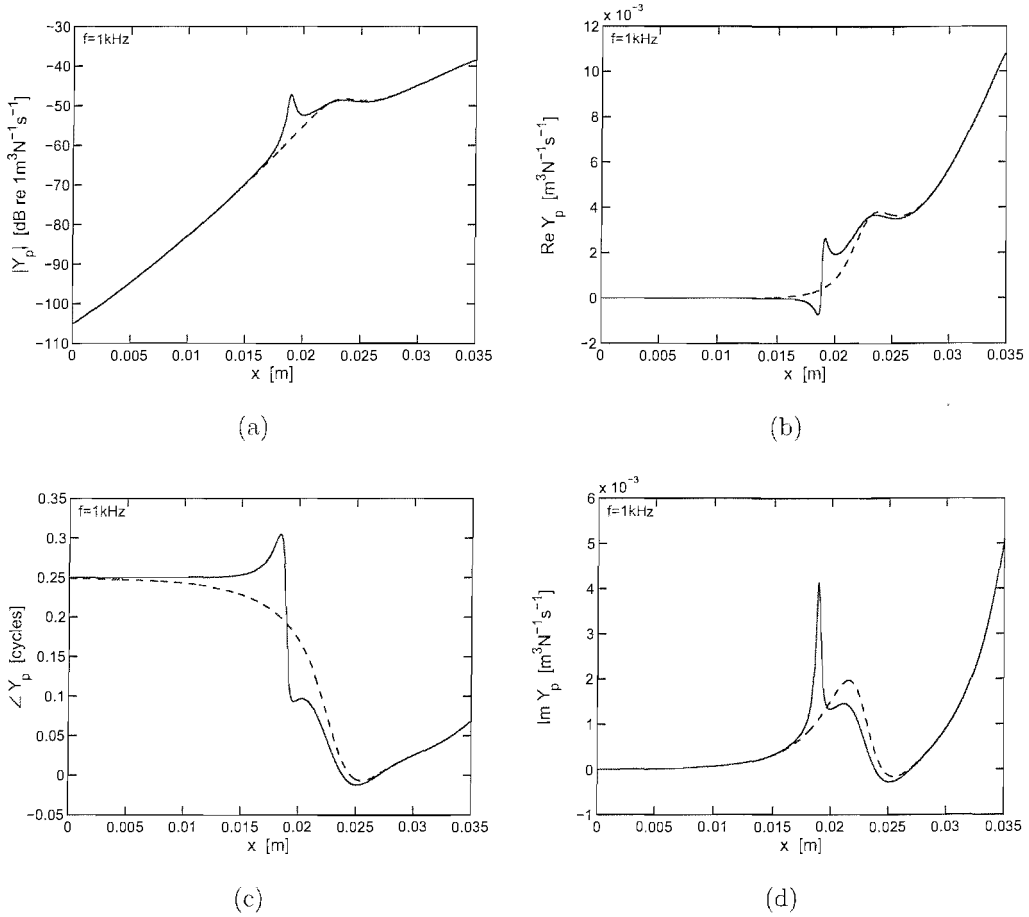

Figure 3.19: The magnitude (a) and phase (c) (left panel), real (b) and imaginary (d) parts (right panel) of the passive (dashed) and active (solid) cochlear partition mobility, Y_p, as a function of position along the cochlea, calculated for the original model of Neely [66]. The frequency was set to f=1kHz, and γ was set to 0 and 1 for the passive and active model, respectively.

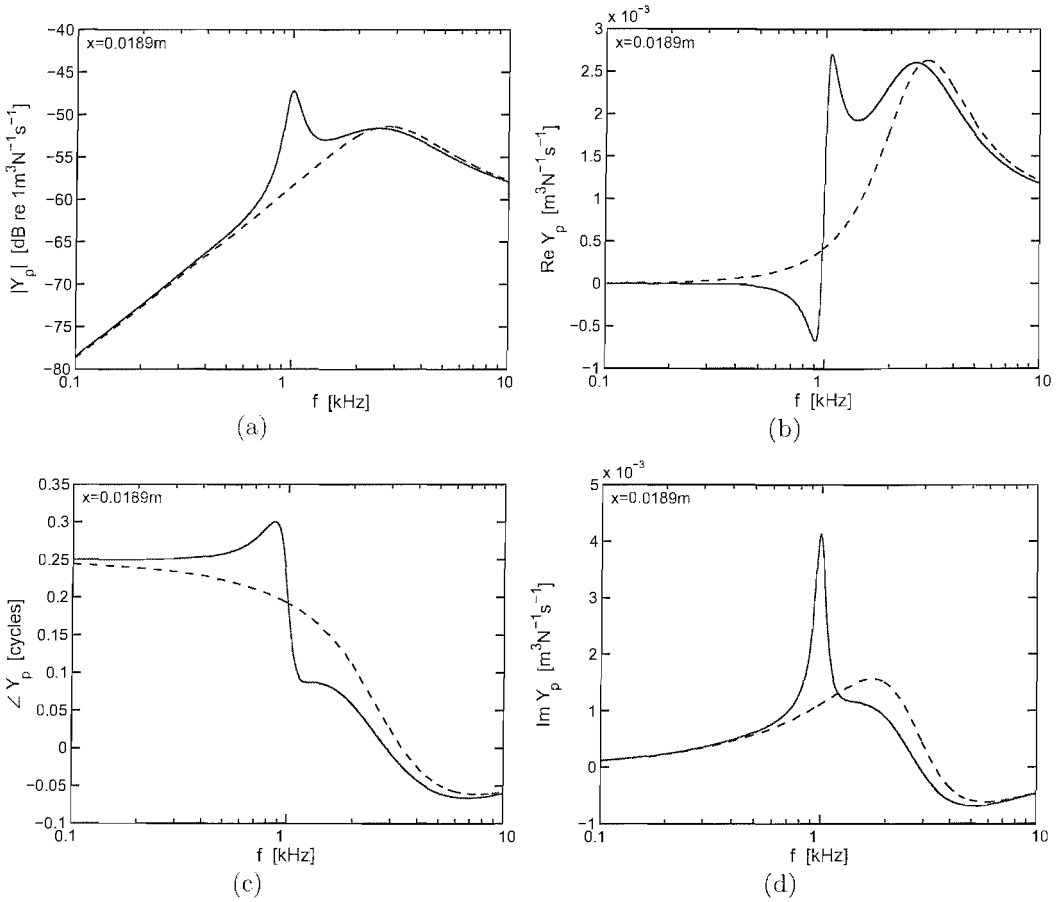

Figure 3.20: The magnitude (a) and phase (c) (left panel), real (b) and imaginary (d) parts (right panel) of the passive (dashed) and active (solid) cochlear partition mobility, Y_p, as a function of frequency, calculated for the original model of Neely [66]. The position along the cochlea was chosen as x=0.0189 m, and γ was set to 0 and 1 for the passive and active model, respectively.

3.6 Modes of vibration in the model of Neely

Equation 3.5.33 shows that the passive (γ=0) impedance of the 1993 model of Neely is consistent with the impedance of the passive Neely and Kim model, since the lever gain g=1, and constants b and $-A_p^{-1}$ are neglected in the formulations of the impedance, Eqs.3.3.8 and 3.5.28, respectively. Thus, assuming the two DOF system shown in Fig.3.16 is freely vibrating and the active displacement ξ_c=0, it will take the same form as the freely vibrating system proposed for the Neely and Kim model depicted in Fig.3.10. Furthermore, the modes of vibration of such a system were analysed in Section 3.4, where using Eqs.3.4.13-3.4.15 distribution of the natural frequencies, $f_{1,2}=\omega_{1,2}/2\pi$, along the cochlea, for the freely vibrating, undamped system, was found. These equations can be applied to the 1993 model of Neely to derive the x-distribution of f_1 and f_2, for the set of parameters proposed by Neely and gathered in Table 3.2.

Figure 3.21 depicts a free, undamped system representing the passive two DOF system proposed by Neely [66] shown in Fig.3.16. The lever gain g is equal to one and thus it was neglected when the displacement of the lower mass, M_b was taken into account.

Equations of motion for such a system will be of the same form as for the system in Fig.3.10, i.e.

$$\begin{aligned} M_b\ddot{\xi_b} &= -K_b\xi_b \quad -K_0(\xi_b - \xi_t), \\ M_t\ddot{\xi_t} &= -K_t\xi_t \quad -K_0(\xi_t - \xi_b), \end{aligned} \tag{3.6.1}$$

and the natural frequencies (Eqs.3.4.13-3.4.15)

$$\omega_1^2 = \frac{M_b(K_t + K_0) + M_t(K_b + K_0) - \sqrt{\Delta}}{2M_bM_t}, \tag{3.6.2}$$

at the first mode, and

$$\omega_2^2 = \frac{M_b(K_t + K_0) + M_t(K_b + K_0) + \sqrt{\Delta}}{2M_bM_t}, \tag{3.6.3}$$

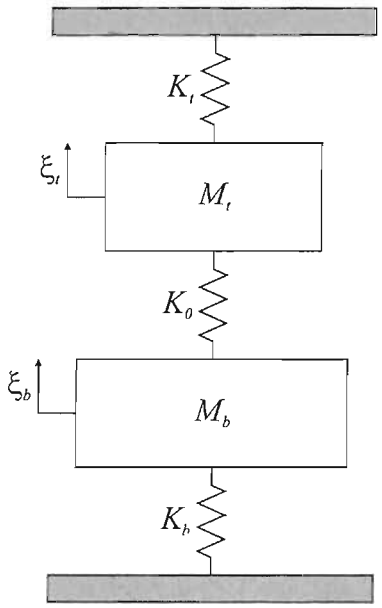

Figure 3.21: Simplified block diagram of the two degree of freedom system proposed by Neely in [66] (Fig.3.16), representing a freely vibrating, undamped mechanical system. All parameters same as in [66] (see Table 3.2).

at the second mode, where

$$\Delta = [M_b(K_t + K_0) + M_t(K_b + K_0)]^2 - 4M_bM_t[K_b(K_t + K_0) + K_tK_0]. \quad (3.6.4)$$

Similar to Section 3.4, $f_{1,2}$=$\omega_{1,2}/2\pi$, can be compared with the estimated resonance frequencies corresponding to the BM and TM, i.e.

$$f_{\mathrm{BM}} = \frac{1}{2\pi}\sqrt{\frac{K_b}{M_b}}, \quad (3.6.5)$$

$$f_{\mathrm{TM}} = \frac{1}{2\pi}\sqrt{\frac{K_t + K_0}{M_t}}, \quad (3.6.6)$$

and the one from the cochlear CF/place map of a cat, f_{CF} derived from the formula of Greenwood [39].

Assuming time-harmonic motion, the ratio of the amplitudes $\Xi_{b1,2}/\Xi_{t1,2}$, for the undamped, freely vibrating model of Neely will take the form

$$\frac{\Xi_{b1}}{\Xi_{t1}} = \frac{K_0}{K_b + K_0 - \omega_1^2 M_b} = \frac{K_t + K_0 - \omega_1^2 M_t}{K_0}, \tag{3.6.7}$$

at ω_1, and

$$\frac{\Xi_{b2}}{\Xi_{t2}} = \frac{K_0}{K_b + K_0 - \omega_2^2 M_b} = \frac{K_t + K_0 - \omega_2^2 M_t}{K_0}, \tag{3.6.8}$$

at ω_2, according to Eqs.3.4.22 and 3.4.23. Thus, the motion at the first mode is expressed in the same way as in Eq.3.4.27, whereas at the second mode as in Eq.3.4.28 and constants A, B, C and D are defined in Eqs.3.4.29-3.4.31.

Figure 3.22(a) shows the distribution of the natural frequencies f_1 and f_2 along the cochlea for the set of parameters proposed by Neely [66]. The estimated frequencies of the BM and TM, f_{BM} and f_{TM}, as well as the cat's CF/place map derived from the formula proposed by Greenwood [39], are also plotted in the figure (**NB** the average cat's cochlea length is equal to about 25 mm, thus the CF/place map is calculated for L_c=25 mm and not L=35 mm as for $f_{1,2}$ or $f_{\mathrm{BM,TM}}$). Figure 3.22(b) depicts the ratios of $\log_2(f_2/f_1)$ and $\log_2(f_{\mathrm{BM}}/f_{\mathrm{TM}})$.

The natural frequency f_1 (solid) is lower than f_2 (dashed) through the entire length of the cochlea, from more than two and a half decades at the base to less than two orders of magnitude at the apex for parameters chosen by Neely in the 1993 model [66]. The frequency f_1 spans from about 1.2 kHz at the base to about 316 Hz at 25 mm place and about 87 Hz at the apical end of the cochlea, i.e. 35 mm place. The line of f_1 covers the line of f_{TM} (dot-dashed) estimated for the TM up to about 25 mm site, where f_{TM} is almost equal to f_1 at the base and just about 14 Hz higher, i.e. $f_{\mathrm{TM}}\approx$73 Hz, than f_1 at the apex.

The f_2 ranges from $\approx$562 kHz at the base, through $\approx$13 kHz at L_c=25 mm (cat cochlea length), to $\approx$7 kHz at the apex (L=35 mm) of the cochlea. The estimated BM frequency f_{BM} (dotted line, mostly covered by the line of f_2), equals also about 562 kHz at the base, $\approx$12 kHz at L_c=25 mm, however, about 1.5 kHz at the apex (L=35 mm). It should be noted that the estimated BM resonance frequency, f_{BM}, decreases monotonically from the base to the apex of the cochlea (likewise f_{BM} in the Neely and Kim model in Fig.3.12(a)), whereas

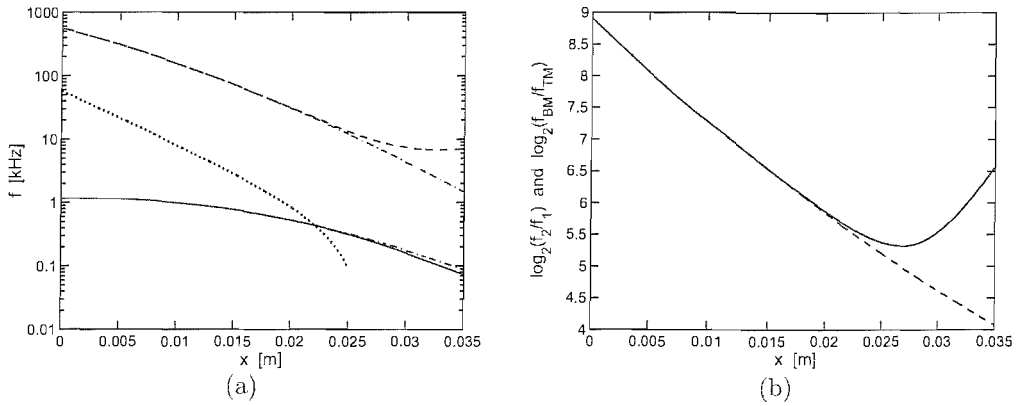

Figure 3.22: Natural frequencies of the system presented in Fig.3.21 plotted as a function of position, x (a). f_1 (solid) and f_2 (dashed), plotted together with the estimated resonance frequencies for the basilar, $f_{\mathrm{BM}}=\frac{1}{2\pi}\sqrt{\frac{K_b}{M_b}}$ and tectorial, $f_{\mathrm{TM}}=\frac{1}{2\pi}\sqrt{\frac{K_t+K_0}{M_t}}$ membranes (dot-dashed; covered by the f_2 and f_1 lines below x=25 mm, respectively), and the CF/place map (dotted) according to Greenwood [39]. (b) comparison of the ratios $\log_2(f_2/f_1)$ (solid) and $\log_2(f_{\mathrm{BM}}/f_{\mathrm{TM}})$ (dashed).

f_2 decreases until about 33 mm site along the cochlea, above which it increases by about 100 Hz till the cochlear apical end is reached.

Similarly to the natural frequencies calculated for the model of Neely and Kim in Section 3.4, $f_{1,\mathrm{TM}}$ and $f_{2,\mathrm{BM}}$, are well below and above, respectively, the CF/place map of a cat, derived according to the formula of Greenwood [39], for almost the entire length of its cochlea (L_c=25 mm). Finally, the slopes of $f_{2,\mathrm{BM}}$ are generally steeper, than those of $f_{1,\mathrm{TM}}$.

The $\log_2(f_2/f_1)$ and $\log_2(f_{\mathrm{BM}}/f_{\mathrm{TM}})$ ratios, shown in Fig.3.22(b), match each other up to about 20 mm place from the base, both decreasing from the value of about 8.9 at the base to about 5.8 at $x\approx$20 mm. Above the 20 mm site, the ratio of the natural frequencies, f_1 and f_2, decreases up to about 27 mm site, after which it increases and reaches about 6.6 value at the apex. However, the ratio of the estimated BM, f_{BM}, and TM, f_{TM}, frequencies decreases to about 4.1 at the cochlear apex. Thus, according to the definition of the ratios, the separation between the frequencies $f_{1,\mathrm{TM}}$ and $f_{2,\mathrm{BM}}$, equals about 9 octaves at the base of

the cochlea, and more than 6 octaves between f_1 and f_2 and about 4 octaves between f_{TM} and f_{BM} at the cochlear apex.

Figure 3.23 shows five periods of the harmonic motion, $\xi_{b1,t1}$ and $\xi_{b2,t2}$, at the first and the second natural frequency calculated for x=0.0189 m along the cochlea, i.e. $f_1 \approx 575$ Hz and $f_2 \approx 37$ kHz, respectively. It can be noted that at the first mode ξ_{b1} and ξ_{t1} move in phase, where the amplitude of ξ_{b1} is much smaller than that of ξ_{t1} (maxima of ξ_{b1} and ξ_{t1} as about 10^{-4} to 0.007. **NB** ξ_{b1} multiplied by factor of ten to facilitate the comparison). However, at the second mode ξ_{b2} and ξ_{t2} move out of phase and the amplitude of ξ_{b2} is higher than the amplitude of ξ_{t2} (maxima of ξ_{b2} and ξ_{t2} as 100 to 0.007. **NB** ξ_{t2} multiplied by factor of 10^3 to be visible together with ξ_{b2} in the plot).

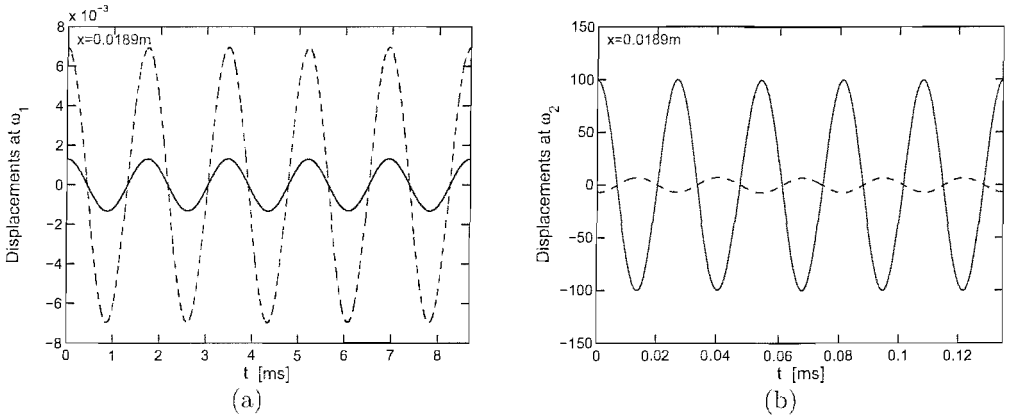

Figure 3.23: Displacements $10\xi_{b1}$ (solid) and ξ_{t1} (dashed) at the first mode of vibration, $\omega_1 \approx 2\pi \times 575$ Hz (a), and ξ_{b2} (solid) and $10^3\xi_{t2}$ (dashed) at the second mode where $\omega_2 \approx 2\pi \times 37$ kHz (b), calculated for parameters proposed by Neely (Table 3.2) [68] (**NB** ξ_{b1} and ξ_{t2} were multiplied by a factor of ten and 10^3, respectively, to facilitate comparison).

We finish the analysis of the modes of vibration of the 1993 model of Neely [66] by plotting the point mobility of the BM, Y_b, and the transfer mobility of the TM, Y_t, derived due to the excitation of the BM by a unit force and for the parameters proposed by Neely (Table 3.2). Similar to the analysis of modes of vibration of Neely and Kim model in Section 3.4, we assume that the lower mass,

M_b, of the system in Fig.3.21 is excited by a time-harmonic force of the form $f{=}Fe^{j\omega t}$, thus

$$Y_b = \frac{V_b}{F} = \frac{j\omega(K_t + K_0 - \omega^2 M_t)}{(K_b + K_0 - \omega^2 M_b)(K_t + K_0 - \omega^2 M_t) - K_0^2},$$
$$Y_t = \frac{V_t}{F} = \frac{j\omega K_0}{(K_b + K_0 - \omega^2 M_b)(K_t + K_0 - \omega^2 M_t) - K_0^2}, \tag{3.6.9}$$

according to Eq.3.4.34, for the parameters proposed by Neely [66]. Furthermore, likewise for the Neely and Kim model in Eqs.3.4.36 and 3.4.37, the BM point mobility and TM transfer mobility of the damped system proposed by Neely in [66], will be defined as

$$Y_b = \frac{V_b}{F} = \frac{j\omega[K_t + K_0 + j\omega(R_t + R_0) - \omega^2 M_t]}{\Omega},$$
$$Y_t = \frac{V_t}{F} = \frac{j\omega(K_0 + j\omega R_0)}{\Omega}, \tag{3.6.10}$$

where

$$\Omega = [K_b + K_0 + j\omega(R_b + R_0) - \omega^2 M_b][K_t + K_0 + j\omega(R_t + R_0) - \omega^2 M_t] - (K_0 + j\omega R_0)^2, \tag{3.6.11}$$

and hence the ratio of the BM and TM velocities for the passive model, will take the form

$$\frac{V_t}{V_b} = \frac{K_0 + j\omega R_0}{K_t + K_0 + j\omega(R_t + R_0) - \omega^2 M_t} \tag{3.6.12}$$

so that the velocity of the TM can be calculated by multiplying known BM velocity by the V_t/V_b ratio.

Referring back to Fig.3.16 it should be noted that the ratio of V_t to V_b will not be given by Eq.3.6.12 when the Neely model is active, since in addition to the BM excitation, the TM is also forced into motion by the active displacement ξ_c. This is in contrast to the analysis for the Neely and Kim model in Section 3.4.

The left side of Fig.3.24 shows the magnitude and phase of point, Y_b (solid), and transfer mobility, Y_t (dashed) derived for the system in Fig.3.21 and parameters in Table 3.2. Because the natural frequencies, f_1 and f_2, derived for the model of Neely [66], are higher than those in the model of Neely and Kim [68], also the frequency range of the mobility response plots was extended to 100 Hz-10^3 kHz.

There are two resonance peaks in each response curve in Fig.3.24(a), because the denominators of Eq.3.6.9 define the frequency equation (compare Eq.3.4.12) and have two distinctive poles. The roots of the frequency equation define the natural frequencies of the system in Fig.3.10; thus the first peak in mobility curves occurs at $f_2 \approx 576$ Hz and the second at $f_1 \approx 37$ kHz, and are almost equal to the estimated frequencies f_{TM} and f_{BM}, respectively, at $x=0.0189$ m (compare Fig.3.22(a)). The Y_t mobility curve exhibits no antiresonance, however, the predicted antiresonance at the frequency of about 577 Hz, as for $f_{\mathrm{TM}}=\frac{1}{2\pi}\sqrt{\frac{K_t+K_0}{M_t}}$ (compare numerator of Y_b in Eq.3.6.9 and Eq.3.6.6), occurs in the curve of Y_b. The resonances coincide with the phase lag of half of a cycle and the antiresonances with a half of a cycle phase lead. However, the antiresonance of Y_b is too close to the resonances of Y_b and Y_t to be visible in the phase response plot (solid line in Fig.3.24(c)). The low-frequency asymptotes have slopes of about 20 dB/decade for both response curves. However, the high-frequency asymptotes have slopes of about -20 dB/decade for Y_b point mobility and -60 dB/decade for the transfer mobility Y_t.

The magnitude and phase response of the point BM mobility and TM transfer mobility defined using Eq.3.6.10 and 3.6.11 for the damped two DOF system proposed by Neely [66] (Fig.3.16), are shown on the right-hand side of Fig.3.24. The BM point mobility Y_b matches the passive partition mobility Y_p plotted in Fig.3.20(a) (dashed curve) and similarly the phase response of Y_b is consistent with the phase of the passive Y_p in Fig.3.20(c). The magnitude of the TM transfer mobility does not differ qualitatively from the BM point mobility up to the responses' maxima, both increasing about 20 dB/decade. However, for frequencies higher than the frequency of the maximum, the TM mobility decreases with a constant slope of about -20 dB/decade, while the slope of the BM mobility

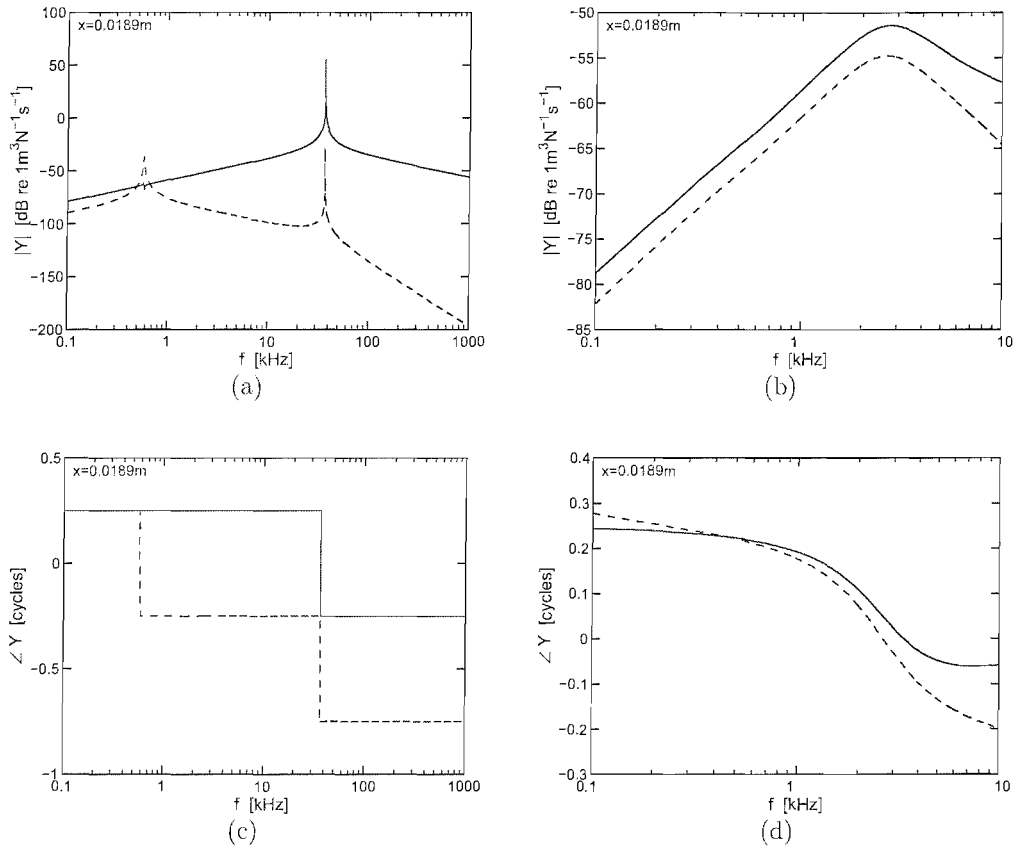

Figure 3.24: Magnitude (a, b) and phase (c, d) of the point mobility of the basilar membrane (solid), and the transfer mobility of the tectorial membrane (dashed), derived for the passive, undamped system in Fig.3.21 (left panel) and the passive, damped two degree of freedom system in Fig.3.16 (right panel), calculated at x=0.0189 m. Both systems were excited by a unit force acting upon the basilar membrane and the parameters proposed by Neely [66] (Table 3.2), were used for the calculations.

decreases with an increase in frequency. Furthermore, the TM's mobility magnitude is smaller than that of the BM in the entire frequency range, and the response maxima are only 100 Hz apart, i.e. about 2.8 and 2.7 kHz for the BM and TM response, respectively.

The phase of the BM mobility shown in Fig.3.24(d), decreases by about 0.3 of a cycle through the entire frequency range, where the slopes below about 1 kHz and above about 4 kHz are very small, so that the phase lag accumulation can be observed mainly in the frequency region around the maximum of the BM's magnitude response. The phase of the TM mobility ranges from about 0.3 of a cycle at 100 Hz to about -0.2 of a cycle at 10 kHz, which gives a total phase lag of about half of a cycle in the examined frequency range. Also in this case the highest phase lag accumulation can be observed in the neighbourhood of the maximum of the TM's mobility amplitude. However, the phase of the TM mobility exhibits a decrease of about 0.08 cycle per decade in the low and high frequency region, instead of an almost constant slope as in the case of the BM's mobility phase.

An interesting feature of the mobility of the damped two degree of freedom system shown in Fig.3.24(b), is a large shift of the maxima of the BM and TM mobility to about 2.8 and 2.7 kHz, respectively, in comparison with the frequency of the maximum of the undamped system's mobility f_2 of about 37 kHz, shown in Fig.3.24(a). Since $R_b \ll R_t < R_0$ at the 0.0189 m position along the cochlea, as can be seen in Fig.3.17(c), it appears that the vibrations of the upper subsystem of the system in Fig.3.21 are heavily damped and thus only a single broad resonance peak at 2.7 kHz can be observed in the TM mobility in Fig.3.24(b). Adding damping to the system causes changes also in the mobility response of the BM, as if the lower subsystem were coupled with a vibration absorber which damps the resonance at f_2 in Fig.3.24(a) and introduces a broad resonance, the broad maximum of the BM mobility at about 2.8 kHz shown in Fig.3.24(b), between the peaks at f_1 and f_2.

Figure 3.25 shows the magnitude and phase of the complex TM/BM velocities ratio formulated in Eq.3.6.12, calculated at 0.0189 m position along the cochlea. The magnitude of the ratio shown in Fig.3.25(a) is negative in the whole frequency

range, so that the velocity of the TM is lower than the velocity of the BM at all stimulus frequencies, as can be seen in Fig.3.24(b). The V_t/V_b ratio until about 3 kHz is roughly constant, above which it decreases rapidly with frequency until the 10 kHz limit, which is consistent with the increasing amplitude difference between the BM and TM mobility shown in Fig.3.24(b) for the damped case. The phase of the TM/BM velocity ratio shown in Fig.3.25(b), exhibits a little variation over the entire frequency range showing overall phase lag of about 0.2 of a cycle. The low slope of the phase is consistent with the lack of a distinctive resonance of the magnitude curve in Fig.3.25(a).

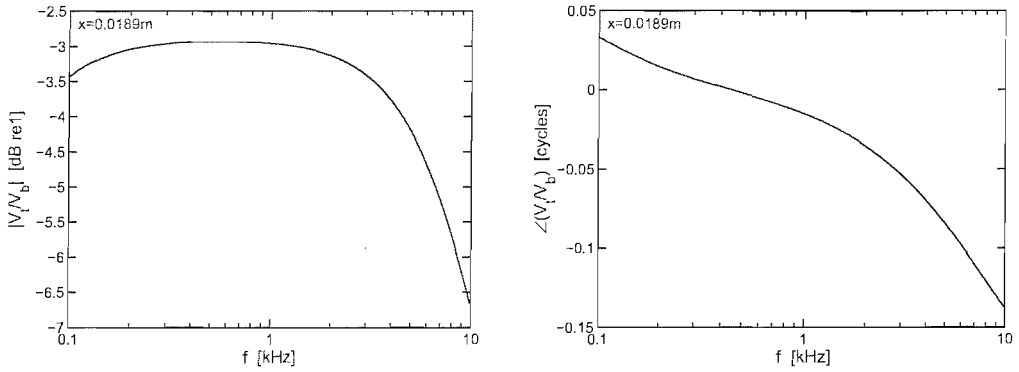

(a) (b)

Figure 3.25: The magnitude (a) and phase (b) of the ratio of the tectorial membrane to basilar membrane velocity, V_t/V_b, as a function of stimulus frequency for the model of Neely [68]. The ratio was calculated using parameters in Table 3.2 evaluated at x=0.0189 m.

3.7 Tectorial membrane inertia in the model of Neely

The cochlear model proposed by Neely in 1993 [66], represented graphically by a block diagram in Fig.3.16, employs an active displacement between the BM and the RL, due to the action of the OHCs as the mechanism of the cochlear

amplifier. This approach contrasts with the model proposed by Neely and Kim in [68] which introduced an additional active force acting on the BM block, as shown schematically in Fig.3.6, counteracting the resistive forces from the cochlear fluids and undamping the BM vibrations. Although, the passive micromechanics of both models is generally the same, as shown in the present section, both models fail to take account for the inertial load of the TM mass in the first degree of freedom, as it was done for the passive model of Allen [1] discussed in Section 3.2.

While the model of Neely and Kim would not be significantly affected by the incorporation of the TM inertial effects [24], which could be accounted for by choosing a suitable modified value of the BM mass, the model of Neely seems to be significantly affected by the TM's load on the organ of Corti. In the model of Neely and Kim the impedance of the BM/organ of Corti component would just be modified by the TM's inertia, whereas the active force, being an external force exerted on the BM/organ of Corti block, would not be affected by the mass of the TM. However, in the model of Neely, the active displacement ξ_c is internal to the organ of Corti and could be thought of as acting between the flexible RL and the mass of the BM. Thus, the load of the TM exerted on the RL, would affect the active displacement that would have to be sufficient enough to 'overcome' the TM loading in order to undamp the motion of the BM.

In Fig.3.26 we present a modified block diagram for the micromechanical model of Neely [66], with the TM mass, M_t, incorporated between the BM mass and the cilia stiffness and damping, represented by the lower block M_b, the spring K_0 and dashpot R_0, respectively. Figure 3.26 shows a single-axis motion diagram of the system, where all motion is in radial direction, as it was shown in Fig.3.16. The load of the TM is inherently connected with the parallel transverse motion of the BM and TM, as described in the model of Allen for the first vibrational DOF [1]. However, it seems to have been ignored in the analysis of the model in [66].

The motion of the BM block is induced by the pressure difference in the cochlear fluids, P_f, which leads to the transverse displacement of the BM, ξ_b. Assuming that the distance between the RL and the TM remains constant [1, 24],

the transverse motion of the BM/organ of Corti leads to the shearing displacement ξ_r of the RL, leading to the displacement of the OHCs cilia. Furthermore, assuming radial resonant motion of the TM, ξ_t, the net radial displacement of the cilia, ξ_0=ξ_r–ξ_t (Eq.3.5.2), deflects the hair cell stereocilia, which leads to the depolarisation and motility of the OHC, and hence active displacement between the RL and the BM. Therefore, the total, transverse displacement at the surface of the RL will amount to ξ_b–ξ_c (depolarisation and contraction of the OHC), so that the TM inertia will also influence the active displacement ξ_c in this modified model.

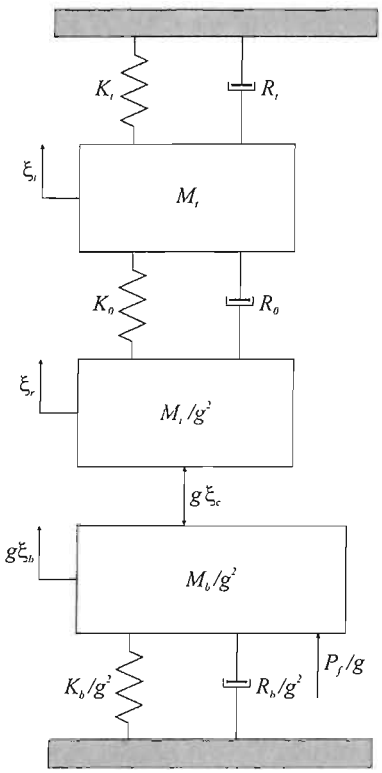

Figure 3.26: Block diagram of a two degree of freedom system of the Neely model [66], modified by incorporating the mass of the tectorial membrane due to its inertial effect on the model's lower subsystem. All the motion is in the radial direction, similarly to the block diagram in Fig.3.16.

We derive the equation of motion for the first DOF of the modified system in

Fig.3.26 as

$$P_f = K_b\xi_b + R_b\dot{\xi}_b + M_b\ddot{\xi}_b + M_t(\ddot{\xi}_b - \ddot{\xi}_c) + g[K_0(\xi_r - \xi_t) + R_0(\dot{\xi}_r - \dot{\xi}_t)], \quad (3.7.1)$$

which can be rewritten as

$$P_f = K_b\xi_b + R_b\dot{\xi}_b + (M_b + M_t)\ddot{\xi}_b + g\left[K_0(\xi_r - \xi_t) + R_0(\dot{\xi}_r - \dot{\xi}_t) - \frac{M_t}{g}\ddot{\xi}_c\right]. \quad (3.7.2)$$

Since $\ddot{\xi}_c = H_c\ddot{\xi}_0$ according to Eq.3.5.1, and using Eq.3.5.2 we have

$$P_f = K_b\xi_b + R_b\dot{\xi}_b + (M_b + M_t)\ddot{\xi}_b + g\left(K_0\xi_0 + R_0\dot{\xi}_0 - \frac{M_tH_c}{g}\ddot{\xi}_0\right), \quad (3.7.3)$$

or

$$P_f = Z_{\mathrm{OC}}\dot{\xi}_b + gZ_{\mathrm{A}}\dot{\xi}_0, \quad (3.7.4)$$

where

$$Z_{\mathrm{OC}} = \frac{K_b}{j\omega} + R_b + j\omega(M_b + M_t) = Z_b + j\omega M_t, \quad (3.7.5)$$

and

$$Z_{\mathrm{A}} = \frac{K_0}{j\omega} + R_0 - \frac{j\omega M_tH_c}{g} = Z_0 - \frac{j\omega M_tH_c}{g}. \quad (3.7.6)$$

It can be noted that the equation of motion for the first DOF in the model of Neely [66], with the additional mass accounting for the effect of the TM's inertia to the motion of the lower subsystem in Fig.3.26, is significantly different from the one for the original model of Neely defined in Eq.3.5.13. Firstly, the effect of the TM load is taken into account in the organ of Corti impedance, Z_{OC}, which could be described as the sum of the BM impedance Z_b and some load impedance, say $Z_{\mathrm{L}}=j\omega M_t$, due to TM's mass M_t, as shown in Eq.3.7.5. Secondly, the inertia of the TM affects the active mechanism in this modified model, since the mass M_t is connected with the active displacement ξ_c in Eq.3.7.1. The effect of the TM mass on the cochlear amplifier is expressed by the active impedance Z_{A} in Eq.3.7.6, in which the TM mass impedance and the OHC gain transfer function, i.e. $j\omega M_tH_c/g$, appear to be acting against the impedance of the cilia Z_0.

The equation of motion governing the second DOF of the system in Fig.3.26 will take the same form as in Eq.3.5.16, which implies that the relationship between the radial displacement ξ_0 and the BM transverse displacement ξ_b is also unaffected by the modification to the original model of Neely, and remains the same as in Eq.3.5.21. Therefore, Eq.3.7.4 will take the form

$$P_f = Z_{\mathrm{OC}}\dot{\xi}_b + gZ_{\mathrm{A}}\frac{gZ_t}{Z_t + gH_cZ_t + Z_0}\,\dot{\xi}_b, \tag{3.7.7}$$

or using Eq.3.5.24

$$P_f = Z_{\mathrm{OC}}\dot{\xi}_b + gZ_{\mathrm{A}}H_0\dot{\xi}_b. \tag{3.7.8}$$

Thus, the CP impedance for the model of Neely [66] with the incorporation of the TM mass inertia, will be defined as[14]

$$Z_p = \frac{P_f}{\dot{\xi}_b} = Z_{\mathrm{OC}} + gZ_{\mathrm{A}}H_0, \tag{3.7.9}$$

or similarly to the expressions given by Neely in [66]

$$Z_p = Z_{\mathrm{OC}}(1 + gZ_{\mathrm{A}}H_0Y_{\mathrm{OC}}), \tag{3.7.10}$$

which in terms of the CP's mobility gives

$$Y_p = Y_{\mathrm{OC}}(1 + gZ_{\mathrm{A}}H_0Y_{\mathrm{OC}})^{-1}. \tag{3.7.11}$$

Setting the TM inertial term $M_t(\ddot{\xi}_b - \ddot{\xi}_c)$ in Eq.3.7.1 to zero, leads to the definition of the CP mobility derived by Neely formulated in Eq.3.5.34.

It is interesting to note the implications of setting the gain of the cochlear amplifier γ in the modified model of Neely. Using Eq.3.7.6 we can write Eq.3.7.9 as

$$Z_p = Z_{\mathrm{OC}} + gZ_0H_0 - j\omega M_tH_cH_0, \tag{3.7.12}$$

[14]We omit again the A_p factor in the formulation of modified Z_p, similarly to Eq.3.5.34. However, the mechanical parameters used for simulations are A_p-scaled as shown in Table 3.2, so that the dimensions of calculated impedances/mobilities in the present chapter are consistent.

or

$$Z_p = Z_{\mathrm{OC}} + (gZ_0 - j\omega M_t H_c)H_0, \tag{3.7.13}$$

which could be expanded using Eq.3.5.24 to give

$$Z_p = Z_{\mathrm{OC}} + \frac{gZ_t(gZ_0 - j\omega M_t H_c)}{Z_t + gH_c Z_t + Z_0}. \tag{3.7.14}$$

The cochlear amplifier's gain γ, is introduced to the above equation via the OHC gain H_c (Eq.3.5.37), i.e.

$$H_c = \gamma T_f T_r = \frac{\gamma g_f g_r}{(1 + j\omega\tau_f)(1 + j\omega\tau_r)}, \tag{3.7.15}$$

and is assumed to take the values between zero, corresponding to the passive cochlea, and one for a fully active cochlea. By setting γ to zero so that H_c=0, Eq.3.7.14 reduces to

$$Z_p = Z_{\mathrm{OC}} + g^2\frac{Z_t Z_0}{Z_t + Z_0} = \underbrace{j\omega M_t}_{Z_{\mathrm{L}}} + Z_b + g^2\frac{Z_t Z_0}{Z_t + Z_0}, \tag{3.7.16}$$

which is similar to the passive partition impedance in the model of Neely [66] defined in Eq.3.5.33. It is worth noting that Eq.3.7.16 differs mainly from Eq.3.5.33 by incorporation of the TM inertia through the additional load impedance, Z_{L}, into the BM impedance. However, the passive partition impedance of the modified model of Neely has exactly the same form as the one formulated in Eq.3.2.18 for the passive cochlear model proposed by Allen in [1] if we neglect the BM damping R_b.

A 'fully' active response of the model is predicted for γ equal to one, for which the partition impedance will take the form as in Eq.3.7.14. In this case Z_p consists of the impedance of the CP of the original model of Neely, and the load impedance, Z_{L}, due to inertial component of the TM mass, M_t, reduced by an additional active impedance $-j\omega M_t H_c H_0$, say Z_{add}, which could be written as

$$Z_{add} = j\omega M_t \frac{gH_c Z_t}{Z_t + gH_c Z_t + Z_0}, \tag{3.7.17}$$

according to Eq.3.7.14, or by extracting gZ_tH_c from the denominator on the right-hand side of Z_{add}, i.e.

$$Z_{add} = \frac{j\omega M_t}{1 + (gH_c)^{-1} + (gH_c)^{-1}Z_0Y_t} = \frac{j\omega M_t}{1 + (gH_c)^{-1}(1 + Z_0Y_t)}. \quad (3.7.18)$$

The partition impedance of the modified active model of Neely can be also expressed using the partition impedance of the original model of Neely in [66]. Using Eq.3.7.12 and Eq.3.7.5 we can write

$$Z_p = Z_b + j\omega M_t + gZ_0H_0 - j\omega M_tH_cH_0 = Z_p^{\mathrm{N}} + j\omega M_t(1 - H_cH_0), \quad (3.7.19)$$

where Z_p^{N} is the partition impedance of the original model of Neely derived in Eq.3.5.34 in Section 3.5. The last term in the above equation can be referred to as a modifying partition impedance, Z_p^{mod}, which can be written explicitly, after substituting for H_0, as

$$Z_p^{mod} = j\omega M_t\left(1 - \frac{gH_cZ_t}{Z_t + gH_cZ_t + Z_0}\right) = j\omega M_t\frac{Z_t + Z_0}{Z_t + gH_cZ_t + Z_0}, \quad (3.7.20)$$

which after dividing the numerator and denominator by the sum of Z_t and Z_0 gives

$$Z_p^{mod} = j\omega M_t\frac{1}{1 + \frac{gZ_t}{Z_t+Z_0}H_c}. \quad (3.7.21)$$

Note that the $gZ_t/(Z_t+Z_0)$ term in the denominator of Eq.3.7.21, which we will call T_{shear}, defines the 'shear transfer function' between the transverse displacement of the RL, $\xi_r^{tr}=\xi_r/g$ (the difference of the transverse BM displacement ξ_b and the active displacement ξ_c, Eq.3.5.3) and the radial shear displacement of the cilia, ξ_0 [24], i.e. using Eq.3.5.3 and 3.5.1

$$T_{shear} = \frac{\xi_0}{\xi_r^{tr}} = \frac{\xi_0}{\xi_b - \xi_c} = \frac{\xi_0}{\xi_b - H_c\xi_0} = \left(\frac{\xi_b}{\xi_0} - H_c\right)^{-1}, \quad (3.7.22)$$

which after substituting for ξ_b/ξ_0 from Eq.3.5.21, gives

$$T_{shear} = \left(\frac{Z_t + gH_cZ_t + Z_0}{gZ_t} - \frac{gH_cZ_t}{gZ_t}\right)^{-1} = \frac{gZ_t}{Z_t + Z_0}. \quad (3.7.23)$$

Thus, the CP impedance of the modified model of Neely can be generally defined as

$$Z_p = Z_p^{\mathrm{N}} + Z_p^{mod} = Z_p^{\mathrm{N}} + \frac{j\omega M_t}{1 + T_{shear} H_c}, \tag{3.7.24}$$

which again shows that for γ=0 (passive model), the impedance of the CP takes almost the same form (i.e. the difference due to the extra term from TM load impedance $j\omega M_t$) as the one proposed by Neely [66] defined in Eq.3.5.34, and is exactly the same as the total BM impedance defined in Eq.3.2.18 for the passive model of Allen in [1] if the BM damping R_b is neglected.

In Fig.3.27 we show the magnitude and phase of the CP mobility of the modified model of Neely calculated using Eq.3.7.11 and parameters in Table 3.2. Figures 3.27(a), 3.27(c) show the mobility as a function of position at 1 kHz stimulus frequency and figures 3.27(b), 3.27(d) show the frequency response of the partition mobility at the position of 0.0193 m along the cochlea. For comparison, the mobility of the original model of Neely calculated from Eq.3.5.34 (A_p factor neglected in the calculations comparing to Eq.3.5.32, however the parameters are A_p-scaled) is plotted with thin lines at the same stimulus frequency and cochlear site. The dashed lines show the magnitude and phase of the passive model (γ=0) and the solid lines the response of the active model (γ=1).

The effect of the TM inertia is visible in the apical region of the magnitude response of the modified model shown in Fig.3.27(a), where the mobility above the characteristic place decreases with the position along the cochlea, different from the mobility of the original model of Neely, where $Y_p(x)$ increases from the characteristic place towards the cochlear apex. The effect of the TM load is also visible in the high frequency region of the frequency response magnitude in Fig.3.27(b), where the response decreases above the CF, unlike the mobility of the original model, which starts decreasing from about 3 kHz until it reaches the 10 kHz frequency limit. Furthermore, the magnitude of the mobility in both $Y_p(x)$ and $Y_p(f)$, is significantly more enhanced, with a shift of the characteristic place/CF towards the apical end and higher frequencies, respectively, for the modified active model than for the original model of Neely.

It should be pointed out however, that instead of the characteristic increase of

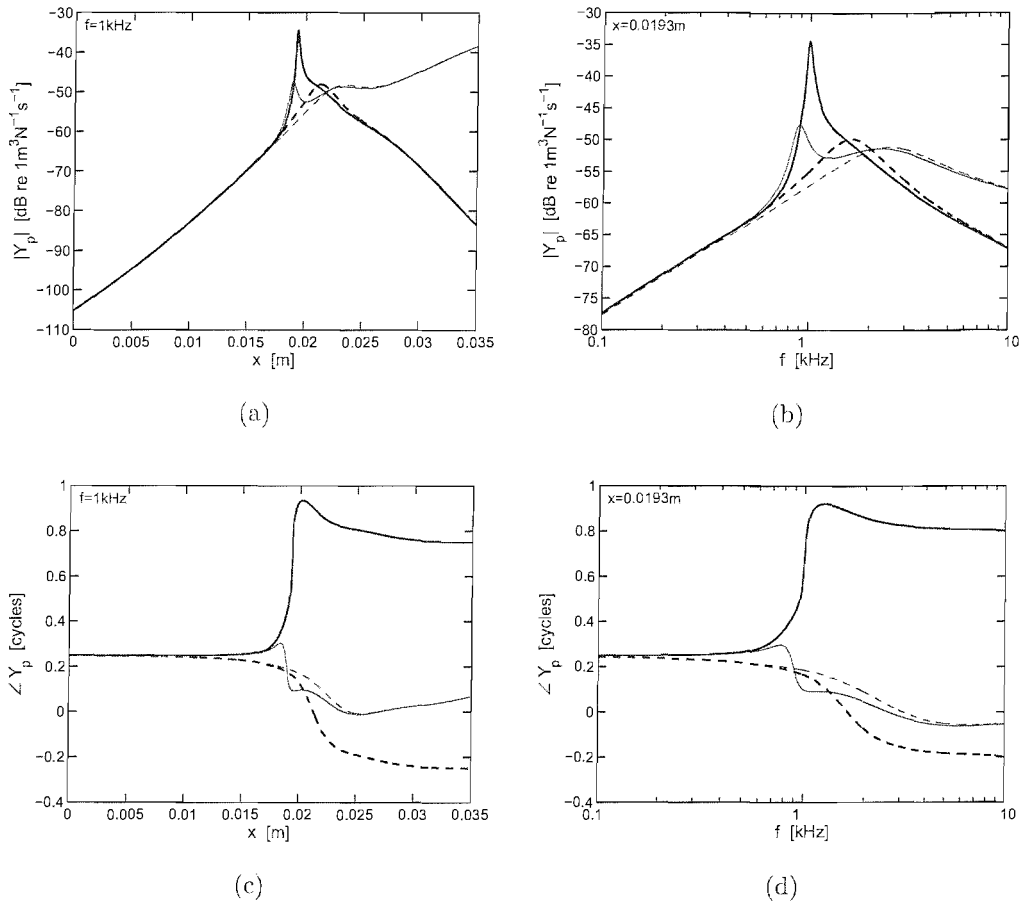

Figure 3.27: The magnitude (a, b) and phase (c, d) of the passive (thick dashed) and active (thick solid) cochlear partition mobility, Y_p, as a function of position along the cochlea (left) and stimulus frequency (right), calculated for the modified model of Neely [66], in which the inertial effects from the tectorial membrane mass were incorporated. The frequency was set to f=1kHz in (a) and (c), whereas the cochlear site to 0.0193 m in (b) and (d). Thin lines represent the partition mobility of the original model of Neely. γ was set to 0 and 1 for the passive and active model, respectively.

the phase lag's slope as for the active response in the original model, the modified model exhibits a phase lead in the vicinity of the characteristic place/CF, as shown in Fig.3.27(c) and 3.27(d). Such a behaviour may indicate instability of the system, which may be due to the decrease of the critical value of the cochlear amplifier's gain for which the system is still stable, and for the responses shown in Fig.3.27 it seems to be lower than one[15]. Therefore we plot the responses of the modified model of Neely for a lower value of gain in the active case, i.e. γ=0.7, as shown in Fig.3.28(a) and 3.28(c) for the modified partition mobility as a function of position along the cochlea at 1 kHz, and in Fig.3.28(b) and 3.28(d) as a function of frequency at 0.0186 m cochlear site. For comparison we also plot the mobility of the original model of Neely with γ=0 and 0.7 (thin lines).

The slopes of the magnitude responses of the modified model calculated for γ=0.7, are negative in the apical region unlike for the original model of Neely where the responses above the characteristic place increase with position along the cochlea. The enhancement of the magnitude of the active response of the modified model is approximately 8 dB, higher than for Neely's original active model. Also a shift of the characteristic place towards the apex in comparison with the characteristic place of the magnitude response of the original model can be seen in Fig.3.28(a).

About 8 dB higher magnitude of the active response of the modified model in comparison with the original model of Neely, and a shift of the CF of about 100 Hz towards higher frequencies for the modified model of Neely, can be seen in the frequency responses in Fig.3.28(b). Also high frequency slope of the amplitude responses of the modified model is slightly higher than the slope of the original model's mobility.

[15]It was observed that the critical value of the cochlear amplifier's gain in the modified model is equal to about 0.91 since the phase response exhibits a lead instead of a phase lag at the characteristic place/CF for γ=0.92. It is also interesting to note that the magnitude of the modified model calculated for the active gain of 0.9 was higher than the magnitude of the same model calculated for the gain of one (results not shown here). This can be regarded as another evidence for the active responses plotted in Fig.3.27 as being computed for an unstable system, but a more thorough stability examination must be carried out to support this hypothesis. Stability of the isolated lumped parameter models will be examined in Chapter 5.

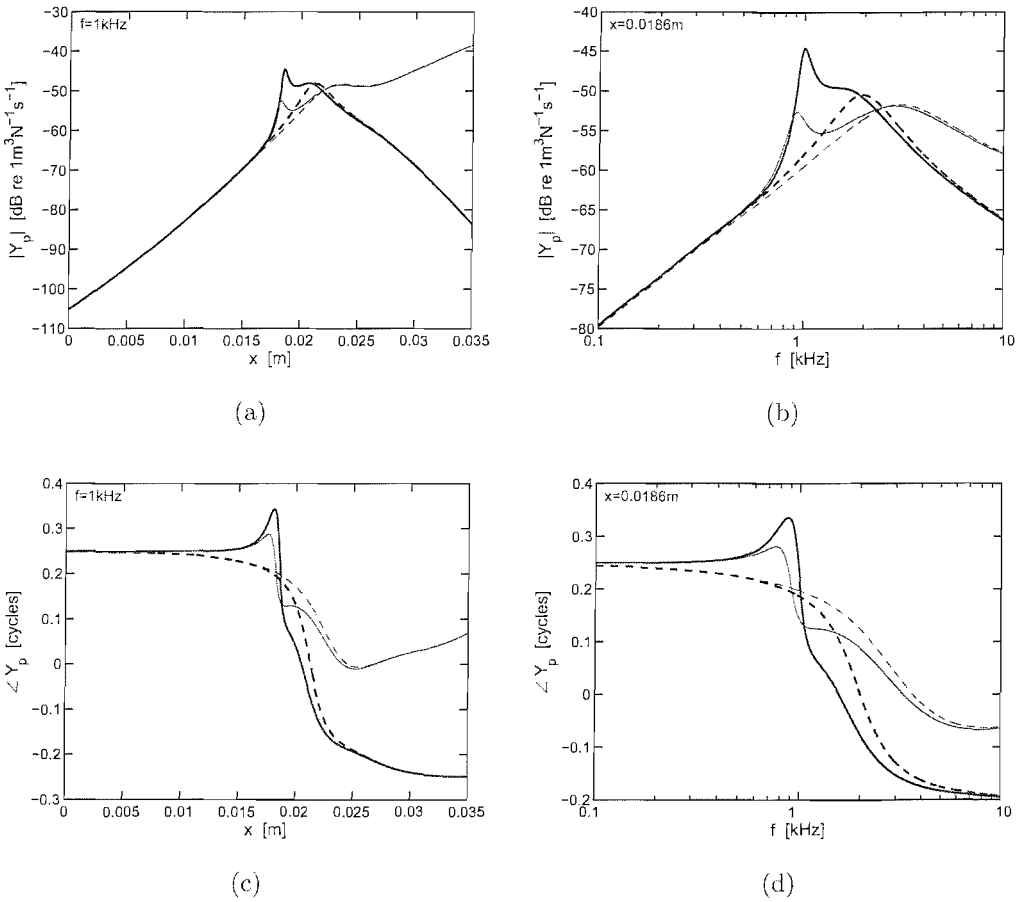

Figure 3.28: The magnitude (a, b) and phase (c, d) of the passive (thick dashed) and active (thick solid) cochlear partition mobility, Y_p, as a function of position along the cochlea at 1 kHz (left panel) and as a function of stimulus frequency at 0.0186 m position along the cochlea (right panel), calculated for the modified model of Neely [66]. Thin lines show the partition mobility of the original model of Neely. γ was set to 0 and 0.7 for the passive and active model, respectively.

The phase responses, shown in Fig.3.28, of the active modified model of Neely computed for γ=0.7 exhibit a lag instead of the lead observed for the phase response in Fig.3.27 calculated for γ=1. The increased slope of the active phase near the characteristic place/frequency point with respect to the phase of the passive model, is consistent with the phase behaviour of the original model of Neely. It is also interesting that the total phase lag of the phase in the modified model's response amounts to about half of a cycle along the cochlea as shown in Fig.3.28(c), and about 0.45 of a cycle in the examined frequency range as shown in Fig.3.28(d), whereas the phase responses calculated for the original model of Neely in these figures reach a total phase lag of about quarter and 0.3 of a cycle, respectively. Because the phase of the partition mobility is the same in the basal and low frequency region in the original as well as modified models, the additional phase lag must be connected with the extra load of the TM.

In the present section we have examined the influence of the TM inertial loading to the mobility of the cochlear model of Neely [66]. The effect of the TM load appears to have been ignored in the original model of Neely. Only the mass of the BM is taken into account when considering the first DOF of the original Neely's model, unlike in the model of Allen [1], but similarly to the model of Neely and Kim [68]. While the effect of the mass of the TM in the equations of motion for the first degree of freedom in the model of Neely and Kim could be neglected and 'compensated for' by increasing the mass of the BM appropriately, it should not be neglected in the model of Neely since it affects the action of the cochlear amplifier as shown here.

It should be noted that by the incorporation of the TM mass, M_t, the mass of the BM/organ of Corti complex in the modified model is M_b+M_t, which at 0.0186 m site along the cochlea is equal to about 0.026 kgm^{-2} that is approximately equal to the mass of the BM (m_1=0.03 kgm^{-2}) in the model of Neely and Kim given in Table 3.1. Thus, effectively the mass of the organ of Corti is higher than the mass of the BM itself in the modified model of Neely.

Secondly, the TM load affects the cochlear amplifier while the TM mass is connected with the active displacement from the OHCs, ξ_c. As a result the mobility responses of the modified model are 'sharper' than those observed for the

original model. Furthermore, the magnitude of modified mobility is higher than the magnitude of mobility functions derived according to the original Neely's model. Another implication of the enhanced mobility responses, seems to be a higher sensitivity of the modified model. In the model of Neely and Kim [68] and the original model of Neely [66], a gain of one is thought to generate a 'fully' active response of the model, which is assumed to be still stable. However, a lower gain of the active component is needed to produce the fully active response, i.e. $\gamma_{critical}$=0.91, in the modified model of Neely. For γ higher than 0.91 the magnitude of the mobility starts to decrease with the increase of the active gain and the phase response of mobility exhibits a lead above the characteristic place/CF, which may indicate that the model is no longer stable.

3.8 Discussion

In the present chapter the basic concepts for modelling the cochlear micromechanics and the lumped parameter micromechanical models of the cochlea proposed by Allen [1], Neely and Kim [68] and Neely [66] were analysed. Furthermore, the modes of vibration of the model of Neely and Kim and Neely were analysed in Sections 3.4 and 3.6, respectively, and the effect of the TM load to the dynamics of the model of Neely was discussed in Section 3.7.

Firstly, a secondary resonator, which must be present in the cochlea [17], is localised within the organ of Corti and assumed to be linked to the TM in the described models [1, 34, 68]. In the models of Allen [1], Neely and Kim [68] and the model of Neely [66], the TM is a fully resonant structure[16] with its independent motion, specified mass, stiffness and damping, which correspond to the mass of its body and attachments to the bony structures of the cochlea, respectively. Thus, in these models a two DOF mechanical system was defined, with two structures, the BM and TM, described by their mechanical impedances. Furthermore, the BM and TM resonators were coupled by the stereocilia of the OHC, which add a stiffness component that together with the damping from the

[16]By fully resonant system we mean a system that possesses a mass and stiffness component and hence is capable of resonance when forced into motion.

cochlear fluid introduces additional impedance into the partition impedance Z_p [1, 66, 68].

Secondly, in their 1986 model Neely and Kim [68] use the idea of Allen [1], who defined the first DOF as the parallel, locked motion of the BM and TM leading to shearing forces acting on the OHC's cilia. Also the second DOF, corresponding to the radial motion of the TM, was employed after the passive model of Allen. However, the displacements in the model of Neely and Kim were defined as if the motion were purely radial, and an active component, represented by an active pressure source acting within the organ of Corti, was added to account for the mechanism of the cochlear amplifier. Furthermore, the 1986 model was developed by Neely in 1993 [66], in which an active displacement between the BM and the RL due to the electromotility of the OHC, was proposed as the cochlear amplifier. However, the basic concepts concerning the micromechanics of the organ of Corti remained unchanged in the 1993 model [66].

Although it was shown that the models of Neely and Kim and Neely exhibit differences regarding the selection of the models' parameters, which leads to discrepancies in the characteristics of the mobility responses plotted for these models, the definition of the passive partition impedance is the same in these models. However, ignoring the inertial load of the TM significantly affects the response of the original model of Neely, as shown in Section 3.7. Furthermore, taking account of the TM load in the dynamics of the model of Neely leads to a definition of the CP impedance consistent with the one derived for the model of Allen [1], but also appears to affect the sensitivity of the cochlear amplifier.

Finally, the overall partition impedance proposed by Neely and Kim [68] and Neely [66] is consistent with the generic form shown in Eq.3.1.9, where the active impedance is defined differently in both models. Thus, the idea of de Boer [16], who argued that locally active models could be converted into a general, equivalent form with the difference in the choice of the meaning of particular parameters, is justified for the example of the lumped parameter models presented here.

Chapter 4

The coupled response of lumped parameter models

In the previous chapter the micromechanics of three widely known lumped parameter models was examined. Each of these models described the passive mechanics of a single, cross-sectional slice of the CP, i.e. the interactions within the organ of Corti and of the organ with the overlying TM, by means of the CP mobility functions. Furthermore, the mechanism of the cochlear amplifier in the active models of Neely and Kim [68] and Neely [66], was discussed, so that an active partition mobility was also formulated for these models, and its dependence on the cochlear position and stimulus frequency was examined and compared with that derived for a passive model.

It has to be remembered however, that the CP is immersed in the cochlear fluid, which is assumed to couple the isolated micromechanical, lumped parameter systems, and induce the CP's travelling wave [17]. Therefore, to compare the cochlear models with the experimental results, a coupled, macromechanical response must be derived.

In the present chapter the CP mobility, Y_p, defined for the model of Neely and Kim [68] and Neely [66], will be implemented into the macromechanical formulation for the travelling wave propagating in the cochlea, and the coupled response of these models will be calculated and compared with experimental results. Furthermore, the ratio of the passive TM and BM velocities, V_t/V_b,

derived in Sections 3.4 and 3.6, will be used to calculate the passive coupled response of the TM in order to compare with the passive coupled CP response and experimental results obtained by Gummer *et al.* [40] and Hemmert *et al.* [43].

4.1 Travelling waves

4.1.1 The wave equation

To facilitate the description of the cochlear macromechanics a number of simplifications are usually assumed as discussed in Section 3.1. Firstly, the cochlea is uncoiled and represented by a rectangular box as in Fig.3.1. The pressure difference across the CP, p_d [1], propagating due to the sinusoidal oscillations of the stapes at the cochlea's oval window, leads to the CP's propagating transverse displacement (travelling wave), ξ_p. Secondly, the cochlear fluids are assumed incompressible and inviscid and, due to the long-wave assumption, the propagation of the travelling wave is considered only in the longitudinal direction, x (the wave equation in Eq.3.1.1). Furthermore, due to symmetry and because the displacement of the CP is caused by the pressure difference, only the upper chamber of the cochlea needs to be considered, which can be geometrically represented as in Fig.4.1.

In the figure, the CP is discretised into a number of two DOF systems, the impedance of which can be defined in ways described in Chapter 3. Although each of the segments forming the CP is independent of its neighbours, they are assumed to be coupled by the fluid within the cochlear chamber. The apical end of the cochlear chamber is terminated by the helicotrema and thus not connected to the CP in this model.

The coupled response of the cochlea can be derived by coupling the partition impedance Z_p into the second-order differential equation for the travelling wave,

[1] We will use a uniform, small letter notation for the pressure difference in this section.

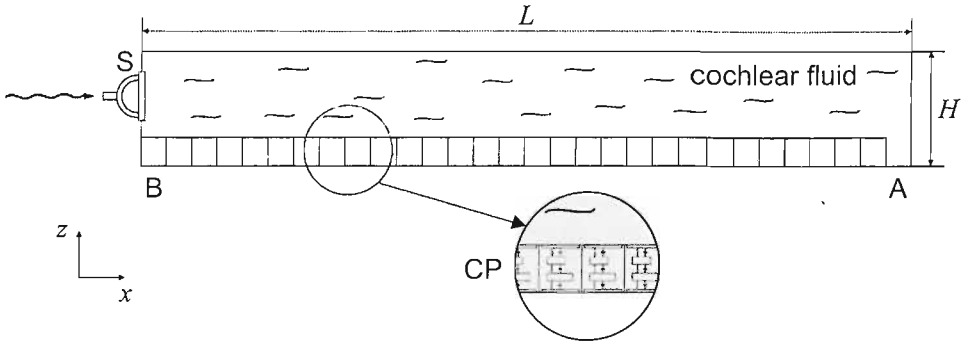

Figure 4.1: Schematic of the cochlea's upper channel of length L and height H, where the cochlear partition (CP) is represented by a number of independent two degree of freedom systems. These systems are coupled via the cochlear fluid, excited by the oscillations of the stapes (S) inducing partition's vertical displacement, which travels in the longitudinal direction, x, from the base (B) to the apex (A) of the cochlea.

i.e.

$$\frac{\partial^2 p_d(x,\omega)}{\partial x^2} - \frac{2j\omega\rho}{Z_p(x,\omega)H}\, p_d(x,\omega) = 0, \tag{4.1.1}$$

where H is the upper chamber's height and ρ is the density of the cochlear fluid[2] [14, 17]. Redefining the above equation into a form of a one-dimensional, homogeneous *Helmholtz equation* gives

$$\frac{\partial^2 p_d(x,\omega)}{\partial x^2} + k_{tw}^2(x,\omega) p_d(x,\omega) = 0, \tag{4.1.2}$$

where

$$k_{tw}^2(x,\omega) = -\frac{2j\omega\rho}{Z_p(x,\omega)H}, \tag{4.1.3}$$

is the wavenumber of the travelling wave, and hence the wavespeed of the travelling wave, c_{tw}=ω/k_{tw}, can be expressed as [59]

$$c_{tw}(x,\omega) = \left(\frac{j\omega Z_p(x,\omega)H}{2\rho}\right)^{\frac{1}{2}}, \tag{4.1.4}$$

[2]Full derivation of the travelling wave equation can be found e.g. in [17, 59].

and like k_{tw} is both frequency- and place-dependent.

The boundary conditions for the travelling wave at the stapes and helicotrema, respectively, are defined as

$$\frac{dp_d(0)}{dx} = -2j\omega\rho u_{st}, \tag{4.1.5}$$

$$p_d(L) = 0, \tag{4.1.6}$$

where u_{st} is the velocity of the stapes [55, 59]. Note that the basal boundary condition is expressed in terms of the stapes velocity u_{st}, the value of which is imposed in our model. In the model of Neely and Kim [68] and Neely [66], the stapes velocity is coupled with the middle ear impedance and is expressed in terms of the pressure at the eardrum. Furthermore, we assume in Eq.4.1.6 that the pressure difference at the helicotrema is equal to zero. Alternatively, a damping element, which represents the passage of the cochlear fluid through the helicotrema, could be introduced into the helicotrema boundary condition as in [66, 68]. However, the model response is thought to be not sensitive to the apical boundary condition provided the characteristic place is located basally to the helicotrema, i.e. the travelling wave decays before reaching the helicotrema, so that the condition in Eq.4.1.6 is justified [55, 59]. Furthermore, preliminary results of the coupled models evaluated at the cochlear site corresponding to the 1 kHz CF (i.e. 0.0186 m and 0.0189 m for the Neely and Kim [68] and Neely [66] models, respectively), have shown that the lowest frequency for which the frequency responses appear not to be affected by the boundary condition in Eq.4.1.6, amounts to about 600 Hz. Therefore, in our simulations the length of the BM was set to 35 mm (with appropriate extrapolation of the models' mechanical parameters), so that the lowest frequency was shifted from 600 Hz to about 10 Hz, and the responses could be plotted from 100 Hz (see Appendix C for details).

4.1.2 Finite difference approximation of the wave equation

In 1981 Neely [64], proposed a direct method of solving the travelling wave equation numerically by using its *finite difference approximation*, and a one-dimensional representation of this method can be found in e.g. [55].

The CP is divided into N components, thus the length of each CP's segment is equal to $\Delta = L/(N-1)$, where L is the CP's length. Using the *Taylor series expansion* for the second derivative of p_d with respect to x, Eq.4.1.1 can be written as

$$\frac{p_d(i+1) - 2p_d(i) + p_d(i-1)}{\Delta^2} - \frac{2j\omega\rho}{Z_p(i)H}\, p_d(i) = 0, \tag{4.1.7}$$

where i denotes the number of the element of the CP and here $i=2, 3, \ldots, N-1$. For $i=1$ and N, the boundary conditions in Eqs.4.1.5 and 4.1.6 are applied, thus

$$\frac{p_d(2) - p_d(1)}{\Delta} = -2j\omega\rho u_{st}, \tag{4.1.8}$$

at the base, and

$$p_d(N) = 0, \tag{4.1.9}$$

at the apex [55].

After discretising the wave equation, the coupled response of the cochlear model can be calculated from a matrix equation of the form

$$(\mathbf{C} - \mathbf{M})\mathbf{p}_d = \mathbf{q}, \tag{4.1.10}$$

where

$$\mathbf{C} = \frac{1}{\Delta^2}\begin{bmatrix} -\Delta & \Delta & & & \\ 1 & -2 & 1 & & 0 \\ & \ddots & \ddots & \ddots & \\ 0 & & 1 & -2 & 1 \\ & & & 0 & \Delta^2 \end{bmatrix}, \tag{4.1.11}$$

is the matrix corresponding to the coupling with the cochlear fluid, $\mathbf{M}$ is the mobility matrix

$$\mathbf{M} = \frac{2j\omega\rho}{H}\begin{bmatrix} 0 & & & \\ & Y_p(2) & & 0 \\ & & \ddots & \\ & 0 & & Y_p(N-1) \\ & & & & 0 \end{bmatrix}, \tag{4.1.12}$$

where $Y_p(i)$=$Z_p(i)^{-1}$,

$$\mathbf{p}_d = \begin{Bmatrix} p_d(1) \\ \vdots \\ p_d(i) \\ \vdots \\ p_d(N) \end{Bmatrix}, \tag{4.1.13}$$

is the pressure difference vector, and

$$\mathbf{q} = \begin{Bmatrix} -2j\omega\rho u_{st} \\ 0 \\ \vdots \\ \vdots \\ 0 \end{Bmatrix}, \tag{4.1.14}$$

is the input source vector [55].

Introducing a tridiagonal, $N\times N$ matrix T, such that

$$\mathbf{T} = \mathbf{C} - \mathbf{M}, \tag{4.1.15}$$

allows Eq.4.1.10 to be written as

$$\mathbf{T}\mathbf{p}_d = \mathbf{q}, \tag{4.1.16}$$

so that the pressure difference distribution can be derived, since

$$\mathbf{p}_d = \mathbf{T}^{-1}\mathbf{q}. \tag{4.1.17}$$

The CP velocity $\dot{\xi}_p$ is related to the pressure difference p_d as [66, 68]

$$\dot{\xi}_p = \frac{p_d}{Z_p} = Y_p p_d, \tag{4.1.18}$$

thus calculating the p_d distribution along the cochlea according to Eq.4.1.17, allows the CP velocity, $\dot{\xi}_p$, and hence the partition's displacement, $\xi_p = \dot{\xi}_p / j\omega$, to be derived.

4.2 Coupled response of the model of Neely and Kim

The wavenumber, k_{tw}, and the wavespeed, c_{tw}, of the travelling wave are defined in Eqs.4.1.3 and 4.1.4, so that using the parameters proposed by Neely and Kim [68] gathered in Table 3.1, the cochlear chamber's height $H=10^{-3}$ m and the density of the cochlear fluid $\rho=10^3\,\mathrm{kgm}^{-3}$, the distribution along the cochlea and the frequency dependence of these quantities as well as the wavelength, $\lambda_{tw}=2\pi/k_{tw}$, can be derived. Figure 4.2 shows the wavespeed and the wavelength of the travelling wave ($Re\{c_{tw}\}$ and $Re\{\lambda_{tw}\}$) as a function of position x calculated for the stimulus frequency of 1 kHz. The dashed lines in the figure correspond to the 'passive' case of the travelling wave, i.e. $\gamma=0$ and $Z_p=Z_{pass}$ (Eq.3.3.8), and the solid lines to the 'active' travelling wave, i.e. $\gamma=1$.

The wavespeed of the 'passive' travelling wave decreases rapidly towards the apex of the cochlea, from $\approx$117.5 to 0.6 ms^{-1}, with an exponential characteristic, as shown in Fig.4.2(a). However, the speed of propagation of the 'active' travelling wave can be divided into two regions. In the first region, the wave decreases rapidly from $\approx$103.2 ms^{-1} at the base to a short 'plateau' region in the vicinity of the characteristic place, $\approx$6.6 ms^{-1} at about 16 mm. In the second region, that is after the 16 mm site, the 'active' wavespeed decreases even faster to reach a plateau of about 1.1 ms^{-1} at the characteristic place, x=0.0186 m. Above the characteristic place the wavespeed is nearly zero until the apex of the cochlea.

The plateau in the apical region in Fig.4.2(a), is consistent with the experimental data, in which a travelling wave plateau can be observed apically from

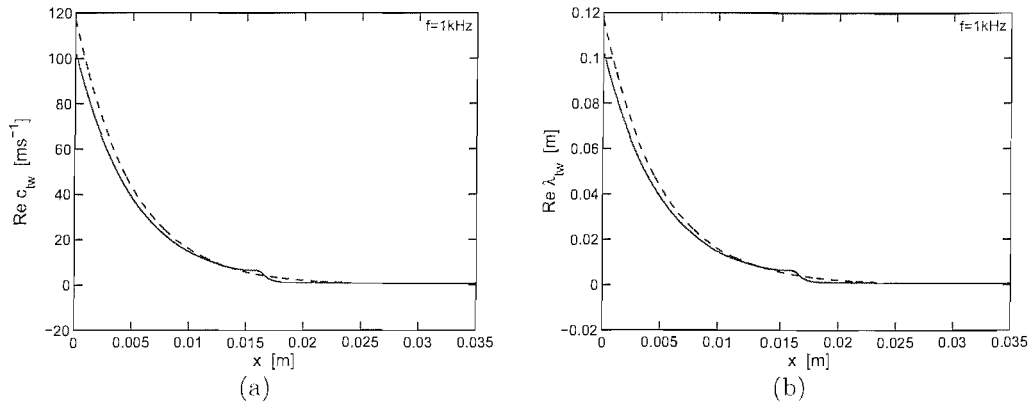

Figure 4.2: The wavespeed, c_{tw} (a) and the wavelength λ_{tw} (b) of the travelling wave as a function of position in the cochlea, calculated at 1 kHz for the model of Neely and Kim [68]. Solid and dashed lines represent both quantities derived for the active and passive partition impedance, respectively.

the characteristic place (or high frequency from the CF) [87]. It should be also noted that in theory the wavespeed should decrease to zero since the wave does not travel beyond the characteristic place. However, this can be accomplished only if the real part of the model's partition mobility (CP's damping) is equal to zero and the imaginary part of the partition's mobility is negative, according to Eq.4.1.4. This condition is not satisfied in the investigated model for any position along the cochlea as shown in Figs.3.8(b)-3.8(d), and any stimulus frequency, as shown in Figs.3.9(b)-3.9(d).

The travelling wave's wavelength, λ_{tw}, Fig.4.2(b), reveals that the wavelength decreases exponentially towards the apex of the cochlea in the passive case, from $\approx$117.5$-$0.6 mm (dashed line), whereas it decreases slightly faster for the active case, from about 103.2 mm until it reaches almost a constant value of $\approx$6.6 mm at the site of about 16 mm. From this place, like the wavespeed, the wavelength of the 'active' travelling wave decreases even more reaching almost a zero plateau towards the apex. Therefore, as the travelling wave approaches the characteristic place, it slows down rapidly and its wavelength becomes short, $\lambda_{tw}\approx$0.6 mm, which implies that the long-wave assumption is not satisfied at this place.

To calculate the coupled response of the Neely and Kim model [68], the formulation for the CP impedance, and hence the partition's mobility since Y_p=Z_p^{-1}, given in Eq.3.3.7, was implemented into the matrix **M** in Eq.4.1.12. Thus, we derive the pressure difference according to Eq.4.1.17. Once the pressure difference is calculated, also the partition velocity for the model of Neely and Kim, $\dot{\xi}_p$, can be derived according to Eq.4.1.18. Knowing the relationship between ξ_p and ξ_b in Eq.3.3.1, we can write

$$\dot{\xi}_p(x) = b\,\dot{\xi}_b(x), \tag{4.2.1}$$

so that the BM velocity will take the form

$$\dot{\xi}_b = \frac{\dot{\xi}_p}{b} = \frac{p_d}{bZ_p} = \frac{Y_p p_d}{b}, \tag{4.2.2}$$

and the BM displacement

$$\xi_b = \frac{p_d}{j\omega b Z_p} = \frac{Y_p p_d}{j\omega b}. \tag{4.2.3}$$

The magnitude and phase response of the pressure difference, p_d, and the BM velocity, $\dot{\xi}_b$, were calculated for the parameters in Table 3.1 and plotted as a function of position in the cochlea, as shown in Fig.4.3. Stimulus frequency was set to 1 kHz and the gain γ to zero and one corresponding to the passive and fully active model.

It can be seen from Fig.4.3(a) that the passive (γ=0, dashed) and fully active (γ=1, solid) pressure difference magnitude curves are almost equal up to about 15 mm from the base of the cochlea. After the 15 mm point the pressure difference of the active model, exhibits a tuned peak with the maximum of about 200 dB (re 2×10^{-5} Pa) at x=0.0185 m. There is no peak in the corresponding passive, γ=0, response curve. However, the magnitude of the passive pressure difference at x=0.0185 m equals to approximately 170 dB, so that in this model, the cochlear amplifier enhances the pressure difference by about 30 dB at the characteristic place for 1 kHz stimulus frequency. Both, the passive and active pressure difference responses roll off rapidly from the characteristic place site, where the slope of the apical side of the active response is slightly steeper. Since

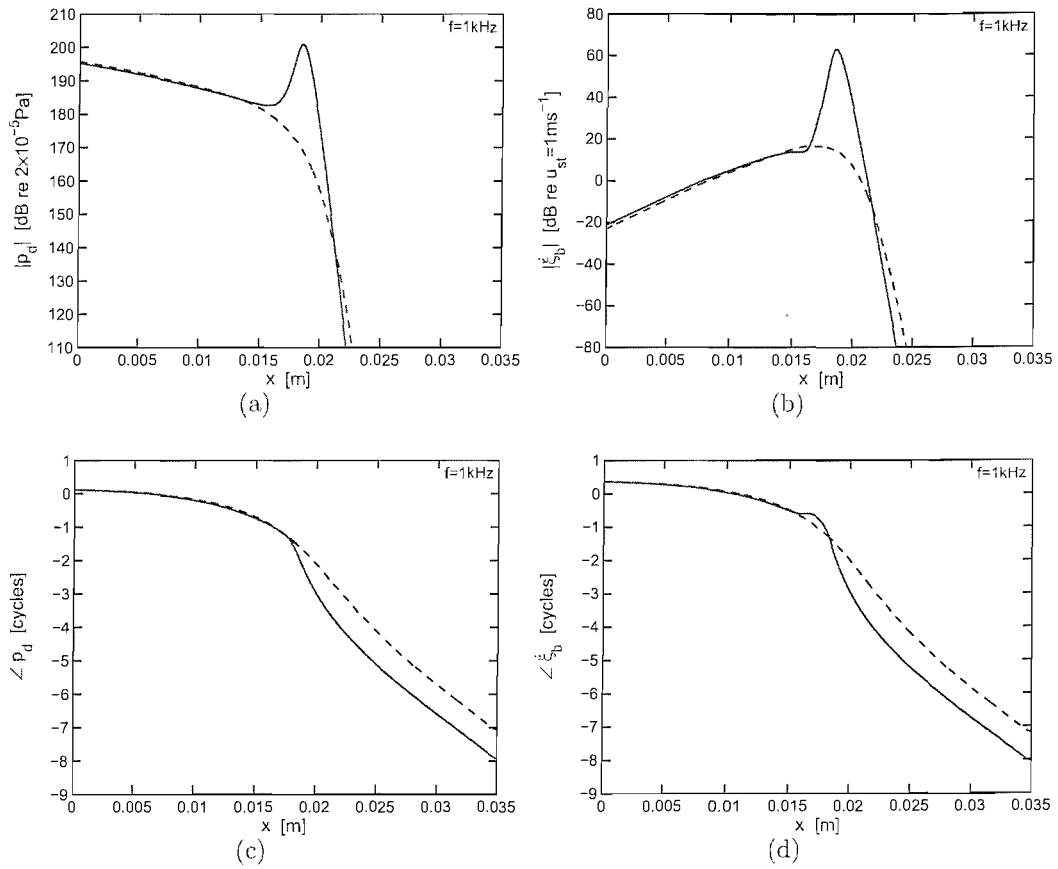

Figure 4.3: Magnitude and phase of the pressure difference p_d (a, c) and the basilar membrane velocity $\dot{\xi}_b$ (b, d) as a function of position in the coupled cochlea for stimulus frequency of f=1 kHz and parameters chosen by Neely and Kim [68]. Solid lines show the active, γ=1, and dashed lines the passive, γ=0, response of the model.

there is no peak in the passive curve, the passive response resembles that of a heavily damped resonant system.

The phases of the passive and active pressure difference shown in Fig.4.3(c), have almost the same value from the base until the vicinity of the characteristic place, i.e. up to about 17.5 mm. After this point the active model's phase lag begins to accumulate faster than that of the passive model reaching about one cycle difference beyond about the 20 mm site. The overall phase lag of the pressure difference amounts to about seven and eight cycles for the passive and active case, respectively.

The passive BM velocity amplitude response depicted in Fig.4.3(b), has its maximum of about 16 dB re u_{st}=1 ms^{-1} at x=0.0169 m. The maximum of the active velocity amplitude response is shifted towards apex by about 1.6 mm, with respect to the maximum of the passive curve, and is observed at x=0.0185 m and equals approximately 63 dB. Thus, the enhancement of the amplitude of the active velocity at 1 kHz stimulus frequency amounts to about 47 dB. The passive and active amplitude curves are almost equal in the basal region of the response, up to about the 13.5 mm place. A notch can be observed below the peak of the active response, which does not occur in the passive response. However, after the maxima in the amplitude velocity responses, a fast roll-off can be observed in the passive and active case, where the passive response decays slightly slower with position along the cochlea.

The phase responses of the BM velocity, are almost equal in the basal region of the cochlea, until around 15 mm, for both the passive and active model, as shown in Fig.4.3(d). Both curves exhibit about one cycle phase lag up to around 15 mm place after which the active phase response begins to lead the passive one, reaching about 0.3 of a cycle lead at around 17 mm site. The passive and active phase curves reach the same value again in the vicinity of the characteristic place ($\approx$0.0182 m), beyond which the phase lag accumulation of the active response becomes larger and reaches almost constant, about one cycle, difference from the passive phase above about 20 mm cochlear site. The overall phase lag of the velocity response amounts to approximately 7.5 and 8.5 cycles for the passive and active case.

Figure 4.4 shows the frequency response of the pressure difference p_d and BM velocity $\dot{\xi}_b$. The frequency responses were calculated at x=0.0185 m and the cochlear amplifier's gain was set to γ=0 (passive) and γ=1 (active).

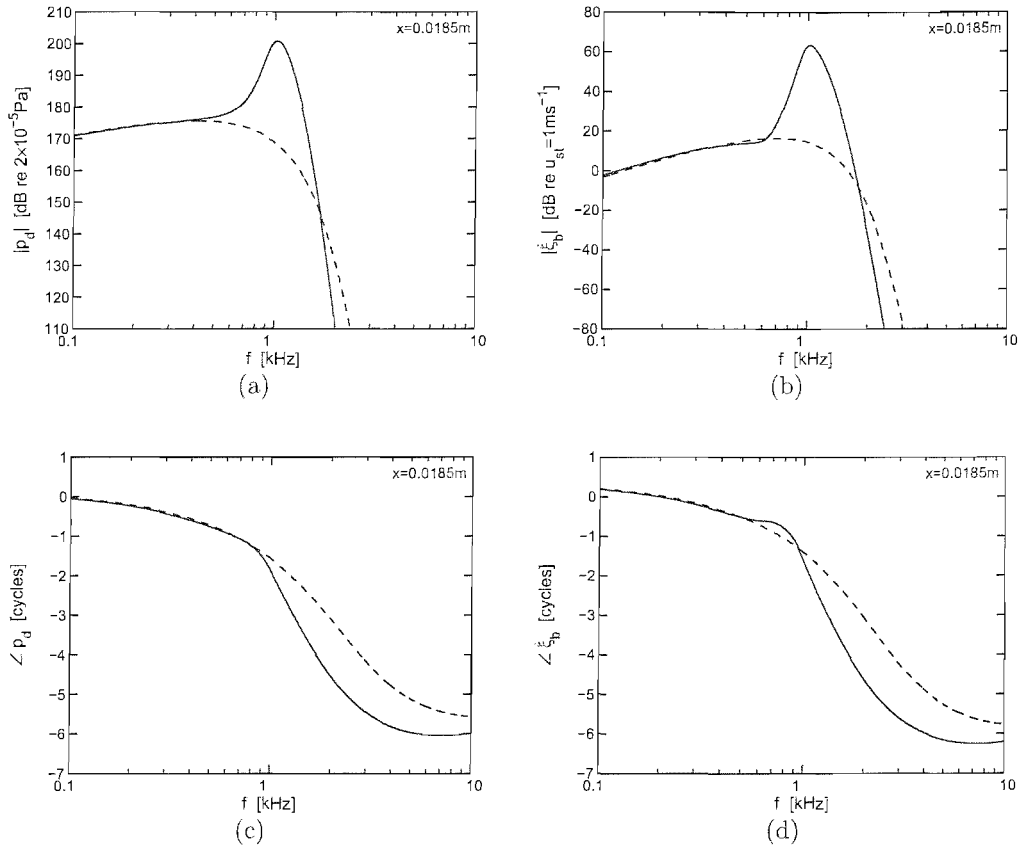

Figure 4.4: Magnitude and phase of the pressure difference p_d (a, c) and the basilar membrane velocity $\dot{\xi}_b$ (b, d) as a function of stimulus frequency, calculated at the cochlear site of x=0.0185 m and for parameters chosen by Neely and Kim [68]. Solid lines, active model (γ=1) and dashed lines, passive model (γ=0).

The amplitudes of the pressure difference, p_d, of both the passive and active model of Neely and Kim, plotted in Fig.4.4(a), are almost equal and increase about 5 dB (re 2×10^{-5} Pa) with the increase of the stimulus frequency from 100 Hz to about 400 Hz. The passive response reaches its maximum at 420 Hz, above which it decreases gradually. There is no distinctive maximum peak in the

frequency response of the passive model.

However, the magnitude of the active model's pressure difference increases rapidly above about 400 Hz, and reaches a maximum peak of about 201 dB at 1.02 kHz, about 25 dB higher than the maximum of the passive pressure difference observed at 420 Hz. It is worth noting that the frequency of the amplitude maximum of the active model is shifted by 600 Hz towards higher frequencies, in comparison with the maximum of the 'passive' p_d. Above 1.02 kHz, the magnitude of the 'active' pressure difference decreases rapidly.

The phase of p_d shown in Fig.4.4(c), exhibits a total phase lag of about 5.5 and 6 cycles for the passive and the active model, respectively. Up to about 800 Hz, the phase of both passive and active model, are almost equal and lag the stapes velocity by about one cycle. Above 800 Hz the slope of the phase of the active response becomes steeper, exhibiting about 5 cycles phase lag accumulation until about 4 kHz, roughly one cycle bigger than the phase lag accumulation of the passive model between 800 Hz and 4 kHz. Both passive and active phase change little above 4 kHz.

The passive and active basilar membrane velocity, $\dot{\xi}_b$, shown in Fig.4.4(c), increase with the same rate at low frequencies and are nearly equal up to approximately 400 Hz. The velocity of the passive model is highest at 700 Hz, and decreases above this frequency. The velocity of the active model however, increases rapidly above about 400 Hz and reaches a sharp peak of about 63 dB (re u_{st}=1 ms^{-1}) at 1020 Hz. For frequencies higher than the CF, the velocity of the active model decreases rapidly. The enhancement of the BM velocity due to the action of the cochlear amplifier, amounts to about 47 dB with respect to the magnitude of the velocity of the passive model, where the peak of the active response is shifted by 320 Hz towards higher frequencies with regard to the maximum of the passive response. It is interesting to note that this upwards shift in the peak response only occurs in the coupled model, and that the uncoupled response of the Neely and Kim model, shown in Fig.3.9, exhibits a downward shift in the frequency of the peak response when the system is active.

The phase of the BM velocity of the passive model is almost equal to the phase of the velocity calculated for the active model until approximately 500 Hz, where

both curves exhibit a phase lag of about -0.5 of a cycle. Above 500 Hz, the passive phase response lags even more so that the total phase lag of the BM velocity of the passive model amounts to about six cycles in the examined frequency range. However, a short phase plateau can be seen in the phase response of the active model between about 500 Hz and 700 Hz. After the plateau region, the phase lag increases again, and the overall phase lag of the 'active' BM velocity amounts to about 6.5 cycles. It should be noted that the slope of the active model's phase lag is higher in the CF region, outside which the phase slopes of both models differ little.

Figure 4.5 depicts the amplitude and phase of the passive (left panel) and active (right panel) BM and TM velocity of the coupled Neely and Kim model [68]. The TM velocity was calculated by multiplying the velocity of the BM, ξ_b, derived for the passive and active coupled model of Neely and Kim at 0.0185 m, shown in Fig.4.4(b), by the ratio V_t/V_b defined in Eq.3.4.38, computed at the same cochlear place.

The magnitude of the 'passive' TM velocity in Fig.4.5(a) is smaller than the magnitude of the BM velocity response almost over the entire frequency range but the narrow frequency region around the maximum of the TM's velocity. However, the magnitude difference is not large and both velocity responses are qualitatively comparable. The maximum of the BM velocity response can be observed at frequency of 700 Hz, whereas the peak of the TM velocity response is at 630 Hz. Thus, the BM damped resonance frequency is higher than the damped resonance frequency of the TM in this passive model, similarly to the undamped or damped case for the BM point and TM transfer mobility depicted in Fig.3.14 for the isolated two degree of freedom system proposed by Neely and Kim [68].

The difference between the maximum amplitude of the passive BM and TM velocity amounts to about 8 dB, i.e. $|V_b|_{max} \approx 16$ dB and $|V_t|_{max} \approx 24$ dB, respectively. Furthermore, the slope of the TM velocity shown in Fig.4.5(a) is almost equal to that calculated for the BM in the low and high frequency regions.

The phase of the BM and TM velocity shown in Fig.4.5(c) are almost equal up to frequency of about 400 Hz. Above 400 Hz, the slope of the TM velocity phase becomes steeper so that the TM phase lag becomes slightly higher than

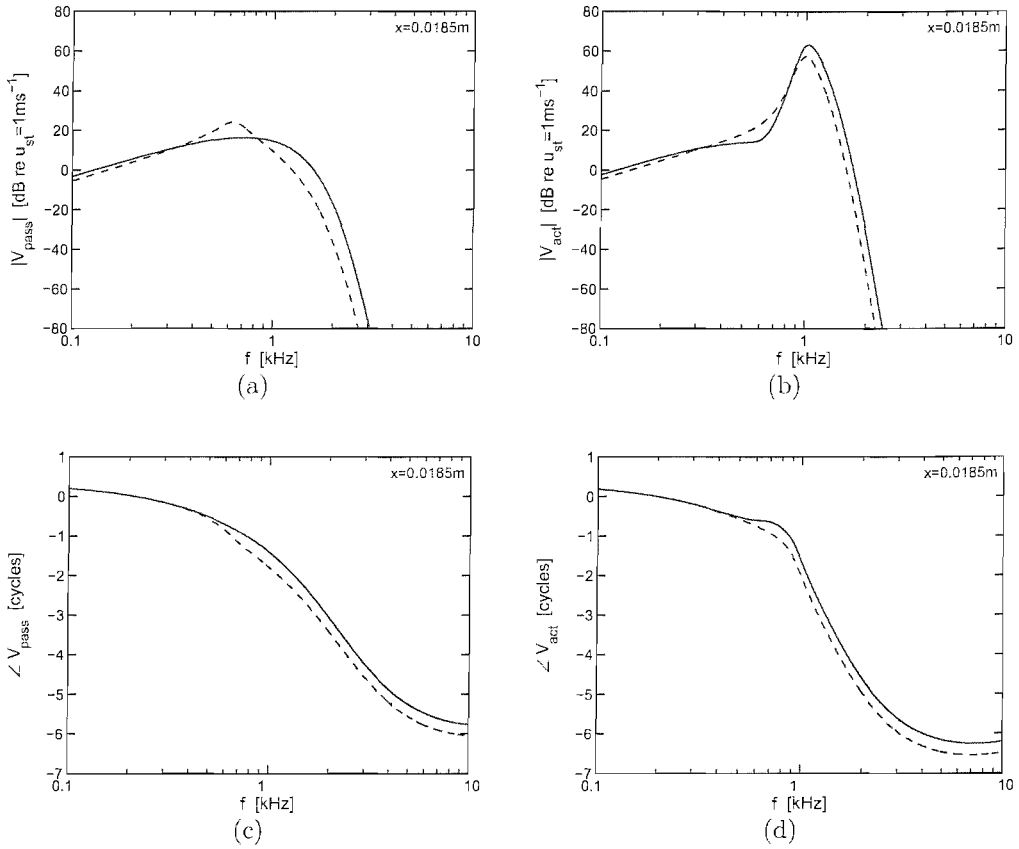

Figure 4.5: Magnitude and phase of the frequency response of the basilar membrane, V_b (solid), and tectorial membrane velocity, V_t (dashed), calculated for the passive, γ=0 (V_{pass}; a, c), and active, γ=1 (V_{act}; b, d), coupled model of Neely and Kim [68] at x=0.0185 m along the cochlea.

that of the BM, reaching a difference of about quarter of a cycle at about 700 Hz. This quarter of a cycle difference between the phase of the BM and TM velocity remains almost constant until the upper frequency limit, hence the total phase lag of the BM velocity amounts to about six cycles and that of the TM velocity to about 6.25 cycles.

The TM velocity response shown in Fig.4.5(b), calculated for the active case, has roughly the same characteristics as the velocity of the BM calculated for the active coupled model of Neely and Kim [68]. The peak of the TM velocity can be observed at 1 kHz, which is 20 Hz below the frequency at which we observe the peak of the BM velocity in the active case. The low and high frequency slopes of the BM and TM velocity are almost equal. However, the low-frequency 'shoulder' (or a shallow antiresonance) in the BM velocity response cannot be seen in the TM velocity curve. Assuming that the shoulder on the low frequency side of the BM velocity corresponds to the heavily damped lower resonance connected with the TM, which is even more heavily damped in the TM velocity response, the lack of the shallow antiresonance implies that the TM velocity response is a transfer response, as was the case for the TM mobility response of the isolated two degree of freedom system, shown in Fig.3.14. The BM velocity can be considered therefore as a point response. This is also consistent with the fact that there is no excitation on the TM, as shown in Fig.3.6, and although the model is active, still only the BM is forced into motion.

In Fig.4.5(d) we show the phase of the BM and TM velocity of the active coupled model of Neely and Kim, which are almost equal up to about 400 Hz stimulus frequency, above which the phase of the BM velocity exhibits a short plateau in the frequency region of the shallow antiresonance in the BM velocity's amplitude in Fig.4.5(b). No such phase plateau can be seen in the TM velocity phase curve. The phase of the BM velocity leads the phase of the TM velocity by more than quarter of a cycle from about 700 Hz, and this phase difference remains almost constant with the increase of the stimulus frequency up to 10 kHz.

4.3 Coupled response of the Neely model

In the present section we calculate the coupled responses of the 1993 model of Neely [66] by implementing the formulation of the CP's mobility, derived in Section 3.5, into the finite difference formulation of the wave equation, and using the set of mechanical parameters chosen for the simulations by Neely (cochlear chamber height is equal to $H{=}10^{-3}\,\mathrm{m}$ and the density of the cochlear fluid to $\rho{=}10^{3}\,\mathrm{kgm}^{-3}$ as for the coupled model of Neely and Kim [68]).

Firstly, we calculate the wavespeed and the wavelength of the 'passive' and 'active' travelling wave for the partition impedance $Z_p{=}Y_p^{-1}$, where Y_p is given in Eq.3.5.34, and plot it as a function of position at the stimulus frequency of 1 kHz as shown in Fig.4.6.

Figure 4.6(a) shows the phase speed of the travelling wave of the passive, $\gamma{=}0$, and active, $\gamma{=}1$, model of Neely. The wavespeed of the passive model ranges from about $23.9\,\mathrm{ms}^{-1}$ at the base to about $0.4\,\mathrm{ms}^{-1}$ at the apex of the cochlea and is almost equal to the wavespeed of the active model at the corresponding cochlear positions. As the distance from the stapes increases, both curves decrease exponentially with the same slope below about 15 mm and above about 24 mm along the cochlea. Between these locations the active travelling wave slows down significantly and reaches a local minimum at about 19 mm site. Above this position the wavespeed of the active wave increases slightly to match the passive curve with which it decreases with position towards the apex.

The wavelength of the travelling wave of the passive model ($\gamma{=}0$) also exhibits an exponential decrease along the cochlea from about 23.9 mm at the base to about 0.4 mm at the cochlear apex, as shown in Fig.4.6(b). The wavelength of the active model ($\gamma{=}1$) is equal to the wavelength of the passive model at the base and the apex of the cochlea, and decreases with the same slope until about 15 mm position along the CP. Beyond the 15 mm site the wavelength of the active model decreases faster than that of the passive model and reaches a local minimum at about 19 mm position in the cochlea. Similarly to the phase speed's behaviour, for cochlear positions higher than the place of the local minimum, the wavelength of the passive travelling wave increases slightly to become roughly equal to the wavelength of the passive wave at about 24 mm site. From the position of 24 mm

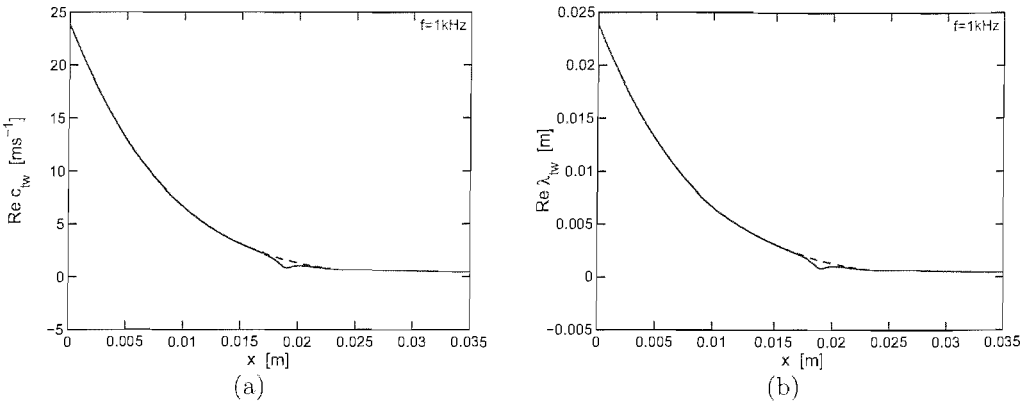

Figure 4.6: The wavespeed, c_{tw} (a) and the wavelength λ_{tw} (b) of the travelling wave as a function of position in the cochlea calculated at 1 kHz for the model of Neely [66]. Solid and dashed lines represent c_{tw} and λ_{tw} derived for the active and passive partition impedance, respectively.

towards the apex, both curves decrease again with the same slope.

It can be noticed that the characteristics of the active and passive phase speed and wavelength of the travelling wave along the cochlea are generally similar to those observed for the coupled Neely and Kim model shown in Figs.4.2(a) and 4.2(b). However, at the cochlear base both the wavespeed and the wavelength calculated for the model of Neely, are significantly lower than those calculated for the model of Neely and Kim, which can be attributed to the difference of the mechanical parameters chosen for both models.

There is no observable difference between the wavespeed and the wavelength characteristics of the passive and active model of Neely apart from near the characteristic place. Furthermore, while the wavespeed and wavelength of the active travelling wave exhibit a short plateau in the vicinity of the characteristic place in the model of Neely and Kim, a small, local minimum can be observed in the model of Neely below the characteristic place. These discrepancies between the Neely and Kim and the Neely model must be due to the different definitions of the active CP's mobility.

To derive the coupled responses of the model of Neely [66], we first calculate

the pressure difference p_f using Eq.4.1.17 (p_f refers to P_f in the model of Neely), after implementing the partition's mobility Y_p calculated according to Eq.3.5.32 into the matrix $\mathbf{M}$ in Eq.4.1.12. Having calculated the pressure difference, p_f, we derive the partition's velocity $\dot{\xi}_p$ using Eq.4.1.18 and the relationship between $\dot{\xi}_p$ and $\dot{\xi}_b$ defined in Eq.3.5.4. Thus, the BM velocity takes the form

$$\dot{\xi}_b = -Y_p p_f, \tag{4.3.1}$$

and hence the BM displacement will be defined as

$$\xi_b = -\frac{Y_p p_f}{j\omega}. \tag{4.3.2}$$

Note that the dimension of the CP's admittance in Eq.3.5.32 is $[\mathrm{m^5N^{-1}s^{-1}}]$ (ratio of volume velocity and pressure difference; the mechanical parameters are scaled by the effective area of the CP), hence before implementing into the matrix $\mathbf{M}$, Y_p was divided by the factor of A_p to obtain consistent dimension of $[\mathrm{m^3N^{-1}s^{-1}}]$ (ratio of linear velocity and pressure difference; the mechanical parameters scaled by the effective area of the CP). Consequently, the BM velocity $\dot{\xi}_b$ was not divided by A_p despite the relationship in Eq.3.5.4, however, the minus sign was taken into account due to the opposite directions of $\dot{\xi}_b$ and $\dot{\xi}_p$ [66].

The magnitudes of the pressure difference, plotted as a function of cochlear position, of the passive and active (γ=0 and 1, respectively) coupled model of Neely [66] derived for the set of parameters in Table 3.2, are shown in Fig.4.7(a). Both curves are almost equal in the basal region of the cochlea and decrease up to about the 10 mm point along the cochlea. Beyond the 10 mm site, the 'passive' pressure difference drops further with gradually increasing slope until about the 20 mm cochlear site after which it decreases rapidly with almost constant slope. However, the pressure difference calculated for the active model decreases until about 15 mm place along the cochlea, above which it increases towards a peak at around 18.8 mm place, close to the characteristic place calculated for the CP mobility of Neely's model. The apical side of magnitude of the pressure difference of the active model falls rapidly with position along the cochlea.

The phase of the pressure difference of the passive model of Neely decreases with a gradually increasing slope and reaches about nine cycles phase lag at about

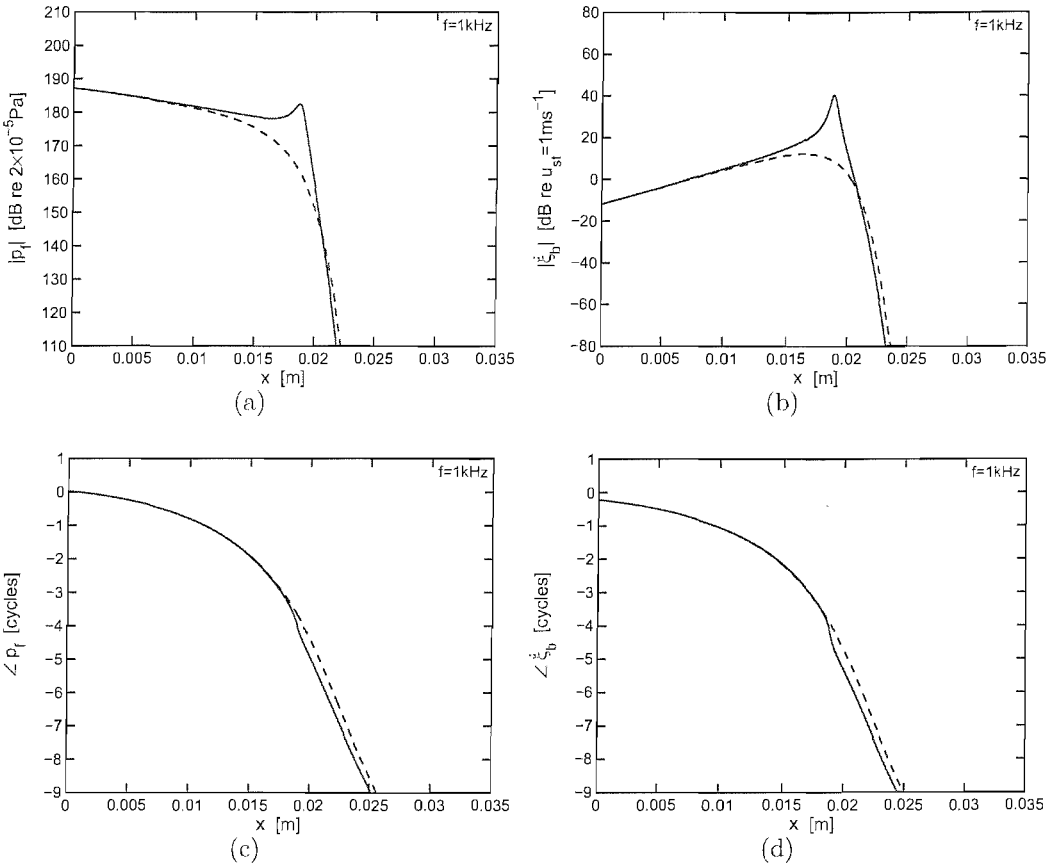

Figure 4.7: Magnitude and phase of the pressure difference p_f (a, c) and the basilar membrane velocity $\dot{\xi}_b$ (b, d) as a function of position in the cochlea for stimulus frequency of f=1 kHz and parameters chosen by Neely [66]. Solid lines, active model (γ=1) and dashed lines, passive model (γ=0).

25.2 mm along the cochlea, as shown in Fig.4.7(c). Similarly, the phase of the pressure difference of the active model decreases with gradually increasing slope, and is almost equal to that observed for the passive model up to about 15 mm along the cochlea. For positions beyond the 15 mm site the active model's phase lag increases faster than that of the 'passive' phase, and around the place of the maximum in the magnitude response of the active model they reach a difference of about half of a cycle, which remains roughly constant towards the more apical positions.

The distribution of the BM's velocity along the cochlea calculated for the model of Neely, is shown in the right panel of Fig.4.7. The magnitude of the velocity of both the passive (γ=0) and active (γ=1) model shown in Fig.4.7(b) increase with position along the cochlea, being almost equal up to about the 10 mm site in the cochlea. The passive response has a broad maximum at about 16.5 mm, after which it decreases on the apical side of the response. The magnitude of the BM velocity of the active model starts to increase rapidly as it approaches the characteristic place and reaches its maximum, about 30 dB higher than the maximum velocity of the passive model, at 18.9 mm, that is the characteristic place predicted from the mobility functions calculated in Section 3.5.1. Beyond the characteristic place velocity of the active model decays rapidly with position along the cochlea.

In Fig.4.7(d) we show the phase of the BM velocity as a function of position in the cochlea. The phase of the BM velocity of the passive and active model are almost equal up to about 18.5 mm along the cochlea where they both reach about -3.5 cycles phase lag. However, the slope of the active model's phase response increases before the characteristic place (18.9 mm), so that about a quarter of a cycle difference can be observed between the phase of the passive and active model at the characteristic place. The difference between the phase of the passive and active velocity response equals roughly a half of a cycle on the apical side of the cochlea.

The magnitude and phase of the pressure difference calculated for the coupled model of Neely [66] at 0.0185 m along the cochlea as a function of stimulus frequency, are shown in Fig.4.8 and 4.8(c), respectively. Both, the passive, γ=0,

and the active, γ=1, amplitude response of p_f increase with an increase of the stimulus frequency at low frequencies, and are almost equal up to about frequency of 300 Hz. There is no distinctive maximum in the magnitude of the passive response, which starts to decrease for stimulus frequencies higher than about 500 Hz. However, the pressure difference of the active model exhibits a peak at about 1 kHz, above which it decreases rapidly with increasing stimulus frequency.

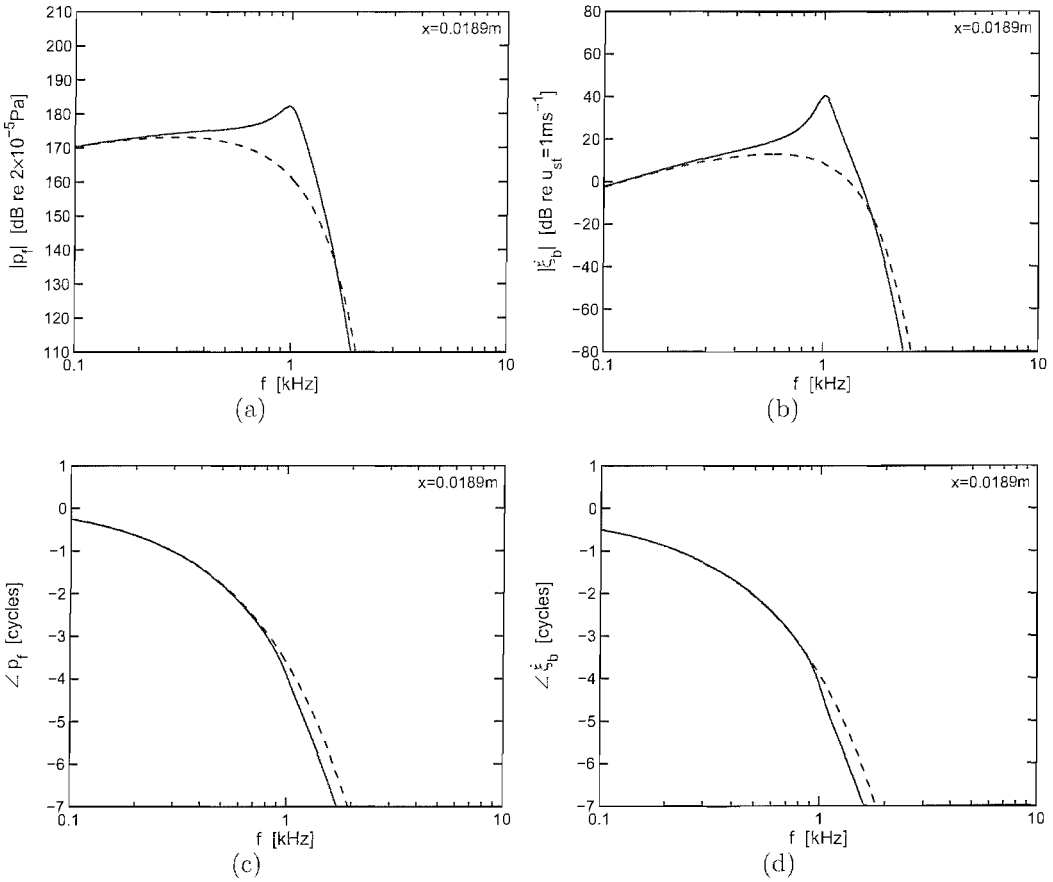

Figure 4.8: Magnitude and phase of the pressure difference p_f (a, c) and the basilar membrane velocity $\dot{\xi}_b$ (b, d) as a function of stimulus frequency, at the site of x=0.0189 m in the cochlea and for parameters chosen by Neely [66]. Solid lines, active model (γ=1) and dashed lines, passive model (γ=0).

The phase of the pressure difference, shown in Fig.4.8(c), decreases with in-

creasing stimulus frequency for both passive and the active model, and the slope of the phase increases as the frequency approaches the CF. In the vicinity of 1 kHz, the phase lag of p_f of the active model accumulates faster than that of the passive model and the difference between the phase of the passive and active model equals more than a quarter of a cycle. For frequencies above 1 kHz, the difference between the phase of p_f of the active and passive Neely model increases to about a half of a cycle and remains almost constant in the high frequency region.

Figure 4.8(b) shows the magnitude of the BM velocity of the coupled Neely model as a function of stimulus frequency. The passive BM velocity, calculated for γ=0, increases for low stimulus frequencies and decreases in the high frequency region. The passive amplitude response has a broad tuning with a maximum of about 13 dB (re 1 ms^{-1}) at 590 Hz. When the active gain is set to γ=1, the BM velocity becomes sharply tuned with the maximum at 1.01 kHz stimulus frequency and the amplitude enhanced to about 40 dB. In the low frequency region the amplitude of the active model's BM velocity increases with almost the same slope as that observed for the passive model, whereas for frequencies above 1.01 kHz the BM velocity response decreases rapidly.

Accumulation of the phase lag of the BM velocity depicted in Fig.4.8(d) increases with the same rate for the passive and active case at low frequencies. Just below the CF, the phase lag of $\dot{\xi}_b$ derived for the active model of Neely, accumulates faster than for the passive model and the relative difference between the two phase responses increases from about a quarter of a cycle around the CF to more than a half of a cycle at high stimulus frequencies.

It is interesting to note that the pressure difference and the BM velocity responses calculated for the coupled model of Neely [66] have generally the same characteristics as those derived for the coupled model of Neely and Kim [68]. Setting the active gain γ=1 causes a significant enhancement of the amplitude of the response, which also becomes more sharply tuned in comparison with the passive responses calculated for γ=0. However, the low-frequency shoulder or a local 'dip' below the characteristic place or CF in the BM velocity, and the corresponding phase plateau in the same cochlear/frequency region, was observed

only for the model of Neely and Kim, as shown in Fig.4.3 and 4.4. The phase lag of the pressure difference and the BM velocity, accumulates gradually in the basal region of the cochlea or at lower stimulus frequencies in the Neely model, as shown in Fig.4.7 and 4.8, respectively. However, the phase accumulation of the pressure difference and the BM velocity calculated for the Neely and Kim model, exhibit a fast accumulation in the narrow region around the characteristic place or the CF, being roughly constant outside of that region.

The passive (γ=0) velocity responses of the BM and TM of the coupled cochlear model of Neely [66], are shown in Fig.4.9. The TM velocity was derived in a similar way as for the plot in Fig.4.5 (a, c) for the Neely and Kim model [68], i.e. by multiplying the passive BM velocity shown in Fig.4.8(b) by the ratio of the TM and BM velocities, V_t/V_b, defined in Eq.3.6.12 for the model of Neely. Both responses were plotted as a function of frequency for the fixed position along the cochlea, equal to 0.0189 m. Note that because the TM is forced into motion by the displacement ξ_c, we cannot easily predict the TM velocity of the coupled model when the Neely model is active.

Figure 4.9(a) reveals that the velocity amplitudes of the BM and TM are qualitatively comparable in the entire examined frequency range, but the magnitude of the TM velocity is slightly lower than the magnitude of the velocity of the BM. The peak of both the BM and TM velocity occurs at the same stimulus frequency of 590 Hz. The phase responses of the BM and TM velocity shown in Fig.4.9(b) remain almost equal through the whole frequency range and reach about two cycles phase lag at the frequency of the maximum velocity amplitude shown in Fig.4.9(a).

4.4 Comparison with the results of experimental measurements

Measurements of the relative motion of the BM and the TM have been presented by Gummer *et al.* [40] and Hemmert *et al.* [43]. In both experiments the BM and TM vibration response was measured in the apical turn of the guinea pig cochlea. Gummer *et al.* used a novel measurement set-up to measure the res-

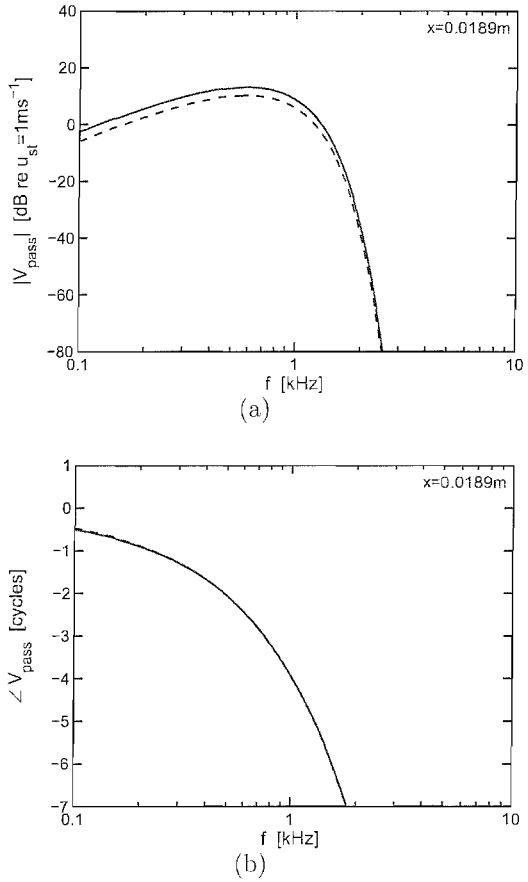

Figure 4.9: Magnitude and phase of the frequency response of the basilar membrane, V_b (solid), and tectorial membrane velocity, V_t (dashed), calculated for the passive, γ=0 (V_{pass}) coupled model of Neely [66] at x=0.0189 m along the cochlea.

ponses to electrical and acoustic stimulation in the radial and vertical directions, while Hemmert *et al.* developed a measurement set-up to allow vibration response measurements in three dimensions, i.e. longitudinal, radial and vertical[3], and used only acoustical stimuli [40, 43].

The vibration responses obtained experimentally can be compared with those calculated using the models considered above. Because only the acoustical stimulation was considered in the previous sections, we will concentrate on comparison with the results for acoustic stimuli in the experiments of Gummer *et al.* To begin with we describe the experimental protocol and results presented in [40].

4.4.1 Experiment of Gummer *et al.* [40]

In their 1996 experiment Gummer *et al.* [40] used two paradigms. Firstly, they measured the transverse component of vibrations in response to electrical stimulation by current injection just above the site of measurement in the scala vestibuli of the cochlea, to investigate the resonant motion of the TM and locate the resonant frequency of the BM. In this case the stimuli corresponded to sinusoidal forces, exerted by the OHCs on the cilia/TM and Deiters' cell/BM complexes. The positive current injection was thought to simulate the hyperpolarisation of the hair cell, hence its elongation, so that the BM and the TM were displaced in the scala tympani and vestibuli directions, respectively.

Secondly, an acoustic stimulation, corresponding to the excitation by the cochlear fluid pressure difference between the cochlear chambers that induces the vibrations of the CP, was used to excite the velocity in the transverse direction and displacement in the radial direction of the cochlea [40]. Gummer *et al.* note that the acoustic responses, which were referred to the sound pressure near the tympanic membrane, were not corrected for the middle ear response because measured response of the stapedial crux was found to be frequency-independent up to 2 kHz.

Isolated temporal bone preparations of the guinea pig cochleae were used in

[3]Only measurements in the radial and transverse directions were simultaneous, whereas the measurement set-up was rotated by 90 degrees to allow measurements in the longitudinal direction [43].

the experiments. The helicotrema remained intact and the Reissner's membrane was opened to place reflective microspheres on the TM for all measurements and on the BM for measuring the electrically induced vibration response [40]. The vibrations were recorded about 20 minutes *post mortem*, usually in the fourth cochlear turn at the site of about a quarter of a turn distance from the third turn or approximately 2.3 mm from the apex of the cochlea[4] [40]. Figure 4.10(a) shows the measurement conditions in the experiment of Gummer *et al.*, where the angles indicated in the figure can be seen in the organ of Corti in the basal part of the fourth turn of the guinea pig cochlea, a cross-section of which is shown in Fig.4.10(b) [40].

The RL of the preparation was reported to be inclined about 35° relative to the BM, the long axes of the OHC's about 55° relative to the RL, and the optical measurement system, which measured the vertical and radial vibrations and was constructed of a Laser Doppler Velocimeter (LDV in Fig.4.10), photodiode (PD) and a microscope (M), that was located above the organ of Corti. However, the data were not corrected to account for the nonparallel arrangement of the RL with the radial direction [40]. Furthermore, in the velocity measurements, the response of the TM was reported to be coupled with the response of the Hensen cells due to the TM attachment to these cells.

As reported by Gummer *et al.*, major differences in the responses of the BM and the TM were revealed in the results of current injection experiments, but were not observed in the acoustic stimulation case [40]. The acoustically induced motion of the TM was observed to have a larger amplitude response than that of the BM, however, the frequency response curves had similar forms for frequencies up to 1kHz, as reproduced in Fig.4.11 A. The best frequency, defined by the largest response in the acoustic paradigm, was equal to 660 Hz. It was assumed to correspond to the resonance frequency of the BM, and it was estimated from the frequency at which the amplitude response started to decay rapidly. The TM resonance frequency was identified from the maximum at 450 Hz in the electrical

[4]According to the formula of Greenwood for the CF/place map of a guinea pig [39], CF=$350(10^{2.1x/L}-0.85)$ [Hz], where x and L are the distance from the apex and the length of the cochlea in mm, the 2.3 mm site from the apex corresponds to a CF of about 341 Hz.

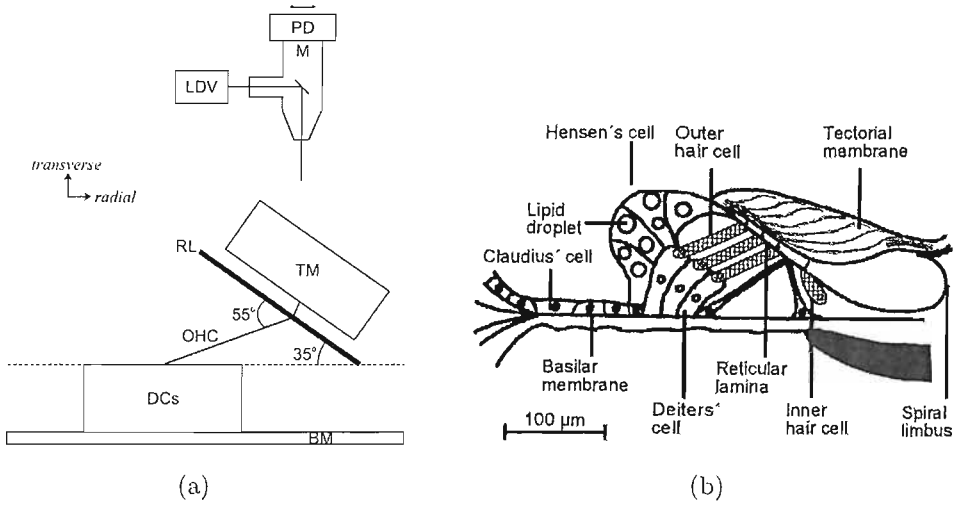

(a) (b)

Figure 4.10: Schematic of the experimental set-up (a) and illustration of the cross-section of the guinea pig organ of Corti observed at the basal part of the fourth cochlear turn in the preparation used for the measurements of Gummer *et al.* [40] (b). The angles in (a) show the relative geometrical arrangement of the organ of Corti structures. The optical system consisting of the microscope (M), photodiode (PD) and the laser Doppler velocimeter (LDV) is located above the organ (BM-basilar membrane; DCs-Deiters' cells). Figure (b) reprinted from Fig.1 in Gummer, A. W., Hemmert, W. and Zenner, H.-P. (**1996**) "Resonant tectorial membrane motion in the inner ear: Its crucial role in frequency tuning," Proceedings of the National Academy of Sciences of the U.S.A., **93**, 8727-8732, with permission from the publisher. Copyright (1996) National Academy of Sciences, U.S.A.

stimulation response, Fig.4.11C, which is half an octave below the best frequency.

The phase of the BM and TM velocity due to acoustical stimuli did not show a significant difference, apart from the region around the best frequency and around 1 kHz where a difference of about half of a cycle can be observed, as shown in Fig.4.11 B. However, the phase response to electrical stimuli exhibited a half cycle difference between the BM and the TM motion at frequencies below 250 Hz and above 900 Hz as depicted in Fig.4.11 D. Therefore, Gummer *et al.* argue that the mechanical resonance associated with the TM-cilia complex is responsible for the electrically induced tuning of the TM [40]. Furthermore, the electrical stimulation phase measurements were used to justify the definition of the best frequency corresponding to the site where the BM motion lagged the TM motion by a quarter of a cycle, as can be seen at the 600 Hz site in Fig.4.11 D [40].

A minimum or antiresonance after the best frequency of 660 Hz, and the 890 Hz maximum, can be observed in acoustically stimulated responses in Fig.4.11 A. The second minimum, at 1 kHz, coincides with the phase plateau at this frequency as shown in Fig.4.11 B, and was assumed to indicate the end of the travelling wave motion [40]. However, the first antiresonance was assumed to be connected with the maxima at the best frequency and at 890 Hz, as could be predicted for a two resonator system of TM-cilia and BM-Deiters cells complex, or it could account for an internal antiresonance in the organ of Corti as suggested by Gummer *et al.* [40].

The displacement or velocity response of the cochlea to tonal stimuli measured by other authors, usually decays rapidly after the peak in the response, with no additional antiresonances or resonances beyond that point (see e.g. [87]). The rapid fall-off of the travelling wave coincides with a phase plateau observed in this corresponding frequency region [85, 86]. However, in the responses to acoustical stimuli recorded by Gummer *et al.*, a phase plateau can be observed in Fig.4.11 B above around 1 kHz which coincides with the frequency of the secondary antiresonance observed in Fig.4.11 A. The antiresonances in Fig.4.11 A are probably the result of opening the cochlea when the hole in the cochlear wall was made for the vibration recordings. This was pointed out in the later paper

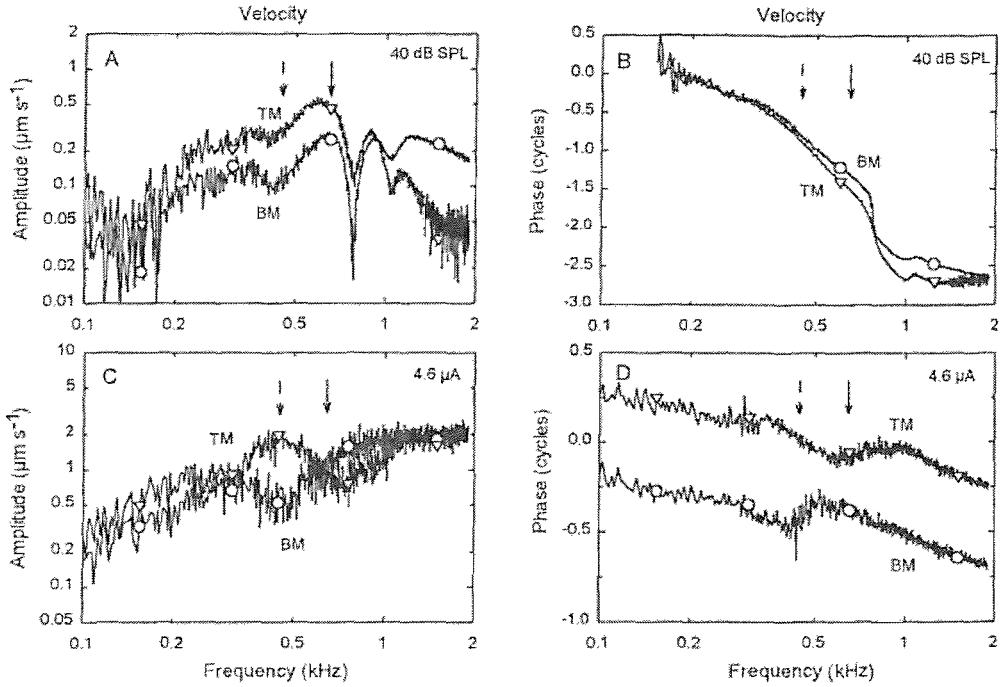

Figure 4.11: Experimental results of Gummer *et al.* [40]. The upper panels, A-B, show the transverse velocity response of the basilar membrane (BM, ○) and the tectorial membrane (TM, ▽) for the acoustic stimulation, whereas the lower, C-D, show results for the current injection paradigm. The arrows indicate the estimated basilar (solid) and tectorial membrane's (dashed) resonance frequencies. Reprinted from Fig.2 in Gummer, A. W., Hemmert, W. and Zenner, H.-P. (**1996**) "Resonant tectorial membrane motion in the inner ear: Its crucial role in frequency tuning," Proceedings of the National Academy of Sciences of the U.S.A., **93**, 8727-8732, with permission from the publisher. Copyright (1996) National Academy of Sciences, U.S.A.

of the same authors, Hemmert *et al.* [43], where the vibration recordings were corrected, using a technique described in [42], for the open cochlea condition. Such antiresonances, also referred to as the 'mid-frequency notches', were also observed by other authors in the displacement responses to acoustic stimulus measured in an unsealed cochlea [10, 18].

A second series of experiments was carried out by Gummer *et al.* [40] to measure the two-dimensional motion of the TM. The velocity and displacement of the acoustically driven TM vibrations were measured in the transverse and radial directions, respectively. The amplitude and phase response revealed at least two DOF of the TM vibration as can be seen in Fig.4.12 A. However, only a single DOF was said to be observed in the BM vibration in this experiment[5].

The trajectories plotted in Fig.4.12 A show that the dominating radial component is almost parallel to the RL, and assumed by Gummer *et al.* to correspond to the radial (translational) motion of the TM for frequencies from 360 to 670 Hz [40]. Additionally, the peak observed at about 500 Hz coincides with the antiresonance in the transversal component, about 0.4 octave below the best frequency for this experiment, which was reported to be about 735 Hz [40]. Similarly, the second peak in the radial component's response curve was observed together with a shallow antiresonance of the transverse component at the frequency of 908 Hz. The observed mid-frequency notches, as well as any additional resonance peaks and antiresonances in the above results, are probably the effect of the unsealed cochlea condition [43]. Finally, it was reported that the recording angle influenced the depth of the antiresonances in such a way that an anticlockwise, 30° rotation of the preparation gives a shallower antiresonance of the velocity response in the transverse direction together with an increased accumulation of phase in the corresponding phase response [40]. This is shown by the dotted lines in Fig.4.12.

[5]The BM vibration was reported to be orthogonal to the BM [40], hence we assume it was the transverse vibration that was measured in this series of experiments. However, the data of the BM vibrations recording were not illustrated, nor were the results discussed in the paper.

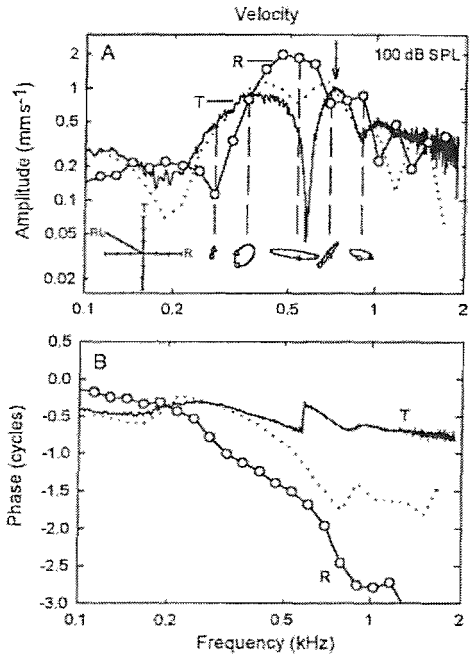

Figure 4.12: The amplitude and phase of the transverse (T) and radial (R, ○) motion of the tectorial membrane measured by Gummer *et al.* [40] for acoustic excitation. The arrow indicates the best frequency, equal to 735 Hz, and the inset in subfigure A shows the trajectories calculated from the amplitudes and phases of both components. Dotted lines indicate the TM transverse response if the preparation was rotated 30° counterclockwise. Reprinted from Fig.3 in Gummer, A. W., Hemmert, W. and Zenner, H.-P. (**1996**) "Resonant tectorial membrane motion in the inner ear: Its crucial role in frequency tuning," Proceedings of the National Academy of Sciences of the U.S.A., **93**, 8727-8732, with permission from the publisher. Copyright (1996) National Academy of Sciences, U.S.A.

4.4.2 Experiment of Hemmert *et al.* [43]

Hemmert *et al.* used the same experimental set-up as in [40], however, the measurement system could be rotated by 90 degrees to allow recordings in the third, longitudinal direction (orthogonal to radial and transversal directions in Fig.4.10). The temporal bone preparations of the guinea pig cochlea were used for the measurements. The cochlea was opened at a distance of 2.3 mm from the apex of the cochlea and the vibrations were recorded after delivering a sound stimulus to the ear canal [43]. The responses were corrected for the sound pressure measured near to the eardrum and given relative to 60 dB SPL, and polystyrene microspheres were placed on the TM and BM because of the low contrast of these structures. Finally, contrary to the measurements of Gummer *et al.* that contained unsealed cochlea condition artefacts, the recordings in [43] were corrected off-line, using a procedure described in [42], to account for the opening in the apex of the cochlea. This was done to remove a so-called fast-wave component from the recordings, so that the characteristics of the response refer only to the slow-wave component, which corresponds to the travelling wave response of the CP [18, 43].

Hemmert *et al.* measured the vibrations on microspheres, which were attached to either: the Claudius cell on the surface of the BM, the Hensen cell located close to the OHC and another Hensen cell (to examine differences in recordings from different animals), and the top of the TM [43]. However, we will consider only the results of measurements on the BM and TM, as relevant to the models investigated in Sections 3.4 and 3.6.

Figure 4.13 depicts the velocity amplitude and phase of the BM measured in three orthogonal directions, longitudinal (full squares), radial (full circles) and transversal (open symbols). Note that the transversal component was measured three times during the whole recording session, i.e. once at the beginning of the measurement (inverted triangles) and twice at the end, after all three orthogonal components were measured. This was done to document the preparation's 'stability', where the final control measurements of the transversal component were carried out using a multitone signal (diamonds) and band-limited white noise (triangles). After the first measurement of the BM transversal component (inverted

triangles in the figure; using LDV and band-limited white noise), the longitudinal (full squares; PD and multitone signal), radial (full circles; PD rotated by 90° and multitone signal) and two control transverse (1. diamonds; LDV and multitone signal, 2. triangles; LDV and band-limited white noise) components were measured after 5, 7, 12 and 14 mins, respectively [43].

The phase responses were plotted against the linear frequency range, to emphasise pure delays as straight lines in the response [43]. The magnitudes of all velocity components shown in Fig.4.13 A, reveal a single resonance peak. The transversal and radial components were reported to be tuned to about 590 Hz (indicated by the arrow in the figure), and the longitudinal component to about 700 Hz (arrowhead in the figure)[6], where the frequency of 590 Hz was estimated as the one from which the response began to decay rapidly [43]. 590 Hz is referred to as the characteristic frequency (CF), and Hemmert *et al.* reserved the term 'CF' for the transversal component[7]. There is no significant difference between the three transversal magnitude curves. However, a difference of about 15 dB can be noticed between the magnitude of the radial and transversal components, and the magnitude of the longitudinal component is about 6 dB lower than that of the transversal component, for frequencies below the CF [43]. The trajectory of the motion, which was reconstructed from the amplitude and phase data of the BM vibration in three directions, is presented in Fig.4.14.

Elliptical projections of the motion in the radial-transversal plane are almost rectilinear with the major axis of about 80°. The projections in the longitudinal-transversal plane (Fig.4.14 B) were more opened, with the axis of 116° for all frequencies [43]. Because, the BM was inclined at −6° to the radial axis and at

[6]Hemmert *et al.* state that the distance of 2.3 mm from the apex corresponds to the cochlear location of 16 mm according to von Békésy [8], so that the length of the guinea pig cochlea is equal to L=18.3 mm and not 18.5 mm as given in [39]. Thus, the CF at 2.3 mm from the apex is equal to $350(10^{2.1x/L}-0.85)\approx345$ Hz [39], which is not significantly different from the CF calculated for L=18.5 mm, ≈340 Hz, especially at the apical side of the cochlea where the tuning is broader compared to that in the basal region. However, it is still significantly smaller than the maximum of the transversal velocity component, i.e. 590 Hz measured in [43].

[7]Note that the travelling wave is a longitudinally propagating transverse displacement of the CP, and thus corresponds to the measured transversal velocity component at a fixed position along the cochlea.

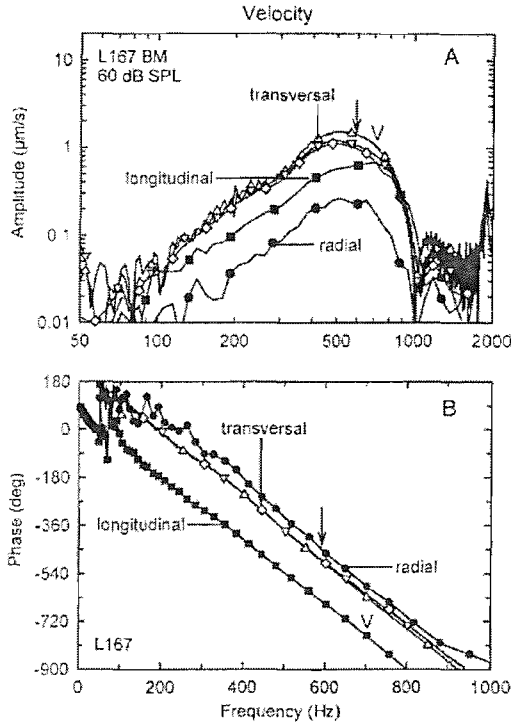

Figure 4.13: Amplitude (A) and phase (B) of the transversal (inverted triangles, diamonds, triangles), radial (full circles) and longitudinal (full squares) components of the basilar membrane velocity, measured by Hemmert *et al.* [43]. Additional transversal component's magnitude curves (diamonds and triangles), were plotted to document the 'stability' of the preparation (L167). Note that the phase was plotted against a linear frequency range, to emphasise pure delays by straight lines. The arrows indicate the assumed characteristic frequency of the transversal and radial component, ≈590 Hz, and the arrowhead the frequency of the maximum of the longitudinal component ≈700 Hz. Reprinted from Fig.3 in Hemmert, W., Zenner, H.-P. and Gummer, A. W. (**2000**) "Three-dimensional motion of the organ of Corti," Biophysical Journal, **78**, 2285-2297, with permission from the publisher. Copyright (2000) Biophysical Society.

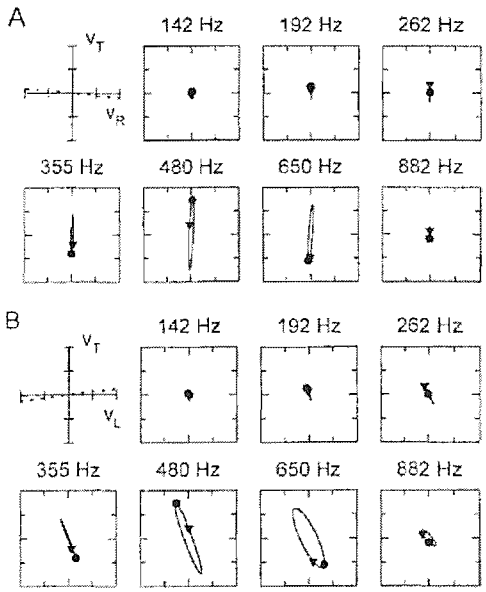

Figure 4.14: Trajectories of the basilar membrane motion in the radial-transversal (A) and longitudinal-transversal plane (B) for different stimulus frequencies, reconstructed from the velocity's amplitude and phase data in Fig.4.13 [43]. The symbols on the ellipses denote t=0 (circles) and t=$T/4$ (triangles), which were used to determine the direction of motion. The dotted lines on the coordinate systems show the inclination of the basilar membrane with respect to the radial (A, $-6°$) and longitudinal (B, $8°$) axis. Reprinted from Fig.4 in Hemmert, W., Zenner, H.-P. and Gummer, A. W. (**2000**) "Three-dimensional motion of the organ of Corti," Biophysical Journal, **78**, 2285-2297, with permission from the publisher. Copyright (2000) Biophysical Society.

8° to the longitudinal axis in this preparation, the motion was almost orthogonal to these axes, which implies that the motion was orthogonal to the BM surface for all frequencies [43].

The transverse and radial component of the TM vibration, measured at the same position in the cochlea but in a different preparation, is shown in Fig.4.15. The transverse component was measured three times, where the second (control, multitone) and third (control, band-limited white noise) measurement was done after the measurement of the radial component. The transversal component was measured first using the LDV and band-limited white noise (triangles), then, after 13 min, the radial component (PD, multitone; full circles), and finally, after 15 min and 16 min, the control transverse components (LDV; diamonds, inverted triangles) [43].

It can be seen from Fig.4.15 A, that the amplitude of control measurements of the transversal component (diamonds, inverted triangles) decreased over the entire frequency range by about 7.6 dB relative to the first measurement, although the phase is relatively unchanged. Hemmert *et al.* report that the transverse vibration was tuned to 650 Hz, whereas the maximum of the radial component was observed at 550 Hz. For frequencies well below the CF, the relative phase between the radial and transversal components was small. About half an octave below the characteristic frequency of the transversal component (≈490 Hz), however, the relative phase began to increase reaching 60° around the CF, 608 Hz. Thus, the motion trajectories, reconstructed from the TM's velocity magnitude and phase data, change from being almost rectilinear well below the CF, to become nearly circular in the vicinity of the CF as shown in Fig.4.16. Therefore, there is a component of motion at higher frequencies, almost parallel to the RL (ellipses' major axis to the radial axis ranged between 60 and 70° for 200-700 Hz, where the RL was inclined about 145° with regard to the radial axis). This mode of vibration is assumed to appear for frequencies from above half an octave below the CF [43].

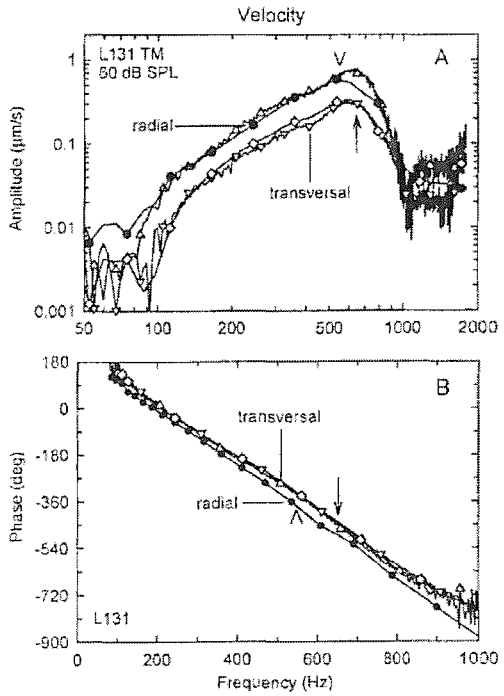

Figure 4.15: Amplitude (A) and phase (B) of the transversal (triangles, diamonds, inverted triangles) and radial (full circles) components of the tectorial membrane velocity, measured by Hemmert *et al.* [43]. Additional transversal component's magnitude curves (diamonds and inverted triangles) were measured after 15 and 16 minutes to document the 'stability' of the preparation (L131). Likewise in Fig.4.13 the phase was plotted against a linear frequency range, to emphasise pure delays by straight lines. The arrows indicate the assumed characteristic frequency of the transverse component, ≈650 Hz, and the arrowheads indicate the frequency of the maximum of the radial component, ≈550 Hz. Reprinted from Fig.9 in Hemmert, W., Zenner, H.-P. and Gummer, A. W. (**2000**) "Three-dimensional motion of the organ of Corti," Biophysical Journal, **78**, 2285-2297, with permission from the publisher. Copyright (2000) Biophysical Society.

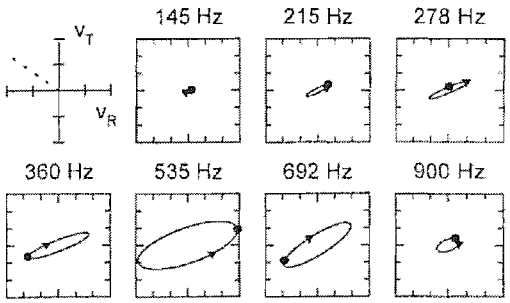

Figure 4.16: Trajectories of the tectorial membrane motion in the radial-transversal plane for different stimulus frequencies, reconstructed from the velocity's amplitude and phase data in Fig.4.15 [43]. The symbols on the ellipses, used to determine the direction of motion, denote t=0 (circles) and t=$T/4$ (triangles). The dotted line on the coordinate system shows the inclination of the reticular lamina, 145°, the basilar membrane was almost horizontal in this preparation. Reprinted from Fig.10 in Hemmert, W., Zenner, H.-P. and Gummer, A. W. (**2000**) "Three-dimensional motion of the organ of Corti," Biophysical Journal, **78**, 2285-2297, with permission from the publisher. Copyright (2000) Biophysical Society.

Comparison with the models

Although, the results obtained by Gummer *et al.* appear to be contaminated by the artefacts due to the unsealed cochlea condition [18], the same authors state in their later article [43] that the main conclusion of their experiment remains the same, i.e. a second vibrational degree of freedom can be observed in the TM's motion, and that this result is consistent with that obtained in [43]. Hemmert *et al.* conclude that the organ of Corti is vibrating as a rigid body, whose motion is driven by the BM, at least up to the CF [43]. Furthermore, the rigid organ of Corti rotates about the point near the spiral limbus in the way shown in Fig.2.10.

However, a somewhat different observation was made by Reuter and Zenner in 1990 [84], who excited the organ of Corti of pigmented guinea pigs with an electrical field and reported that active forces from OHC induced a transverse motion of the RL, but also a radial displacement of the cuticular plates of the OHC. Additionally, Reuter and Zenner found that the coupling between the OHC and IHC is weak due to compliance in the RL region [84]. Rigid body motion of the organ of Corti also contradicts the results of Fridberger and de Monvel [31], who observed different points of rotation for the RL (point close to the IHC or on the prolongation line of the RL's long axis) and for the BM (feet of the inner pillar cells or under the fibres contacting the IHC) after the sound stimulation of the guinea pig cochlear explants. The results of Reuter and Zenner and Fridberger and de Monvel reveal an internal shearing within the organ of Corti, in opposition to the rigid body motion observed by Hemmert *et al.*

Despite the open cochlea condition artefacts and inconsistency with results of other experiments, the BM and TM vibration measurements of Gummer *et al.* [40], and Hemmert *et al.* [43], seem to be suitable for comparison of the BM and TM vibrations examined for the models of Neely and Kim [68] (Section 3.4) and Neely [66] (Section 3.6).

In the first instance, it has to be emphasised that the experiments of Gummer *et al.* and Hemmert *et al.* were carried out on the guinea pig cochlea, whereas the model of Neely and Kim and the model of Neely simulate the mechanics of a cat cochlea. Thus the comparison will be mainly qualitative, indicating the main features of the observed frequency responses. Also the measurements were taken

close to the apex of the cochlea, whereas the predictions were calculated for a position some way along the cochlea.

The calculated responses of the Neely and Kim model and the Neely model are relevant only to the responses obtained for the acoustic stimulation paradigms in the experiments of Gummer *et al.* shown in Figs.4.11 A, B and 4.12 [40]. Although some active component of the OHC activity is presumably still present in the preparations, since they respond to electrical stimulation, the lack of a sharp peak in the responses suggests that measurements would be best compared with the passive cochlea simulations.

To begin with, we compare the experimental results of Gummer *et al.* in the transverse direction with the BM and TM velocity responses derived for the passive model of Neely and Kim [68], shown in Fig.4.5 (a, c), and the passive model of Neely [66], shown in Fig.4.9.

The BM and TM velocity calculated from the models differs significantly from the acoustically stimulated responses measured by Gummer *et al.*, shown in Fig.4.11 A, since the responses fall off rapidly after the main peak. No additional peaks and notches were observed in the modelled response, which supports the idea that those in the measured responses are due to the artefact of the unsealed cochlea preparation.

The phase curves of the modelled BM and TM velocity shown in Fig.4.5(c) are nearly equal at low frequencies, as are the phase responses measured by Gummer *et al.* shown in Fig.4.11 B. For frequencies higher than the TM resonance in the passive Neely and Kim model, the phase of the modelled TM velocity becomes lower than the phase of the modelled BM velocity, which can also be seen in the measured phase responses to sound stimulation above the estimated TM resonance frequency as shown in Fig.4.11 C. The phase response of the Neely model, Fig.4.9, does not show this phase difference.

The modelled responses of both the passive model of Neely and Kim and that of Neely are in better qualitative agreement with the result obtained by Hemmert *et al.* [43], in Figs.4.13 and 4.15, because the measured responses were corrected for the open cochlea condition.

The velocity of the TM calculated for the Neely and Kim model seems to

be more sharply tuned than that of the BM as can be seen in Fig.4.5(a), which can be also seen for the transversal components of the BM and the TM measured response in Fig.4.13 A and 4.15 A. The amplitude of the TM's velocity transversal component shown in Fig.4.15 A appears to be slightly smaller than the amplitude of the BM one in Fig.4.13 A (although these measurements were not made on the same preparation), which is comparable with the modelled responses shown in Fig.4.5(a) for all frequencies except the region of the TM's response maximum.

It appears from Figs.4.13 B and 4.15 B, that the BM and TM phase responses measured by Hemmert *et al.*, are almost equal in the low frequency region up to between 400-500 Hz beyond which the TM phase lag is smaller than the phase lag of the BM until the high frequency limit. Figure 4.5(c) shows also a relative phase difference from about 400 Hz to the upper frequency limit, but in the modelled case the TM phase lag is larger than that of the BM phase response.

The BM and TM velocity calculated for the Neely model, shown in Fig.4.9(a), are broadly tuned and the frequencies of the maxima in these curves are equal. The phase of the BM and the TM velocity of the Neely model shown in Fig.4.9(b) are also almost equal for all stimulus frequencies.

From this limited comparison it would appear that the Neely and Kim [68] model more accurately predicts the measured results than that of Neely [66]. The comparison does, however, highlight the difficulties of defining the conditions under which the measurements are made, to ensure that the modelled conditions are similar.

4.5 Discussion

In this chapter the coupled responses of Neely and Kim's [68] and Neely's [66] models were examined. The coupled TM velocity was calculated using the BM velocity responses and the ratio of mobilities derived for both models in Chapter 3. The coupled velocity of the BM and TM was compared with the velocity responses of these structures measured by Gummer *et al.* [40] and Hemmert *et al.* [43].

The pressure difference and the BM velocity of the Neely and Kim model and

the model of Neely, exhibit a sharply tuned peak at the characteristic place or CF when the model is active. The tuning of the passive models is broad and the maximum of the passive responses is shifted towards basal positions along the cochlea or lower frequencies with respect to the maxima of the active models. Also the phase lag accumulation for the active models is faster than that observed for the passive models above the characteristic place and CF.

It was shown that the tuning of the active Neely model is sharper than that of the active Neely and Kim model. This coincides with a steeper phase responses in the Neely model with regard to the phase responses of the Neely and Kim model. Also the phase of the active Neely and Kim model exhibits a phase lead in the vicinity of the characteristic place or CF which coincides with a notch in the active BM velocity below the peak. This was not observed in the Neely model due to the fact that the damped resonances in the passive mobility of the TM and BM of the Neely model (Fig.3.24(b)) occur at almost the same stimulus frequency, whereas the maxima of the passive mobility of the TM and BM of the Neely and Kim model (Fig.3.14(b)) are well separated and must produce a local notch when the coupled response is calculated.

Comparison of the BM and TM coupled velocities reveals that both responses are broadly tuned and comparable in magnitude in the whole frequency range in the passive Neely model. The amplitude maxima of the BM and TM velocity nearly coincide with each other. This is in contrast to the BM and TM velocity responses observed for the passive Neely and Kim model in which the BM magnitude has no distinctive peak but a broadly tuned peak can be observed in the TM velocity. The maximum of the BM velocity is at higher frequency then the maximum of the TM velocity in the passive Neely and Kim model. There is no observable difference in the passive phase responses of the Neely model. However, the phase of the TM velocity lags that of the BM velocity for frequencies higher than the frequency of the magnitude peak of the TM velocity for both the passive and active model of Neely and Kim.

The agreement of the passive coupled BM and TM velocity responses with the results of Gummer *et al.* [40] is poor since their measurements were contaminated by the unsealed cochlea artefact. However, the calculated BM and TM velocities

are in good qualitative agreement with the velocities of these structures measured by Hemmert *et al.* [43]. It was shown that the Neely and Kim model predicts the results obtained by Hemmert *et al.* more accurately than the model of Neely. However, the accuracy of such a comparison depends on compatibility of the model's and measurement's conditions.

Chapter 5

Stability and nonlinearity in lumped micromechanical models

Classical models of cochlear micromechanics often represent the active mechanism using a form of control system operating within the cochlea [32, 34, 65, 68] as first suggested in 1948 by Gold [37]. An important feature of a feedback controller is its stability [69], which is considered here for various isolated micromechanical models.

The response of the cochlea is also known to possess nonlinear properties (as discussed in Section 2.3). Although it is difficult to reproduce all nonlinear phenomena in one comprehensive model, these phenomena have to be taken into account in any model to give a complete picture of cochlear function [1, 68]. The quasi-linear model of Kanis and de Boer [47] provides a simple method of accounting for the compressive nonlinearity of the micromechanics and is extended in this chapter to include the model of Neely and Kim [68], for consistency with the work above.

5.1 Stability in the model of Neely and Kim

In the model of Neely and Kim [68], active processes (the cochlear amplifier) responsible for the sharp tuning and high sensitivity of the cochlea are represented by an additional pressure source. After being stimulated by the deflections of the

OHCs cilia, the active pressure source pumps energy locally into the system, i.e. undamps the BM vibrations by adding negative damping to the partition's impedance close to (just basal to) the characteristic place [68]. Neely and Kim assume a frequency-dependent phase shift between the active pressure P_a and the velocity of the OHCs stereocilia, $\dot{\xi}_c$ [68], which is represented by the impedance Z_4 in Eq.3.3.6. The displacement ξ_c, and hence the velocity $\dot{\xi}_c$, of the OHC stereocilia is a consequence of shearing between the TM and the BM, driven by the acoustic pressure P_d. In other words the cilia velocity $\dot{\xi}_c$ is the output of the passive two DOF system subject to an input of cochlear pressure difference P_d. Thus, the active force, P_a, which is also dependent on the output $\dot{\xi}_c$ and 'fed back' to the system with a phase shift of Z_4, will close a loop of the active two DOF system. This can be represented by a classical feedback diagram as shown in Fig.5.1, in which G is the passive response from the cochlear pressure difference to cilia velocity, and H is the feedback path corresponding to the impedance Z_4 in the Neely and Kim model [68]. It should be noted that the proposed diagram represents a system with a negative feedback loop, since the active pressure has the opposite direction to that of the pressure difference P_d.

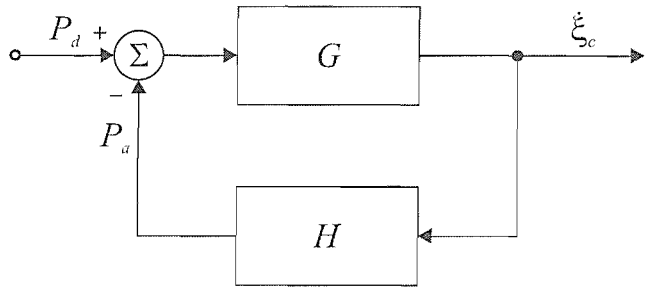

Figure 5.1: Block diagram of the feedback loop representing the active component in the model of Neely and Kim [68]. The acoustic pressure difference excitation, P_d, is the input and the stereocilia velocity $\dot{\xi}_c$ the output of the feedback loop. G and H denote the plant and the controller, respectively, which can be derived from the equations of motion for the two degree of freedom micromechanical model in Fig.3.6.

Figure 5.2 depicts the block diagram of the two DOF system proposed by Neely and Kim with indication of the feedback loop acting between the BM and

TM. In the figure the shear velocity between the RL and TM, $\dot{\xi}_c$, is 'sensed' and delivered to the input of the impedance Z_4 which feeds back the active pressure to the system. Thus, the active pressure P_a is controlled and shifted in phase with regard to the radial shearing velocity $\dot{\xi}_c$ by the impedance Z_4, and either counteracts or reinforces the transverse pressure difference P_d.

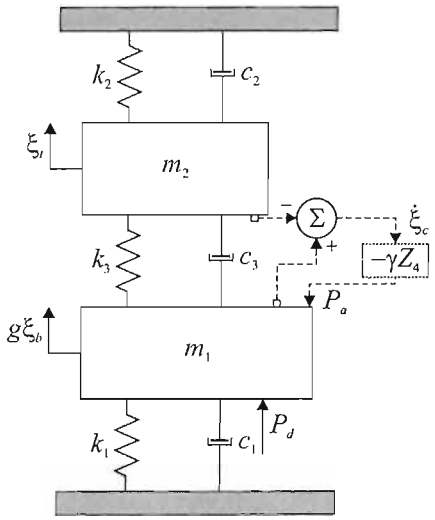

Figure 5.2: Lumped component system proposed by Neely and Kim [68] with indication of the feedback loop. The element $-\gamma Z_4$ accounts for the phase shift between the active pressure P_a and output velocity $\dot{\xi}_c$, where γ represents the control of the model in a 'global' sense corresponding to the condition of the cochlea [68].

To derive the expressions for the plant G and the controller H of the feedback loop in Fig.5.1 we use the equations of motion, Eqs.3.3.4 and 3.3.5, for the two DOF micromechanical system proposed by Neely and Kim in Fig.3.6 [68]. Since the shear velocity $\dot{\xi}_c(x)$ is the output of the control loop we differentiate Eq.3.3.3 with respect to time, so that

$$\dot{\xi}_c(x) = g(x)\dot{\xi}_b(x) - \dot{\xi}_t(x), \tag{5.1.1}$$

hence[1]

$$g(x)\dot{\xi}_b(x) = \dot{\xi}_c(x) + \dot{\xi}_t(x), \tag{5.1.2}$$

From the equation of motion for the second degree of freedom, Eq.3.3.5, we know that

$$\dot{\xi}_t(x) = \frac{Z_3}{Z_2}\dot{\xi}_c(x), \tag{5.1.3}$$

which after substituting to Eq.5.1.2 gives

$$g(x)\dot{\xi}_b(x) = \left(1 + \frac{Z_3}{Z_2}\right)\dot{\xi}_c(x) = \frac{Z_2 + Z_3}{Z_2}\dot{\xi}_c(x), \tag{5.1.4}$$

Substituting the above equation and the expression for the active pressure P_a in Eq.3.3.6 to the equation for the first degree of freedom of the system (Eq.3.3.4), gives

$$P_d(x) - (-\gamma Z_4)\dot{\xi}_c(x) = \frac{Z_1(Z_2 + Z_3)}{Z_2}\dot{\xi}_c(x) + Z_3\dot{\xi}_c(x), \tag{5.1.5}$$

or equivalently

$$P_d(x) - (-\gamma Z_4)\dot{\xi}_c(x) = \frac{Z_1(Z_2 + Z_3) + Z_2Z_3}{Z_2}\dot{\xi}_c(x). \tag{5.1.6}$$

Dividing Eq.5.1.6 by the fraction on the right-hand side gives

$$\underbrace{\frac{Z_2}{Z_1(Z_2 + Z_3) + Z_2Z_3}}_{G} P_d(x) - \underbrace{\frac{Z_2}{Z_1(Z_2 + Z_3) + Z_2Z_3}}_{G}\underbrace{(-\gamma Z_4)}_{H}\dot{\xi}_c(x) = \dot{\xi}_c(x), \tag{5.1.7}$$

where G denotes the plant and H the controller of the feedback loop. Thus,

$$GP_d(x) - GH\dot{\xi}_c(x) = \dot{\xi}_c(x), \tag{5.1.8}$$

therefore

$$\dot{\xi}_c(x) = \frac{G}{1 + GH}P_d(x), \tag{5.1.9}$$

[1]For clarity, we only write explicitly the dependence of variables on x although, apart from the lever gain g, they also depend on the stimulus frequency ω.

which appears in the form of a classical negative feedback system [19], where G and H are functions of ω and x, and are formulated in Eq.5.1.7.

We will examine the stability using the *Nyquist stability criterion*, i.e. by plotting the polar plot of the open loop response $G(j\omega)H(j\omega)$, only for single isolated systems. In general, since both G and H are functions of x, the stability of each closed feedback loop representing particular place along the cochlea has to be tested separately to give reliable mobility responses as those calculated in Chapter 3[2].

The closed loop under investigation is a negative feedback system, and it can be seen that it becomes unstable when the denominator on the right-hand side of Eq.5.1.9 is equal to zero, that is when $G(j\omega)H(j\omega)$ is equal to -1. In terms of the Nyquist stability criterion, the denominator of the transfer function in Eq.5.1.9 reaches its root when the Nyquist plot of the open loop response encircles the point $(-1,0)$ in the complex plane [69]. The Nyquist plots are plotted at three chosen positions along the cochlea and for frequencies, ω, ranging from $-10^9\,\mathrm{rad\,s^{-1}}$ to $10^9\,\mathrm{rad\,s^{-1}}$. Furthermore, since the controller's gain depends on the active gain γ, the Nyquist plots at each chosen position, have been calculated for four values of gain, i.e. γ=1, 1.1, 1.2 and 1.3.

The Nyquist plots shown in Fig.5.3 reveal that the negative feedback systems in the Neely and Kim model [68], are conditionally stable, that is, the systems are only stable below some gain limit, specific to each position along the cochlea. It can be noted that the gain limit increases with the distance from the stapes, i.e. the Nyquist plot evaluated at 0.0135 m, 0.0185 m and 0.0235 m almost enclose the $(-1,0)$ point for the gain of 1.11, 1.21 and 1.49, respectively. Furthermore, the Nyquist plots evaluated at the cochlear sites and for corresponding gain limits given above, cross the real axis, i.e. $Im\{G(j\omega)H(j\omega)\}$=0, at frequencies of about 3.26 kHz, 1.11 kHz and 374 Hz, going from the base towards the apex of the cochlea. Thus, the frequency responses of the Neely and Kim model [68], calculated at these positions and their corresponding gains, will reach their maximum. The cochlear amplifier thus operates closer to instability near the base than the apex

[2]All models considered earlier in the thesis were checked as stable, apart from the modified model of Neely solved for γ=1 as shown in Fig.3.27.

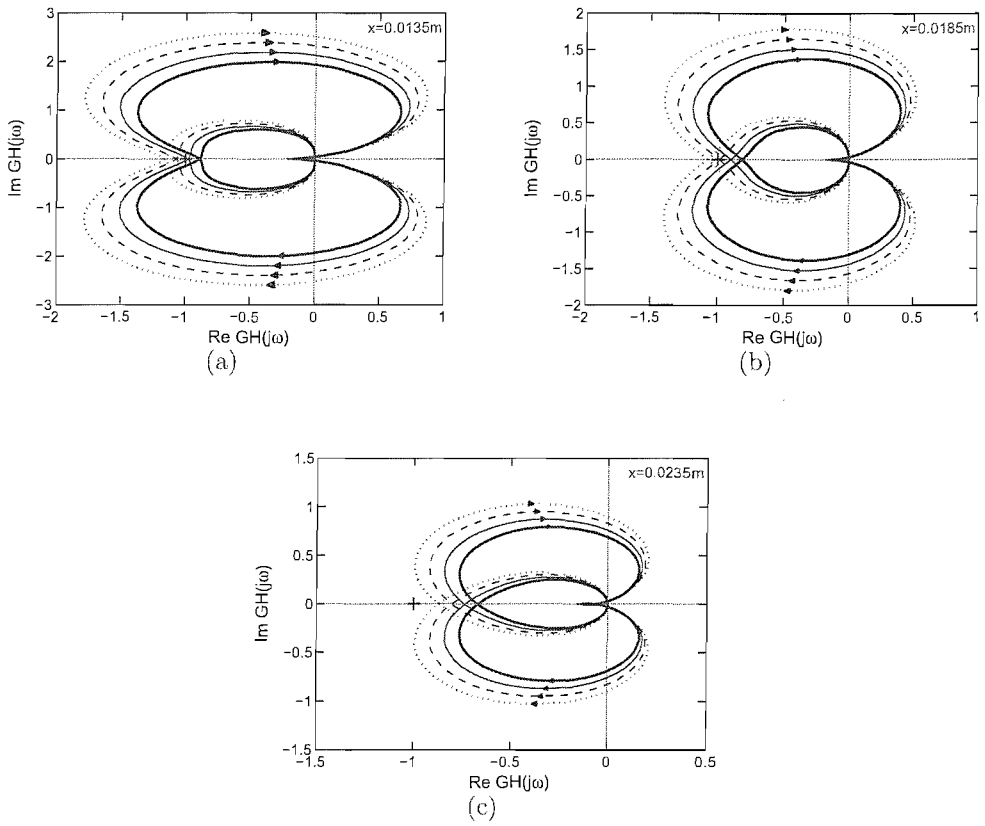

Figure 5.3: Nyquist plots of the isolated feedback loops calculated at x=0.0135 (more basal site; a), 0.0185 (characteristic place for 1 kHz stimulus frequency; b) and 0.0235 m (apical site; c), derived for the Neely and Kim model [68]. The active gain, γ, was set to 1 (fully active; bold solid), 1.1 (feint solid), 1.2 (dashed) and 1.3 (dotted). The cross indicates the (−1,0) point of singularity and the arrows the direction of the increasing positive and negative frequency.

for a fully active, γ=1, Neely and Kim model, hence the enhancement of the model's response is highest at the base of the cochlea or for high stimulus frequencies. Such behaviour of the model is consistent with the cochlear responses measured experimentally, where the highest sensitivity of the cochlea is observed in its basal regions or for high CFs [87].

The existence of spontaneous oscillations in the inner ear, known as spontaneous otoacoustic emissions, accompanied by the corresponding BM vibrations [87], suggests that the cochlea is not always stable. It has to be noted that in reality the response of a healthy cochlea was found to be profoundly nonlinear in the basal (high CF) regions (see Section 2.3), so that the amplitude of any instability would not continue to grow exponentially, as it would in a linear system, but would be limited to a low amplitude.

5.2 Stability in the model of Neely

In this section the feedback loop for the model of Neely [66] is first defined, followed by the derivation of the corresponding equations defining the loop's components. Finally, the Nyquist plots calculated for the parameters selected by Neely, as shown in Table 3.2, are examined.

The major difference between the two models discussed here is that the activity in the model of Neely [66] is represented by an active displacement due to the contraction of the OHC and not the active pressure as in the Neely and Kim model [68]. The contraction of the hair cell body is triggered by the shearing displacement of the cilia ξ_0, therefore the output of the feedback loop in this model is the shearing velocity $\dot{\xi}_0$. This velocity controls the somatic motility, where we assume that the positive direction of the cilia motion, towards the tallest cilia of the bundle, produces the contraction of the OHC body and thus the active displacement ξ_c subtracts from the displacement of the BM, ξ_b.

We use the equations of motion as derived in Section 3.5 to formulate the transfer function of the closed loop response in the model of Neely [66]. From

Eq.3.5.3, we know that

$$\dot{\xi}_b = \frac{\dot{\xi}_r}{g} + \dot{\xi}_c, \tag{5.2.1}$$

however,

$$\xi_r = \dot{\xi}_0 + \dot{\xi}_t, \tag{5.2.2}$$

according to Eq.3.5.2, and hence, knowing that

$$\dot{\xi}_t = \frac{Z_0}{Z_t}\dot{\xi}_0, \tag{5.2.3}$$

from Eq.3.5.16 for the second degree of freedom, substituting to Eq.5.2.1 gives

$$\dot{\xi}_b = \frac{1}{g}\left(1 + \frac{Z_0}{Z_t}\right)\dot{\xi}_0 + \dot{\xi}_c = \frac{Z_t + Z_0}{gZ_t}\dot{\xi}_0 + \dot{\xi}_c. \tag{5.2.4}$$

From the relationship between the active displacement ξ_c and the shearing displacement of the cilia ξ_0 in Eq.3.5.1 we can write

$$\dot{\xi}_c = H_c\dot{\xi}_0, \tag{5.2.5}$$

so that

$$\dot{\xi}_b = \frac{Z_t + Z_0}{gZ_t}\dot{\xi}_0 + H_c\dot{\xi}_0. \tag{5.2.6}$$

Substituting the above equation to the equation of motion for the first degree of freedom of the system in Fig.3.16 (Eq.3.5.13), gives

$$P_f = Z_b\left(\frac{Z_t + Z_0}{gZ_t}\dot{\xi}_0 + H_c\dot{\xi}_0\right) + gZ_0\dot{\xi}_0, \tag{5.2.7}$$

and

$$P_f - Z_bH_c\dot{\xi}_0 = \frac{Z_b(Z_t + Z_0)}{gZ_t}\dot{\xi}_0 + gZ_0\dot{\xi}_0, \tag{5.2.8}$$

thus

$$P_f - Z_bH_c\dot{\xi}_0 = \frac{Z_b(Z_t + Z_0) + g^2Z_tZ_0}{gZ_t}\dot{\xi}_0. \tag{5.2.9}$$

It can be seen that the second term on the left-hand side of Eq.5.2.9, can be treated as the controller gain of the negative feedback loop, i.e. $Z_b H_c$ controlled by the output shear velocity $\dot{\xi}_0$. However, to eradicate the cascade of the Z_b and H_c components we divide both sides by Z_b, therefore

$$\frac{P_f}{Z_b} - H_c\dot{\xi}_0 = \frac{Z_b(Z_t + Z_0) + g^2 Z_t Z_0}{g Z_b Z_t}\,\dot{\xi}_0, \tag{5.2.10}$$

and

$$\underbrace{\frac{g Z_b Z_t}{Z_b(Z_t + Z_0) + g^2 Z_t Z_0}}_{G}\frac{P_f}{Z_b} - \underbrace{\frac{g Z_b Z_t}{Z_b(Z_t + Z_0) + g^2 Z_t Z_0}}_{G}\underbrace{H_c}_{H}\dot{\xi}_0 = \dot{\xi}_0, \tag{5.2.11}$$

so that we arrive to the expression for the negative feedback formulated by

$$\dot{\xi}_0(x) = \frac{1}{Z_b}\frac{G}{1 + GH}P_f(x). \tag{5.2.12}$$

We have chosen to write the system's closed loop response in a form presented above, to emphasise that the active displacement, ξ_c, contributes to the amount of the BM displacement ξ_b in the model of Neely [66], and an additional component of Z_b^{-1} is present between the loop and the pressure difference input, P_f. This is shown schematically in a block diagram in Fig.5.4.

To examine the stability of the feedback loop in Fig.5.4, we calculate the Nyquist plots of the open loop $G(j\omega)H(j\omega)$ at the characteristic place corresponding to the stimulus frequency of 1 kHz, which in the model of Neely is equal to about 0.0189 m. The Nyquist plots have also been plotted for two different positions basally, x=0.0139 m, and apically, x=0.0239 m, from the characteristic place. In all cases the open loop responses were calculated for three different values of the gain γ, i.e. γ=1, 1.4 and 1.8 and the frequency, ω, from $-10^{-9}\,\mathrm{rad\,s^{-1}}$ to $10^{-9}\,\mathrm{rad\,s^{-1}}$.

The amplitude of the frequency response of the model of Neely [66] is highest at the basal positions in the cochlea and decreases with the increase of the position towards the apex, according to Fig.5.5. The Nyquist contours derived for the negative feedback in the model of Neely are shown after magnification around the point of singularity (−1,0) in Fig.5.6. They are seen to enclose this point for the

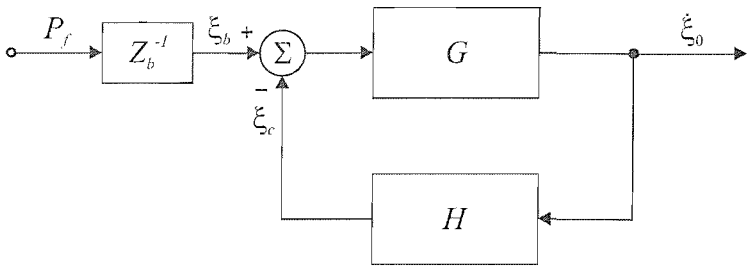

Figure 5.4: Block diagram of the feedback loop representing the active component in the model of Neely [66]. The acoustic pressure difference excitation, P_f, is the input to the Z_b^{-1} block which precedes the feedback loop in this model. The actual input to the loop is the displacement of the basilar membrane, ξ_b, whereas the stereocilia velocity $\dot{\xi}_0$ is the output of the feedback loop. G and H denote the plant and the controller, respectively, which are derived from the equations of motion for the two degree of freedom micromechanical model in Fig.3.16. The output of the control loop is the active displacement ξ_c which appears due to the contraction of the outer hair cell body.

gain of γ=1.4 and 1.8 at 0.0139 m and for γ=1.8 at 0.0189 m, whereas the (−1,0) point is not enclosed for any of the chosen gains at 0.0239 m. Thus, the system is only stable for gains not larger than a place-dependent limit of the feedback gain, so that the system exhibits conditional stability. The gain limit increases with the distance from the base and can be estimated to about 1.37, 1.71 and 3.09 at x=0.0139 m, 0.0189 m and 0.0239 m, respectively. Furthermore, the Nyquist plot crosses the real axis in the vicinity of the (−1,0) point ($Im\{G(j\omega)H(j\omega)\}\approx 0$) at frequency of about 4.21 kHz at x=0.0139 m and γ=1.37, 1.37 kHz at 0.0189 m and γ=1.71 and 410 Hz at 0.0239 m and for γ=3.09. These frequencies therefore specify the frequencies at which the frequency responses of the model of Neely [66] will reach their maximum when evaluated at the sites along the cochlea and corresponding gains given above.

It is interesting to note that the Nyquist plots, and thus the cochlear responses of the model of Neely [66], are much larger than those of the model of Neely and Kim [68] discussed in the previous section. Also, the gain limits estimated for the model of Neely are much higher than the ones estimated for the model of Neely

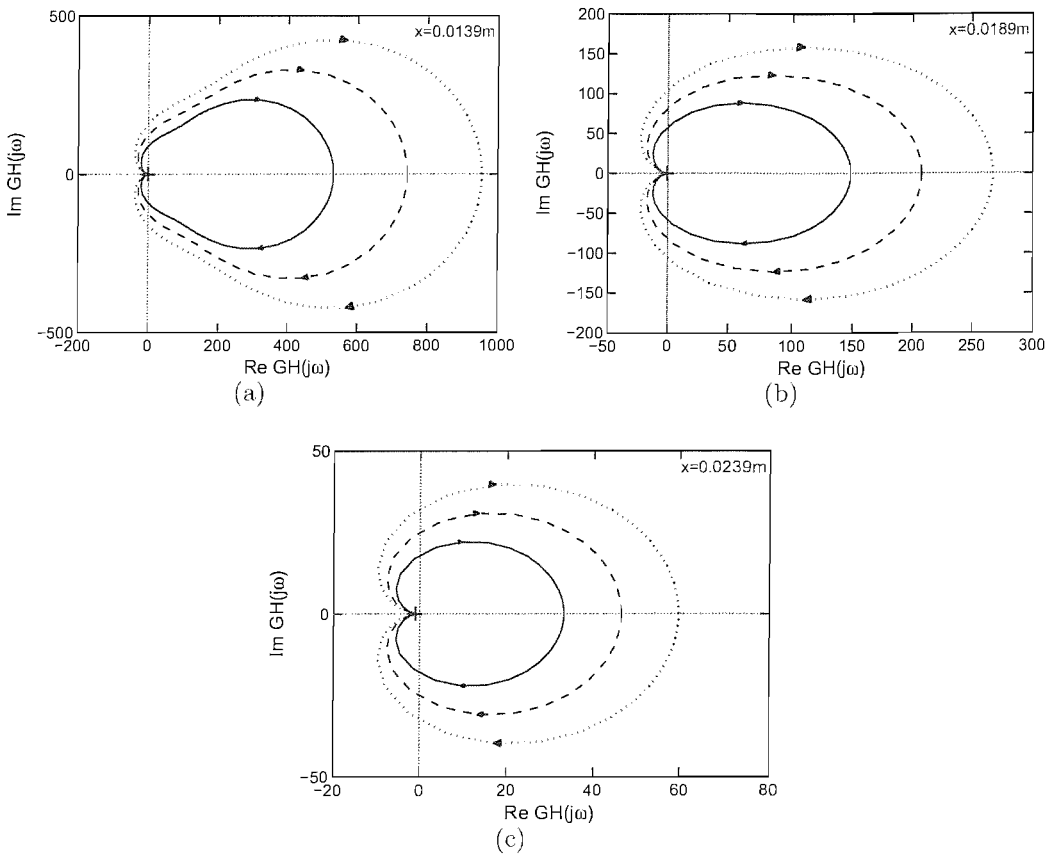

Figure 5.5: Nyquist plots of the isolated feedback loops calculated at x=0.0139 m (basal from the characteristic place; a), 0.0189 m (characteristic place for 1 kHz stimulus frequency; b) and at x=0.0239 m (apical from the characteristic place; c), derived for the model of Neely [66]. The active gain, γ, was set to 1 (fully active; solid), 1.4 (dashed) and 1.8 (dotted). The cross indicates the point of singularity (−1,0) and the arrows the direction of the increasing positive and negative frequency.

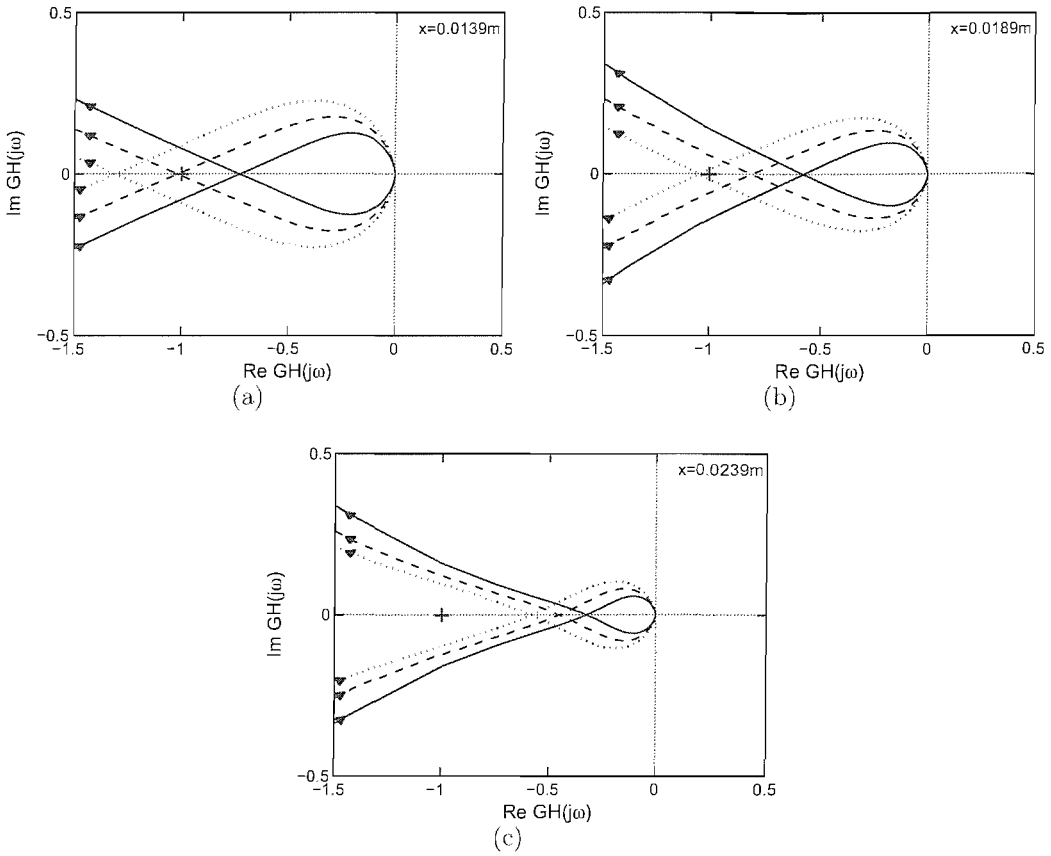

Figure 5.6: Nyquist plots of the isolated feedback loops magnified in the vicinity of the point of singularity (−1,0), calculated for the model of Neely [66] at x=0.0139 (a), 0.0189 (b) and 0.0239 m (c). The active gain, γ, was set to 1 (solid), 1.4 (dashed) and 1.8 (dotted). The cross indicates the point of singularity (−1,0) and the arrows the direction of the increasing positive and negative frequency.

and Kim and so the Neely model is inherently more stable.

5.3 Stability in the model of Kolston

In 1999 Kolston discussed a three-dimensional (3D) model of the organ of Corti [50], based on the *Finite Element* 3D model of the cochlear micromechanics proposed by Kolston and Ashmore in 1996 [49]. The results in this paper led to the argument that an increase in the generation of the OHCs force which was exerted on the BM, leads paradoxically to a decrease of the cochlear amplifier's gain and therefore to a decrease of the BM displacement [50]. This paradoxical behaviour of the BM response may be the effect of the model becoming unstable after the active gain was nearly doubled. We have shown in Sections 5.1 and 5.2 that only a small increase in the active gain, expressed either as an active force/pressure or displacement, is needed for the active feedback loop to become unstable at basal positions in the cochlea. Once a linear system has become unstable its calculated frequency response has no physical meaning since the response never settles to a steady state. Therefore, in this section we will investigate the calculated frequency response of the feedback loop examined for the Neely and Kim model in Section 5.1 for the conditions proposed by Kolston in [50].

Although the model of Kolston [50] is a distributed parameter model, it resembles in many aspects the model of Neely and Kim [68]. The cochlea in the model of Kolston is represented by 10 μm sections in the longitudinal, radial and transverse directions, which discretise the physical equations represented by their finite difference formulations [50]. The length of the modelled organ of Corti was taken as 30 mm, whereas its width and the height as 1 mm and 0.5 mm, respectively. Each cross-section of the model consists of the solid structures of the CP, which were divided into several elements connected by elastic or viscoelastic elements in one or two dimensions and were coupled by the surrounding fluid of density $10^3\,\mathrm{kgm}^3$ [50]. Apart from the BM, TM and the OHC cilia, which were modelled by Neely and Kim in [68], the model of Kolston also takes into account the structures like the RL, OHCs, pillar cells and Deiters' cells. Kolston also assumes rotation of the pillar cells about the spiral lamina, which leads to the

radial motion of the tops of the pillar cells due to the transverse motion of the BM. The radial motion of the pillar cells' apices is determined by the ratio of the cell's height to the cell's width [50], which resembles the lever gain g proposed by Allen [1] - the concept used also by Neely and Kim [24, 68].

The density of all solid structures was equal to $1.3\times10^{3}\,\mathrm{kgm}^{3}$ excluding the TM. To take into account the TM's assumed height of $40\,\mu$m, the density of the TM mass elements was increased four times ($5.2\times10^{3}\,\mathrm{kgm}^{3}$) since the discretisation step was equal to $10\,\mu$m [50]. Thus, knowing that the volume of each element was equal to $10\,\mu\mathrm{m}\times10\,\mu\mathrm{m}\times10\,\mu\mathrm{m}=10^{-15}\,\mathrm{m}^{3}$, the mass of a single element of the TM amounts to $5.2\times10^{-12}\,\mathrm{kg}$ and of all the remaining structures to $1.3\times10^{-12}\,\mathrm{kg}$.

It is interesting to note that the mass of the BM is four times smaller than the mass of the TM in the model of Kolston [50], unlike in the model of Neely and Kim [68] for instance. However, it has to be remembered that for the estimate of the BM mass, Neely and Kim took into account the mass of the structures (and probably the fluids) in the organ of Corti, thus the effective mass of the BM/organ of Corti is higher than the mass of the TM in their model. Assuming the length of the BM in Kolston's model spanned the width of the cochlea, W=1 mm, the membrane would be discretised by 100 elements radially. Thus, the BM mass in a single cochlear slice of $1\,\mathrm{mm}\times10\,\mu$m would be equal to $1.3\times10^{-10}\,\mathrm{kg}$, or specified per slice's unit area of $10^{-8}\,\mathrm{m}^{2}$, it would amount to $0.013\,\mathrm{kgm}^{-2}$. Furthermore, assuming the length of the TM in the model of Kolston is half that of the cochlear width, the model would require 50 elements to model the TM, which implies the mass of the TM would amount to $2.6\times10^{-10}\,\mathrm{kg}$, or $0.026\,\mathrm{kgm}^{2}$. It would appear therefore, that the mass of a single slice of the TM in the model of Kolston [50] is more than five times bigger than the TM mass in the model of Neely and Kim [68] (almost equal to the BM mass of $0.03\,\mathrm{kgm}^{2}$ in the Neely and Kim model), whereas the mass of a single slice of the BM in the model of Kolston would be more than two times smaller than the BM mass proposed by Neely and Kim.

The stiffness of the BM was reported to decrease by a half of its value every 2.5 mm from the base, where the stiffness of all other structures decreased by a half every 7.5 mm from the base of the cochlea. Hence, the distribution of the

stiffness along the cochlea will take the form

$$k_{\mathrm{BM}}(x) = k_0 2^{-x/0.025} = k_0 2^{-400x}, \tag{5.3.1}$$

for the BM, where x is expressed in metres and k_0 [Nm^{-1}] is the stiffness at the base, and

$$k_{\mathrm{TM}}(x) = k_0 2^{-x/0.075} \approx k_0 2^{-130x}, \tag{5.3.2}$$

for the TM and all other modelled structures, where x is expressed in metres and k_0 [Nm^{-1}] denotes the stiffness at the base.

The transverse BM point stiffness at the base (measured at the radial centre of the BM) was chosen by Kolston to be equal to $5\,\mathrm{Nm}^{-1}$, after measurements of Olson and Mountain [75], who estimated the CP stiffness from the ratio of the measured partition's restoring force to the sinusoidal excursion of a force transducer with a $20\,\mu$m diameter probe tip deflecting the CP at different radial positions in the basal turn of a gerbil cochlea. The transverse stiffness of the TM, assumed to be equal to $0.05\,\mathrm{Nm}^{-1}$ [50], was taken from the results for the second turn of a Mongolian gerbil cochlea estimated by Zwislocki and Cefaratti who measured the displacement of the TM due to a force exerted on it by downward movements of an elastic micropipette inserted into the membrane's margin (almost parallel to the TM's top surface) [105]. The BM resistance was set to $1.4\times10^{-6}\,\mathrm{Nsm}^{-1}$, in order to obtain correct response when there was no OHC motility[3], and the OHC stereocilia bending stiffness, according to measurements of Strelioff and Flock in the guinea pig cochlea [91], to $0.1\,\mathrm{Nm}^{-1}$ [50].

A resistance of $6\times10^{-8}\,\mathrm{Nsm}^{-1}$, corresponding to the separation of $5\,\mu$m between the stereocilia bundles, was added to each bundle to account for the effects of the subtectorial fluid's viscosity [50]. It has to be noted that the model of Kolston also assumes a finite axial stiffness of the Deiters cells and axial and transverse stiffness of the RL and the pillar cells. However, the transverse RL stiffness was set high to assure the rotation of the RL/pillar cells complex as a single unit [50].

[3]We deduce the resistance was constant over the length of the cochlea (and remaining orthogonal directions), although it was not stated explicitly in the article.

The motility of the OHC was modelled by assuming axial, counterphasic (with respect to the ends of the cell) forces exerted by the cell, which were controlled by the cell's membrane potential [50]. The potential is related to the displacement of the hair cell bundle, which undergoes radial displacement due to the shearing motion of the RL and TM. Thus, the mechanism of active force excitation is similar to that assumed in the model of Neely and Kim [68], which further justifies the use of their model for examination of the conditions used by Kolston in [50].

The magnitude of the motile force, referred to as the 'normal motility' [50], expressed in terms of the ratio of the axial force to the stereocilia bundle deflection, was set to $330\,\mathrm{pNnm^{-1}}$. Furthermore, Kolston reported that the phase of the OHC motility, which was defined as the lag between the force exerted downwards on the Deiters cells with regard to the deflection of the stereocilia in the inhibitory direction (towards the short stereocilia of the bundle), was equal to 135° [50].

Two types of excitation were assumed by Kolston in his 1999 model [50]: first, sinusoidal stimuli provided by the stapes motion and second, a localised excitation of a single OHC row at 3 mm from the base (40 kHz) with the force of magnitude $50\,\mathrm{pNnm^{-1}}$ and no stapes motion. The response of the model excited by the stapes motion at stimulus frequency of 30 kHz, was calculated for three values of the OHC motility magnitude, i.e. zero, $330\,\mathrm{pNnm^{-1}}$ ('normal motility') and $560\,\mathrm{pNnm^{-1}}$ ('enhanced motility'). Therefore, in our lumped parameter approximation of Kolston's model, we will use the model of Neely and Kim [68] excited at the stapes (u_{st}=1 $\mathrm{ms^{-1}}$) at the frequency of 1 kHz and 30 kHz, for which the active gain γ, corresponding to the OHC motility magnitudes assumed by Kolston [50], is 0 (passive), 1 ('fully active') and 1.7 ('enhanced motility').

Figure 5.7 shows the magnitude and phase response of the coupled Neely and Kim model [68] as a function of position, calculated for parameters in Table 3.2. The model was evaluated at stimulus frequency of 1 kHz (left) and 30 kHz (right) for four values of the active gain γ=0 (dotted), 0.5 (dot-dashed). 1 (dashed) and 1.7 (thick solid). For both 1 kHz (Fig.5.7(a)) and 30 kHz (Fig.5.7(b)) stimuli, the magnitude of the velocity responses increases with the increase of the gain from 0 to 1, which is in agreement with the behaviour of the responses of the Neely

and Kim coupled model discussed in Section 4.2. However, increasing the gain of the cochlear amplifier to 1.7 leads to reduction of the amplitude of the BM velocity, consistent with Kolston's observation [50]. The phase responses shown in Fig.5.7 (c, d), exhibit an increasing phase lag along the cochlea when the gain γ is set to 0, 0.5 and 1. For γ=1.7 however, the phase of the response at 1 kHz increases up to about 20 mm in the cochlea beyond which it lags again until it reaches the cochlear apex. The response calculated at 30 kHz for γ=1.7 exhibits a phase lead up to about 10 mm position on the CP above which it decreases very slowly along the remaining length of the cochlea. The phase leads observed in responses to 1 kHz and 30 kHz stimuli indicate that the model is unstable when γ=1.7.

The Nyquist plots in Fig.5.8, evaluated using the theory derived in Section 5.1 at positions where the amplitude of the BM velocity at 1 kHz and 30 kHz reaches a maximum for γ=1, i.e. x=0.0185 m and 0.0023 m, respectively, show that for γ=1.7, the Nyquist plots enclose the point of singularity (−1,0). Thus, when the gain of the cochlear amplifier is increased to 1.7 the velocity responses can no longer be trusted since the system becomes unstable. In Section 5.1 the gain limit for which the cochlear response at 1 kHz is still stable was estimated to about 1.21, whereas the gain limit for the response at 30 kHz, which corresponds to the basal portion of the cochlea, should be much smaller (cf. Fig.5.3(a)) and was estimated here to about 1.04. Thus, in both cases the active gain of 1.7 significantly exceeds the gain limits estimated from Nyquist plots at 0.0185 m and 0.0023 m for which the cochlear responses are still stable. The increase of the OHC gain, corresponding to the increase of the motility in the model of Kolston [50], thus does indeed lead to a reduction of the amplitude of the cochlear response, however, the model of Kolston lacks an examination of stability and most probably the calculated responses at high OHC motilities cannot be trusted.

In Fig.5.9 we plot the dependence of the magnitude of the maximum of the BM velocity, $|\dot{\xi}_b|_{max}$, on the level of gain, γ, calculated for the model of Neely and Kim at 30 kHz. It can be seen that with the increase of the gain up to about γ=1.029, the magnitude of the maximum of the BM velocity (peak magnitude) increases, but begins to drop for higher gains. In principle the maximum magnitude would

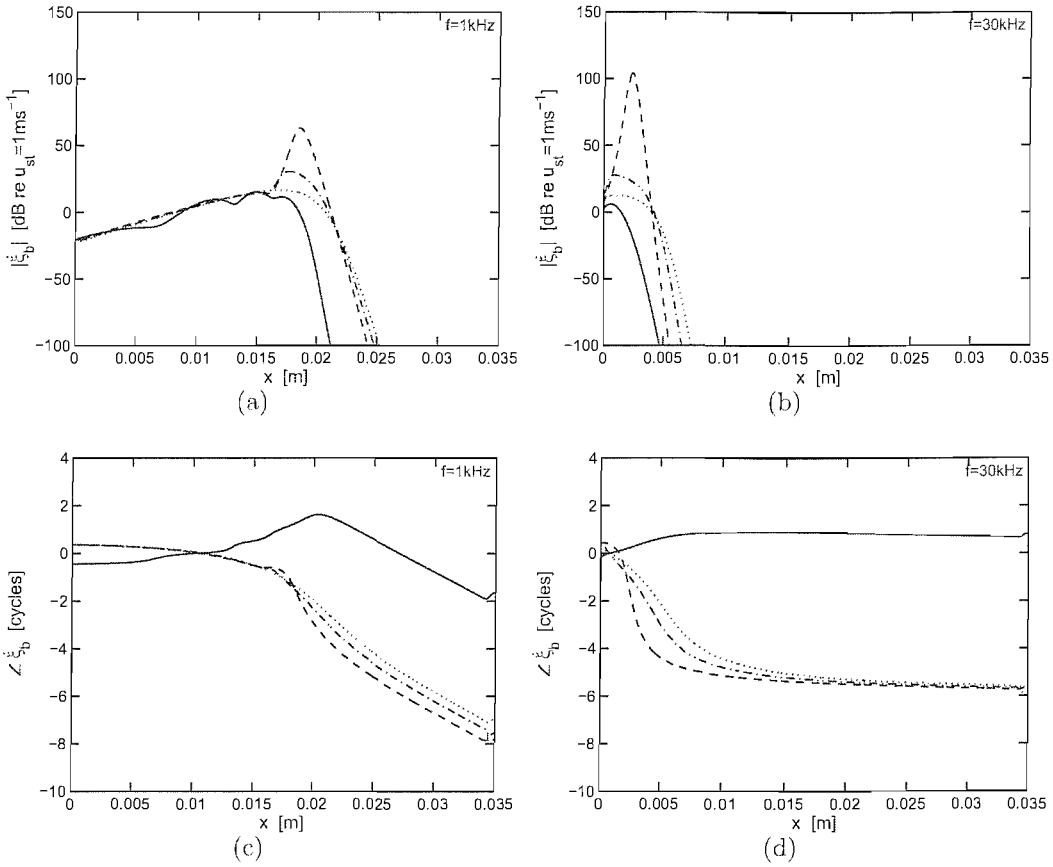

Figure 5.7: Magnitude (a, b) and phase (c, d) of the basilar membrane velocity $\dot{\xi}_b$ as a function of position, x, calculated for stimulus frequency of 1 kHz (left) and 30 kHz (right), and parameters chosen by Neely and Kim [68]. The active gain, γ, was set to zero (dotted), 0.5 (dot-dashed), 1 (dashed), and 1.7 (solid).

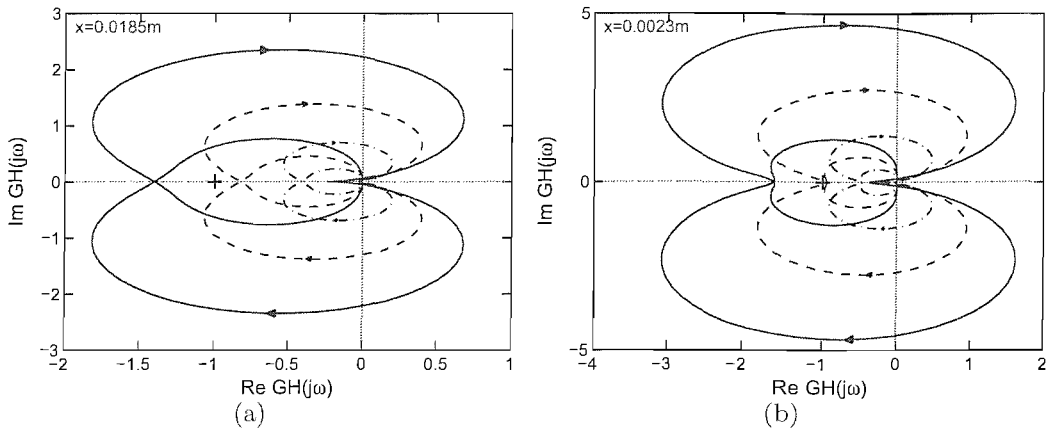

Figure 5.8: Nyquist plots of the isolated open feedback loops calculated at x=0.0185 m (a) and 0.0023 m (b), derived for the model of Neely and Kim [68]. The active gain, γ, was set to 0.5 (dot-dashed), 1 (fully active; dashed) and 1.7 ('enhanced activity'; solid). The crosses indicate the point of singularity (−1,0) and the arrows the direction of the increasing positive and negative frequency.

tend to infinity if we were to select exactly the right value of γ, but any plot with a finite resolution of γ will give a finite maximum value. For values of γ above 1.03 the system is unstable and so the calculated frequency response is spurious. This example reinforces again the need for a stability test to establish the reliability of the frequency response of a cochlear model.

5.4 Quasi-linear model of Neely and Kim

Improvement of the BM response measurement techniques led to the discovery of the BM nonlinearity (Section 2.3). The BM displacement observed by Rhode in 1971 [85] revealed a nonlinear dependence on the stimulus level, so that the normalised BM response was sharply tuned at low levels but started to decrease in magnitude and broaden with the increase of the stimulus level. The compressive nonlinearity of the BM response appears to be most pronounced in the region of its highest sensitivity (in the close vicinity of the response peak) [87].

The cochlear amplifier is thought to be the source of the level-dependent

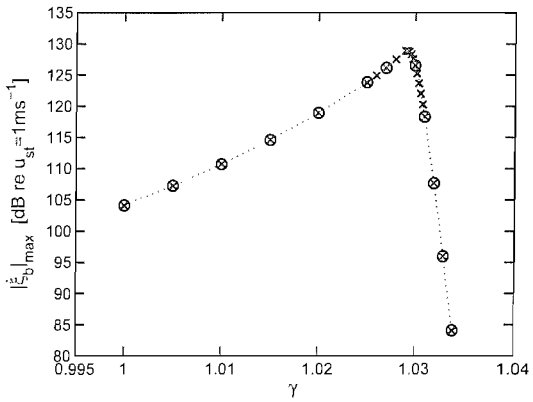

Figure 5.9: Maximum magnitude of the basilar membrane velocity, $|\dot{\xi}_b|_{max}$, calculated for the Neely and Kim model at 30 kHz for different values of gain γ. The curve marked with crosses was calculated for larger number of values of γ than the curve marked with circles.

compressive nonlinearity, since it is most pronounced in the vicinity of the characteristic place. Thus, a comprehensive active model of the cochlea requires compressive nonlinearity to be taken into account.

In the present section we will extend the quasi-linear approach proposed by Kanis and de Boer [47], in which an iterative calculation of the amplitude response and hence the active nonlinear gain leads to a compressive nonlinear response, to include the cochlear micromechanical model of Neely and Kim [68].

The motivation for this work is to illustrate the generality of the quasi-linear approach, and to calculate some nonlinearly compressed frequency responses which are consistent with the micromechanical model used elsewhere in the thesis and can be compared with physiological measurements.

5.4.1 Nonlinear positive feedback system

A nonlinear cochlear model can be considered as a sequence of coupled positive feedback systems with a nonlinear element in the feedback path between an energy input source and some sort of output, as suggested by Yates [99, 100]. This feedback controller model can be represented by a block diagram, as depicted in Fig.5.10, in which the feedback path consists of a plant G (feedforward gain), non-

linear network Φ and a frequency-selective network, β (a bandpass filter selecting the fundamental component of the loop output $v(t)$). The frequency-selective network provides a gain which we also denote as β, to the input signal. Hence, when the input is tonal the network β amplifies the fundamental frequency after attenuating the harmonics [23].

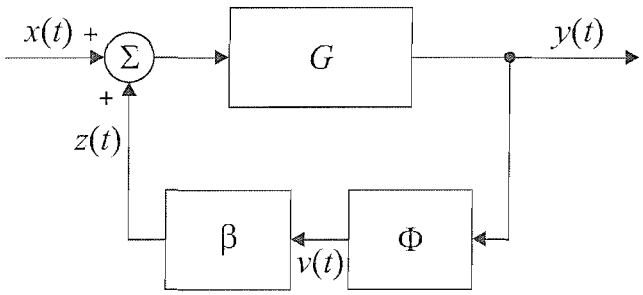

Figure 5.10: Block diagram of the positive feedback loop proposed by Yates [99]. G denotes the plant, the response of the output $y(t)$ to the input $x(t)$, where $y(t)$ is fed back to the nonlinear network Φ. The output of Φ, $v(t)$, is connected with the frequency-selective network β leading to the control loop output $z(t)$.

According to Yates [99], the input of the feedback loop is analogous to the pressure difference in the cochlear fluids, the plant, G, to the BM with its motion, whereas the reduction of the gain of the frequency-selective network, β, can account for the changes in the cochlear sensitivity corresponding to the damage within the cochlea. However, the nonlinear network Φ is assumed to be a saturating function with an input/output characteristic of the form

$$v(t) = \frac{Ay(t)}{A + y(t)}, \tag{5.4.1}$$

where $y(t)$ denotes the input of Φ, $v(t)$ its output and A is a threshold amplitude [100].

Thus, the instantaneous gain, $\Phi(t)$, can be explicitly expressed by

$$\Phi(t) = \frac{v(t)}{y(t)} = \frac{A}{A + y(t)}. \tag{5.4.2}$$

The overall gain of the nonlinear feedback system depicted in Fig.5.10, G_{closed}, can be formulated in the frequency domain by

$$G_{closed} = \frac{Y(j\omega)}{X(j\omega)} = \frac{G}{1 - \beta\Phi_D G}, \tag{5.4.3}$$

where G and β are linear constants, chosen to give a product of βG slightly less than unity, typically β=0.999 [100], and Φ_D (D stands for 'describing') is a real number that reflects the average value of $\Phi(t)$ depending on the amplitude of the output signal [23].

Since $y(t)$ is a time-varying waveform, the instantaneous gain $\Phi(t)$ will be higher or lower than unity through one cycle of the sinusoidal variation of Y, which will cause distortions in the output of Φ, $v(t)$. However, only the fundamental component of $v(t)$ will be delivered to the summing point in Fig.5.10 due to the selective network β [23].

5.4.2 Positive feedback in the model of Neely and Kim

We will apply the theory of the positive feedback nonlinear model proposed by Yates [99, 100], to a single micromechanical element using the model of Neely and Kim [68], so that the formulations for the plant and controller of the positive feedback loop will be derived in a similar way as in Section 5.1. We assume that the input to the feedback loop is represented by the pressure difference P_d, which refers to $x(t)$ in Fig.5.10, whereas the output of the feedback loop is the velocity of the BM, $\dot{\xi}_b$ ($y(t)$ in Fig.5.10).

Notice that the assumed output of the system is the BM velocity, $\dot{\xi}_b$, instead of the relative velocity between the BM and TM, $\dot{\xi}_c$ in Fig.5.1, so that the interpretations of G and H are slightly different and need to be re-derived.

Rearranging Eq.5.1.4, derived from the equations of motion for the Neely and Kim model [68] for the shear velocity $\dot{\xi}_c$ in terms of the BM velocity $\dot{\xi}_b$, gives

$$\dot{\xi}_c(x) = \frac{Z_2}{Z_2 + Z_3} g(x)\dot{\xi}_b(x), \tag{5.4.4}$$

thus the equation of motion for the first DOF in the model of Neely and Kim

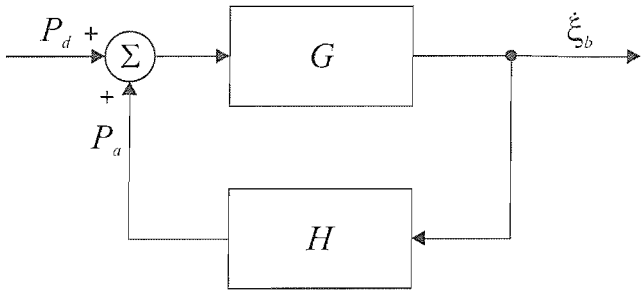

Figure 5.11: Block diagram of the positive feedback loop for the Neely and Kim model [68]. The acoustic pressure P_d represents the input, the basilar membrane velocity, $\dot{\xi}_b$, the output of the loop. G and H denote the plant and the controller, respectively.

will read

$$P_d(x) - (-\gamma Z_4)\frac{Z_2}{Z_2+Z_3}\,g(x)\dot{\xi}_b(x) = g(x)Z_1\dot{\xi}_b(x) + \frac{Z_2Z_3}{Z_2+Z_3}\,g(x)\dot{\xi}_b(x), \quad (5.4.5)$$

or

$$P_d(x) + \frac{\gamma Z_2Z_4}{Z_2+Z_3}\,g(x)\dot{\xi}_b(x) = \left[\frac{Z_1(Z_2+Z_3)+Z_2Z_3}{Z_2+Z_3}\right] g(x)\dot{\xi}_b(x), \quad (5.4.6)$$

After dividing the above equation by the term in the square bracket on the right-hand side we have

$$\underbrace{\frac{Z_2+Z_3}{Z_1(Z_2+Z_3)+Z_2Z_3}}_{G}\,P_d(x) + \underbrace{\frac{Z_2+Z_3}{Z_1(Z_2+Z_3)+Z_2Z_3}}_{G}\underbrace{\left(\frac{\gamma Z_2Z_4}{Z_2+Z_3}\right)}_{H} g(x)\dot{\xi}_b(x) = g(x)\dot{\xi}_b(x), \quad (5.4.7)$$

or

$$\underbrace{\frac{Z_2+Z_3}{Z_1(Z_2+Z_3)+Z_2Z_3}}_{G}\,\frac{P_d(x)}{g(x)} + \underbrace{\frac{Z_2+Z_3}{Z_1(Z_2+Z_3)+Z_2Z_3}}_{G}\underbrace{\left(\frac{\gamma Z_2Z_4}{Z_2+Z_3}\right)}_{H}\dot{\xi}_b(x) = \dot{\xi}_b(x), \quad (5.4.8)$$

where G denotes the plant, and H the controller of the closed feedback loop.

The pressure difference in Eq.5.4.8 is divided by the lever gain g, so that we introduce an equivalent pressure difference P_d^E=P_d/g, where the superscript E stands for 'equivalent'. For consistency we also define the active pressure P_a as an equivalent active pressure P_a^E. Note, however, that the equivalent definitions do not affect the numerical result since the lever gain was assumed by Neely and Kim to be equal to one as shown in Table 3.1.

Rewriting Eq.5.4.8 in terms of G and H gives

$$G\frac{P_d(x)}{g(x)} + GH\dot{\xi}_b(x) = GP_d^E + GH\dot{\xi}_b(x) = \dot{\xi}_b(x), \tag{5.4.9}$$

which leads to the classical formulation for a positive-feedback system of the form [19]

$$\dot{\xi}_b(x) = \frac{G}{1-GH}P_d^E. \tag{5.4.10}$$

To introduce the nonlinear element into the feedback path of the Neely and Kim model, we replace the gain of the active component, γ, with the level-dependent gain which is assumed to take the form

$$\gamma = \beta\Phi_{\mathrm{D}} = \frac{\beta A}{A + |\dot{\xi}_b|}, \tag{5.4.11}$$

where $|\dot{\xi}_b|$ denotes the magnitude of the velocity response of the BM at the frequency of interest. Note that for very low excitation levels, for which $|\dot{\xi}_b|$ is much less than A, then γ is equal to β. Therefore, the feedback path gain H defined in Eq.5.4.8, will be rewritten to take the form

$$H = \underbrace{\left(\frac{\beta A}{A + |\dot{\xi}_b|}\right)}_{\beta\Phi_{\mathrm{D}}=\gamma}\frac{Z_2Z_4}{Z_2+Z_3}, \tag{5.4.12}$$

and the diagram in Fig.5.11 will be modified to a positive feedback system shown in Fig.5.12, in which P_d^E is the equivalent pressure difference input, G is the plant, and H is the controller whose gain is now dependent on the amplitude of the BM velocity, $\dot{\xi}_b$.

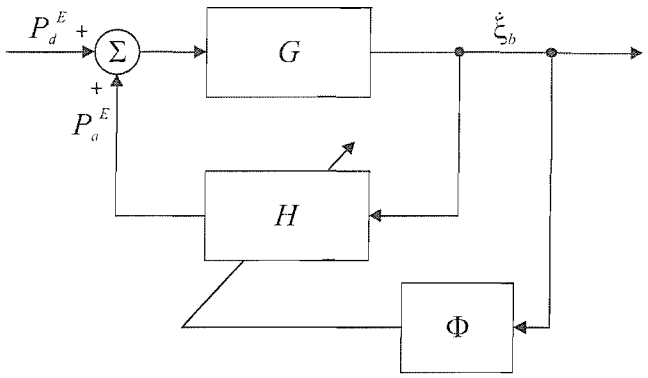

Figure 5.12: Schematic of the positive feedback loop for the Neely and Kim model [68] with the nonlinear network Φ scheduled on the output, the basilar membrane velocity $\dot{\xi}_b$, and adapting the controller gain H. The output of the feedback path is an equivalent active pressure, P_a^E, summing to the equivalent pressure difference, P_d^E.

It should be noted that the active gain γ in Eq.5.4.11 is a positive, real number which is initially assumed to be the same for all positions in the cochlea at particular stimulus frequency. In this case, γ may be referred to as a 'global' gain, say γ_{global}, which at single stimulus frequency demonstrates global changes to the cochlear amplifier, in which case $|\dot{\xi}_b|$ is calculated as the peak at the characteristic position along the cochlea. If we assume, however, that each positive feedback system in the quasi-linear model acts locally, that is the nonlinear network Φ is scheduled at the local response of the BM, we can also define a place/frequency specific 'local' active gain $\gamma_{\text{local}}(x)$

$$\gamma_{\text{local}}(x) = \beta\Phi_{\text{D}}(x,\omega) = \frac{\beta A}{A + |\dot{\xi}_b(x,\omega)|}, \tag{5.4.13}$$

where $|\dot{\xi}_b(x,\omega)|$ is now the magnitude of the velocity response of the BM calculated at the particular place along the cochlea and stimulus frequency. Hence, H

will be defined as

$$H = \underbrace{\left(\frac{\beta A}{A + |\dot{\xi}_b(x,\omega)|}\right)}_{\beta\Phi_{\mathrm{D}}(x,\omega)=\gamma_{\mathrm{local}}(x)} \frac{Z_2 Z_4}{Z_2 + Z_3}. \tag{5.4.14}$$

5.4.3 Coupled response of the quasi-linear model with global gains

Having formulated an expression for the gain of the quasi-linear model, based on the micromechanical model of Neely and Kim [68], we can calculate the response of the model using the theory for coupled cochlea discussed in Chapter 4. To begin with, we analyse the response of the quasi-linear model with a global active gain, γ_{global}, computed according to Eq.5.4.11, where the constant A was set to 1.5×10^{-5} and β was set to 5/6 ($\approx$0.83)[4], both estimated after preliminary results in [82].

The peak BM velocity at any point along the cochlea, was calculated by solving the Neely and Kim model for the pressure difference P_d with the gain of γ=1 when excited by a tone at 1 kHz, which was substituted to Eq.5.4.10 to calculate the BM velocity and find its maximum value. This was used to calculate the new global value of gain according to Eq.5.4.11, and the coupled cochlea model was solved again for this value of γ. This was repeated in an iterative loop of ten steps (not counting the gain of γ=1, which we will refer to as step 0) to stabilise the gain and converge the BM velocity. The convergence behaviour of this iterative procedure is described in Appendix D.

The model was solved for different magnitudes of the stapes velocity, u_{st}, corresponding to the stimulus level of 20, 40, 60, 80 and 100 dB re 2×10^{-5} Pa. The stapes velocity was calculated for 0 dB, as $u_{st}^0 \approx 9.15\times10^{-11}$ ms^{-1} (the upper index denotes the desired stimulus level), and for stimulus levels increasing in 20 dB steps u_{st} was calculated from the expression

$$u_{st}^L = 10^{L/20} \cdot 9.15 \times 10^{-11}\,\mathrm{ms}^{-1},$$

[4]The convergence of the model was improved when the value of β was made equal to 5/6 instead of 0.999 or 0.99 as assumed by e.g. Yates [100], or other trial values.

where L denotes the desired stimulus level. It has to be emphasised that the stimulus levels do not refer to the sound pressure levels measured at the eardrum but to the maximum pressure difference inside the cochlea at the frequency of 1 kHz.

The BM velocity calculated from the quasi-linear model, was divided by a factor of $j\omega$ to obtain the BM displacement ξ_b, which was plotted as a function of position in the cochlea and stimulus frequency for different stimulus levels, as shown in Fig.5.13. Additionally, the *normalised* BM displacement as a function of position along the cochlea and stimulus frequency is shown in Fig.5.14.

The magnitudes of the displacement of the quasi-linear model increase with the increasing stimulus level, as depicted in Fig.5.13. The responses increase almost linearly outside the characteristic place (characteristic frequency), where the response curves are parallel, that is equal magnitude increments occur below $\approx$0.015 m (Fig.5.13(a)) and 600 Hz (Fig.5.13(b)). However, compressive nonlinearity can be observed in the close vicinity of the characteristic place/CF, where the active enhancement decreases with the increase of stimulus level. Figure 5.13(b) resembles the measured frequency response of the guinea pig cochlea shown in Fig.2.12. Such behaviour indicates the connection between the compressive nonlinearity and the action of the cochlear amplifier in the present model, since the model's response changes from active at 20 dB to almost passive at 100 dB. The active-to-passive response change can be also observed in the phase plots in Fig.5.13(c) and 5.13(d), in which the phase lag accumulation decreases slightly with the increase of the stimulus level and the characteristic, short phase lead in the proximity of the characteristic place/frequency, disappears for high levels of the input stimuli.

An interesting feature of the quasi-linear displacement response is the shift of the characteristic place towards the basal end of the cochlea when the stimulus level is increased. In the response of the quasi-linear model with the global active gain γ_{global}, the characteristic frequency shifts towards lower frequencies in Fig.5.13(b) between the response for 20 and 100 dB stimulus level, which is consistent with the responses to single tones in experiments carried out on mammalian species discussed e.g. by Robles and Ruggero in [87].

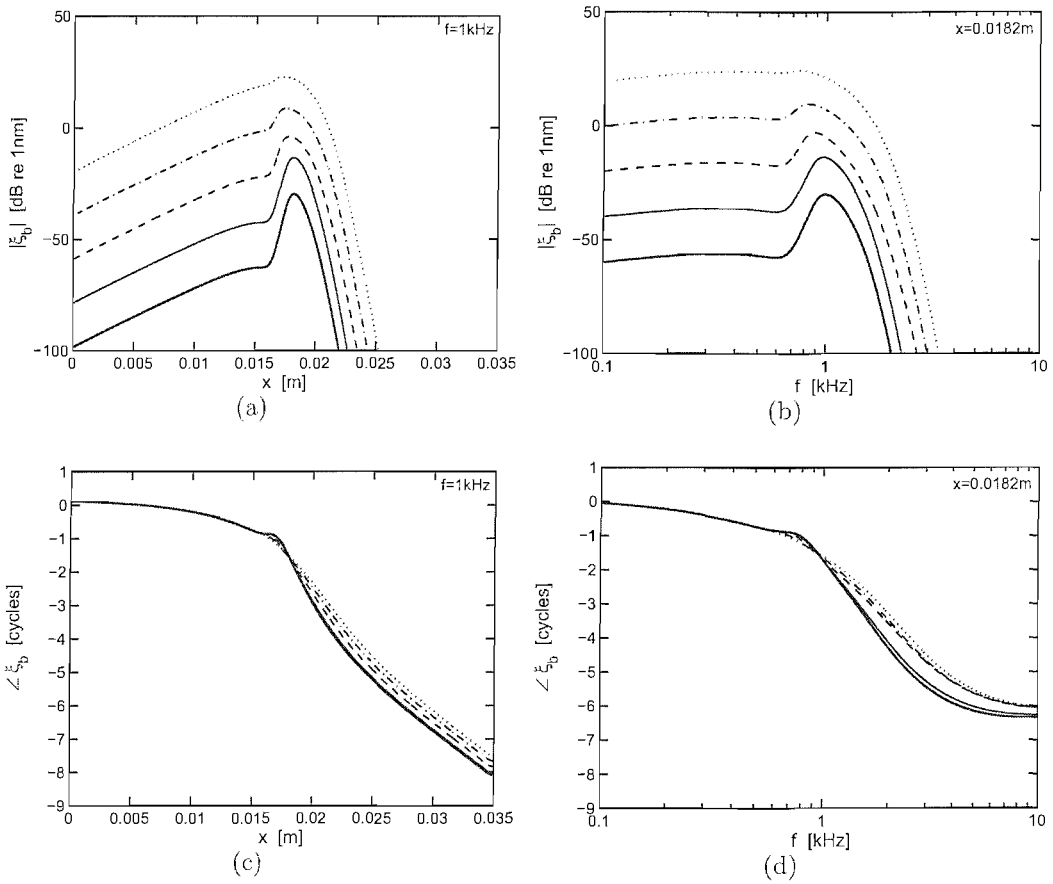

Figure 5.13: Magnitude (upper panel) and phase (lower panel) of the basilar membrane displacement (ξ_b) response of the quasi-linear model solved using global active gain, γ_{global}, and parameters chosen by Neely and Kim [68], for stimulus levels of 20 dB, thick solid; 40 dB, solid; 60 dB, dashed; 80 dB, dot-dashed and 100 dB (re 2×10^{-5} Pa), dotted. The left panel (a, c) shows the responses as a function of position along the cochlea where the stimulus frequency was set to 1 kHz, whereas the right panel (b, d) shows the responses as a function of stimulus frequency at the site of x=0.0182 m.

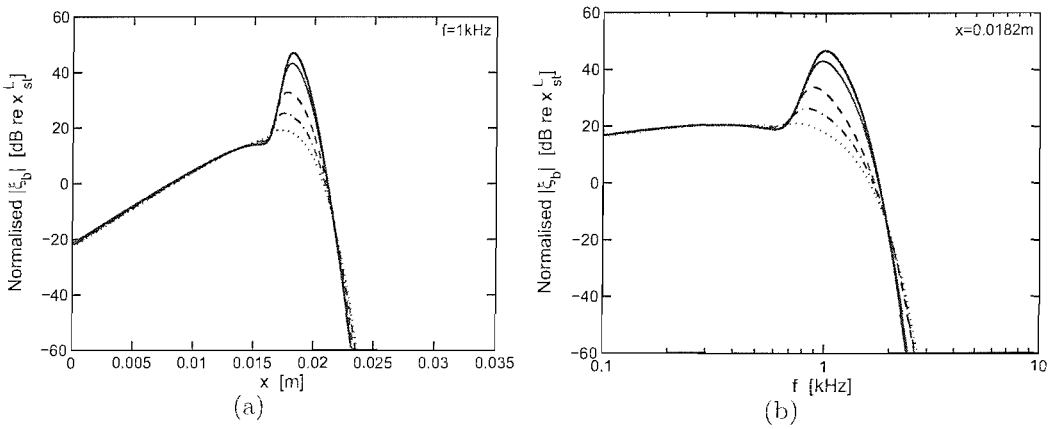

Figure 5.14: Normalised magnitude of the basilar membrane displacement (ξ_b/u_{st}) of the quasi-linear model solved using global active gain, γ_{global}, and parameters chosen by Neely and Kim [68], for stimulus levels of 20 dB, thick solid; 40 dB, solid; 60 dB, dashed; 80 dB, dot-dashed and 100 dB (re 2×10^{-5} Pa), dotted. Particular displacement response ξ_b^L was plotted with reference to corresponding stapes displacement x_{st}^L at 1 kHz. (a) responses as a function of position along the cochlea at the stimulus frequency of 1 kHz; (b) responses as a function of stimulus frequency at the site of x=0.0182 m (**NB** corresponding phase responses are the same as in Fig.5.13(c) and 5.13(d), respectively).

Figure 5.15 shows input/output, i.e. velocity/intensity curves at a single position in the cochlea, x=0.0182 m, which corresponds to the model CF of 1 kHz for 20 dB excitation. The left panel of the figure shows the velocity of the BM $\dot{\xi}_b$ for stimulus frequencies lower to equal to the CF, i.e. 0.5−1 kHz, whereas the right panel of Fig.5.15 shows the velocity/stimulus level curves for frequencies equal and higher than the CF, that is from 1−2 kHz, with 100 Hz steps in both cases. The compressive growth of the BM velocity is most prominent at the CF and it diminishes outside this frequency approaching almost 1 dB/1 dB, as indicated by the auxiliary dotted lines in the figure. For the data shown in Fig.5.15 the compression in the input-output curve at 1 kHz was approximately equal to 0.8 in the range from 20−40 dB, 0.4 dB/dB for 40−60 dB, 0.6 dB/dB for 60−80 dB and 0.7 dB/dB for 80−100 dB. We can also deduce that for 0 dB and 120 dB stimulus levels the response would have been closer to that of a fully active and passive model, respectively and the input-output curves in the ranges of 0−20 dB and 100−120 dB stimulus level would grow with a rate even closer to that of 1 dB/dB justifying no or insignificant compression in these regions. Such behaviour would be also consistent with the schematic input-output curve in Fig.2.13, and reasonably consistent with the measured data [87].

5.4.4 Coupled response of the quasi-linear model with local gains

The responses of the quasi-linear model were also calculated using the formula for the local active gain γ_{local} in Eq.5.4.13. In this case the value of each of the gains was scheduled on the response magnitude computed at corresponding place along the CP so that it was frequency and place specific. The constant A and gain β in Eq.5.4.13 were again chosen to be 1.54×10^{-5} and 0.83 and stapes velocities were derived in the same way as described above.

Figure 5.16(a) shows the magnitude of the BM displacement ξ_b as a function of the position along the cochlea, calculated for the quasi-linear model with locally changing active gain γ_{local} at 1 kHz stimulus frequency and stimulus levels of 20 dB, 40 dB, 60 dB, 80 dB and 100 dB. The corresponding results for x=0.0182 m as a function of frequency are shown in Fig.5.16(b). Both of these results are extremely

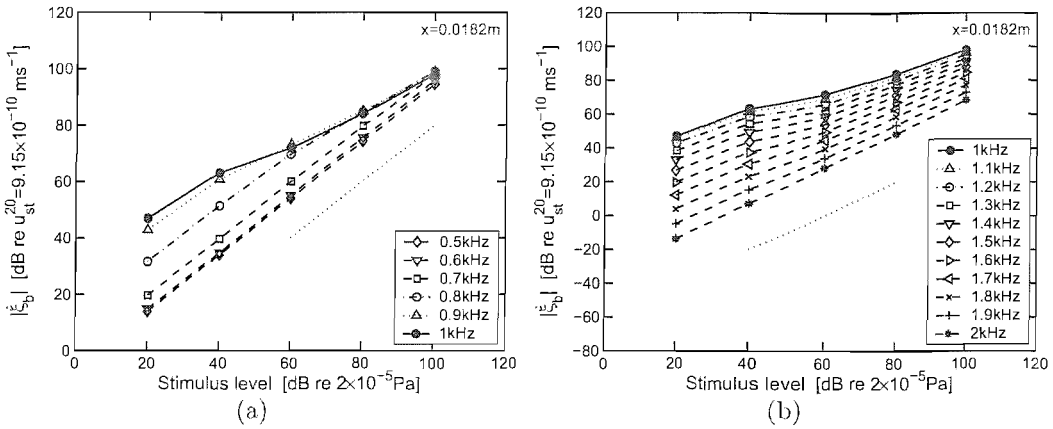

Figure 5.15: Input-output relationship between the magnitude of the basilar membrane velocity and stimulus levels for the quasi-linear model with global active gain, γ_{global}, solved at 0.0182 m using parameters chosen by Neely and Kim [68] at the characteristic frequency of 1 kHz and frequencies below (a) and above (b) that frequency. The auxiliary dotted lines have slope of 1 dB/dB.

similar to those obtained with the global gain (Fig.5.13).

The phase response in Fig.5.16(d) is not entirely 'smooth' in the high frequency region, above about 3 kHz, however, and some ripples occur mainly in the response curves to 40 dB and 60 dB stimulus level. However, the corresponding magnitude of the frequency response function has fallen by several hundreds of decibels in this high-frequency region, so that the ripples in the phase responses are not significant.

The normalised amplitude of the BM displacement, depicted in Fig.5.17, was calculated for the locally active quasi-linear model using the same normalisation method as in the case of globally active model and has almost the same characteristics as that with the globally active case shown in Fig.5.14.

The input-output curves of the quasi-linear model with the locally changing gain were also plotted as shown in Fig.5.18 and again these are similar to the global model in Fig.5.15. The input-output curves calculated for frequencies higher than the CF, depicted in Fig.5.18(b), however, exhibit some features of *expansive* nonlinearity. At frequencies above 1.7 kHz the input-output curves have

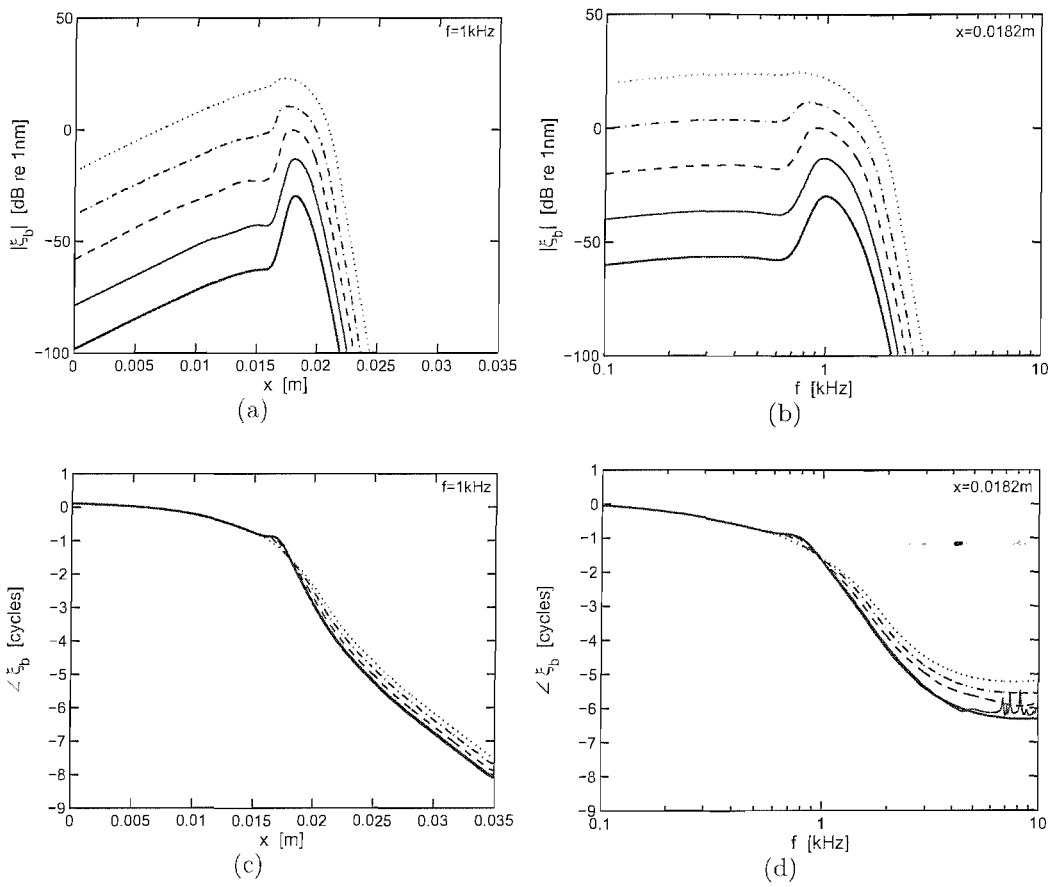

Figure 5.16: Magnitude (upper panel) and phase (lower panel) of the basilar membrane displacement (ξ_b) response of the quasi-linear model solved using local active gain, γ_{local}, and parameters chosen by Neely and Kim [68]. Stimulus levels were set to 20 dB, thick solid; 40 dB, solid; 60 dB, dashed; 80 dB, dot-dashed and 100 dB (re 2×10^{-5} Pa), dotted. The left panel (a, c) shows the responses as a function of position along the cochlea where the stimulus frequency was set to 1 kHz, whereas the right panel (b, d) responses as a function of stimulus frequency at the site of x=0.0182 m.

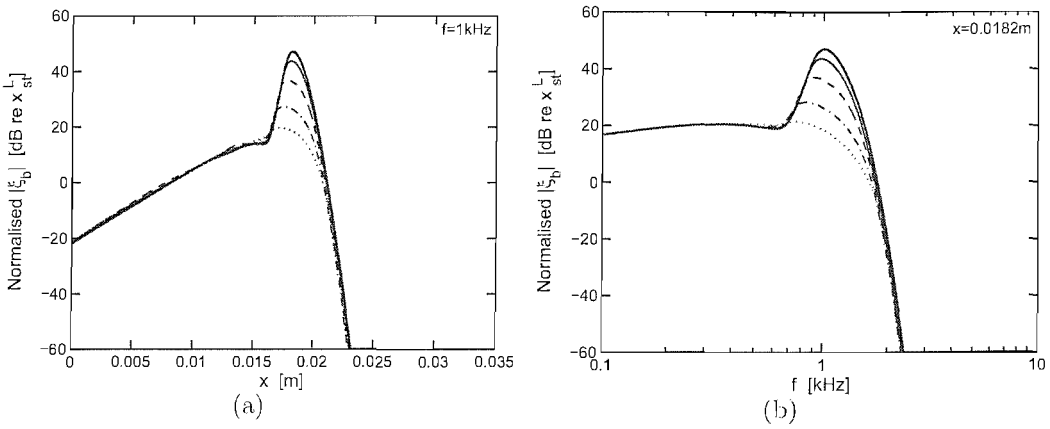

Figure 5.17: Normalised magnitude of the basilar membrane displacement of the quasi-linear model solved using local active gain, γ_{local}, and parameters chosen by Neely and Kim [68], for stimulus levels of 20 dB, thick solid; 40 dB, solid; 60 dB, dashed; 80 dB, dot-dashed and 100 dB (re 2×10^{-5} Pa), dotted. Particular displacement response ξ_b^L was plotted with reference to corresponding stapes displacement x_{st}^L at 1 kHz. (a) responses as a function of position along the cochlea at the stimulus frequency of 1 kHz; (b) responses as a function of stimulus frequency at the site of x=0.0182 m (**NB** corresponding phase responses are the same as in Fig.5.16(c) and 5.16(d), respectively).

a clear tendency to increase their slopes with each 20 dB step of the stimulus level, to as high as approximately 1.3 dB/dB at 2 kHz. This is a counter-intuitive result, although a single case of expansive nonlinearity was observed in the apical site (CF≈300−400 Hz) of the guinea pig cochlea [87].

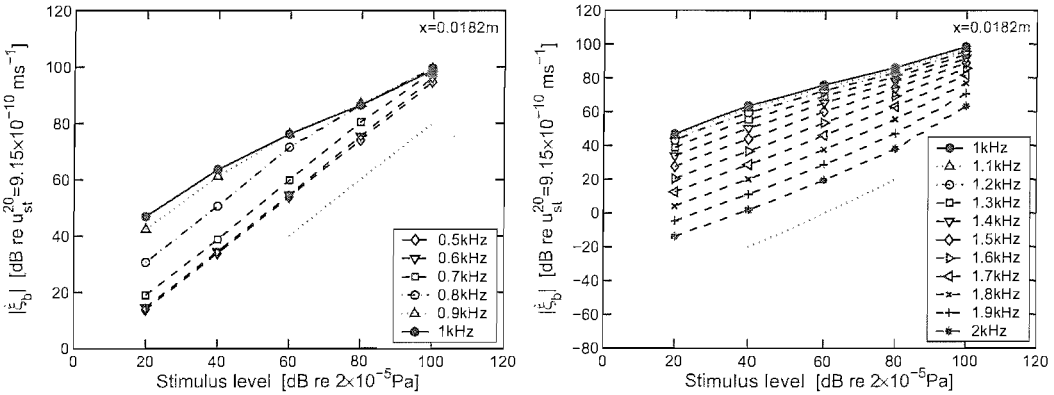

Figure 5.18: Input-output relationship between the magnitude of the basilar membrane velocity and stimulus levels for the quasi-linear model with local active gain, γ_{local}, solved at 0.0182 m using parameters chosen by Neely and Kim [68] at the characteristic frequency of 1 kHz and frequencies below (a) and above (b) that frequency. The auxiliary dotted lines have slope of 1 dB/dB.

It is worth noting, that in the global quasi-linear model the active gain is indirectly dependent on both place and frequency, since γ depends on the maximum velocity anywhere on the BM. Thus, the quasi-linear model acts as if the nonlinear phenomena in the cochlea were conditioning the OHC's force magnitude (active gain) on the 'global' response in the cochlea.

Although the overall result of the local model are consistent with the one for the global model, that is, the main features of the compressive nonlinearity in the BM displacement response and the input-output curves are reproduced almost identically, care needs to be taken with both quasi-linear models to avoid convergence problems during the iterative determination of the gain, as described in Appendix D. Such problems prevent the method being used for high frequency excitation.

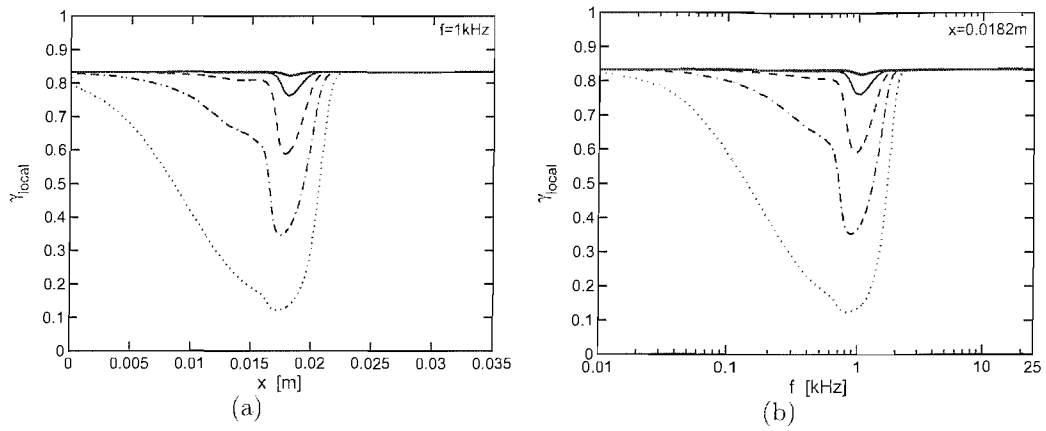

Figure 5.19: Dependence of the local active gain, γ_{local}, calculated for the local quasi-linear model using parameters chosen by Neely and Kim [68], on the position along the cochlea (at f=1 kHz, a) and stimulus frequency (at x=0.0182 m, b), for stimulus levels of 20 dB (thick solid), 40 dB (solid), 60 dB (dashed), 80 dB (dot-dashed) and 100 dB (dotted).

The local active gain γ_{local} converges to a different value at each particular position x or stimulus frequency f when the stimulus level is varied from 20 dB to 100 dB, as can be seen in Fig.5.19(a) and 5.19(b), respectively. In particular, at 20 dB stimulus level (thick solid lines) the gain appears to be almost constant, approximately equal to β, at all positions and stimulus frequencies. As the stimulus level is increased, γ_{local} starts to deviate from the constant value, first in the vicinity of the characteristic place/CF for 60 dB input level, and above 80 dB stimulus level in the region basal to the characteristic place in Fig.5.19(a) and lower than the CF in Fig.5.19(b). It should be noted that the gain is almost constant apically from the characteristic place and above the CF, because the amplitude of the response decays with a very high rate, which enables fast stabilisation of gain.

5.5 Discussion

In the present chapter the stability of the isolated models of Neely and Kim [68] and Neely [66] was examined. We have also analysed the stability of the Neely and Kim coupled model using gains corresponding to those chosen by Kolston [50]. Finally, a quasi-linear model with global and local active gains was proposed to include compressive nonlinearity in the Neely and Kim model.

It was shown that the model of Neely and Kim and the Neely model are conditionally stable, i.e. there is a gain limit for which the Nyquist plots calculated for these models still do not enclose the point of singularity. The estimated gain limits increase with an increase of the position along the cochlea, and the gains estimated for the Neely model are larger than those estimated for the model of Neely and Kim. Thus the Neely model is inherently more stable.

It was also shown that for gains larger than the gain limit at a particular cochlear position, the magnitude of the coupled response of the Neely and Kim model starts to decrease rather than increase when the gain is increased, as observed by e.g. Kolston [50]. Since the model is no longer stable in such a case, the calculated responses cannot be trusted, and hence we conclude that the stability of the model should be ensured before analysing the response plots.

The quasi-linear model of Neely and Kim exhibits compressive nonlinearity around the characteristic place and CF when the stimulus level of the model's input is increased. This was observed for both global and local active gain. In both cases the model gives about 30 dB difference between the maxima of responses at 20 dB and 100 dB stimulus level. The input/output curves become nearly linear outside the CF for both models, and an expansive nonlinearity can be observed at frequencies higher than 1.7 kHz in the quasi-linear model with local gains. However, the expansive nonlinearity is thought to occur solely due to the model's convergence conditions at these frequencies, so that it does not have any physical meaning in this case.

Chapter 6

'Squirting' waves in the subtectorial space

Within the lumped parameter micromechanical models described above, the TM and RL were assumed to move as rigid bodies. The fluid in the subtectorial space between them is then sheared by their parallel motion. Due to the extreme difficulty of taking direct measurements of the fluid in this gap in a living cochlea, this assumption has rarely been tested. It is thus possible that a more complicated dynamic interaction may occur between the fluid in the gap and the surfaces of the RL and TM that face it. This possibility has been emphasised by Bell and Fletcher [9], who also point out that unless a more subtle interaction does occur there appears to be little point in there being three rows of outer hair cells in the radial direction, or for them to be arranged in such an orderly way.

In this chapter we examine the dynamics of the 'squirting' wave model proposed by Bell and Fletcher in [9]. Firstly, we derive the wave equation for the waves propagating in the subtectorial space of the organ of Corti and investigate their dynamics. We extend the published theory for the 'squirting' waves by incorporating the effects of the subtectorial fluid's viscosity. Finally, we propose a feedback controller model connected with the electromotile action of the outer hair cells to overcome the viscosity of the fluid and undamp the resonances predicted in the duct of the subtectorial space.

6.1 Introduction

A form of cochlear amplification, involving a 'squirting' wave, the symmetric Lloyd-Redwood wave [60], has been proposed recently by Bell and Fletcher [9]. The 'squirting' wave, propagating in the radial direction of the subtectorial space within the organ of Corti, is a subtectorial fluid wave which arises due to vertical vibrations of the TM and RL. Thus, the TM and the RL constitute a duct comprised of two vibrating, thin plates, whose stiffness is coupled to the inertia of the fluid propagating in the very narrow gap in between.

This model can suggest another form of amplification in the cochlea, as the electromotile responses of the outer hair cells could transfer forces needed to induce the vibrations of the duct and if the conditions were right, the interactions between the fluid and the duct might amplify the natural motion. The transfer of force from the tops of the OHCs attached in the lower plate (RL) to the upper plate of the duct (TM), can be achieved via the tallest rows of the OHC's stereocilia, which are embedded in the TM [58]. Furthermore, knowing that the OHCs are assumed to respond to the BM displacement, the 'squirting' model may add more insight into the overall micromechanics of the cochlea.

There are many issues that still need to be clarified in such a model, however, like the anatomical and physiological validation of the model's components. For instance, although the RL could account for the lower, stiff plate of the duct, as it is thought to be a tight lattice made of the tops of the sensory and supporting cells constituting a boundary for separation of the cochlear fluids, the TM, on the contrary, is usually described as a gelatinous, nonhomogeneous structure [11]. However, it could be assumed that a segment of the layer-like arrangement of the TM may refer to the upper plate of the duct in the 'squirting' wave model and a possible candidate for the plate is the fibrous layer known as Kimura's membrane [58] as depicted in Fig.6.1.

The influence of damping on the properties of the waves propagating in the duct and response of the model should also be examined. While Bell and Fletcher argue in their article that the 'squirting' wave would be attenuated by the fluid's viscosity [9] this viscosity is not explicitly accounted for in their formulation.

Furthermore, Bell and Fletcher [9] consider mainly the fluid motion in the

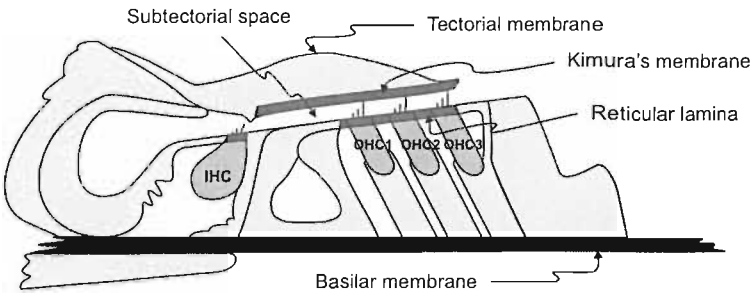

Figure 6.1: Schematic of the organ of Corti anatomy with the inner (IHC) and three rows of outer hair cells (OHC1-3) indicated. The reticular lamina and Kimura's membrane are thought to constitute a duct in which the 'squirting' waves are propagating.

duct, which drives the response of the inner hair cells (IHCs). This is crucial since the stereocilia of the IHCs are not attached to the TM and are thought to be deflected by the subtectorial fluid flow in response to the BM velocity. However, this flow appears also in the passive responses of the cochlea as shown e.g. by Raftenberg [83], so that more interest should be put into the actual mechanism of the excitation of the duct plates, in other words to the mode of coupling of the OHC's force with the plate's vibrations and the resulting fluid flow, which was again not considered by Bell and Fletcher.

To investigate these issues, a new model is introduced, in which the nature of the plate-fluid-plate interactions is investigated and the viscosity of the fluid is included into the wave equation to examine its effect on the 'squirting' waves. The action of the OHCs is then incorporated into a feedback loop to enhance the response of the system and justify the potential role of the 'squirting' waves mechanism in the cochlear amplifier.

6.2 Plate dynamics

The 'squirting' wave model was first suggested by Lloyd and Redwood [60] but was studied most comprehensively by Hassan and Nagy [41]. It can be considered as the oscillation of a fluid layer in a solid-fluid-solid trilayered structure [41].

To work out the input characteristics of the 'squirting' wave in the duct, the equations concerning a plate's bending deformations will be introduced using the notation of Hassan and Nagy.

A vertical displacement, $w(y,t)$, of a plate of thickness equal to $2h_s$ (**NB** h_s refers to the semi-thickness of the plate in this section), the Young's modulus, E, and the Poisson's ratio, ν, as depicted in Fig.6.2, due to the external fluid pressure, $p(y,t)$, can be derived from the equations governing plate dynamics (or a beam if only a cross-section of the organ of Corti is considered) [94].

The bending moment of the beam, M takes the form (for clarity we omit the dependants y and t in the equations),

$$M = -EI\,\frac{\partial^2 w}{\partial y^2}, \tag{6.2.1}$$

the force, F, acting on the beam

$$F = -EI\,\frac{\partial^3 w}{\partial y^3}, \tag{6.2.2}$$

and finally the pressure, p, assumed to act against the stiffness of the plate, namely

$$p = -EI\,\frac{\partial^4 w}{\partial y^4}, \tag{6.2.3}$$

where the moment of inertia, I, is expressed as

$$I = \frac{2h_s^3}{3(1-\nu^2)}. \tag{6.2.4}$$

Taking the conservation of momentum equation for the fluid with density, ρ, and longitudinal displacement[1], $u(y)$,

$$\rho\,\frac{\partial^2 u}{\partial t^2} = -\frac{\partial p}{\partial y}, \tag{6.2.5}$$

[1]Note that the fluid motion is considered along the width of the CP (radial direction y), orthogonally to the travelling waves propagating in the longitudinal direction along the cochlea. Thus in the present chapter the fluid displacement is referred to as longitudinal with respect to the subtectorial duct in a single cross-section of the cochlea.

the continuity equation of an incompressible fluid

$$w = \frac{d_2}{2}\frac{\partial u}{\partial y}, \tag{6.2.6}$$

where d_2 denotes the thickness of the fluid layer (distance between the plates), and combining them with Eq.6.2.3 gives a sixth-order wave equation of the form

$$\rho\frac{\partial^2 w(y,t)}{\partial t^2} - \frac{EId_2}{2}\frac{\partial^6 w(y,t)}{\partial y^6} = 0. \tag{6.2.7}$$

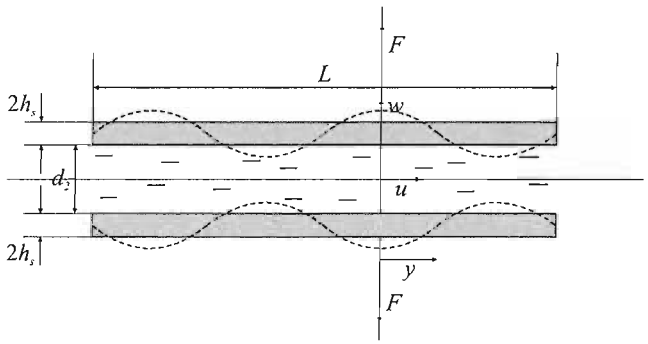

Figure 6.2: Schematic of the subtectorial duct comprising two thin plates corresponding to the reticular lamina (bottom) and the tectorial membrane (top) with the subtectorial fluid confined in between. The displacements, vertical of the plate, w, and longitudinal of the fluid, u, are shown with the arrows indicating positive directions. The excitation forces, F, acting on the plates due to the external driving pressure or internal forces from the outer hair cells, are also shown. d_2 duct's height, $2h_s$ thickness of the plates, L the length of the plate.

Assuming harmonic vibration of the plate of a form $w{=}Ae^{j(\omega t-kx)}$, and differentiating with respect to y and t, Eq.6.2.7 can be written as

$$\omega^2 = \frac{EId_2}{2\rho}k^6, \tag{6.2.8}$$

and hence, k, the wavenumber is equal to

$$k = \left(\frac{2\rho\omega^2}{EId_2}\right)^{\frac{1}{6}}. \tag{6.2.9}$$

The coordinate system of the plate-fluid-plate system in the considerations of Hassan and Nagy was located in the centre of the fluid layer, thus the 'squirting' wave is symmetric with respect to the horizontal axis in the middle of the fluid film [41], as shown in Fig.6.2. Using the symmetry about the centre line in Fig.6.2, it can be seen that a similar fluid mode to that of a 'squirting' mode will exist in a fluid film confined between a bending plate and a solid substrate [41]. Therefore, we introduce a modified model in which the 'squirting' waves propagate in the fluid layer between an elastic plate undergoing vertical oscillations and a rigid surface, where the thickness of the fluid layer, say d_{duct}, is equal to half that assumed originally by Hassan and Nagy. This is likely to be a more realistic model of the subtectorial gap since the RL is considerably more rigid than the TM [20, 88].

The thickness of the plate is redefined to be $h{=}2h_s$ and the overall thickness of the fluid layer is redefined as $d{=}2d_2$ to be consistent with [41]. Therefore, we rewrite the wave equation in Eq.6.2.7 for a wave propagating between two elastic plates, to obtain the wave equation of the lossless 'squirting' wave propagating between a rigid surface of the RL and an elastic plate of the TM under-surface of thickness h, located d above the rigid surface. The modified duct is shown in Fig.6.3.

The wave equation will now take the form

$$\rho \frac{\partial^2 w(y,t)}{\partial t^2} - EId \frac{\partial^6 w(y,t)}{\partial y^6} = 0, \tag{6.2.10}$$

so that

$$k = \left(\frac{\rho \omega^2}{EId} \right)^{\frac{1}{6}}, \tag{6.2.11}$$

and the moment of inertia, I, will be equal to

$$I = \frac{h^3}{12(1-\nu^2)}. \tag{6.2.12}$$

Since k is not directly proportional to ω the wave is dispersive, i.e. its wave-speed is a function of frequency. The wavenumber, k, propagation speed, $c{=}\omega/k$,

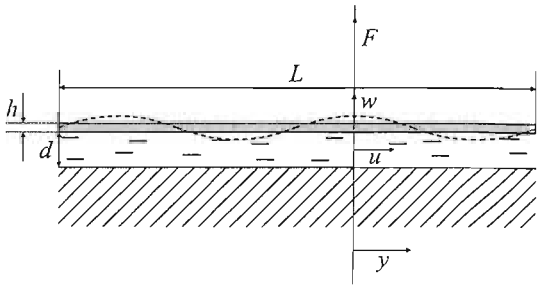

Figure 6.3: Schematic of the subtectorial duct comprising a rigid surface corresponding to the reticular lamina (bottom), a thin plate corresponding to the under-surface of the tectorial membrane, with the subtectorial fluid confined in between. The vertical displacement, w, and longitudinal displacement of the fluid, u, are shown with the arrows indicating positive directions. The excitation force, F, acting on the plate due to the external pressure excitation or internal forces from the outer hair cells, is also shown. The duct's height, d, is equal now to half that assumed by Hassan and Nagy [41] and the thickness of the plates is equal to h. L is the length of the plate.

and the wavelength, $\lambda=2\pi/k$, were calculated according to Eq.6.2.11 for parameters chosen by the present authors[2] gathered in Table 6.1. The thickness of the plate, with Young's modulus E=8 kPa [30, 89] and Poisson's ratio ν=0.49, was set to h=1 μm. The thickness of the layer of fluid (duct's height) of density that of water ρ=1000 kgm^{-3}, was set to d=3 μm [98]. The plots of the propagation speed and the wavelength as a function of frequency are shown in Fig.6.4.

The Young's modulus used in the present work is equal to 8 kPa which can be derived from the TM stiffness measurements of Shoelson *et al.* [89] and Freeman *et al.* [30] (see Chapter 7). However, Bell and Fletcher [9] assumed a Young's modulus of the TM and RL plates to be equal to 2 kPa.

Figure 6.4(a) shows that the 'squirting' wave is very slow and at the frequency

[2]All quantities examined in this section, were first calculated for the parameters given by Bell and Fletcher in [9]. The values of most parameters were changed to ensure that the values were more consistent with the literature, but the value of h was adjusted to tune the vibration of the plate to the fourth mode at 1 kHz, as in [9].

PARAMETER	VALUE
h [μm]	1
d [μm]	3
E [kPa]	8
ν	0.49
ρ [kgm^{-3}]	1000

Table 6.1: Parameters used for simulations of the 'squirting' waves.

of 1 kHz its propagation speed amounts to $\approx$40 mms^{-1}, which corresponds to a wavelength of $\approx$40 μm in this lossless case. The wavespeed of the lossless 'squirting' wave increases by more than a decade in the examined frequency range ($c \propto \omega^{1/3}$) from about 8.6 mms^{-1} at 100 Hz to 185.7 mms^{-1} at 10 kHz, whereas its wavelength, λ, decreases by less than a decade, from about 86.2 μm at 100 Hz to 18.6 μm at 10 kHz. Note that at 1 kHz, the wavelength of the lossless 'squirting' wave is equal to half that of the duct length L=80 μm, so that the vibrations of the plate are tuned to the fourth mode at this frequency.

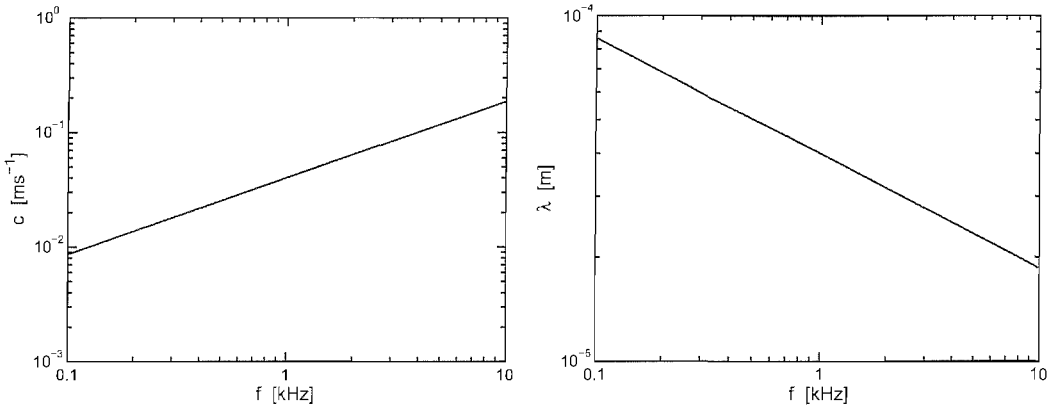

(a) (b)

Figure 6.4: The phase speed (a) and wavelength (b) of the 'squirting' wave without losses taken into account, as a function of frequency.

6.3 Incorporation of the effects of viscosity

In the following section the viscosity of the fluid will be introduced into the wave equation to examine damping effects to the model's behaviour. Recalling Eq.6.2.5 (the conservation of momentum equation for the fluid), defining the force per unit distance which acts on the fluid in the duct in the absence of any losses, an additional term, due to the fluid drag, will be introduced assuming that the fluid is viscous. In such conditions the fluid flow in the duct will have approximately parabolic, Poiseuille velocity profile [54].

The fluid drag depends on its layer thickness, d (duct's height), and the viscous boundary layer defined by [48]

$$\delta = \left(\frac{2\eta}{\rho\omega}\right)^{\frac{1}{2}}, \tag{6.3.1}$$

where η is the coefficient of viscosity, which for water at body temperature is equal to about $6.6\times10^{-4}\,\mathrm{kgm^{-1}s^{-1}}$ [81], ρ is the density of the fluid and ω is the radian frequency. The force, which is required to overcome the viscosity of the fluid is equal approximately to [54]

$$F = \frac{16\eta}{d^2}\frac{\partial u}{\partial t}, \tag{6.3.2}$$

which, after incorporating into Eq.6.2.5 will determine the fluid force equation for the viscous waves, i.e.

$$\rho\frac{\partial^2 u}{\partial t^2} + \frac{16\eta}{d^2}\frac{\partial u}{\partial t} = -\frac{\partial p}{\partial y}, \tag{6.3.3}$$

where the fluid displacement, u, is now to be interpreted as the average displacement over the fluid layer confined in the duct. Thus, the wave equation for the viscous 'squirting' waves propagating between the RL and the TM modelled as a plate, will take the form (Appendix E.4)

$$\rho\frac{\partial^2 w(y,t)}{\partial t^2} + \frac{4\eta}{d^2}\frac{\partial w(y,t)}{\partial t} - EId\frac{\partial^6 w(y,t)}{\partial y^6} = 0. \tag{6.3.4}$$

Assuming a harmonic vibration of the plate of the form $w{=}Ae^{j(\omega t-ky)}$, the

wavenumber of the viscous 'squirting' wave, k_v, will take the form

$$k_v = \left(\frac{\rho\omega^2}{EId} - j\frac{4\eta\omega}{EId^3} \right)^{\frac{1}{6}}. \tag{6.3.5}$$

The propagation speed, c_v=$\omega/Re\{k_v\}$, and the wavelength, λ_v=$2\pi/Re\{k_v\}$, were calculated using the wavenumber defined in Eq.6.3.5, for the parameters given in Table 6.1 and viscosity η=$6.6\times10^{-4}\,\mathrm{kgm^{-1}s^{-1}}$, as shown in Fig.6.5.

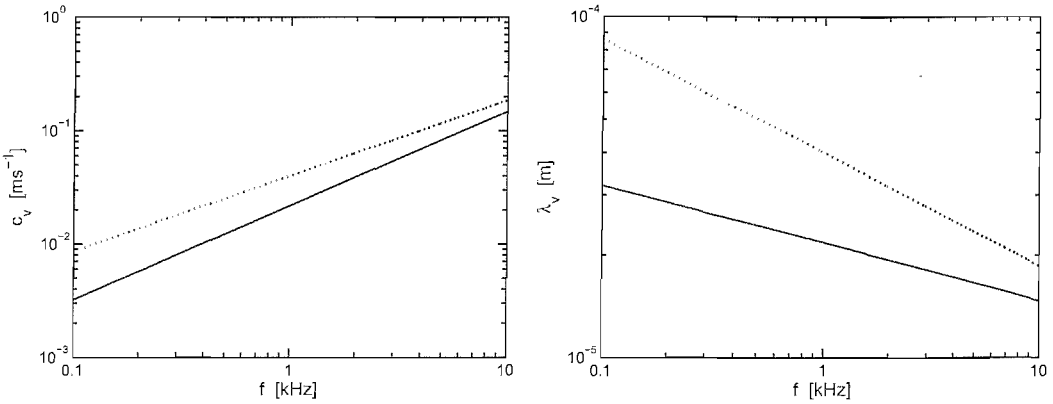

Figure 6.5: The phase speed (a) and wavelength (b) of the viscous 'squirting' waves (solid) as a function of frequency. Dotted lines show the phase speed and wavelength of the lossless 'squirting' wave for comparison.

It can be seen from Figure 6.5(a) that after adding viscous terms into the wave equation, the 'squirting' wave, which was already very slow for the undamped case (dotted line), was slowed even more, and equals nearly a half that of the wavespeed of the lossless case at the frequency of 1 kHz, $\approx$21.8 $\mathrm{mms^{-1}}$. This corresponds to a wavelength, λ_v, of $\approx$21.8 μm at 1 kHz, which is also almost a half of the wavelength of the lossless 'squirting' wave at the corresponding frequency and nearly a quarter of the duct's length assumed to be equal to 80μm in this model. The wavespeed increases by less than two decades, from about 3.2 $\mathrm{mms^{-1}}$ at 100 Hz to about 146.9 $\mathrm{mms^{-1}}$ at 10 kHz and the slope of c_v is somewhat steeper than the slope of the wavespeed of the lossless wave, c. The wavelength of the viscous 'squirting' wave λ_v, decreases slower than the wavelength of the lossless

wave, and it amounts to about 32.04 μm at 100 Hz and about 14.70 μm at 10 kHz. It should be noted that as well as reducing its wavespeed, the effect of viscosity is also to severely attenuate the wave, such that at 1 kHz the wave is attenuated by about 14 dB as it travels a distance equal to a wavelength.

6.4 Response of the model to OHC excitation

The plate's deformation and fluid's displacement properties are described in Appendix E. We now consider the effect of an active model on the 'squirting' wave, initially by examining its excitation by an OHC. The standing nearfield described in Appendix E is neglected and only propagating waves are taken into account. The response will be evaluated for the finite duct with viscosity effects included, in which a single OHC at position y=0 is introduced as depicted in Fig.6.6. The OHC is assumed to drive the plate with a force f.

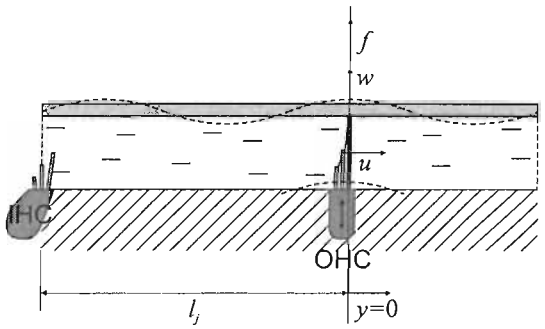

Figure 6.6: Schematic of the subtectorial duct with a single outer hair cell at y=0. The tallest stereocilia of the outer hair cell are embedded in the plate. The smaller stereocilia are subject to the fluid displacement, u, whereas the tallest cilia produce the wall displacement, w. f is the input force from the outer hair cell at a distance l_j from the inner hair cell along the duct (**NB** dimensions exaggerated and proportions not preserved).

The more general relationship between the governing equations for a complete system, where three rows of the OHCs are giving feedback is shown in the block diagram of Fig.6.7. All inputs and outputs to the duct are presented on the left

side of the figure and represented in control system block diagram on the right.

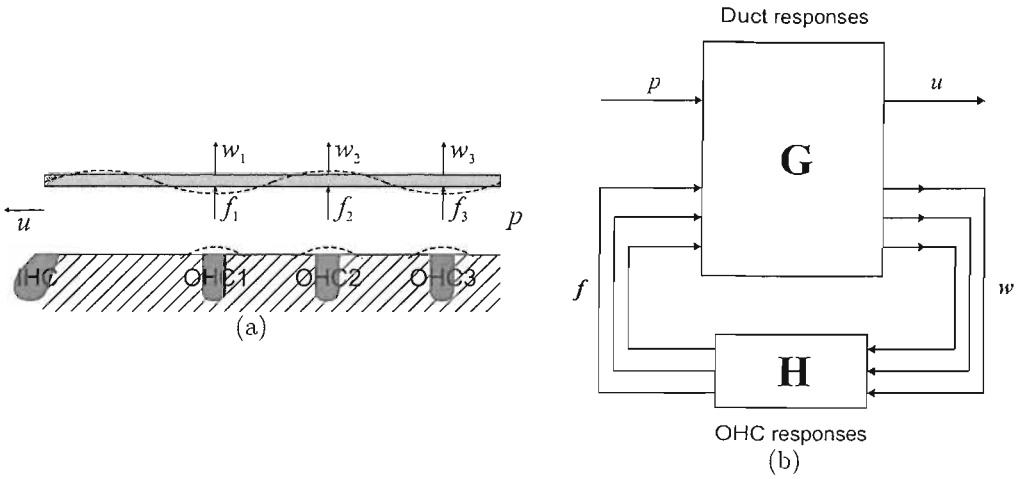

Figure 6.7: Schematic of the subtectorial duct with the internal inputs from the outer hair cells, f_{1-3}, and internal outputs being the plate's displacements, w_{1-3}. The external input, the pressure of the endolymph, p, and the external output, subtectorial fluid displacement, u, are also shown. The fourth mode of vibration of the plates is sketched on the plate. The 'squirting' wave, active cochlear model represented as a control block diagram is shown on the right.

It is assumed that the fluid is driven by an external pressure of the endolymph of the scala media, p. The resulting response is the output of the IHC, which is dependent on the flow of the fluid in the subtectorial space, u. The OHCs exert forces, f_{1-3}, on the upper duct plate[3], and depend on the plate's displacements, w_{1-3}. The excitation of the OHC is due physically to the shearing motion of the sterocilia, as described in Chapter 2. The bending motion of the plate will induce shearing motion as a consequence of its out of plane motion, and for simplicity these are assumed to be proportional to each other. The out of plane plate displacements, fed back to the OHC's forces through the matrix of gains, $\mathbf{H}$, are gathered in a vector $\mathbf{w}$, whereas the resulting OHC forces f_{1-3} are contained in the vector $\mathbf{f}$. The response of the duct is a generalised plant represented by the matrix, $\mathbf{G}$, as shown in the control diagram.

[3]The reactive forces exerting on the bottom wall of the duct due to the OHCs electromotility are not considered here.

The equations for the system in which the OHCs are assumed to behave linearly are defined in the frequency domain as

$$u = G_{up}\, p + \mathbf{G}_{uf}\mathbf{f}, \tag{6.4.1}$$

$$\mathrm{w} = \mathbf{G}_{wp}\, p + \mathbf{G}_{wf}\mathbf{f}, \tag{6.4.2}$$

where the individual responses are defined to be: G_{up}, response at the IHC due to the external pressure; G_{uf}, response at the IHC due to each OHC excitation; G_{wp}, response at the OHC positions due to the external pressure and G_{wf}, response at the OHC positions due to each OHC excitation.

Furthermore, the forces of the OHCs are defined to be

$$\mathbf{f} = \mathbf{H}\mathrm{w}, \tag{6.4.3}$$

where, since each OHC is assumed to act locally, the matrix of gains, $\mathbf{H}$, is diagonal and defines a decentralised control system.

Assuming the feedback loops are stable, the overall response can be derived from Eqs.6.4.1-6.4.2. and formulated by

$$u = [G_{up} + \mathbf{G}_{uf}\mathbf{H}(\mathbf{I} - \mathbf{G}_{wf}\mathbf{H})^{-1}\mathbf{G}_{wp}]p. \tag{6.4.4}$$

Equations for the individual responses within the duct are derived in Appendix E.

6.4.1 Overall response with and without feedback

The overall response between the external pressure and the IHC velocity, $j\omega u/p$ according to Eq.6.4.4, is denoted G_{total} here, and is plotted for the passive and active cases below.

The active part of the system is driven by the linear, electromotile responses of the OHCs after their stereocilia are deflected as a consequence of the BM motion. The elongation of the OHC applies force to the upper plate, however, which is

assumed to be delayed in time with regard to the deflections of the stereocilia, so that, in the time domain,

$$f(t) = \gamma w(t - \tau), \tag{6.4.5}$$

where γ denotes the active gain, having the dimension of stiffness [Nm^{-1}], and τ is the delay.

The Fourier transform of Eq.6.4.5 will give

$$\frac{F(j\omega)}{W(j\omega)} = \gamma e^{-j\omega\tau}, \tag{6.4.6}$$

and hence

$$H(j\omega) = \gamma e^{-j\omega\tau}. \tag{6.4.7}$$

The delay was chosen to be equal to 1 ms in order to obtain positive feedback at 1 kHz and for which there is a whole cycle of phase shift at this frequency. Note that the reaction force lags the applied displacement and thus the mechanical impedance has a negative real part, which is characteristic for an active system as discussed in Section 3.3.1.

After formulating all the individual responses of Eq.6.4.4 in Appendix E.5, the overall velocity responses, G_{total}, were calculated for parameters in Table 6.1 and the coefficient of viscosity η=6.6×10^{-4} kgm^{-1}s^{-1}. In the first instance we calculate the passive response, i.e. the duct velocity response G_{total}=$j\omega G_{up}$ since γ=0 and hence H=0, for the 'squirting' waves without and with viscosity taken into account, as shown in Fig.6.8.

Figure 6.8(a) shows sharply tuned resonances in the passive duct response for the lossless 'squirting' waves, but these resonances are heavily damped when the viscosity of the subtectorial fluid is taken into account, as it was predicted by Bell and Fletcher [9], and the overall level of the response along the duct drops by about 80 dB due to the viscosity. However, after introducing feedback from only a single OHC, the predicted resonances are undamped, as shown in Fig.6.9, where the velocity response G_{total} was calculated for the active viscous 'squirting' wave model with the electromotility from the OHC2 (Fig.6.7(a)) and the active

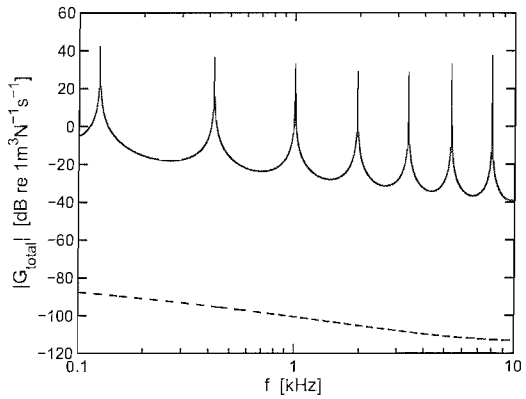

(a)

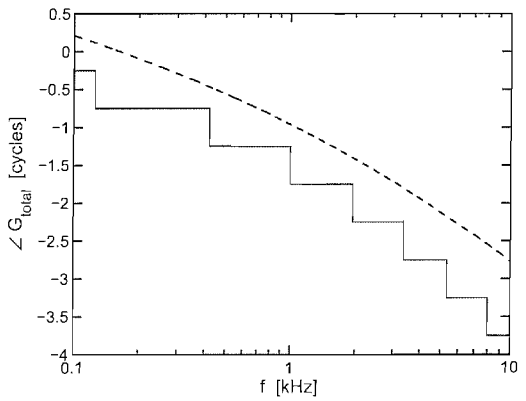

(b)

Figure 6.8: Magnitude (a) and phase (b) of the passive duct velocity response for lossless (solid) and viscous (dashed) 'squirting' waves, as a function of frequency.

gain γ=30. The active OHC force enhances the response at about 1 kHz. In fact, the first resonance frequency in Fig.6.9(a), is somewhat below 1 kHz since the viscosity slows the wave, thus lowering the resonance frequency.

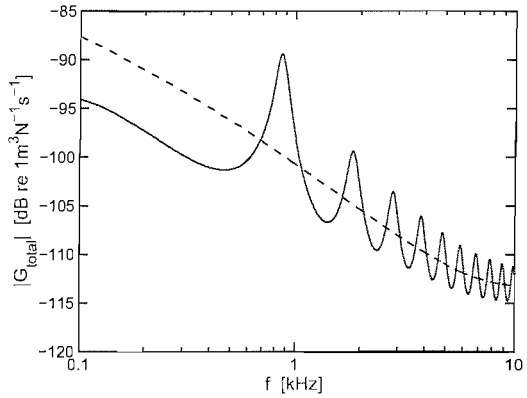

(a)

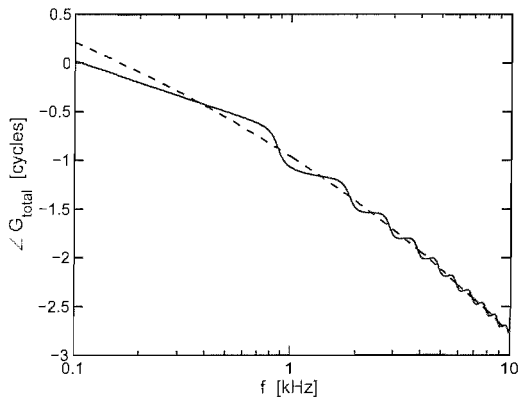

(b)

Figure 6.9: Magnitude (a) and phase (b) of the active (γ=30; solid) and passive (γ=0; dashed) duct velocity response of the 'squirting' wave model with only single active outer hair cell (OHC2), as a function of frequency.

The standing wave resonances in the subtectorial duct are also undamped when all three OHCs are active, (OHC1-3 in Fig.6.7(a)), as shown in Fig.6.10. However, feedback gain of only γ=15 is needed to nearly match the resonance amplitudes in the velocity response with the single OHC active shown in Fig.6.9(a). In this case the gains from all three OHCs were equal, i.e. H_{11}=H_{22}=H_{33} in the

H matrix in Eq.6.4.4.

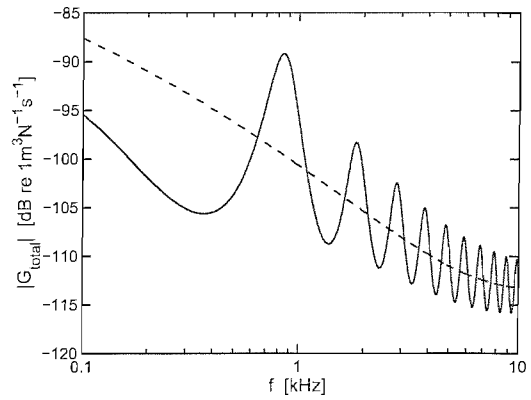

(a)

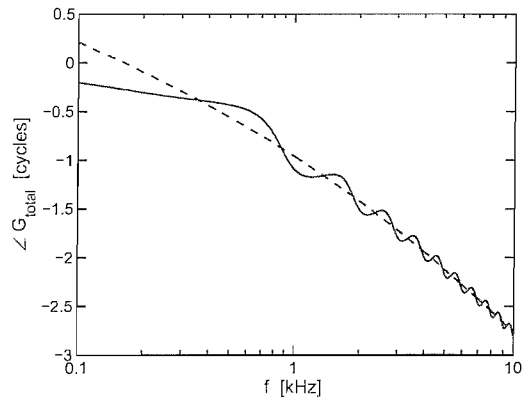

(b)

Figure 6.10: Magnitude (a) and phase (b) of the active (γ=15; solid) and passive (γ=0; dashed) duct velocity response of the 'squirting' wave model with all three outer hair cells active (OHC1-3), as a function of frequency.

In Fig.6.11(a) we show the Nyquist plots for the model with single OHC active, $G_{w_2 f_2} H_{22}$, for the gain of γ=30, and in Fig.6.11(b) for the largest eigenvalue of the model with all three OHCs active, eig($\mathbf{G}_{wf}\mathbf{H}$), for which γ=15 and H_{11}=H_{22}=H_{33}, both evaluated for the frequency range from 100 Hz to 10 kHz[4].

[4]The Nyquist point is on the right-hand side of the origin here since a positive feedback convention is implicitly used in Fig.6.7, instead of on the left-hand side of the origin in Section 5.1, where a negative feedback convention was used.

The eigenvalue analysis of the open loop system for the model with the multichannel feedback, calculating the eigenvalues and eigenvectors of the system at each frequency, was carried out in the same way as described in [7].

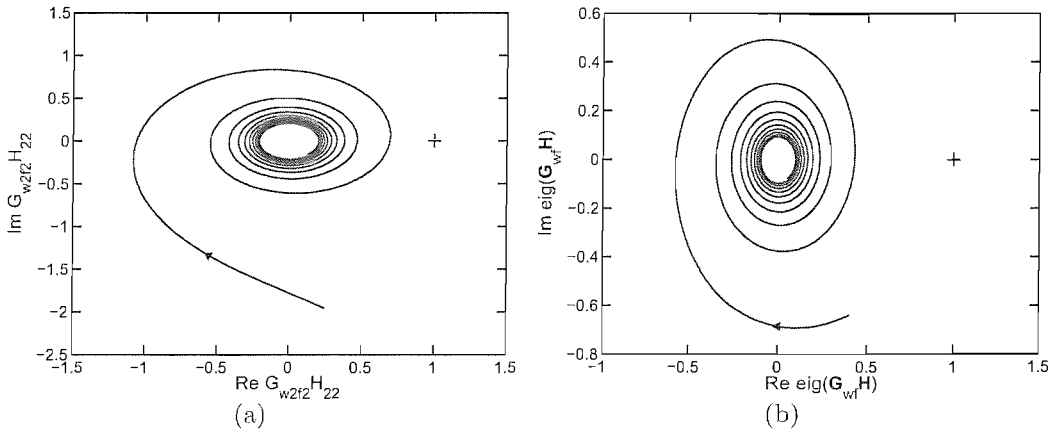

Figure 6.11: The Nyquist plots for the active 'squirting' wave model with only second outer hair cell active (OHC2) and γ=30 (a) and for the largest magnitude eigenvalue of the model with all three outer hair cells (OHC1-3) active and γ=15 (b). The '+' sign indicates the Nyquist point and the arrows indicate the direction of increasing frequency.

It appears that for both the single channel and multichannel feedback active models, the system is stable since the point (+1,0) is not enclosed, but the Nyquist plot passes in its vicinity. Therefore the system enhances the disturbances at this frequency and the response of the system is increased.

6.5 Discussion

In this chapter, the properties of the 'squirting' wave model, proposed by Bell and Fletcher in [9], were investigated. The model was also extended by incorporating the viscosity of the subtectorial fluid into the wave equation and implementing the motility of a single and three OHCs in the feedback loop to give the response of the active model.

It was shown that, because the waves in the duct are attenuated due to the viscosity of the fluid, resonances in the passive response of the duct are very well damped. It was also shown, however, that incorporating the feedback of just a single OHC significantly enhances the overall response of the system, and this effect can also be observed when all three OHCs are active for significantly lower gains. The activity of the OHCs thus provides an efficient and perhaps a sufficient mechanism to overcome the damping in the model.

The OHC stereocilia attached to the TM enable the transfer of the OHC active forces to the TM plate in the 'squirting' wave active model. Because the feedback gains in the active model have dimension of stiffness, reduction of gain could be interpreted as a reduction of the stereocilia stiffness. This reduction would lead to a reduction of the vertical displacement of the upper wall of the subtectorial duct and hence the overall model's response. However, when all three OHCs are active they must collectively force the TM into motion due to the structural coupling in the TM plate, so that the amplitude response of the model is enhanced similarly as in the case with only a single OHC active, even though the gains are halved.

The feedback gain has a phase lag associated with it. It can be understood as 'timing' of the OHC forces transfer to the TM plate, vibrating due to the external pressure alone, in order to obtain most efficient amplification at each frequency. Thus, apart from the correct amplitude of the gain in a model with three OHCs active, to match the response of the model with a single active OHC also the phase of each of the OHCs must be correct. However, the relative phases between the OHC1-3 forces are not studied here.

Finally, it was shown that the system achieves the best performance when operating close to instability, which is thought to be a vital condition for the cochlear amplifier to gain the highest sensitivity in the cochlea [55, 82]. However, significantly lower gains are needed to enhance the response of the model with three OHCs feedback, so that the loops of the Nyquist plots for this model are further away from the Nyquist point than the loops obtained for a single OHC feedback. Thus, the responses of both models are comparable for the gains used here, but the model with three OHCs active is more stable than the model with

only a single active OHC.

Chapter 7

Fluid-elastic wave model

7.1 Elastic half-space model

A model of fluid-structural waves propagating in the radial direction of the subtectorial space within the organ of Corti, that relies on the bulk elasticity of the tectorial membrane, rather than its bending stiffness in the model of Bell and Fletcher [9], was recently suggested by Elliott [20, 22]. Experimental evidence for the elastic model of the tectorial membrane comes from measurements of the mechanical impedance of the TM by Freeman *et al.* [30]. These measurements provide evidence that the dynamic behaviour of this structure, when excited by a force probe, could be represented by a lossy stiffness, which could be modelled reasonably well by a complex stiffness

$$K = K_0(1 + j\mu), \tag{7.1.1}$$

where K_0 denotes the magnitude of the stiffness and μ is a loss factor [20]. The measurements of Freeman *et al.* show that the phase of the mechanical impedance of the tectorial membrane, Z_{TM}, has a nearly constant frequency dependence, and in the transverse direction amounts to about $-60°$. Thus, according to Eq.7.1.1 the phase of the mechanical impedance can be evaluated as $\angle Z_{\mathrm{TM}}=K/j\omega=-\tan^{-1}\frac{1}{\mu}$, so that the loss factor μ in the transverse direction will be approximately 0.5 [20]. Additionally, the measurements of the organ of Corti by Scherer and Gummer [88] revealed viscoelastic properties of the struc-

ture, where both the stiffness and damping of the organ could be reasonably well represented by a lossy spring defined in equation 7.1.1 and the loss factor μ equal to 0.5 [20].

The fluid-elastic wave model assumes that longitudinal fluid waves propagate in the subtectorial space due to the vertical vibrations of the TM. However, because of the experimental results described above, the fluid-elastic model assumes that the waves are sustained by the elasticity of an elastic half-space rather than a thin bending plate, as in the model of Bell and Fletcher [9]. Furthermore, since the stiffness of the RL appears to be much stiffer than that of the TM [88] it is again considered as being rigid in the fluid-elastic model.

For such a model, the predicted mechanical stiffness, according to Shoelson [89], is approximately equal to

$$K = \frac{Ea}{2(1-\nu)}, \tag{7.1.2}$$

where E and ν are the Young's modulus and Poisson's ratio of the elastic half-space and a is the effective radius of the indenter used in the measurements. The Young's modulus of the elastic half-space can be estimated from the above equation and the stiffness measurement of Freeman *et al.* [30], who reported that the dynamic behaviour of the TM measured with a force probe of diameter of $50\,\mu$m ($=2a$) can be represented by a stiffness of approximately $0.2\,\mathrm{Nm}^{-1}$, up to several kilohertz. Thus, assuming the Poisson's ratio of the gelatinous TM to be 0.49, its Young's modulus will be equal to approximately 8 kPa.

7.2 Fluid-elastic waves

In this section the wave equation for the fluid-elastic waves will be derived [22]. A schematic of the subtectorial duct in which the bottom surface corresponds to the rigid RL and the top surface to the TM modelled as an elastic half-space, is presented in Fig.7.1. The height of the duct (thickness of the fluid layer) is assumed to be equal to d=3 μm and the length of the subtectorial duct to L=80 μm similar to the values assumed for the 'squirting' wave model. The coordinate system x, y, z corresponding to the longitudinal, radial and transverse

directions in the cochlea are indicated in the figure. The vertical displacement of the wall of the elastic half-space, $w(y,t)$, and the fluid pressure, $p(y,t)$ are assumed to be functions of the radial position y (position along the duct), whereas the fluid displacements in the y and z directions denoted by $u(y,z,t)$ and $v(y,z,t)$, respectively, are functions of both y and z (position across the fluid layer). All the variables are considered to be constant in the x direction. For clarity of notation, all the variables will be written without their dependence on y, z and t.

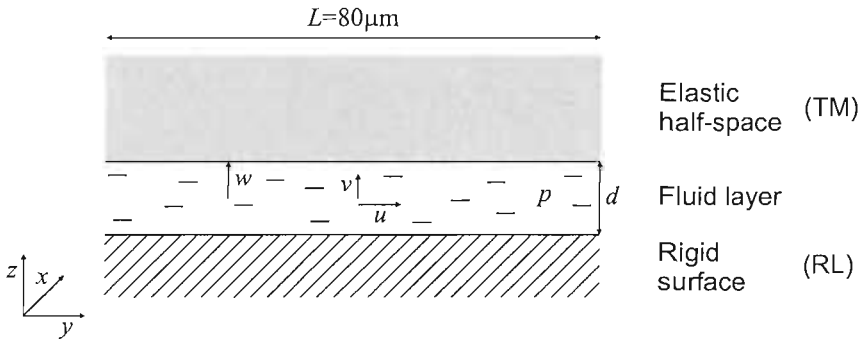

Figure 7.1: Fluid-elastic model of the organ of Corti. The tectorial membrane (TM) is represented by an elastic half-space and the reticular lamina (RL) by a rigid surface both forming a duct of height d and length L. The vertical displacement of the elastic layer is w, whereas the transverse and radial (with respect to the cochlea) fluid displacements are respectively v and u. The fluid's pressure within the duct, p, is also indicated.

Assuming incompressibility of the fluid, the conservation of its mass gives

$$\frac{\partial u}{\partial y} + \frac{\partial v}{\partial z} = 0, \tag{7.2.1}$$

and ignoring the viscous effects in the first instance, if the fluid's density equals ρ, then the conservation of the fluid momentum is expressed as

$$\rho \frac{\partial^2 u}{\partial t^2} = -\frac{\partial p}{\partial y}, \tag{7.2.2}$$

Assuming linear variation of the fluid displacement in the transverse direction,

and knowing that $v(y,0,t)$=0 and $v(y,d,t)$=$w(y,t)$

$$v = \frac{z}{d}\, w. \tag{7.2.3}$$

However, the momentum in the vertical direction z can be ignored assuming that $d \ll \lambda$ [14, 17].

Differentiating Eq.7.2.3 with respect to z and substituting into Eq.7.2.1 gives

$$\frac{\partial u}{\partial y} = -\frac{w}{d}, \tag{7.2.4}$$

and after differentiating the above equation twice with respect to time

$$\frac{\partial^3 u}{\partial y \partial t^2} = -\frac{1}{d}\,\frac{\partial^2 w}{\partial t^2}, \tag{7.2.5}$$

and comparing with Eq.7.2.2 differentiated with respect to y, i.e.

$$\frac{\partial^2 p}{\partial y^2} = -\rho\,\frac{\partial^3 u}{\partial y \partial t^2}, \tag{7.2.6}$$

a second-order wave equation can be obtained

$$\frac{\partial^2 p}{\partial y^2} - \frac{\rho}{d}\,\frac{\partial^2 w}{\partial t^2} = 0. \tag{7.2.7}$$

Assuming that both the elastic half-space displacement and the pressure are of the complex, time-harmonic form, i.e. $w(\omega,k)e^{j(\omega t - ky)}$ and $p(\omega,k)e^{j(\omega t - ky)}$, where ω is the radian frequency and k is the wavenumber, we can write Eq.7.2.7 as

$$-k^2 p(\omega,k) + \frac{\rho\omega^2}{d}\, w(\omega,k) = 0. \tag{7.2.8}$$

According to Graff [38], the ratio of $p(\omega,k)$ and $w(\omega,k)$, which we will refer to as the wall stiffness, can be expressed as

$$\frac{p(\omega,k)}{w(\omega,k)} = \frac{E\left[4k^2(k^2-k_1^2)^{\frac{1}{2}}(k^2-k_2^2)^{\frac{1}{2}} - (2k^2-k_2^2)^2\right]}{2(1+\nu)k_2^2(k^2-k_1^2)^{\frac{1}{2}}}, \tag{7.2.9}$$

where k_1=ω/c_1 and k_2=ω/c_2, where c_1 and c_2 are the compressional and shear wave speed in an infinite medium, respectively.

For a value of k such that, for a given ω, ω/k is equal to the speed of a Rayleigh wave, the wall stiffness in Eq.7.2.9 falls to zero [38]. For materials with $\nu \approx 0.5$ (gel-like materials similar to that of the TM) k_2 is much larger than k_1 and the speed of a Rayleigh wave is nearly the same as the speed of the bulk shear wave. However, assuming that the fluid-elastic wave is travelling slower than the Rayleigh wave, k^2 will be much larger than k_2^2 [22]. Thus, taking into account the above conditions, i.e. $k^2 \gg k_2^2 \gg k_1^2$, Eq.7.2.9 can be reduced to

$$\lim_{k^2 \gg k_2^2 \gg k_1^2} \frac{p(\omega,k)}{w(\omega,k)} = \frac{kE}{(1+\nu)} = S_{wall}, \tag{7.2.10}$$

Using the relationship between the elastic half-space displacement, w, and the pressure, p from the above equation, after differentiating twice with respect to time and substituting into the wave equation in Eq.7.2.7 we have

$$\frac{\partial^2 p}{\partial x^2} - \frac{\rho}{S_{wall} d} \frac{\partial^2 p}{\partial t^2} = 0, \tag{7.2.11}$$

or taking

$$c = \sqrt{\frac{S_{wall} d}{\rho}}, \tag{7.2.12}$$

the wave equation will take a second order form widely used to describe the compressional waves, i.e.

$$\frac{\partial^2 p}{\partial x^2} - \frac{1}{c^2} \frac{\partial^2 p}{\partial t^2} = 0. \tag{7.2.13}$$

It is worth noting here that although the derived wave equation appears in a concise form, the phase velocity of the fluid-elastic wave, using Eq.7.2.12 and Eq.7.2.10 for the wall stiffness in which we substitute for $k=\omega/c$, will be defined by

$$c = \left(\frac{E\omega d}{(1+\nu)\rho} \right)^{\frac{1}{3}}. \tag{7.2.14}$$

Thus the wavespeed of the fluid-elastic wave is dispersive and for the lossless case it is proportional to $\omega^{1/3}$ and so the wavelength $\lambda \propto \omega^{-2/3}$. Figures 7.2(a) and 7.2(b) depict the phase speed and the wavelength of the lossless fluid-elastic

wave calculated according to Eq.7.2.14 for E=8 kPa [30], ν=0.49, d=3 μm [9] and ρ=1000 kgm^{-3} (compare Table 6.1).

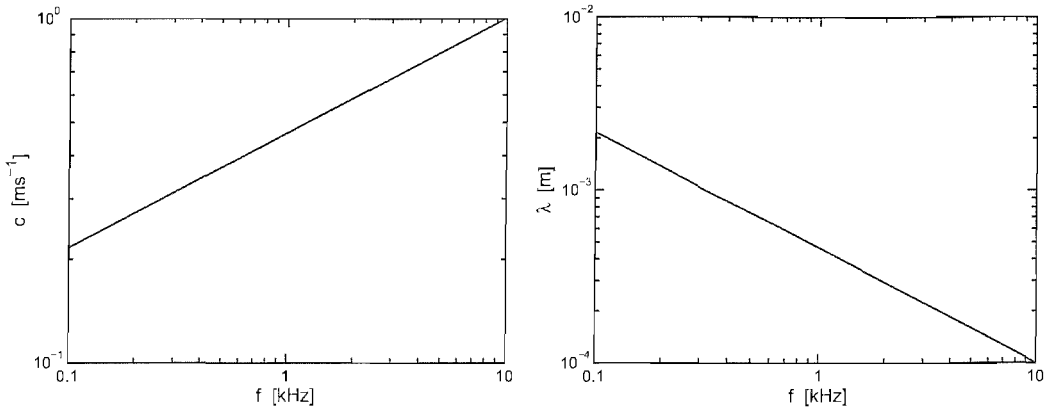

(a) (b)

Figure 7.2: The phase speed (a) and wavelength (b) of the lossless fluid-elastic wave as a function of frequency.

The speed of the fluid-elastic wave when the losses in the subtectorial fluid and the elastic half-space are ignored increases with frequency from about 0.22 ms^{-1} at 100 Hz to about 1 ms^{-1} at 10 kHz, that is by less than a decade in the examined frequency range (an increase of a decade per three decades of frequency according to Eq.7.2.14), as shown in Fig.7.2(a). It can be noted that, for the assumed set of parameters, the lossless fluid-elastic waves propagate with a phase speed of about 466 mms^{-1} at 1 kHz which is very slow comparing to e.g. speed of sound in water, but relatively fast taking into account that the distance these waves have to travel along the subtectorial gap amounts to 80 μm in this model. As predicted from Eq.7.2.14, the wavelength of the lossless fluid-elastic wave decreases with increasing frequency (two decades per three decades of frequency increase), such that at 100 Hz it amounts to about 2.2 mm and to about 0.1 mm at 10 kHz for the assumed parameters. At 1 kHz the wavelength of the lossless wave is equal to about 466 μm, which is roughly six times bigger than the assumed length of the subtectorial duct, L=80 μm.

7.3 Fluid-elastic waves with losses

The viscosity of the subtectorial fluid was shown to affect significantly the propagation of the 'squirting' waves. Because the fluid-elastic waves are assumed to propagate in the gap of the same size, the fluid flow also occurs within the viscous boundary layer in this model and the same force as defined in Eq.6.3.2 for the 'squirting' wave is needed to overcome viscosity effects. Furthermore, according to the measurements of Freeman *et al.* [30], who observed that the local stiffness of the TM reveals a loss, where the loss factor was estimated to be about 0.5, the structural damping in the elastic half-space also has to be taken into account in the propagation of fluid-elastic waves.

Introducing an additional term due to the viscosity of the fluid into the lossless fluid force equation in Eq.7.2.2 gives the same expression as in Eq.6.3.3 obtained to derive the 'squirting' wave equation with losses, which can be also written as

$$\rho \frac{\partial^2 u}{\partial t^2} = -\frac{\partial p}{\partial y} - \frac{16\eta}{d^2}\frac{\partial u}{\partial t}, \tag{7.3.1}$$

and thus, after differentiating the above equation once with respect to y,

$$\rho \frac{\partial^3 u}{\partial y \partial t^2} = -\frac{\partial^2 p}{\partial y^2} - \frac{16\eta}{d^2}\frac{\partial^2 u}{\partial y \partial t}. \tag{7.3.2}$$

Hence, according to the relation in Eq.7.2.4 and Eq.7.2.5,

$$-\frac{\rho}{d}\frac{\partial^2 w}{\partial t^2} = -\frac{\partial^2 p}{\partial y^2} + \frac{16\eta}{d^3}\frac{\partial w}{\partial t}, \tag{7.3.3}$$

which leads to a modified version of Eq.7.2.7 in which the viscosity effect is taken into account, and

$$\frac{\partial^2 p}{\partial y^2} - \frac{16\eta}{d^3}\frac{\partial w}{\partial t} - \frac{\rho}{d}\frac{\partial^2 w}{\partial t^2} = 0. \tag{7.3.4}$$

Assuming again sinusoidal, complex variations of the pressure, $p(y,t)$, and the elastic half-space displacement, $w(y,t)$, Eq.7.2.8 will now take the form

$$-k^2 p(\omega,k) - \frac{j\omega 16\eta}{d^3} w(\omega,k) + \frac{\rho\omega^2}{d} w(\omega,k) = 0. \tag{7.3.5}$$

It was shown in Eq.7.2.10 that the ratio of the pressure and the wall displacement, the wall stiffness S_{wall}, is directly proportional to the Young's modulus and inversely proportional to the wavelength. However, to take the losses in the local stiffness into account, the lossy wall stiffness will be modified by including the lossy version of the Young's modulus $E_0(1+j\mu)$, where E_0 denotes the magnitude of the Young's modulus (compare Eq.7.1.1), and since $\lambda \propto Re\{k\}$ where $Re\{k\}$ is the real part of the wavenumber, it will be formulated by

$$S_{wall} = \frac{p(\omega,k)}{w(\omega,k)} = \frac{Re\{k\}E_0(1+j\mu)}{(1+\nu)}, \tag{7.3.6}$$

where μ is the damping factor of the elastic half-space. Thus, in the frequency domain,

$$-k^2 p(\omega,k) - \frac{j\omega 16\eta(1+\nu)}{Re\{k\}E_0(1+j\mu)d^3}p(\omega,k) + \frac{\rho\omega^2(1+\nu)}{Re\{k\}E_0(1+j\mu)d}p(\omega,k) = 0, \tag{7.3.7}$$

so that the dispersion relation for the fluid-elastic waves with the losses taken into account takes the form

$$k^2 Re\{k\} = \frac{\rho\omega^2(1+\nu)}{E_0(1+j\mu)d} - j\,\frac{16\eta\omega(1+\nu)}{E_0(1+j\mu)d^3}, \tag{7.3.8}$$

which can be solved to give a complex wavenumber at each frequency using the method described in Appendix F.

Figure 7.3 depicts the phase speed, wavelength, the real part of k, and the imaginary part of the wavenumber (or attenuation coefficient), for the fluid-elastic wave with losses taken into account. The light solid line represents the quantities with the losses set to zero, i.e. μ=η=0, for comparison. The dashed, dotted and thick solid lines correspond to waves with the losses only in the elastic half-space (μ=0.5, η=0), losses only in the fluid (μ=0, η=6.6×10^{-4} kgm^{-1}s^{-1}) and losses in both the elastic half-space and the fluid (μ=0.5, η=6.6×10^{-4} kgm^{-1}s^{-1}). All the parameters used for calculation are listed in Table 7.1.

Figure 7.3(a) reveals that the wavespeed of the fluid-elastic wave in which the losses in the elastic half-space were taken into account, is almost parallel to and slightly higher than that of the wave with no losses in the whole examined frequency range. However, when only the viscosity of the fluid is taken into account

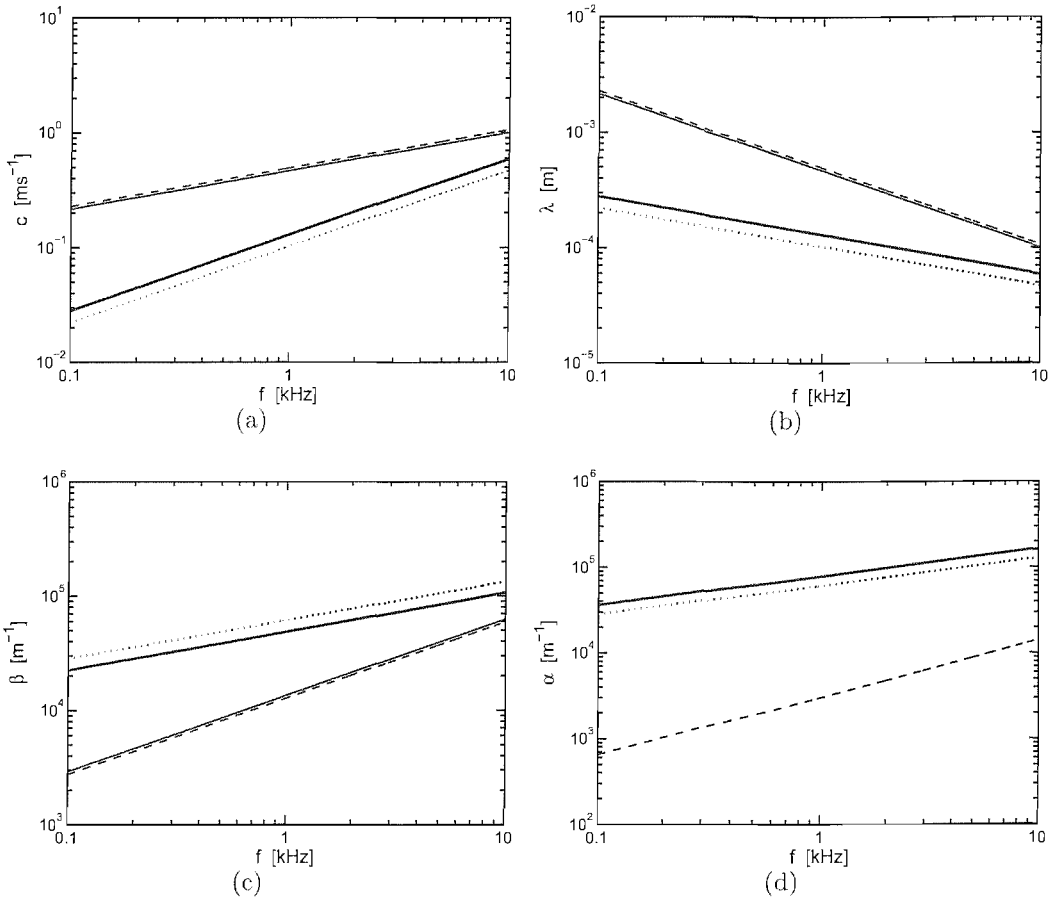

Figure 7.3: The phase speed (a), wavelength (b), the real part of the wavenumber, β, (c) and the attenuation coefficient, α, (d) of the fluid-elastic wave with no losses (μ=η=0; light solid), losses only in the elastic half-space (μ=0.5 and η=0; dashed), losses only in the fluid (μ=0 and η=$6.6\times10^{-4}\,\mathrm{kgm^{-1}s^{-1}}$; dotted) and with losses in both elastic half-space and the fluid (μ=0.5 and η=$6.6\times10^{-4}\,\mathrm{kgm^{-1}s^{-1}}$; thick solid) plotted as a function of frequency.

PARAMETER	VALUE
E_0 [kPa]	8
d [μm]	3
ν	0.49
ρ [kgm^{-3}]	1000
η [kgm^{-1}s^{-1}]	6.6×10^{-4}
μ	0.5

Table 7.1: Parameters used for the simulations of the fluid-elastic waves.

the magnitude of the phase speed of the fluid-elastic wave is significantly reduced in comparison with the lossless wave, but it increases faster with frequency. When the losses from both the elastic half-space and the fluid are considered, the speed of the wave increases slightly in comparison with the one calculated for the wave with only viscosity taken into account. Thus the slope of the wavespeed in this case is still higher than the slope of a lossless fluid-elastic wave. The losses in the subtectorial fluid thus have a bigger influence on the propagation of the fluid-elastic waves than the losses in the elastic half-space.

The wavelength of the fluid-elastic wave for which the damping in the elastic half-space was taken into account, dashed line in Fig.7.3(b), decreases with an increase of frequency, and it is slightly higher than the one of the lossless wave though both curves have nearly the same slopes. When the fluid-elastic wave is attenuated by the viscosity of the fluid only, the wavelength of the wave decreases with frequency significantly slower than the wavelength of the lossless wave.

The wavelength of the fluid-elastic wave at 1 kHz, when fluid and elastic losses are accounted for, is equal to about 130 μm, which is roughly one and a half times the assumed duct length, L. The attenuation coefficient in Fig.7.3(d) is also most strongly affected by the fluid viscosity and is about $10^5\,\mathrm{m}^{-1}$ at 1 kHz, which corresponds to an attenuation of about 54 dB per wavelength travelled. Thus the viscosity of the fluid has the major effect on the propagation of the fluid-elastic waves, slowing the waves significantly in comparison with the lossless waves, and adding significant attenuation.

7.4 Response of the model to OHC excitation

In the previous sections, the fluid viscosity was shown to severely attenuate the fluid-elastic wave. The action of the outer hair cells, however, might again help to overcome the effect of these losses (and so enhance the response at particular frequencies), as it was shown to do for the 'squirting' wave model.

The assumed geometry of the subtectorial space in the fluid-elastic model can be represented schematically as in Fig.7.4. The length of the subtectorial duct is again assumed to be equal to L=80 μm with the IHC located at y=0, and the first, second and third row of the OHCs located at positions y equal to l_1=30 μm, l_2=50 μm and l_3=70 μm, respectively. The duct is again driven by an external pressure, p_{ext}, which displaces the thin fluid layer at the position of the IHC by u. The OHC is assumed to contract and elongate, and hence produce a fluctuating area displacement into the duct, s, which is assumed to produce a localised pressure, p, that displaces the wall of the elastic layer by w, and enhances the displacement of the subtectorial fluid, u at y=0.

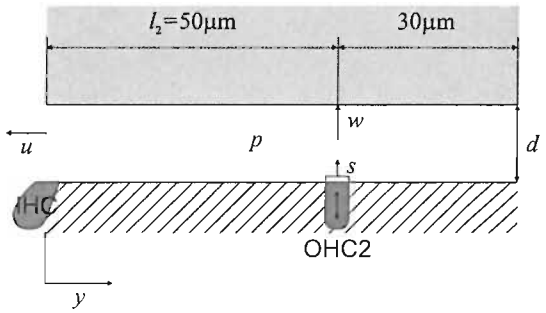

Figure 7.4: Schematic of the subtectorial space duct of length L=80 μm in the organ of Corti with indication of the inner (IHC) and second outer hair cell (OHC2). A volume displacement, s, due to the action of the outer hair cell, the pressure load, p, the elastic layer's displacement, w, and the displacement, u, of the subtectorial fluid, are also shown.

The control block diagram used for the active 'squirting' wave model, shown in Fig.6.7, can again be used to calculate the overall active response of the fluid-elastic model. The modified control system is shown in Fig.7.5(b), where the

external pressure p and the OHC area displacements, s, drive the fluid displacement, u, at the end of the duct and the duct wall displacements, w, to constitute the duct response $\mathbf{G}$.

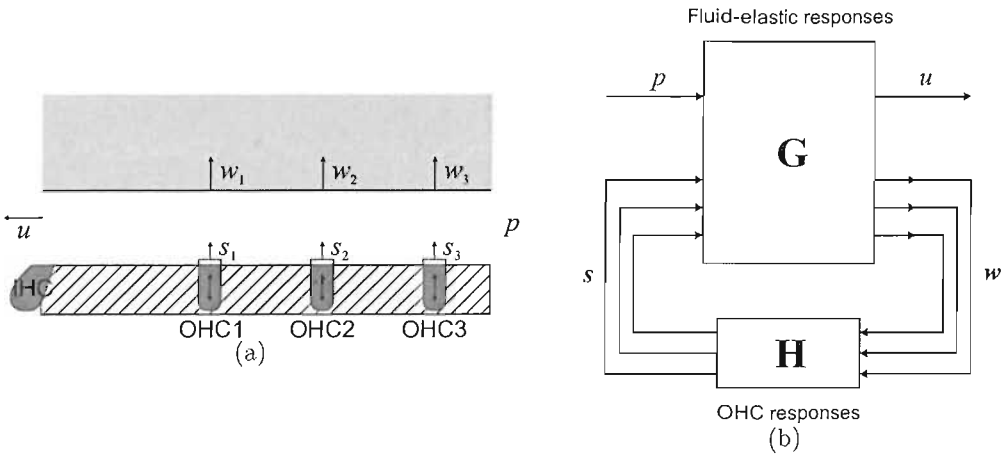

Figure 7.5: Schematic of a duct comprising of a rigid surface (bottom) and an elastic half-space (top) with the internal inputs from the outer hair cells, s_{1-3}, and outputs being the elastic layer's wall displacements, w_{1-3}. The external input, the pressure of the endolymph, p, and the external output, subtectorial fluid displacement, u, are also shown. The active fluid-elastic wave model represented as a control block diagram is shown on the right.

The governing equations for the fluid and wall displacement, assuming the system in Fig.7.5(b) is linear, are similar to those for the 'squirting' wave active model and take the form

$$u = G_{up}\, p + \mathbf{G}_{us}\mathbf{s}, \tag{7.4.1}$$

$$\mathbf{w} = \mathbf{G}_{wp}\, p + \mathbf{G}_{ws}\mathbf{s}, \tag{7.4.2}$$

where G_{up} is the response at the IHC due to the external pressure excitation, G_{us} relates the fluid displacement at the IHC to the internal source area displacement, G_{wp} specifies the elastic half-space wall displacement due to the external pressure input, and finally G_{ws} relates the wall displacement due to the internal area

displacement excitation. The area displacement due to the outer hair cell motility and the displacement of the elastic layer are assumed to be related by

$$\mathrm{s} = \mathbf{H}\mathrm{w}, \tag{7.4.3}$$

where the controller matrix, $\mathbf{H}$, is again diagonal because each of the components of the vector of sources, s, is thought to only act locally. However, the controller gain is formulated in a different way than that of the 'squirting' wave model, in which $H(j\omega)$ had a constant, unit magnitude and a linear phase lag. Here, a second-order low-pass filter function of the form

$$H(j\omega) = \frac{S(j\omega)}{W(j\omega)} = \gamma \left(\frac{1}{1 + j\omega\tau} \right)^2, \tag{7.4.4}$$

is used for the OHC gain, where γ denotes a gain term with units of [m] and τ is a time constant. A second-order, low-pass filter is also used in the model of Neely [66] discussed in Section 3.5, although the gain function defined in Eq.7.4.4 is a simplified version of that used by Neely, H_c, since $\tau_f{=}\tau_r{=}\tau$ and $g_f{=}g_r{=}1$.

The overall response of the system shown in Fig.7.5(b), can again be derived according to Eqs.7.4.1-7.4.3, and will take the form

$$u = \left[G_{up} + \mathbf{G}_{us}\mathbf{H} \left(\mathbf{I} - \mathbf{G}_{ws}\mathbf{H} \right)^{-1} \mathbf{G}_{wp} \right] p, \tag{7.4.5}$$

To solve for the constitutive responses of the overall system response, expressions must again be derived for the pressure in the duct of the subtectorial space, and the elastic half-space and subtectorial fluid's displacements due to the external pressure and area displacement source excitation. The derivations of the individual responses in Eq.7.4.5, are set out in Appendix G.

7.4.1 Response with and without feedback

Equation 7.4.5 can be used to define the total response, G_{total}, from external pressure to velocity at the IHC, $j\omega u/p$. Figure 7.6 shows the overall velocity response of the passive fluid-elastic wave model without and with the losses taken into account, i.e. for $\mu{=}\eta{=}0$, and $\mu{=}0.5$ and $\eta{=}6.6{\times}10^{-4}\,\mathrm{kgm^{-1}s^{-1}}$, respectively. A single, sharp resonance can be observed in the response of the lossless model

at about 5 kHz for the examined frequency range. However, this resonance is damped when the losses are taken into account and the level of the response again drops by about 80 dB.

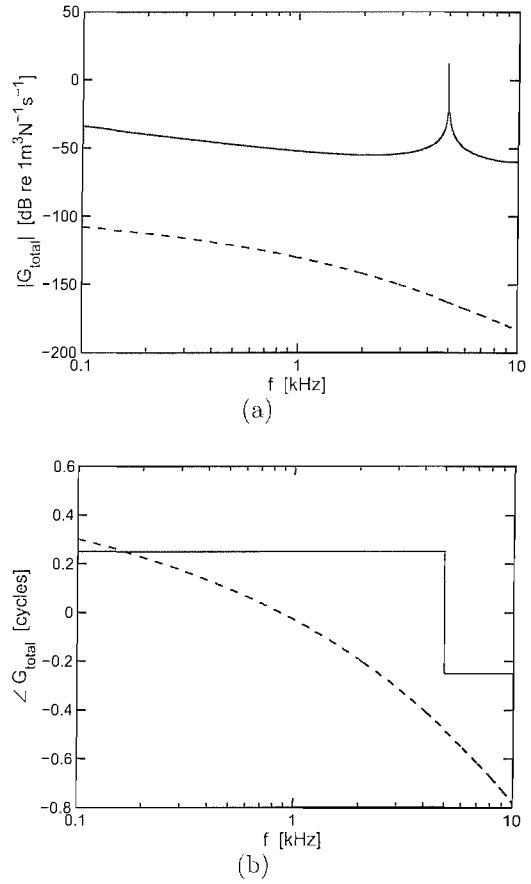

Figure 7.6: Magnitude (a) and phase (b) of the passive duct velocity response for lossless (solid) and lossy (dashed) fluid-elastic waves, as a function of frequency.

The OHC gain, defined in terms of a second-order, low-pass filter (Eq.7.4.4), is assumed to have the same form for all three OHCs, and it is shown as a function of frequency in Fig.7.7 for the time constant τ=45 μs and the gain of γ=22.5 μm.

When only the middle outer hair cell, OHC2, is active, a resonance is again observed as shown in Fig.7.8, which is now at about 1 kHz due to the effects of viscosity and the low-pass OHC filter characteristics, i.e. the time constant τ=45 μs, which was chosen by trial and error to tune the resonance to 1 kHz. The

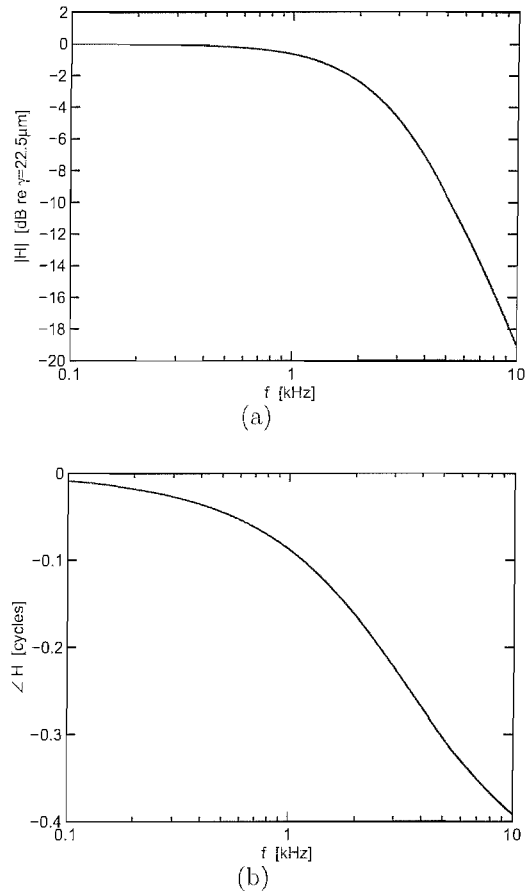

Figure 7.7: Magnitude (a) and phase (b) of the outer hair cell gain function, $H(j\omega)$, calculated for the gain of γ=22.5 μm and the time constant τ=45 μs.

active gain was set to 22.5 μm for the single channel feedback.

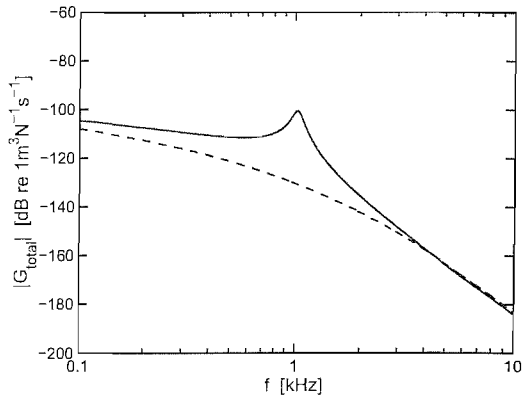

(a)

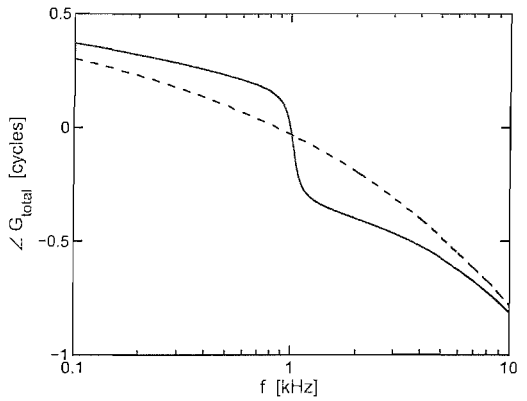

(b)

Figure 7.8: Magnitude (a) and phase (b) of the active (γ=22.5 μm; solid) and passive (γ=0; dashed) duct velocity response of the fluid-elastic wave model with only single outer hair cell active (OHC2), as a function of frequency.

A slightly lower gain of γ=20 μm is needed to undamp the resonances within the subtectorial gap when all three OHCs (OHC1-3) are active, as shown in Fig.7.9. However, the main resonance peak is shifted in this case to about 700 Hz, and a second damped resonance can be observed above 1 kHz. The response of the multichannel feedback controller in the fluid-elastic model requires almost the same value of gain to achieve this resonance in the subtectorial space as in the single OHC case. This situation contrasts with the 'squirting' wave model

in which the duct dynamics more strongly influenced the overall response of the model. Nevertheless, it is clear that the OHC local action can enhance the response of the model if its dynamics are correctly tuned.

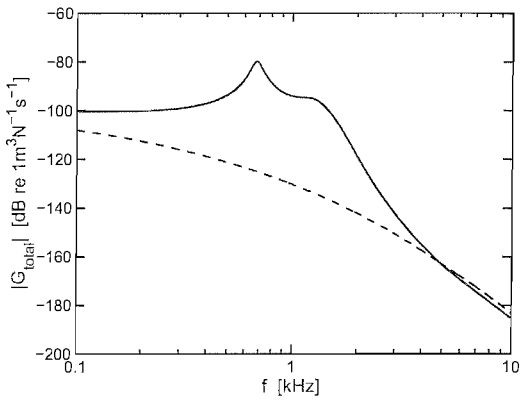

(a)

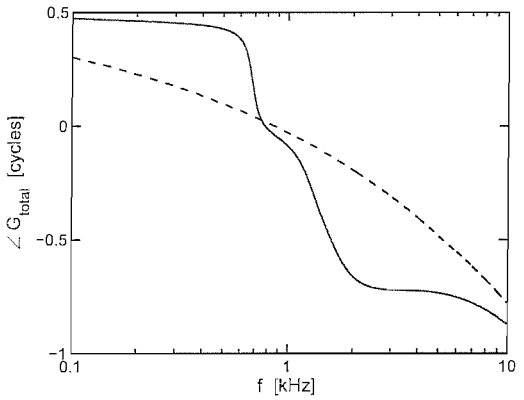

(b)

Figure 7.9: Magnitude (a) and phase (b) of the active (γ=20 μm; solid) and passive (γ=0; dashed) duct velocity response of the fluid-elastic wave model with all three outer hair cells active (OHC1-3), as a function of frequency.

Figures 7.10(a) and 7.10(b) show the Nyquist plots of the single channel feedback controller $G_{w_2s_2}H_{22}$ for γ=22.5 μm and τ=45 μs, and for the largest eigenvalue of the multichannel feedback controller, $\mathbf{G}_{ws}\mathbf{H}$, calculated for γ=20 μm and τ=45 μs. The frequency used for the calculation of the Nyquist plots was set to 100 Hz–10 kHz.

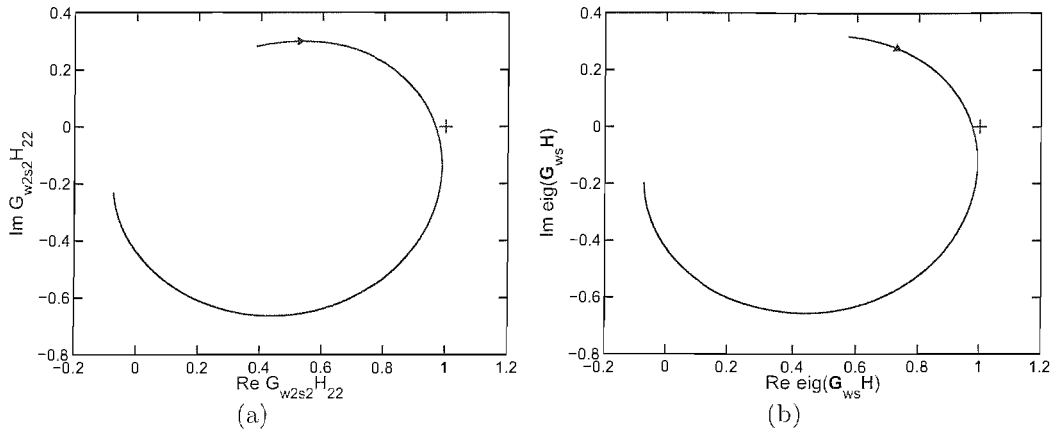

Figure 7.10: The Nyquist plots for the active fluid-elastic wave model with only second outer hair cell active (OHC2) and γ=22.5 μm (a) and for the largest magnitude eigenvalue of the model with all three outer hair cells (OHC1-3) active and γ=20 μm (b). The '+' sign indicates the Nyquist point and the arrows indicate the direction of increasing frequency.

It can be seen from Fig.7.10 that both the single channel and multichannel feedback models are stable since the corresponding Nyquist plots do not enclose the (+1,0) point. However, in both cases the Nyquist plot passes in the vicinity of (+1,0), at about 1 kHz in the single channel model and about 700 Hz in the multichannel model, so that the overall responses, G_{total}, are enhanced at these frequencies.

7.5 Discussion

The use of the fluid-elastic model proposed by Elliott [20] in an active model, was examined in this section. The physics of the fluid-elastic waves in the subtectorial space of the organ of Corti were investigated and a feedback controller model was proposed by incorporating the motility of a single and three OHCs to overcome the effects of viscosity of the subtectorial fluid and undamp the overall response of the model.

As for the 'squirting' wave model discussed in Chapter 6, feedback from only a

single OHC is required to enhance the overall response of the fluid-elastic model. If all three OHCs are active, the enhancement of the modelled overall velocity response can be also observed for a slightly lower gain, although a shift of the first resonance peak towards lower frequency and a second, damped resonance could be observed in this case. Nevertheless, if the controller model is tuned correctly, the activity of the OHCs appears to provide sufficient means to overcome damping in the model. It was also shown that to achieve this, the system must again be operating close to instability.

The OHC gain in the fluid-elastic model is of the form of a second-order low-pass filter which is a simplified version of the OHC gain function proposed by Neely [66]. It can be physiologically identified with the filtering properties of the OHC as it was done for the Neely model. However, the OHC gain and phase in the fluid-elastic model were tuned to obtain positive feedback at 1 kHz and may not be physiologically realistic.

The dimension of the OHC gain in the fluid-elastic wave model is that of a displacement since it is defined by the ratio of the TM displacement to the area displacement of the RL due to the OHC motility. The transfer of force via the tallest row of stereocilia embedded in the TM is neglected in this case, and it is assumed that the local area displacement of the RL is transferred to the TM via the incompressible fluid in the subtectorial space.

The TM in the fluid-elastic model does not possess the bending stiffness as it was in the case of the 'squirting' wave model, so that the displacements of the TM are local and decrease significantly when the gain of the OHC feedback is reduced. Thus, we can obtain comparable amplitudes of the overall responses of the fluid-elastic model with three OHCs active to those of the model with a single OHC active, only when the OHC gains have comparable magnitudes. This also causes the Nyquist plots to pass very close to the point of instability in both cases.

The model of the TM considered as an elastic half-space seems to be more physiologically plausible, than the plate model of the TM proposed by Bell and Fletcher [9], since the TM is usually described as a gelatinous structure (Chapter 2). However, both models require feedback from the OHCs to amplify the motion

of both types of waves in the subtectorial space. This is in agreement with the measurements of Nowotny and Gummer [74], who observed more complex dynamics of the subtectorial space, than those suggested by the lumped parameter models of the organ of Corti, as a result of the OHC somatic motility.

The complex, counterphasic motion of the RL and TM was observed by Nowotny and Gummer for frequencies up to about 3 kHz [74]. Above this frequency these authors suggest that the OHC somatic motility couples mainly with the BM motion inducing the shearing motion between the RL and TM, as it was shown for the classical lumped parameter models in Chapter 3. Therefore, the 'squirting' or fluid-elastic mode of fluid motion in the subtectorial space should be interpreted as an additional mechanism of amplifying the transduction at the IHCs and contributing to the cochlear amplifier observable at the level of the BM.

A number of assumptions have had to be made to obtain numerical results for both of these models, which remain to be tested, and so this study must only be considered as preliminary. It is hoped that a combination of modelling and direct observation could be used to refine our knowledge of the dynamics in the subtectorial space, and thus better understand the mechanisms of amplification in the cochlea.

Chapter 8

Conclusions and suggestions for future work

8.1 Lumped parameter cochlear models

8.1.1 Micromechanical models of the cochlea

Three micromechanical models of the cochlea were analysed in Chapter 3. The model of Allen proposed in 1980 [1] introduces the second vibrational degree of freedom into the formulation of the CP impedance, which corresponds to the radial motion of the TM and introduces a spectral zero in the model's response. Although the model of Allen is passive it provides important insight into the dynamics of the organ of Corti structures.

The micromechanics in the models of Neely and Kim [68] and Neely [66] employ the idea of the secondary resonator connected with the radial motion of the TM and include a local feedback loop to account for the mechanism of the cochlear amplifier. The analysis of the modes of vibration of both models carried out in Sections 3.4 and 3.6 reveals two separate modes of vibration for the basilar and tectorial membranes, which vibrate in and out of phase with each other, respectively.

The mobility of the CP in the micromechanical models of Neely and Kim [68] and Neely [66] is modified by an additional, active component modelling the

electromotile action of the OHCs. This component causes the real part of the CP mobility to become locally negative, so that the model's response is undamped. However, the active component in the model of Neely and Kim [68] is modelled as a pressure source acting on the BM, whereas in the later model of Neely [66], it is modelled as a displacement source between the BM and RL, that is inside the organ of Corti. Also, the model of the OHCs is represented by a negative damper in the model of Neely and Kim, while it is of the form of a second-order low-pass filter in the model of Neely, which is thought to represent the low-pass filtering properties of the OHC membrane.

Although the response of the active models of Neely and Kim and Neely resemble the responses observed for a real cochlea, we note that the active pressure in the model of Neely and Kim is not reacted by any other structure, which does not seem physically plausible. On the other hand, we argue that the active contribution to the BM displacement in the model of Neely would be affected by the TM's inertia, an effect not accounted for by Neely. Therefore, in Section 3.7 the original model of Neely has been extended by adding an additional mass component to his two DOF system, and the effects of such a loading on the action of the cochlear amplifier and response of the model have been investigated. The CP mobility of the modified model of Neely exhibits a roll-off in the region above the characteristic place or CF in contrast to increasing mobility for the original model of Neely in these regions. Also the active gain for which the modified model of Neely is still stable is reduced with respect to that observed for the original Neely model.

Finally, the mechanical parameters used for the simulations of the model of Neely [66] differ significantly from those used by Neely and Kim in 1986 [68]. The ratio of BM and TM masses are physiologically unrealistic in the model of Neely [66], since it suggests that the mass of the TM is a few orders larger than that of the BM. This choice of parameters causes the distribution of the natural frequency corresponding to the BM component of the two DOF system to be shifted to frequencies well above the distribution of the corresponding natural frequency calculated according to parameters chosen by Neely and Kim in 1986 [68], though the passive micromechanics of both models were found to be similar.

The parameters chosen for the simulations are fitted to obtain coupled responses comparable to those observed from a cat cochlea, rather than being based on the real mechanical properties of the cochlear structures.

8.1.2 Coupled responses of the cochlear models

The mobility functions of the cochlear micromechanical models of Neely and Kim [68] and Neely [66] were incorporated into the finite difference approximation of the wave equation of the cochlear travelling wave and the coupled responses of these models were calculated in Chapter 4. The activity and tuning of the models was examined, and it was observed that setting the gain parameter γ to zero gives a broad, passive response like the one observed for a dead cochlea. However, for γ equal to one the responses were sharply tuned with a peak at characteristic place or frequency similarly to the responses of a live cochlea.

The acoustically stimulated passive BM and TM velocity responses were also derived to compare with experimental results of Gummer *et al.* [40] and Hemmert *et al.* [43]. It was found that the modelled responses resemble quite well the BM and TM velocity responses measured by Hemmert *et al.* The agreement with the measurements of Gummer *et al.* was much poorer, although the main features of the modelled responses could be found in the experimental ones. This discrepancy can be attributed to the likely contamination of the measurements of Gummer *et al.* due to the unsealed cochlea artefacts.

8.1.3 Stability and quasi-linear cochlear models

The Nyquist criterion has been used to assess the stability of various micromechanical models in isolation. These models are closer to instability, and hence give more enhancement, near the base than the apex of the cochlea. It is shown that frequency responses calculated from these models can be misleading unless stability is ensured, and can erroneously lead to a conclusion that increasing the cochlear amplifier gain can lead to decreases in the BM response as in [50].

The quasi-linear technique is a simple method of incorporating compressive nonlinearity into the calculated frequency response. The method has been ex-

tended to include the micromechanical model of Neely and Kim [68], as used elsewhere in the thesis, with both global and local variation of the cochlear amplifier gain. Results are in qualitative agreement with the BM responses measured at different amplitudes.

It was noted that under some conditions the quasi-linear approach can lead to unrealistic frequency responses, which are thought to be due to instability in the coupled model. There is thus clearly a need for analysis tools which allow the stability of the coupled models to be analysed.

8.2 Distributed model for the fluid in the subtectorial space

Two fluid-structural wave models have been examined for the fluid in the subtectorial space, the 'squirting' wave model of Bell and Fletcher [9] and the fluid-elastic model of Elliott [20], to investigate their possible contribution to the amplification of the cochlear response. The original model of Bell and Fletcher has been extended by incorporating the viscosity of the subtectorial fluid into the wave equation for the 'squirting' wave to examine its effect on the wave dynamics.

It was shown that both types of waves are slow and dispersive, and that the subtectorial fluid's viscosity damps the standing wave resonances that are predicted in the duct. However, it was also shown that implementing feedback from only a single OHC into the fluid-structural wave model is sufficient to overcome the effects of viscosity and undamp the resonances in the duct. Feedback from all three OHCs acting simultaneously enhances the response of these models even more. This observation suggests that local motion in the subtectorial space could provide another mechanism for cochlear amplification by providing direct coupling of the OHC motility to the transduction at the IHC and contributing to the cochlear amplification at the level of the BM.

It would appear that the fluid-elastic model is more plausible and consistent with the measurements of the organ of Corti and the TM impedance, since it would appear more reasonable to model the TM as a gel-like structure than a bending beam. It has to be noted, however, that significant assumptions have

been made about the geometry and material properties of the TM and the action of the OHCs, which require validation.

8.3 Suggestions for future work

8.3.1 Further comparisons between the measured and modelled motion of the BM and TM

Although some initial comparisons have been made between the micromechanical model of Neely and Kim [68] and the measurements of Hemmert *et al.* [43], uncertainty over the conditions of measurements makes it difficult to draw clear conclusions.

The vibration pattern of the BM and TM measured by Gummer *et al.* [40] was distorted by an artefact of the cochlear preparation used in their experiment, the so-called unsealed cochlea condition. It was shown by Cooper and Rhode [10] and Dong and Cooper [18] that the hole drilled in the cochlear wall to enable an optical measurement of vibration of the organ of Corti structures, must be sealed properly to avoid contamination by fast travelling waves in the cochlea. These fast travelling waves are thought to distort what would be a classical pattern of the BM/CP vibration as observed by e.g. von Békésy [8], referred to as a slow travelling wave in [10, 18] or [42], by introducing additional resonances and antiresonances in the vibration pattern. Alternatively, an off-line mathematical procedure, described e.g. by Hemmert *et al.* [42], can be used to correct the measured vibration response for the fast travelling wave component.

Instead of correcting the experimental results, it may be possible to simulate the conditions under which the actual measurements were taken. The measured fast travelling component could be modelled using a lumped parameter macromechanical model in which the cochlear chamber was assumed to have a hole in its wall as the one drilled in the cochlear wall in the physiological experiments. The size of the hole, say the area being the product of the CP's width and assumed number of CP longitudinal slices, could be modelled by a local change in the 'wall' boundary conditions of the cochlear chambers. Furthermore, two separate cases

of such a model can be considered due to the methodology of the physiological experiments. The hole could be defined in the apical portion of scala vestibuli (upper chamber of the macromechanical model) or in basal region of scala tympani (lower chamber of the macromechanical model) wall of the cochlea, enabling a comparison of the model's results with the measurements in the apical or basal, respectively, regions of the cochlea. Additionally, the generation of the fast travelling wave and its effect on the cochlear response could be modelled by the so-called push-push (pull-pull) condition at the oval and round windows of the cochlea [59], to compare with experimental results and the model with the hole in the cochlear chambers.

8.3.2 Estimation of the shear gain

The shear gain g defined in the model of Allen [1], was assumed to be equal to one in the simulations of the models of Neely and Kim [68] and Neely [66]. According to Eq.3.2.5 the shear gain can be estimated from the ratio of the height of the organ of Corti, h, and the width of the BM, W. In his 1986 paper Lim [58] refers to the measurements of the dimensions of the organ of Corti and inclination of the RL with respect to the BM in the chinchilla cochlea (Fig.2 and 3 in [58]). Knowing the dimensions of the organ of Corti or the angle of the RL's inclination and the BM width at a certain longitudinal position in the cochlea we can estimate the height of the organ of Corti at this position (and perhaps certain radial position), and hence g. The estimate of g could be also compared with an estimate in which the height of the cilia, was taken into account, according to Eq.3.2.4.

More importantly, knowing the height of the organ of Corti at a specific radial, W_1, and longitudinal, x, position in the cochlea from such a geometrical derivation, as well as measuring the magnitude of the BM displacement ξ at the same longitudinal and radial position, and the height of the subtectorial space, we could indirectly derive the amount of the radial shear displacement from Eq.3.2.3 and examine the assumptions of Allen about the geometry of the shearing mechanism. On the other hand, having measured for example the transverse motion of the BM and the radial motion of the TM simultaneously as it was done

e.g. by Hemmert *et al.* [43], and knowing the radial position of the measurement, W_1, using Eq.3.2.3 we can also examine if the sum of $\epsilon+h$ is constant, which could provide some information about the rigidity of the organ of Corti or the OHC stereocilia.

8.3.3 Modelling the dynamic properties of the OHC

Many different models of the OHC's overall dynamics, from stereocilia deflection to somatic length change, have been used in the literature, and different models are used at various places within the thesis reflecting this diversity. The models generally have a low-pass characteristic, but the cut-off frequency of the filter is currently adjusted by different authors, including this one, to give the best results with their particular models rather than being based on direct physiological measurements. These measurements are very difficult and depend on the mechanical as well as the chemical environment of the cells, but are very important if the plausibility of any model is to be established.

8.3.4 Comparisons between the measured and modelled fluid motion in the subtectorial space

More detailed comparison of the model predictions with measurements of motion of individual parts of the organ of Corti can be carried out using results of e.g. Nowotny and Gummer [74]. Nowotny and Gummer have measured the dynamics of the subtectorial space, which was modelled by the fluid-structural models presented in the thesis. The shape changes of the subtectorial gap during external electrical field stimulation in the measurements of Nowotny and Gummer could give information about the relative phases of the OHCs action, and could be modelled using the fluid-structural wave models. These shape changes could be also used to compare with the assumed motions between the RL and the TM in the micromechanical models. Of even greater importance would be to compare the measured and predicted OHC action under acoustic excitation, although such measurements would be very difficult to take. Finally, the boundary conditions assumed for the fluid-structural models could be analysed with regard to the

results obtained by Nowotny and Gummer in [74].

8.3.5 Incorporation of the middle and outer ear model

The coupled models presented in the thesis assume sinusoidal excitation at the stapes. The coupled models could be thus extended by incorporating a middle and outer ear model as it was done in e.g. [55], [68] or [66]. In such a case the stimulation of the coupled model could be expressed in terms of the sound pressure level at the eardrum and so could be the responses of the quasi-linear model of the cochlea presented in this work.

8.3.6 Physical parameter estimation

Further work regarding the estimation of the physical parameters used in the models should be carried out. Although it is hard to obtain these parameters directly from the physiological measurements, so that they are usually fitted to the model, the analysis of the modes of vibration could be done for any lumped parameter cochlear model to assess the plausibility of the assumed mechanical parameters. A more physiologically realistic and uniform set of geometrical and mechanical parameters is also required for the fluid-structural models.

8.4 Conclusions

In this thesis the basic concepts of the micromechanical modelling of the cochlea were investigated. The dynamics of two classical cochlear models proposed by Neely and Kim [68] and Neely [66] was examined in terms of the models' original assumptions and the mechanism of the cochlear amplifier. An analysis of the modes of vibration of the above models was shown here for the first time. The stability analysis was also carried out for these models in order to ensure the validity of their CP mobility responses, which was not done in the original work of Neely and Kim [68] and Neely [66].

Another novel aspect of the present thesis is the derivation of the coupled velocities of the BM and TM using the CP mobility responses for both the Neely

and Kim model and the model of Neely, and comparison with the relative motion of these structures measured by Gummer *et al.* [40] and Hemmert *et al.* [43]. Furthermore, the model of Neely and Kim was extended to include the compressive nonlinearity in the cochlea and the original model of Neely was modified to investigate the effect of the TM inertia on the model's dynamics and the active contribution to the BM displacement.

The dynamics of the 'squirting' wave model proposed by Bell and Fletcher [9] were examined here. The model was extended by incorporation of viscosity into the wave equation for the 'squirting' waves to examine its effect on their propagation in the subtectorial space. Finally, a feedback controller model was proposed for coupling the OHC motility with the IHC transduction and investigating the role of the 'squirting' waves in the amplification of the cochlear response.

A new model for amplification of fluid waves in the subtectorial space, the fluid-elastic wave model [20], was developed here. The dynamics of the lossless and viscous fluid-elastic waves were investigated and a feedback controller model was implemented to examine the coupling of the OHC behaviour to the response at the IHC.

Appendix A

Derivation of the principal modes of vibration of the Neely and Kim model [68]

The block diagram in Fig.3.6, proposed for the micromechanical model of Neely and Kim [68], can be represented as a freely vibrating, undamped two DOF system as shown in Fig.3.10. For such a system the equations of motion will take the form

$$\begin{aligned} m_1 g\ddot{\xi}_b &= -k_1 g\xi_b \quad -k_3(g\xi_b - \xi_t), \\ m_2\ddot{\xi}_t &= -k_2\xi_t \quad\quad -k_3(\xi_t - g\xi_b). \end{aligned} \tag{A.1}$$

However, the lever gain g is equal to one according to Table 3.1, so that

$$\begin{aligned} m_1\ddot{\xi}_b &= -k_1\xi_b \quad -k_3(\xi_b - \xi_t), \\ m_2\ddot{\xi}_t &= -k_2\xi_t \quad -k_3(\xi_t - \xi_b), \end{aligned} \tag{A.2}$$

which can be expressed equivalently, after rearrangement, as

$$\begin{aligned} m_1\ddot{\xi}_b + (k_1 + k_3)\xi_b - k_3\xi_t = 0, \\ m_2\ddot{\xi}_t + (k_2 + k_3)\xi_t - k_3\xi_b = 0. \end{aligned} \tag{A.3}$$

The above equations can be written in matrix notation as

$$\begin{bmatrix} m_1 & 0 \\ 0 & m_2 \end{bmatrix} \begin{Bmatrix} \ddot{\xi}_b \\ \ddot{\xi}_t \end{Bmatrix} + \begin{bmatrix} k_1 + k_3 & -k_3 \\ -k_3 & k_2 + k_3 \end{bmatrix} \begin{Bmatrix} \xi_b \\ \xi_t \end{Bmatrix} = \begin{bmatrix} 0 \\ 0 \end{bmatrix}, \tag{A.4}$$

or

$$\mathbf{M}\,\ddot{\boldsymbol{\xi}} + \mathbf{K}\,\boldsymbol{\xi} = 0, \tag{A.5}$$

where

$$\mathbf{M} = \begin{bmatrix} m_1 & 0 \\ 0 & m_2 \end{bmatrix}, \tag{A.6}$$

is the mass matrix,

$$\mathbf{K} = \begin{bmatrix} k_1 + k_3 & -k_3 \\ -k_3 & k_2 + k_3 \end{bmatrix}, \tag{A.7}$$

is the stiffness matrix, and

$$\ddot{\boldsymbol{\xi}} = \begin{Bmatrix} \ddot{\xi}_b \\ \ddot{\xi}_t \end{Bmatrix}, \tag{A.8}$$

and

$$\boldsymbol{\xi} = \begin{Bmatrix} \xi_b \\ \xi_t \end{Bmatrix}, \tag{A.9}$$

are the acceleration and displacement vectors respectively.

Assuming time-harmonic solutions of the form $\xi_b = \Xi_b e^{j\omega t}$ and $\xi_t = \Xi_t e^{j\omega t}$, so that

$$\begin{aligned} \ddot{\xi}_b &= -\omega^2 \Xi_b e^{j\omega t}, \\ \ddot{\xi}_t &= -\omega^2 \Xi_t e^{j\omega t}, \end{aligned} \tag{A.10}$$

substituting the above relationships to Eq.A.3 gives

$$\begin{aligned} -\omega^2 m_1 \Xi_b e^{j\omega t} + (k_1 + k_3)\Xi_b e^{j\omega t} - k_3 \Xi_t e^{j\omega t} = 0, \\ -\omega^2 m_2 \Xi_t e^{j\omega t} + (k_2 + k_3)\Xi_t e^{j\omega t} - k_3 \Xi_b e^{j\omega t} = 0. \end{aligned} \tag{A.11}$$

After dividing by the $e^{j\omega t}$ terms, the relationships in Eq.A.11 take the form

$$\begin{aligned} -\omega^2 m_1 \Xi_b + (k_1 + k_3)\Xi_b - k_3 \Xi_t = 0, \\ -\omega^2 m_2 \Xi_t + (k_2 + k_3)\Xi_t - k_3 \Xi_b = 0, \end{aligned} \tag{A.12}$$

or after rearrangement

$$\begin{aligned} (k_1 + k_3 - \omega^2 m_1)\Xi_b - k_3 \Xi_t = 0, \\ (k_2 + k_3 - \omega^2 m_2)\Xi_t - k_3 \Xi_b = 0. \end{aligned} \tag{A.13}$$

First relationship in Eq.A.13 gives the solution of the form

$$\Xi_t = \frac{k_1 + k_3 - \omega^2 m_1}{k_3} \Xi_b, \tag{A.14}$$

so that the second relationship becomes

$$\left[\frac{(k_1 + k_3 - \omega^2 m_1)}{k_3} (k_2 + k_3 - \omega^2 m_2) - k_3 \right] \Xi_b = 0. \tag{A.15}$$

Taking Ξ_b=0 gives the trivial solution Ξ_b=Ξ_t=0, which implies no motion and the system stays at rest. However, equating the bracketed term in Eq.A.15 to nought (expanding the characteristic determinant), gives a quadratic equation in ω^2 with two real and positive values for ω^2 [94]

$$(k_1 + k_3 - \omega^2 m_1)(k_2 + k_3 - \omega^2 m_2) - k_3^2 = 0, \tag{A.16}$$

and

$$\omega^4 m_1 m_2 - \omega^2 [m_1(k_2 + k_3) + m_2(k_1 + k_3)] + k_1(k_2 + k_3) + k_2 k_3 = 0, \tag{A.17}$$

from which the natural frequencies, of the first and second mode, ω_1 and ω_2, respectively, can be calculated as two roots of quadratic in ω^2, i.e.

$$\omega_1^2 = \frac{m_1(k_2+k_3)+m_2(k_1+k_3)-\sqrt{\Delta}}{2m_1m_2}, \tag{A.18}$$

and

$$\omega_2^2 = \frac{m_1(k_2+k_3)+m_2(k_1+k_3)+\sqrt{\Delta}}{2m_1m_2}, \tag{A.19}$$

where

$$\Delta = [m_1(k_2+k_3)+m_2(k_1+k_3)]^2 - 4m_1m_2[k_1(k_2+k_3)+k_2k_3]. \tag{A.20}$$

Using the relationships in Eq.A.13 we can specify the ratio of the displacement amplitudes, i.e.

$$\frac{\Xi_b}{\Xi_t} = \frac{k_3}{k_1+k_3-\omega^2m_1} = \frac{k_2+k_3-\omega^2m_2}{k_3}, \tag{A.21}$$

thus, at the natural frequency of ω_1

$$\frac{\Xi_{b1}}{\Xi_{t1}} = \frac{k_3}{k_1+k_3-\omega_1^2m_1} = \frac{k_2+k_3-\omega_1^2m_2}{k_3}, \tag{A.22}$$

and at ω_2

$$\frac{\Xi_{b2}}{\Xi_{t2}} = \frac{k_3}{k_1+k_3-\omega_2^2m_1} = \frac{k_2+k_3-\omega_2^2m_2}{k_3}, \tag{A.23}$$

where the second index of Ξ refers to the natural frequency ω_1 and ω_2, respectively.

Choosing one of the amplitudes equal to some arbitrary value, the amplitude ratios in Eqs.A.22-A.23 will be normalised to this value, and the normal modes $\phi_{1,2}(\xi)$ can be obtained. We choose the amplitudes of the BM displacement, ξ_b, Ξ_{b1} (at ω_1) and Ξ_{b2} (at ω_2) to be equal to one, so that the normal modes will be

formulated by

$$\phi_1 = \left\{ \begin{array}{c} 1 \\ \Xi_{t1} \end{array} \right\},$$
$$\phi_2 = \left\{ \begin{array}{c} 1 \\ \Xi_{t2} \end{array} \right\}, \tag{A.24}$$

where Ξ_{t1} and Ξ_{t2} can be derived from Eq.A.22 and A.23.

Because a time harmonic motion of the system was assumed, the motion at the first mode will amount to

$$\left\{ \begin{array}{c} \xi_{b1} \\ \xi_{t1} \end{array} \right\} = \left\{ \begin{array}{c} 1 \\ \Xi_{t1} \end{array} \right\} e^{j\omega_1 t}, \tag{A.25}$$

and at the second mode

$$\left\{ \begin{array}{c} \xi_{b2} \\ \xi_{t2} \end{array} \right\} = \left\{ \begin{array}{c} 1 \\ \Xi_{t2} \end{array} \right\} e^{j\omega_2 t}, \tag{A.26}$$

or, using a general solution of the form

$$e^{j\omega t} = A \sin \omega t + B \cos \omega t, \tag{A.27}$$

we have

$$\left\{ \begin{array}{c} \xi_{b1} \\ \xi_{t1} \end{array} \right\} = \left\{ \begin{array}{c} 1 \\ \Xi_{t1} \end{array} \right\} (A \sin \omega_1 t + B \cos \omega_1 t), \tag{A.28}$$

$$\left\{ \begin{array}{c} \xi_{b2} \\ \xi_{t2} \end{array} \right\} = \left\{ \begin{array}{c} 1 \\ \Xi_{t2} \end{array} \right\} (C \sin \omega_2 t + D \cos \omega_2 t), \tag{A.29}$$

where A, B, C and D are real constants of integration, determined by the initial conditions [94].

The general free vibration is represented by the superposition of independent free vibrations in each of the two modes expressed in Eqs.A.25-A.26 (A.28-A.29)

thus

$$\left\{ \begin{array}{c} \xi_b \\ \xi_t \end{array} \right\} = \left\{ \begin{array}{c} \Xi_{b1} \\ \Xi_{t1} \end{array} \right\} (A \sin \omega_1 t + B \cos \omega_1 t) \; + \; \left\{ \begin{array}{c} \Xi_{b2} \\ \Xi_{t2} \end{array} \right\} (C \sin \omega_2 t + D \cos \omega_2 t) \, . \tag{A.30}$$

Assuming the initial conditions at t=0: ξ_b=100, ξ_t=0, $\dot{\xi}_b$=$\dot{\xi}_t$=0, taking Ξ_{b1} and Ξ_{b2} equal to one, and[1]

$$\left\{ \begin{array}{c} \dot{\xi}_b \\ \dot{\xi}_t \end{array} \right\} = \left\{ \begin{array}{c} \Xi_{b1} \\ \Xi_{t1} \end{array} \right\} \omega_1 \, (A \cos \omega_1 t - B \sin \omega_1 t) \; + \; \left\{ \begin{array}{c} \Xi_{b2} \\ \Xi_{t2} \end{array} \right\} \omega_2 \, (C \cos \omega_2 t - D \sin \omega_2 t) \, , \tag{A.31}$$

after applying to Eq.A.30, we have

$$\left\{ \begin{array}{c} 100 \\ 0 \end{array} \right\} = \left\{ \begin{array}{c} 1 \\ \Xi_{t1} \end{array} \right\} B \; + \; \left\{ \begin{array}{c} 1 \\ \Xi_{t2} \end{array} \right\} D, \tag{A.32}$$

and from Eq.A.31

$$\left\{ \begin{array}{c} 0 \\ 0 \end{array} \right\} = \left\{ \begin{array}{c} 1 \\ \Xi_{t1} \end{array} \right\} \omega_1 A \; + \; \left\{ \begin{array}{c} 1 \\ \Xi_{t2} \end{array} \right\} \omega_2 C. \tag{A.33}$$

Thus

$$B + D = 100, \tag{A.34}$$

$$\Xi_{t1} B + \Xi_{t2} D = 0, \tag{A.35}$$

$$\omega_1 A + \omega_2 C = 0, \tag{A.36}$$

$$\omega_1 \Xi_{t1} A + \omega_2 \Xi_{t2} C = 0. \tag{A.37}$$

Solving Eq.A.36 for A and substituting to Eq.A.37 gives

$$\omega_2 (\Xi_{t2} - \Xi_{t1}) C = 0. \tag{A.38}$$

[1]We set ξ_b=100 to facilitate comparison of the displacements in the figures of Chapter 3.

Because ω_2, Ξ_{t1} and $\Xi_{t2}\neq 0$ and $\Xi_{t1}\neq\Xi_{t2}$, then Eq.A.38 can be satisfied only for $C=0$, and thus according to Eq.A.36 $A=0$. However, from Eq.A.34 we have

$$B = 100 - D, \tag{A.39}$$

and hence from Eq.A.35

$$(\Xi_{t1} - \Xi_{t2})D = 100\Xi_{t1}, \tag{A.40}$$

so that

$$D = \frac{100\Xi_{t1}}{\Xi_{t1} - \Xi_{t2}}, \tag{A.41}$$

which we substitute into Eq.A.39 to derive B. Therefore, the constants A, B, C and D are equal to

$$A = 0, \tag{A.42}$$

$$B = \frac{100\Xi_{t2}}{\Xi_{t2} - \Xi_{t1}}, \tag{A.43}$$

$$C = 0, \tag{A.44}$$

$$D = \frac{100\Xi_{t1}}{\Xi_{t1} - \Xi_{t2}}. \tag{A.45}$$

In summary, the actual motion will be time harmonic at two natural frequencies, ω_1 and ω_2, and defined as

$$\left\{ \begin{array}{c} \xi_b \\ \xi_t \end{array} \right\} = \left\{ \begin{array}{c} 1 \\ \Xi_{t1} \end{array} \right\} B\cos\omega_1 t \; + \; \left\{ \begin{array}{c} 1 \\ \Xi_{t2} \end{array} \right\} D\cos\omega_2 t. \tag{A.46}$$

Knowing the equations of motion for the free, undamped system, the receptance, and hence mobility, of the system can be derived to a known input.

Assuming that the lower mass, m_1, of the two DOF system in Fig.3.10 is excited by a time-harmonic force of the form $f{=}Fe^{j\omega t}$, Eq.A.11 can be rewritten as

$$\begin{aligned} -\omega^2 m_1 \Xi_b e^{j\omega t} + (k_1 + k_3)\Xi_b e^{j\omega t} - k_3 \Xi_t e^{j\omega t} &= F e^{j\omega t}, \\ -\omega^2 m_2 \Xi_t e^{j\omega t} + (k_2 + k_3)\Xi_t e^{j\omega t} - k_3 \Xi_b e^{j\omega t} &= 0, \end{aligned} \tag{A.47}$$

and after dividing by the $e^{j\omega t}$ terms

$$\begin{aligned} -\omega^2 m_1 \Xi_b + (k_1 + k_3)\Xi_b - k_3 \Xi_t &= F, \\ -\omega^2 m_2 \Xi_t + (k_2 + k_3)\Xi_t - k_3 \Xi_b &= 0, \end{aligned} \tag{A.48}$$

or in the matrix form

$$\left(-\omega^2 \begin{bmatrix} m_1 & 0 \\ 0 & m_2 \end{bmatrix} + \begin{bmatrix} k_1 + k_3 & -k_3 \\ -k_3 & k_2 + k_3 \end{bmatrix} \right) \begin{Bmatrix} \Xi_b \\ \Xi_t \end{Bmatrix} = \begin{Bmatrix} F \\ 0 \end{Bmatrix}, \tag{A.49}$$

and hence

$$\frac{(-\omega^2 \mathbf{M} + \mathbf{K})}{j\omega} \begin{Bmatrix} V_b \\ V_t \end{Bmatrix} = \begin{Bmatrix} F \\ 0 \end{Bmatrix}, \tag{A.50}$$

where $\mathbf{M}$ and $\mathbf{K}$ are defined as in Eqs.A.6-A.7, and $V{=}j\omega\Xi$ where V denotes velocity, where V_b and V_t are the BM and TM velocities, respectively. Thus, defining the BM point mobility and the TM transfer mobility as the ratio of respective velocities to the unit force, we obtain

$$\begin{Bmatrix} Y_b \\ Y_t \end{Bmatrix} = \frac{1}{F} \begin{Bmatrix} V_b \\ V_t \end{Bmatrix} = j\omega \left(-\omega^2 \mathbf{M} + \mathbf{K} \right)^{-1} \begin{Bmatrix} 1 \\ 0 \end{Bmatrix}. \tag{A.51}$$

More rigorously, from the second relationship in Eq.A.48 we have (compare with Eq.A.21)

$$\Xi_t = \frac{k_3}{k_2 + k_3 - \omega^2 m_2} \Xi_b, \tag{A.52}$$

which after substituting to the upper expression in Eq.A.48 gives

$$(k_1 + k_3 - \omega^2 m_1)\Xi_b - \frac{k_3^2}{k_2 + k_3 - \omega^2 m_2} \Xi_b = F, \tag{A.53}$$

so that

$$\frac{(k_1+k_3-\omega^2 m_1)(k_2+k_3-\omega^2 m_2)-k_3^2}{(k_2+k_3-\omega^2 m_2)}\,\Xi_b = F, \tag{A.54}$$

and

$$\frac{\Xi_b}{F} = \frac{(k_2+k_3-\omega^2 m_2)}{(k_1+k_3-\omega^2 m_1)(k_2+k_3-\omega^2 m_2)-k_3^2}, \tag{A.55}$$

which defines the point receptance, the displacement ξ_b due to the unit force excitation on the lower subsystem in Fig.3.10.

Substituting the above equation to Eq.A.52 for Ξ_b gives

$$\frac{\Xi_t}{F} = \frac{k_3}{(k_1+k_3-\omega^2 m_1)(k_2+k_3-\omega^2 m_2)-k_3^2}, \tag{A.56}$$

which defines the transfer receptance for the displacement ξ_t due to the unit force exerted on the lower subsystem in Fig.3.10. Knowing that $j\omega\Xi{=}V$, we can formulate the explicit expressions for the mobility Y_b and Y_t as

$$\begin{aligned} Y_b &= \frac{V_b}{F} = \frac{j\omega(k_2+k_3-\omega^2 m_2)}{(k_1+k_3-\omega^2 m_1)(k_2+k_3-\omega^2 m_2)-k_3^2}, \\ Y_t &= \frac{V_t}{F} = \frac{j\omega k_3}{(k_1+k_3-\omega^2 m_1)(k_2+k_3-\omega^2 m_2)-k_3^2}, \end{aligned} \tag{A.57}$$

where the denominators of the above relationships have the same form as the frequency equation in Eq.A.17 and define the resonance frequencies (poles) of the mobility functions. The numerators of the above equation determine the frequencies at which the antiresonance (zero) in the mobility functions can be found, and for the system considered here there is a single antiresonance in the BM point mobility, Y_b, at the frequency of $\sqrt{(k_2+k_3)/m_2}/2\pi$.

Taking into account the damping within the system we arrive to a two degree of freedom system in Fig.3.6, as proposed by Neely and Kim [68], where there are no active forces acting in the system and the lower mass, m_1 is excited by a unit force. Knowing that the damping is proportional to velocity, $\dot{\xi}_b$ or $\dot{\xi}_t$, the

corresponding equations of motion can be written as

$$\begin{aligned}
&-\omega^2 m_1 \Xi_b e^{j\omega t} + j\omega(c_1+c_3)\Xi_b e^{j\omega t} + (k_1+k_3)\Xi_b e^{j\omega t} - (k_3+j\omega c_3)\Xi_t e^{j\omega t} = F e^{j\omega t},\\
&-\omega^2 m_2 \Xi_t e^{j\omega t} + j\omega(c_2+c_3)\Xi_t e^{j\omega t} + (k_2+k_3)\Xi_t e^{j\omega t} - (k_3+j\omega c_3)\Xi_b e^{j\omega t} = 0,
\end{aligned} \tag{A.58}$$

so that after dividing by $e^{j\omega}$ terms and rearranging we have

$$\begin{aligned}
&[k_1+k_3+j\omega(c_1+c_3)-\omega^2 m_1]\Xi_b - (k_3+j\omega c_3)\Xi_t = F,\\
&[k_2+k_3+j\omega(c_2+c_3)-\omega^2 m_2]\Xi_t - (k_3+j\omega c_3)\Xi_b = 0.
\end{aligned} \tag{A.59}$$

Since

$$\Xi_t = \frac{k_3+j\omega c_3}{k_2+k_3+j\omega(c_2+c_3)-\omega^2 m_2}\,\Xi_b, \tag{A.60}$$

and

$$\Xi_b = \frac{k_2+k_3+j\omega(c_2+c_3)-\omega^2 m_2}{k_3+j\omega c_3}\,\Xi_t, \tag{A.61}$$

according to the second relationship in Eq.A.59, substituting Eqs.A.60-A.61 into the first relationship of Eq.A.59 and taking $j\omega\Xi{=}V$, gives respectively

$$\begin{aligned}
Y_b &= \frac{V_b}{F} = \frac{j\omega[k_2+k_3+j\omega(c_2+c_3)-\omega^2 m_2]}{\Omega},\\
Y_t &= \frac{V_t}{F} = \frac{j\omega(k_3+j\omega c_3)}{\Omega},
\end{aligned} \tag{A.62}$$

where Y_b and Y_t are now the point BM and transfer TM mobility of the passive, damped two DOF system, and

$$\Omega = [k_1{+}k_3{+}j\omega(c_1{+}c_3){-}\omega^2 m_1][k_2{+}k_3{+}j\omega(c_2{+}c_3){-}\omega^2 m_2]{-}(k_3{+}j\omega c_3)^2. \tag{A.63}$$

Alternatively, we can write Eq.A.62 analogously to Eq.A.51, so that

$$\left\{ \begin{array}{c} Y_b \\ Y_t \end{array} \right\} = \frac{1}{F} \left\{ \begin{array}{c} V_b \\ V_t \end{array} \right\} = j\omega \left(-\omega^2 \mathbf{M} + j\omega \mathbf{C} + \mathbf{K} \right)^{-1} \left\{ \begin{array}{c} 1 \\ 0 \end{array} \right\}, \tag{A.64}$$

where

$$\mathbf{C} = \left[\begin{array}{cc} c_1 + c_3 & -c_3 \\ -c_3 & c_2 + c_3 \end{array} \right], \tag{A.65}$$

is the damping matrix.

Appendix B

Derivation of the parameters for the model of Neely [66]

Model parameters for three specified locations on the CP, i.e. x=0, $L/2$ and L, used to solve the partition admittance of the Neely's model [66], are given in Table 3.2. However, the values for the other sites of the CP were not given explicitly in [66]. Neely reported that a quadratic polynomial curve fitting to the logarithm of the three locations specified in the table, was used to interpolate the remaining values of the x-dependent parameters [66]. Thus, the theory for interpolation of the model's parameters, is presented here.

We use a quadratic polynomial of the form

$$y = ax^2 + bx + c, \tag{B.1}$$

where a, b and c are the polynomial's coefficients. Because the polynomial was fitted to the logarithm of the parameter, thus substituting for x=0, x=$L/2$ and x=L, gives

$$\begin{cases} \log y_0 = c, \\ \log y_{L/2} = \frac{L^2}{4}a + \frac{L}{2}b + c, \\ \log y_L = L^2 a + Lb + c, \end{cases} \tag{B.2}$$

where subscripts 0, $L/2$ and L denote the position along the cochlea.

Using the first relationship in Eq.B.2, we substitute for c into remaining two relationships, so that

$$\begin{cases} \log y_{L/2} = \frac{L^2}{4}a + \frac{L}{2}b + \log y_0, \\ \\ \log y_L = L^2 a + Lb + \log y_0, \end{cases} \tag{B.3}$$

and after multiplying the first relationship in Eq.B.3 by two and subtracting from the second relationship, we have

$$2\log y_{L/2} - \log y_L = -\frac{L^2}{2}a + \log y_0. \tag{B.4}$$

Hence

$$\frac{L^2}{2}a = \log y_0 + \log y_L - 2\log y_{L/2}, \tag{B.5}$$

and

$$a = \frac{2}{L^2}\left(\log y_0 + \log y_L - 2\log y_{L/2}\right). \tag{B.6}$$

Substituting for a into the second expression of Eq.B.3 gives

$$\log y_L = L^2\left[\frac{2}{L^2}\left(\log y_0 + \log y_L - 2\log y_{L/2}\right)\right] + Lb + \log y_0, \tag{B.7}$$

so that

$$\log y_L = 2\log y_0 + 2\log y_L - 4\log y_{L/2} + Lb + \log y_0, \tag{B.8}$$

$$Lb = 4\log y_{L/2} - 3\log y_0 - \log y_L, \tag{B.9}$$

and hence

$$b = \frac{4}{L}\log y_{L/2} - \frac{3}{L}\log y_0 - \frac{1}{L}\log y_L. \tag{B.10}$$

Knowing

$$\begin{cases} a = \frac{2}{L^2}\left(\log y_0 + \log y_L - 2\log y_{L/2}\right), \\ b = \frac{1}{L}\left(4\log y_{L/2} - 3\log y_0 - \log y_L\right), \\ c = \log y_0, \end{cases} \tag{B.11}$$

the quadratic polynomial can be obtained. Finally, it has to be noted that the quadratic was fitted to the log of the parameter, i.e.

$$\log y = ax^2 + bx + c, \tag{B.12}$$

so that

$$y = 10^{ax^2+bx+c}. \tag{B.13}$$

For example, if

$$\begin{cases} y_0 = \frac{K_{b0}}{A_p}, \\ y_{L/2} = \frac{K_{bL/2}}{A_p}, \\ y_L = \frac{K_{bL}}{A_p}, \end{cases} \tag{B.14}$$

where K_{b0}, $K_{bL/2}$ and K_{bL} are specified in Table 3.2, then

$$\begin{cases} a_{K_b} = \frac{2}{L^2}\left(\log \frac{K_{b0}}{A_p} + \log \frac{K_{bL}}{A_p} - 2\log \frac{K_{bL/2}}{A_p}\right), \\ b_{K_b} = \frac{1}{L}\left(4\log \frac{K_{bL/2}}{A_p} - 3\log \frac{K_{b0}}{A_p} - \log \frac{K_{bL}}{A_p}\right), \\ c_{K_b} = \log \frac{K_{b0}}{A_p}, \end{cases} \tag{B.15}$$

from Eq.B.11. Thus, according to Eq.B.13

$$\frac{K_b}{A_p} = 10^{a_{K_b}x^2 + b_{K_b}x + c_{K_b}}, \tag{B.16}$$

and analogously for all other parameters dependent on x.

Appendix C

Effect of the helicotrema boundary condition on the response of the coupled models

The frequency response plots shown in Fig.C.1, show an example of preliminary calculations of the magnitude and phase responses of the BM velocity. The figures are plotted for the passive and active model of Neely and Kim [68] (a, c) and the model of Neely [66] (b, d), in which the length of the BM was set to 25 mm (average length of a cat cochlea). It can be seen that all curves are not smooth in the low frequency region, and this low frequency behaviour is thought to be connected with the zero pressure boundary condition at the helicotrema. As it was discussed in Chapter 4, in the 1986 model of Neely and Kim and 1993 model of Neely, a damping component at the helicotrema was introduced to account for the helicotrema boundary condition. However, the model of macromechanics presented in this work assumes that the pressure difference at the helicotrema is equal to zero.

Such a choice of the apical boundary condition does not affect the responses, provided they are calculated at the site located sufficiently away from the apex or for sufficiently high stimulus frequencies. The responses in Fig.C.1 appear to be affected by the reflections from the helicotrema for frequencies up to about 400 Hz. According to the CF/place map obtained by Liberman [56], the low

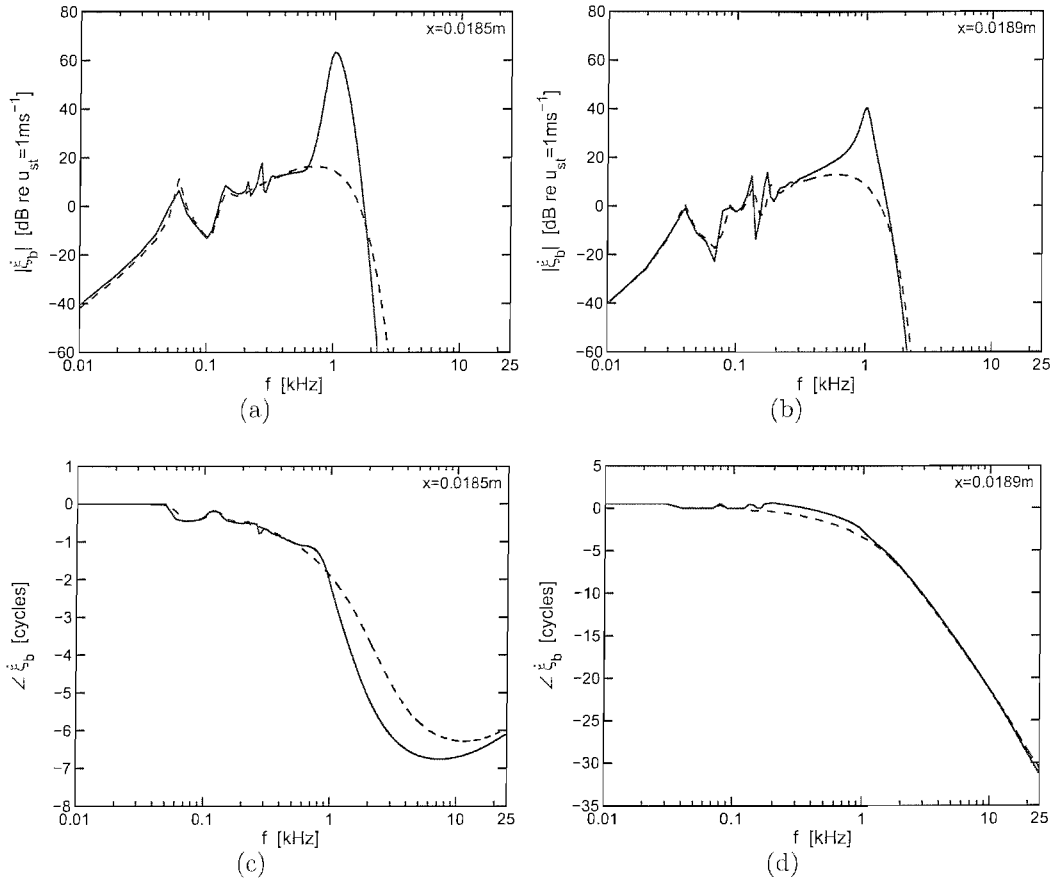

Figure C.1: Magnitude and phase response of the basilar membrane velocity $\dot{\xi}_b$ as a function of stimulus frequency, calculated at the cochlear site of x=0.0185 m for the model of Neely and Kim [68] (a, c) and at x=0.0189 m along the cochlea for the model of Neely [66] (b, d). In both cases the length of the cochlea was assumed to be equal to 25 mm. Solid lines, active model (γ=1) and dashed lines, passive model (γ=0).

frequency limit for the cat cochlea amounts to about 97 Hz, therefore we can neglect the response characteristic below 100 Hz. Nevertheless, the preliminary results (also pressure difference responses not shown here) had shown consistently that the response of the coupled model with the zero pressure difference apical boundary condition becomes reliable only above 400 Hz, which corresponds to the place of approximately 0.021 m when the BM length is set to 25 mm.

Appendix D

Convergence of the iterative procedure used in the quasi-linear model

The quasi-linear model discussed in Section 5.4, was solved for the coupled model of Neely and Kim [68] with the active gain γ derived using either Eq.5.4.11 for the global model, or Eq.5.4.13 for the local model. In the first instance we describe the derivation of the global active gain γ_{global}.

To calculate γ_{global} in the quasi-linear model, we need to know the velocity of the BM, $\dot{\xi}_b$, since the active gain is scheduled on $|\dot{\xi}_b|$, according to Eq.5.4.11. Thus, the *Matlab* code used for calculation of the responses in Section 4.2, was firstly used to calculate the pressure difference P_d in the Neely and Kim model at particular stimulus level, stimulus frequency and for γ_0=1 ('zero-step', fully active model). After the pressure difference at a single frequency was solved for the active gain of one, it was substituted to Eq.5.4.10 (where G and H are defined in Eq.5.4.8 and 5.4.12) to derive the velocity of the BM. The maximum value of $|\dot{\xi}_b|$ was taken to compute the new value for the active gain at single stimulus frequency, i.e.

$$\gamma_{\text{global}\,1} = \beta\Phi_{\text{D}} = \frac{(5/6)\cdot 1.5\times 10^{-5}}{1.5\times 10^{-5} + |\dot{\xi}_{b\,0}|_{peak}}, \tag{C.1}$$

where the subscripts 0 and 1 refer to the step number. The gain derived from the

above equation is then substituted to the expression for the partition impedance in Eq.3.3.8 to calculate new pressure difference, P_d, used again in Eq.5.4.10 so that the BM velocity can be recalculated. The whole sequence is repeated ten times, after which the last value of the BM velocity is stored, and new ten-step active gain iteration begins for the next stimulus frequency. Thus, in the present model both stimulus frequency and γ were changing iteratively in 2500 steps (10 Hz-25 kHz, frequency range with 10 Hz steps) and ten steps γ_{1-10}, respectively. Using the method described above a 2500×1024, frequency×position (the length of the BM, L, was discretised into 1024 elements) velocity matrix was derived for imposed stimulus level. Also the pressure difference and BM displacement frequency-positions matrices were stored, where the BM displacement was obtained by dividing $\dot{\xi}_b(x,\omega)$ matrix by the factor of $j\omega$.

The constant A and the gain β in Eq.5.4.11 were derived by a trial-and-error method to obtain an optimally converging active gain γ and 'smooth' quasi-linear BM responses at 1 kHz stimulus frequency and different excitation levels, as shown in preliminary calculations in [82]. A was estimated to be 1.5×10^{-5} and β was set to $5/6\approx0.83$ to advance the convergence of the gain, and both remained constant for all computations.

Table D.1 presents the values of the global active gain, γ_{global}, at each step of computation and stimulus level, derived from the global quasi-linear model solved at 1 kHz using the parameters chosen by Neely and Kim, and A and β estimated as discussed earlier. Furthermore, Fig.D.1 shows γ_{global} as a function of the iteration step for different stimulus levels.

The convergence of gain is fast at 20 dB and 100 dB stimulus levels and slower at 40 dB. The gain at 60 and 80 dB however, still oscillates when the end of the iteration is reached. It can be also noted that the last value of γ_{global} calculated at 60 dB is slightly higher than that calculated at 40 dB as shown in Table D.1. Nevertheless, the overall trend of a decreasing gain with the increase of the stimulus level is still noticeable, which leads to the compression of the response from almost fully active at 20 dB to almost passive at 100 dB level of excitation.

In the second paradigm of the quasi-linear model calculation, the active gain was not only changing with stimulus frequency but was also place-dependent.

STEP	STIMULUS LEVEL [dB re 2×10^{-5} Pa]					
	20	40	60	80	100	
0	1	1	1	1	1	γ_{global}
1	0.0741	0.0081	0.0008	0.0001	8×10^{-6}	
2	0.8331	0.8314	0.8143	0.6760	0.2505	
3	0.7911	0.5487	0.1691	0.1003	0.1288	
4	0.8108	0.8121	0.8014	0.6344	0.1871	
5	0.8034	0.6042	0.1973	0.1383	0.1583	
6	0.8065	0.8018	0.7980	0.6141	0.1724	
7	0.8053	0.6292	0.2050	0.1587	0.1655	
8	0.8058	0.7951	0.7970	0.6021	0.1689	
9	0.8056	0.6440	0.2073	0.1712	0.1672	
10	0.8057	0.7902	0.7966	0.5944	0.1680	

Table D.1: Active gain γ_{global} calculated in ten steps for stimulus levels from 20–100 dB (re 2×10^{-5} Pa) in the quasi-linear model discussed in Section 5.4. The step of zero refers to the iteration step in which the gain was set to unity.

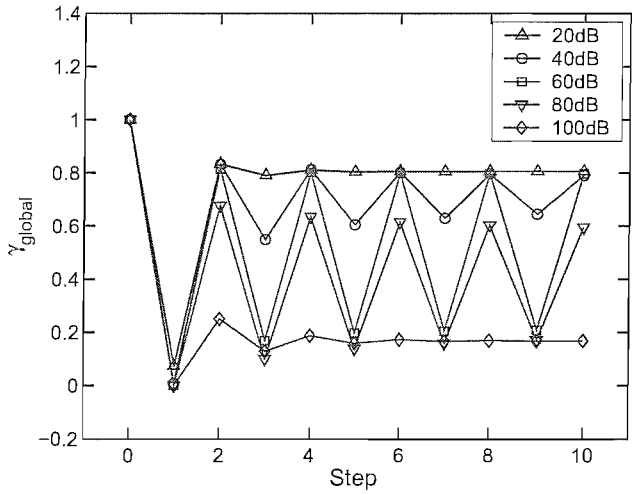

Figure D.1: Active gain γ_{global} as a function of the iteration step for 20 dB (triangles), 40 dB (circles), 60 dB (squares), 80 dB (inverted triangles) and 100 dB (diamonds) stimulus level.

The local gain γ_{local} was solved using Eq.5.4.13 in which A and β have the same value as in the global case, i.e. 1.5×10^{-5} and 5/6, respectively. Firstly, we solved the Neely and Kim coupled model at single frequency with the active gain equal to one, for P_d which was substituted to Eq.5.4.10 to calculate the BM velocity $\dot{\xi}_b$. Subsequently, each local value of $\dot{\xi}_b$ was used to derive the local active gain γ_{local}, used to recalculate the pressure difference, BM velocity, and finally to derive new distribution of active gains γ_{local} along the cochlea. The whole sequence was repeated ten times (not counting the first step in which the gain was set to one) and the same procedure was followed for the next stimulus frequency. Therefore, we derived the frequency×position (2500×1024) matrix of the BM velocity, $\dot{\xi}_b$, BM displacement, $\dot{\xi}_b=\xi_b/j\omega$, and pressure difference P_d. Additionally, a 3D matrix of gains, $\gamma_{\text{local}}(\text{step}, x, \omega)$, was also derived to plot the distribution of the local gain.

The calculated values of γ_{local} at 1 kHz, which are equal in this model to those calculated at 0.0182 m along the cochlea (corresponding characteristic place to the CF=1 kHz), are presented in Table D.2 for different stimulus levels at each step of iteration (including the 'zero-step'). Furthermore, the convergence of the gain, i.e. the locally active gain as a function of the iteration step, is plotted in Fig.D.2. Both the table and the figure show that the convergence of the gain at 1 kHz was fast and by the ninth iteration step it reached a steady value, with accuracy of the second decimal point, for all stimulus levels.

The convergence of the local gain plotted as a function of position and stimulus frequency in Fig.D.3 and D.4, respectively, reveals that for low stimulus levels, i.e. 20−40 dB, the changes of gain are localised around the CF/characteristic place, where the gain is almost constant outside this frequency/place, as depicted in Figs.D.3(a)-D.3(b) and Fig.D.4(a)-D.4(b). However, with the increase of the stimulus level to 60 dB, as well as for higher levels, the gain changes become less localised and extend to almost the whole frequency region below the CF, as shown in Fig.D.4(c)-D.4(e), or basal to the characteristic place in Fig.D.3(c)-D.3(e). Thus, some distortions on the low frequency side or basal portion of the response may occur, and they were observed in the BM displacement response curves for 10 kHz stimulus frequency and 0.007 m position along the cochlea in

STEP	STIMULUS LEVEL [dB re 2×10^{-5} Pa]					
	20	40	60	80	100	
0	1	1	1	1	1	γ_{local}
1	0.7889	0.5331	0.1257	0.0145	0015	
2	0.8229	0.7693	0.7141	0.4413	0.1480	
3	0.8221	0.7742	0.4941	0.3447	0.1349	
4	0.8221	0.7552	0.6445	0.3783	0.1358	
5	0.8221	0.7657	0.5675	0.3641	0.1358	
6	0.8221	0.7624	0.6120	0.3709	0.1358	
7	0.8221	0.7630	0.5877	0.3679	0.1358	
8	0.8221	0.7631	0.6017	0.3691	0.1358	
9	0.8221	0.7629	0.5940	0.3687	0.1358	
10	0.8221	0.7630	0.5983	0.3688	0.1358	

Table D.2: Active gain $\gamma_{\text{local}}(x, f)$ calculated in ten steps at stimulus frequency f=1 kHz or at 0.0182 m site in the cochlea and stimulus levels from 20−100 dB (re 2×10^{-5} Pa) in the local quasi-linear model discussed in Section 5.4.

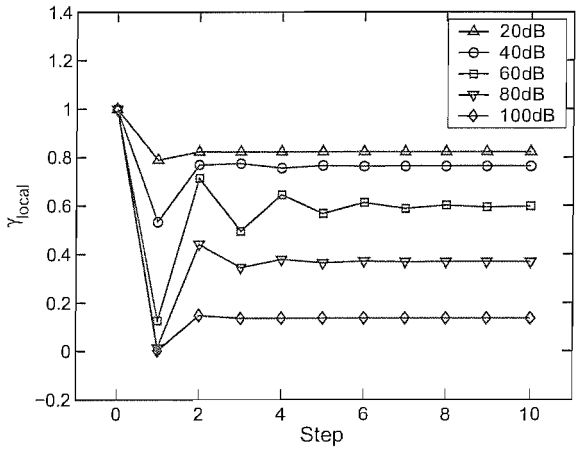

Figure D.2: Active gain γ_{local} calculated at 1 kHz stimulus frequency (or 0.0182 m site along the cochlea), as a function of the iteration step for 20 dB (triangles), 40 dB (circles), 60 dB (squares), 80 dB (inverted triangles) and 100 dB (diamonds) stimulus level.

Fig.D.5 and D.6 (right panels), respectively.

The amplitude and phase response curves computed at 500 Hz shown in Fig.D.5(a) and D.5(c), and 0.0214 m shown in Fig.D.6(a) and D.6(c), are smooth on the low frequency as well as the basal side, respectively, which implies 'stability' of the local gain γ_{local} at frequencies lower than 1 kHz or positions higher than 0.0182 m. It was observed that γ_{local} converges quickly during the iterative procedure (Fig.D.2) and to the same value at particular step and stimulus level in the iteration for both CF=1 kHz and characteristic place of 0.0182 m chosen in the simulations (Table D.2).

However, significant 'instabilities' can be observed, as evidenced by the ripples on their basal/low frequency slopes, in Fig.D.5(b) and D.5(d), which show the magnitude and phase responses, respectively, as a function of cochlear position for the local quasi-linear model calculated at 10 kHz, and the responses calculated at the corresponding site of 0.007 m, as a function of stimulus frequency, shown in Fig.D.6(b) and D.6(d). Therefore, the quasi-linearly compressed responses at higher frequencies than 1 kHz or at positions basal to the characteristic place of 0.0182 m (20 dB excitation level), are not 'stable' on the low frequency/basal side.

Some remarks concerning the stability of the quasi-linear model can therefore be drawn here. It is interesting to note that active gain γ converges always to values lower than one in the present model. Thus, we could assume that the model is stable for all stimulus frequencies and stimulus levels for which the quasi-linear response was calculated, similar as for the coupled responses derived for the gain lower than one for the linear model of Neely and Kim [68]. However, it was shown that for the case where the gain of the model was place-dependent ($\gamma_{\text{local}}(x)$), the gain was not stable at all positions/frequencies as shown in Fig.5.19, and some oscillations could be observed in the calculated responses as it was shown in Fig.D.5(b) and D.6(b). It seems that a possible solution to the stability problems is to introduce a place-dependent gain β. However, even if a realistic cochlear distribution of β could be derived and would help to stabilise the gain of the model at particular isolated sites on the CP (i.e. micromechanical models), it does not guarantee stability of the overall, coupled system.

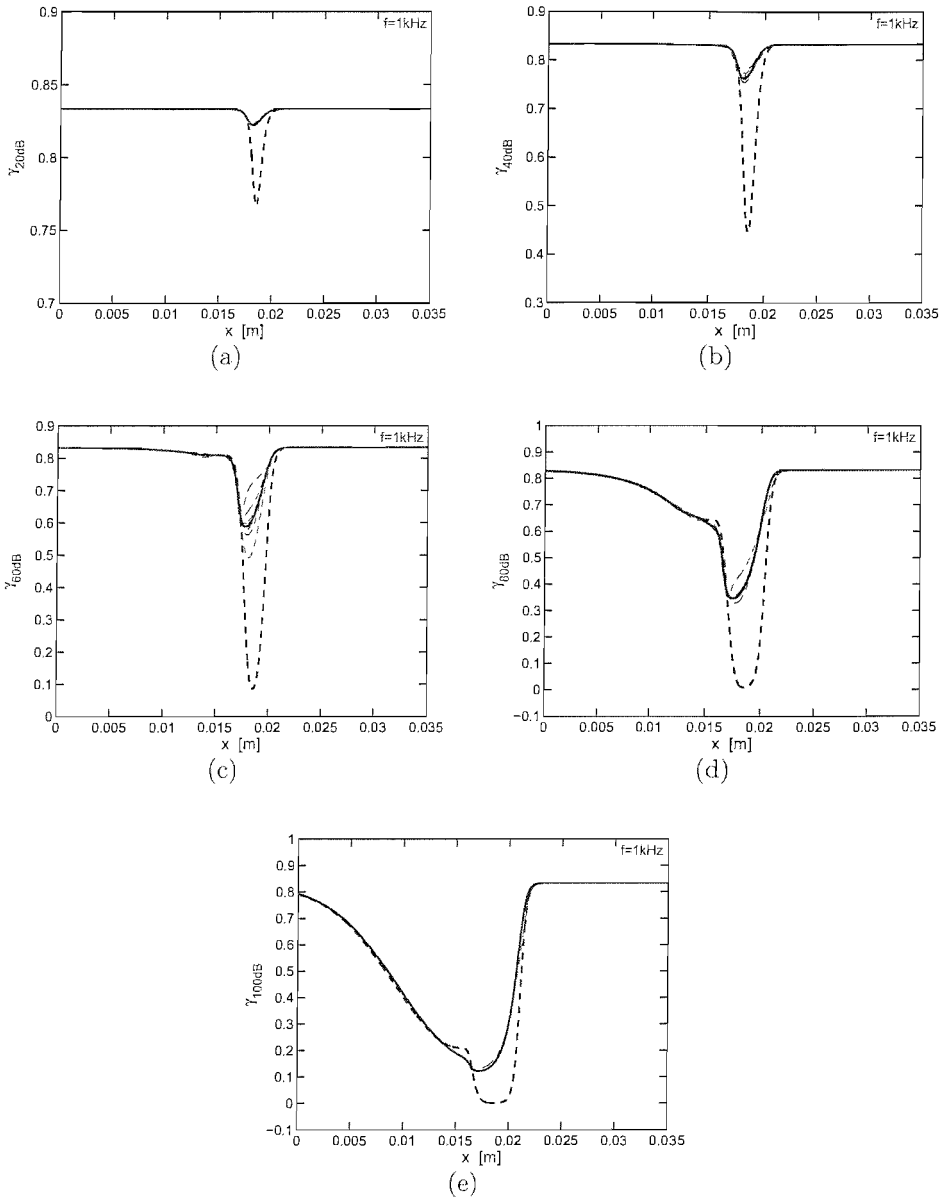

Figure D.3: Iteration steps of the local active gain, γ_{local}, solved for the local quasi-linear model at 1 kHz for stimulus levels of 20 dB (a), 40 dB (b), 60 dB (c), 80 dB (d) and 100 dB (e), as a function of position along the cochlea. The thick dashed line for the first step, thick solid line for the tenth step, other thin dashed lines for steps 2–9.

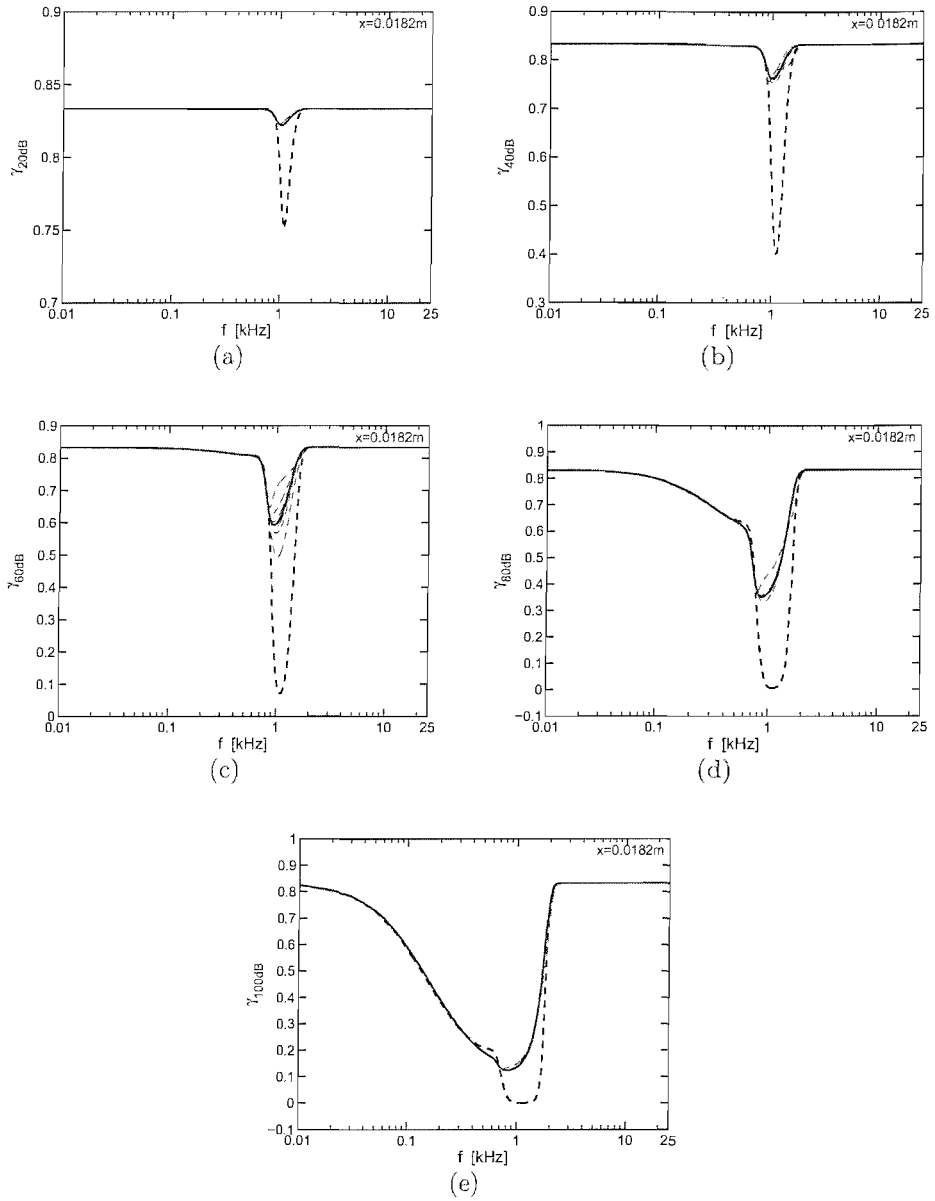

Figure D.4: Iteration steps of the local active gain, γ_{local}, solved for the local quasi-linear model at x=0.0182 m for stimulus levels of 20 dB (a), 40 dB (b), 60 dB (c), 80 dB (d) and 100 dB (e), as a function of stimulus frequency. The thick dashed line for the first step, thick solid line for the tenth step, other thin dashed lines for steps 2–9.

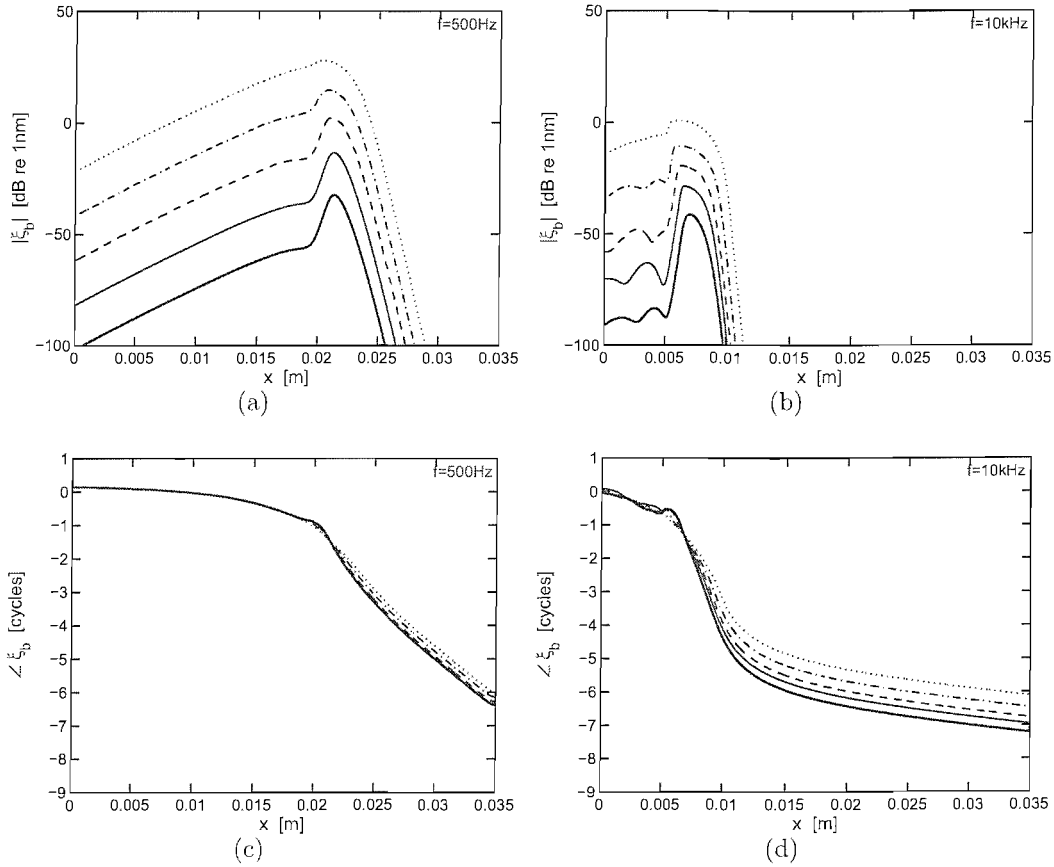

Figure D.5: Magnitude and phase of the basilar membrane displacement, ξ_b, as a function of position along the cochlea, calculated for the local quasi-linear model using parameters chosen by Neely and Kim [68] at f=500 Hz (a) and 10 kHz (b). The stimulus levels were set to 20 dB (thick solid), 40 dB (solid), 60 dB (dashed), 80 dB (dot-dashed) and 100 dB (dotted).

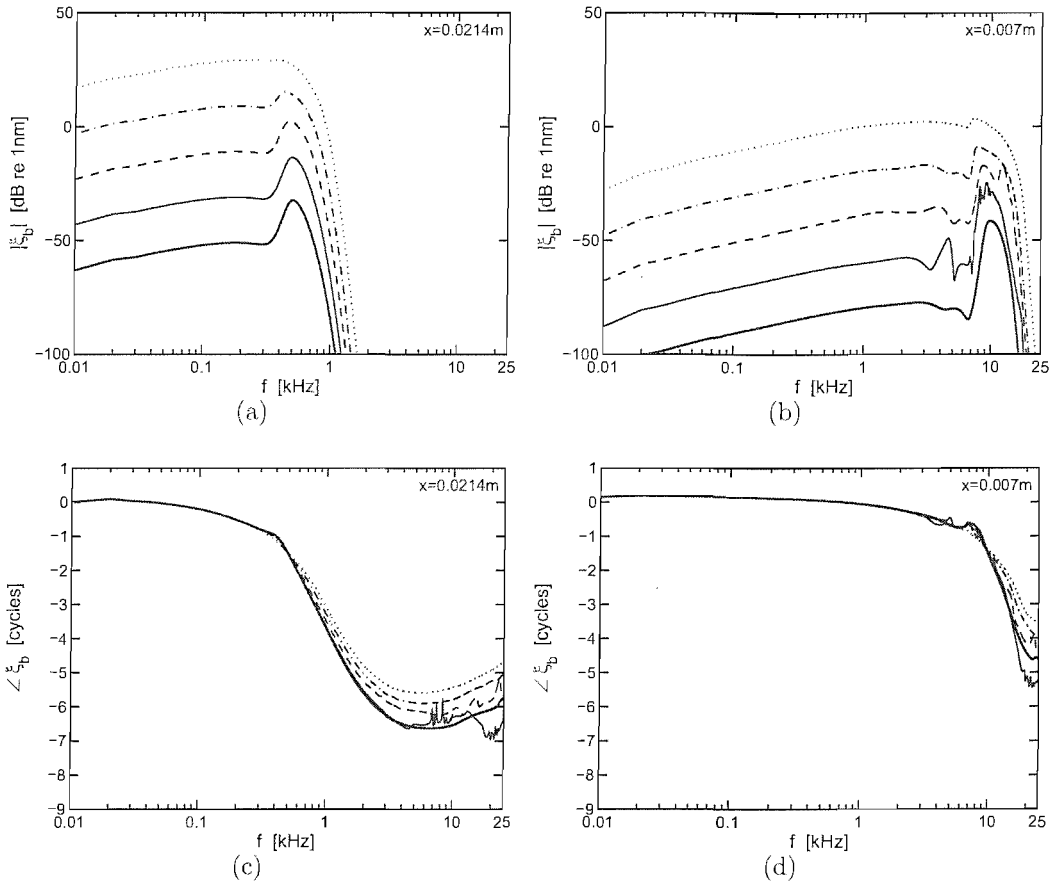

Figure D.6: Magnitude and phase of the basilar membrane displacement, ξ_b, as a function of stimulus frequency, calculated for the local quasi-linear model using parameters chosen by Neely and Kim [68] at x=0.0214 m (a) and 0.007 m (b) along the cochlea. The stimulus levels were set to 20 dB (thick solid), 40 dB (solid), 60 dB (dashed), 80 dB (dot-dashed) and 100 dB (dotted).

Appendix E

Derivation of responses in the 'squirting' wave model

E.1 The wavenumber

In the present appendix we derive the expressions for the forced responses of the 'squirting' wave model discussed in Chapter 6. The input excitations acting in this model, are the external pressure in the scala media p_{ext} and a force due to the electromotile action of the OHCs, which both lead to transverse oscillations of the plate and longitudinal oscillations of the subtectorial fluid in the duct space of the plate-fluid-plate system shown schematically in Fig.6.2.

It should be noted that the wave motion for both the plate and the fluid, is considered only in the radial direction, y, that is along the duct (across the CP). The transverse displacement of the BM and TM plates will be denoted by $w(y,t)$, whereas the particle displacement in the subtectorial fluid by $u(y,t)$. To begin with we write the equations governing bending deformation of the plates.

The bending moment, $M(y,t)$, of a plate is described by [27]

$$M(y,t) = -EI\,\frac{\partial^2 w(y,t)}{\partial y^2}, \tag{E.1.1}$$

where E denotes the Young's modulus and I is the moment of inertia defined as

$$I = \frac{2h_s^3}{3(1-\nu^2)}, \tag{E.1.2}$$

for a plate of thickness $2h_s$ (where subscript 's' denotes a semi-thickness) and Poisson's ratio ν. Note that the negative sign in the bending moment definition, implies that the curvature of the deformation w, is positive in the transverse direction, i.e. the plate is deflected upwards [27].

The shear force acting on the plate is formulated by

$$F(y,t) = -EI\,\frac{\partial^3 w(y,t)}{\partial y^3}, \tag{E.1.3}$$

and the relationship between the load applied on the beam, which is the fluid pressure in this case, and the displacement w is expressed as

$$p(y,t) = -EI\,\frac{\partial^4 w(y,t)}{\partial y^4}. \tag{E.1.4}$$

It should be noted that E and I, and hence h and ν, in Eqs.E.1.1-E.1.4, are assumed constant along the duct in a single slice of the organ of Corti.

We use Eq.E.1.4 as the starting point for the derivation of the wave equation for the 'squirting' wave model, similarly to that presented by Hassan and Nagy in [41]. The conservation of momentum equation for the fluid of density ρ is given by

$$\rho\,\frac{\partial^2 u(y,t)}{\partial t^2} = -\frac{\partial p(y,t)}{\partial y}, \tag{E.1.5}$$

and the continuity equation for an incompressible and inviscid fluid by

$$w(y,t) = \frac{d_2}{2}\,\frac{\partial u(y,t)}{\partial y}, \tag{E.1.6}$$

where d_2 is the thickness of the fluid layer, which is equal to the height of the subtectorial duct in this model. After differentiating Eq.E.1.4 with respect to y and substituting to Eq.E.1.5, we have

$$\rho\,\frac{\partial^2 u(y,t)}{\partial t^2} = EI\,\frac{\partial^5 w(y,t)}{\partial y^5}. \tag{E.1.7}$$

Differentiating Eq.E.1.6 twice with respect to time gives

$$\frac{\partial^2 w(y,t)}{\partial t^2} = \frac{d_2}{2}\,\frac{\partial^3 u(y,t)}{\partial y \partial t^2}, \tag{E.1.8}$$

so that differentiating Eq.E.1.7 with respect to y and substituting $\partial^3 u(y,t)/\partial y \partial t^2$ from the above equation, leads to

$$\rho \frac{\partial^2 w(y,t)}{\partial t^2} = \frac{EId_2}{2} \frac{\partial^6 w(y,t)}{\partial y^6}. \tag{E.1.9}$$

Therefore, the wave equation of the lossless 'squirting' wave can be written as

$$\rho \frac{\partial^2 w(y,t)}{\partial t^2} - \frac{EId_2}{2} \frac{\partial^6 w(y,t)}{\partial y^6} = 0. \tag{E.1.10}$$

Assuming a complex, harmonic plate displacement $w(y,t)=Ae^{j(\omega t - ky)}$, where A is a complex amplitude, ω is the radian frequency and k is a wavenumber, Eq.E.1.10 can be solved, to give the dispersion relationship between the angular frequency and the wavenumber to be

$$\omega^2 = \frac{EId_2}{2\rho} k^6, \tag{E.1.11}$$

and hence the wavenumber k is equal to

$$k = \left(\frac{2\rho\omega^2}{EId_2} \right)^{\frac{1}{6}}. \tag{E.1.12}$$

An interesting feature of the 'squirting' wave mode arises due to the symmetry of the solid-fluid-solid trilayer. The coordinate system of the plate-fluid-plate system in considerations of Hassan and Nagy was located in the centre of the fluid layer (see Fig.1 in [41]), so that the 'squirting' wave is symmetric with respect to the horizontal axis in the middle of the fluid film. Hassan and Nagy also report that a similar fluid mode can be observed in a fluid film confined by an elastic plate and a solid substrate [41]. Therefore, the choice of system coordinates in the present model implies that the 'squirting' waves can propagate between an elastic plate undergoing vertical oscillations and a solid surface at the distance $d=d_2/2$ apart, where d_2 is the original fluid layer thickness used by Hassan and Nagy in [41].

Furthermore, Hassan and Nagy used a semi-thickness of the plates, h_s, so that the plate thickness, h is equal to $2h_s$, twice that proposed by Hassan and Nagy. Therefore, for convenience we rewrite the wave equation of the lossless 'squirting' wave for a wave assumed to propagate between a rigid surface of the RL and an

elastic plate of the TM under-surface, d above the rigid surface and of thickness h.

Taking Eq.E.1.10 and replacing d_2 by $2d$ the wave equation of the lossless 'squirting' wave takes the form

$$\rho \frac{\partial^2 w(y,t)}{\partial t^2} - EId \frac{\partial^6 w(y,t)}{\partial y^6} = 0, \tag{E.1.13}$$

for which the wavenumber will take the form

$$k = \left(\frac{\rho\omega^2}{EId} \right)^{\frac{1}{6}}, \tag{E.1.14}$$

and the moment of inertia I, after replacing h_s by $h/2$ in Eq.E.1.2, will be defined by

$$I = \frac{h^3}{12(1-\nu^2)}. \tag{E.1.15}$$

In the following derivations we consider a duct formed by a rigid surface and an elastic plate with a fluid film confined in between, where the duct's height is equal to d and the thickness of the plate to h.

Note that there are six distinctive roots of Eq.E.1.12, say k_a to k_f, which form a hexagon in a complex plane of k lying on the circle of radius k_a [51], as shown in Fig.E.1 where k was calculated for parameters in Table 6.1 at 1 kHz. Two of the roots of k are real and correspond to lossless waves propagating in the subtectorial duct in the positive and negative y direction, i.e. k_a and k_d, whereas the remaining four, i.e. $k_{b,c,e,f}$ are complex and would form a standing nearfield in an infinite duct.

The hexagon in Fig.E.1 is symmetric with respect to the real and imaginary axis and the angle between each of its two neighbouring vertices is equal to 60°. Assuming that the wavenumber is of the form $k=\beta-j\alpha$ we note that k_a and k_d are both real, equal and opposite and hence equal to β_1 and $-\beta_1$, respectively. Each of the complex wavenumbers $k_{b,c,e,f}$ can be described by two real and imaginary components corresponding to the propagating, $\pm\beta_2$, and decay terms, $\pm\alpha_2$, respectively. Due to the symmetry of the hexagon, we can express β_2 and α_2 in terms of β_1, which we now denote as k_0, so that $k_a=k_0$ and $k_d=-k_0$, and since

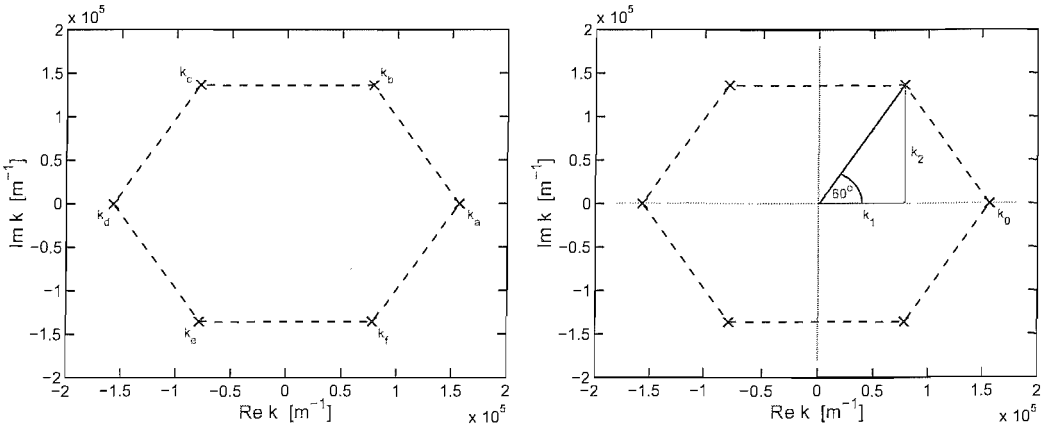

Figure E.1: The roots, k_{a-f} (crosses '$\times$'), of the wavenumber k at 1 kHz (a), and the hexagon, whose vertices are the roots of k, (dashed line). Symmetry of the hexagon and the real, k_1, and imaginary, k_2, parts of the root k_b, are indicated in (b). k_0 is the root corresponding to the travelling waves in the subtectorial duct.

$$\beta_2 = k_0 \cos 60° = \frac{k_0}{2} = k_1, \tag{E.1.16}$$

$$\alpha_2 = k_0 \sin 60° = \frac{\sqrt{3}}{2} k_0 = k_2, \tag{E.1.17}$$

we have

$$k_+^p = k_0, \tag{E.1.18}$$

$$k_-^p = -k_0, \tag{E.1.19}$$

for the waves propagating (upper index 'p') along the duct in the positive and negative direction, respectively, and

$$k_+^n = \pm k_1 - jk_2, \tag{E.1.20}$$

$$k_-^n = \pm k_1 + jk_2, \tag{E.1.21}$$

for the nearfield components (upper index 'n') in the positive and negative direction.

E.2 Wave motion in an infinite duct

The assumed time-harmonic complex plate displacement for the nearfield component of the squirting wave at t=0, will thus take the form

$$w_+^n(y) = Ce^{-jk_+^n y} = Ce^{-j(k_1 - jk_2)y} = Ce^{-jk_1 y}e^{-k_2 y}, \tag{E.2.1}$$

$$w_+^n(y) = Ce^{-jk_+^n y} = Ce^{-j(-k_1 - jk_2)y} = Ce^{jk_1 y}e^{-k_2 y}, \tag{E.2.2}$$

and

$$w_-^n(y) = De^{-jk_-^n y} = De^{-j(k_1 + jk_2)y} = De^{-jk_1 y}e^{k_2 y}, \tag{E.2.3}$$

$$w_-^n(y) = De^{-jk_-^n y} = De^{-j(-k_1 + jk_2)y} = De^{jk_1 y}e^{k_2 y}, \tag{E.2.4}$$

so that

$$w_+^n(y) = C(e^{-jk_1 y} + e^{jk_1 y})e^{-k_2 y} = 2C\cos(k_1 y)e^{-k_2 y}, \tag{E.2.5}$$

$$w_-^n(y) = D(e^{-jk_1 y} + e^{jk_1 y})e^{k_2 y} = 2D\cos(k_1 y)e^{k_2 y}, \tag{E.2.6}$$

in the positive and negative y direction.

Note that in Eqs.E.1.20-E.1.21, we assume that the complex roots in the nearfield wave components with the common decay term (imaginary part of k), have the same amplitude, i.e. k_b with k_c in the positive, and k_e with k_f in the negative direction. Pairing k_b with k_f for example, according to the common propagating term k_1 (real part of k), would lead to a physically unrealistic solutions in which the wave propagating in the direction away from the excitation would increase instead of evanesce.

In general the plate displacement, w, can thus be written as

$$w(y) = \underbrace{Ae^{-jk_0 y} + Be^{jk_0 y}}_{propagating\ waves} + \underbrace{C\cos(k_1 y)e^{-k_2 y} + D\cos(k_1 y)e^{k_2 y}}_{evanescent\ waves}, \tag{E.2.7}$$

where A and B are the amplitudes of the travelling waves propagating in the positive and negative direction (**NB** since $|C|$ and $|D|$ are assumed constant, $2|C|$ and $2|D|$ are also constant and the factors of two were omitted in Eq.E.2.7).

The constants A, B, C and D can be derived applying the boundary conditions for the duct. These are, however, difficult to infer due to the complex anatomy of the organ of Corti.

In order to get an idea of the idealised form of the solution, we initially assume that the duct is infinite. If excited by a force at position y, the amplitudes of waves propagating in the positive and negative direction from the input will be equal, so that A=B and C=D in an infinite duct. Hence, Eq.E.2.7 can be simplified to give

$$w(y) = Ae^{-jk_0y} + Ae^{jk_0y} + C\cos(k_1y)e^{-k_2y} + C\cos(k_1y)e^{k_2y}, \tag{E.2.8}$$

in general, where in this case the solutions on either side of the force can be written as

$$w_+(y) = Ae^{-jk_0y} + C\cos(k_1y)e^{-k_2y}, \qquad \text{for } y > 0, \tag{E.2.9}$$

$$w_-(y) = Ae^{jk_0y} + C\cos(k_1y)e^{k_2y}, \qquad \text{for } y < 0. \tag{E.2.10}$$

The slope of the plate displacement at the point of excitation must be equal to zero, by symmetry, so that

$$\frac{\partial w_+(y)}{\partial y} = -jk_0Ae^{-jk_0y} - Ck_1\sin(k_1y)e^{-k_2y} - Ck_2\cos(k_1y)e^{-k_2y} = 0,$$

$$\frac{\partial w_-(y)}{\partial y} = jk_0Ae^{jk_0y} - Ck_1\sin(k_1y)e^{k_2y} + Ck_2\cos(k_1y)e^{k_2y} = 0, \tag{E.2.11}$$

and, choosing the coordinate system such that the input force is at y=0,

$$\frac{\partial w_+(0)}{\partial y} = -jk_0A - k_2C = 0,$$
$$\frac{\partial w_-(0)}{\partial y} = jk_0A + k_2C = 0. \tag{E.2.12}$$

Therefore

$$k_2C = -jk_0A, \tag{E.2.13}$$

so that

$$C = -j\frac{k_0}{k_2}A, \tag{E.2.14}$$

or using the relationship between k_0 and k_2 in Eq.E.1.17

$$C = -j\frac{2}{\sqrt{3}}A. \tag{E.2.15}$$

Knowing the relative amplitude of the evanescent wave, Eqs.E.2.9 and E.2.10 can be rewritten as

$$w_+(y) = A\left(e^{-jk_0y} - j\frac{2}{\sqrt{3}}\cos(k_1y)e^{-k_2y}\right), \tag{E.2.16}$$
$$w_-(y) = A\left(e^{jk_0y} - j\frac{2}{\sqrt{3}}\cos(k_1y)e^{k_2y}\right). \tag{E.2.17}$$

The plate displacements in an infinite duct were calculated at 1 kHz using expressions for $w_\pm(y)$ in Eqs.E.2.16-E.2.17, for parameters in Table 6.1, as shown in Fig.E.2. The figure shows the displacement, $w(y)$, derived from the formula including the effects of the nearfield (dashed) and the equation without the nearfield components (travelling wave only, solid). For convenience, the assumed relative positions of the three outer hair cells OHC1-3 (compare Fig.6.1) are marked with the vertical lines. We assume that the OHCs are separated by 20 μm from each other.

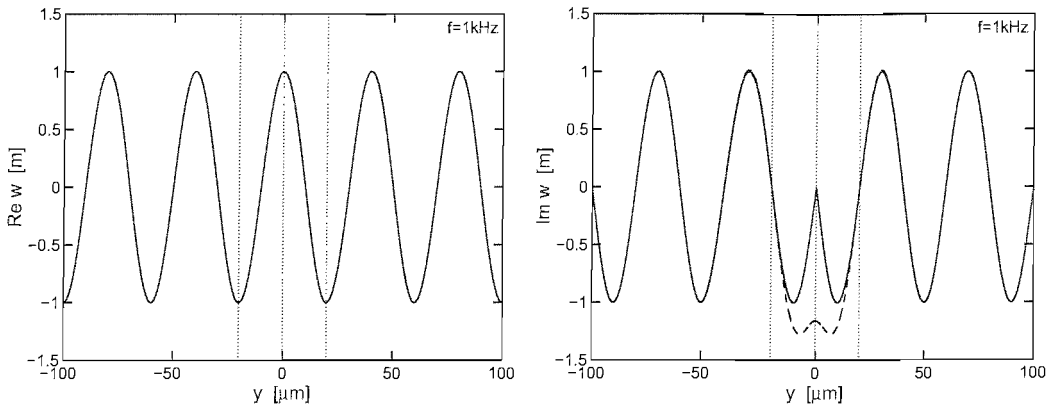

(a) (b)

Figure E.2: Real (a) and imaginary (b) part of the vertical plate displacement, $w(y)$, at 1 kHz propagating in an infinite plate as a function of radial position in the subtectorial duct. The solid and dashed lines show the waves without and with the nearfield component, respectively. Additionally, the relative positions of the outer hair cells are indicated by the vertical lines.

Note that according to Eq.E.1.6, the fluid particle displacement, u, can be derived straightforward using Eqs.E.2.16 and E.2.17, since

$$u = \frac{2}{d} \int w dy. \tag{E.2.18}$$

Thus the fluid particle displacement in the positive direction will be equal to

$$u_+(y) = \frac{2}{d} \int w_+(y) = \frac{2}{d} \int A \left(e^{-jk_0 y} - j\frac{2}{\sqrt{3}} \cos(k_1 y) e^{-k_2 y} \right) dy =$$

$$= \frac{2A}{d} \left[\underbrace{\int e^{-jk_0 y} dy}_{I_1} - j\frac{2}{\sqrt{3}} \underbrace{\int \cos(k_1 y) e^{-k_2 y} dy}_{I_2} \right]. \tag{E.2.19}$$

The first integral on the right-hand side of the above equation can be solved straightaway, so that

$$I_1 = \int e^{-jk_0 y} dy = \frac{j}{k_0} e^{-jk_0 y}, \tag{E.2.20}$$

where we omit the constant of integration (as in all the remaining solutions of integration). Solving by parts the second integral in Eq.E.2.19 gives

$$I_2 = \int \cos(k_1 y) e^{-k_2 y} dy = \frac{1}{k_1^2 + k_2^2}(k_1 \sin(k_1 y) e^{-k_2 y} - k_2 \cos(k_1 y) e^{-k_2 y}). \quad \text{(E.2.21)}$$

Thus, the expression for the fluid particle displacement in the positive direction, takes the form

$$u_+(y) = \frac{j2A}{d}\left[\frac{1}{k_0}\, e^{-jk_0 y} + \frac{2}{\sqrt{3}(k_1^2 + k_2^2)}\left(k_2 \cos(k_1 y) e^{-k_2 y} - k_1 \sin(k_1 y) e^{-k_2 y}\right)\right], \quad \text{(E.2.22)}$$

or knowing that $2/\sqrt{3}{=}k_0/k_2$ according to Eq.E.1.17

$$u_+(y) = \frac{j2A}{d}\left[\frac{1}{k_0}\, e^{-jk_0 y} + \frac{k_0}{k_1^2 + k_2^2}\left(\cos(k_1 y) e^{-k_2 y} - \frac{k_1}{k_2}\sin(k_1 y) e^{-k_2 y}\right)\right]. \quad \text{(E.2.23)}$$

The particle displacement of the subtectorial fluid in the negative direction, can be calculated using Eq.E.2.18 and Eq.E.2.17 defining the plate displacement of the negative-going waves. Hence

$$\begin{aligned} u_-(y) &= \frac{2}{d}\int w_-(y) = \frac{2}{d}\int A\left(e^{jk_0 y} - j\frac{2}{\sqrt{3}}\cos(k_1 y) e^{k_2 y}\right) dy = \\ &= \frac{2A}{d}\left[\underbrace{\int e^{jk_0 y} dy}_{I_3} - j\frac{2}{\sqrt{3}}\underbrace{\int \cos(k_1 y) e^{k_2 y} dy}_{I_4}\right]. \end{aligned} \quad \text{(E.2.24)}$$

Solving the first integral in the above equation, I_3, we have

$$I_3 = \int e^{jk_0 y} dy = -\frac{j}{k_0}\, e^{jk_0 y}. \quad \text{(E.2.25)}$$

Solving the integral I_4 in Eq.E.2.24 by parts, gives

$$I_4 = \int \cos(k_1 y) e^{k_2 y} dy = \frac{1}{k_1^2 + k_2^2}\,(k_1 \sin(k_1 y) e^{k_2 y} + k_2 \cos(k_1 y) e^{k_2 y}), \quad \text{(E.2.26)}$$

so that, using the relationship $2/\sqrt{3}=k_0/k_2$ and Eq.E.2.25, the subtectorial fluid's particle displacement propagating in the negative direction, can be formulated by

$$u_{-}(y) = -\frac{j2A}{d}\left[\frac{1}{k_0}\,e^{jk_0y} + \frac{k_0}{k_1^2+k_2^2}\left(\cos(k_1y)e^{k_2y} + \frac{k_1}{k_2}\sin(k_1y)e^{k_2y}\right)\right]. \tag{E.2.27}$$

Figure E.3 shows the real and imaginary part of the fluid particle displacement in an infinite duct calculated using the expressions in Eq.E.2.23 and E.2.27 for the parameters in Table 6.1. The solid and dashed lines show the fluid displacement for a wave with the nearfield component neglected and taken into account, respectively.

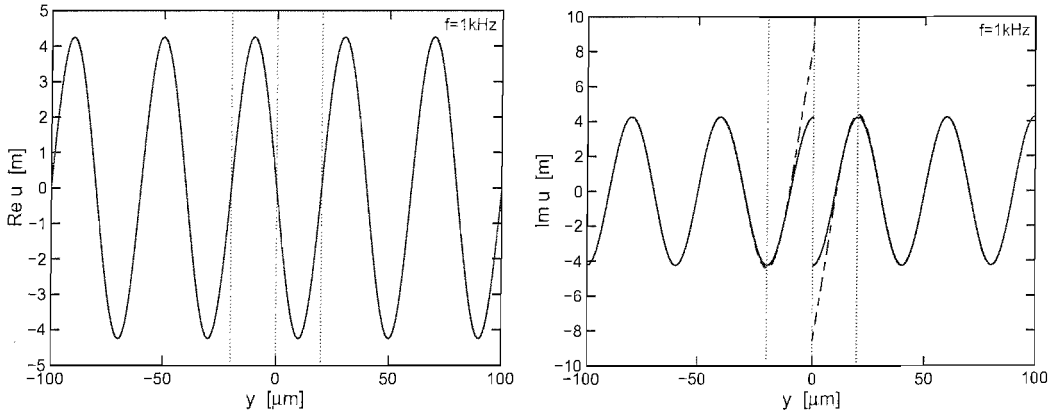

(a) (b)

Figure E.3: Real (a) and imaginary (b) part of the fluid particle displacement, $u(y)$, at 1 kHz propagating in an infinite subtectorial duct as a function of radial position in the duct. The solid and dashed lines show the waves without and with the nearfield component, respectively. Relative positions of the outer hair cells are indicated by the vertical lines.

E.3 Wave motion in a finite duct

In the present section we derive the expressions for the wave motion due to 'squirting' waves in a finite duct. We assume pressure release boundary conditions at the ends of the duct, since the subtectorial fluid travels from a very narrow to a relatively wide cavity of the internal sulcus at the IHC end and the scala media.

The travelling wave component of the 'squirting' wave will be reflected from the ends of the duct and will travel back towards the excitation source creating a standing wave resonance. However, the nearfield components of the 'squirting' wave do not travel very far in the duct, so that they are assumed not to be reflected at the ends of the duct, and hence do not contribute to the standing wave resonance in the subtectorial space. Therefore, we neglect the nearfield components in the following considerations[1].

It should be also noted that the subtectorial duct is not symmetric with regard to the positions of the OHC rows at which the input forces will be considered. Thus, the length of the duct from the IHC end to the position of the 'OHC input' will be denoted as l_j, whereas the length of the duct as L. We also introduce the reflection coefficients for the waves reflected from the ends of the duct, defined by the ratio of amplitudes of the reflected and incident waves [48, 93].

Assuming the pressure wave propagating in the positive and negative directions from the force input within the duct, p_+ and p_- respectively, are of the form

$$p_+(y) = A_i e^{-jk_0 y} + B_r e^{jk_0 y}, \tag{E.3.1}$$

$$p_-(y) = C_i e^{jk_0 y} + D_r e^{-jk_0 y}, \tag{E.3.2}$$

where A_i and C_i are the amplitudes of the incident waves and B_r and D_r are the amplitudes of the reflected waves, and applying the pressure release boundary conditions, we have

[1]The subtectorial fluid's viscosity, effect of which will be described later, attenuates the waves in the duct even more, so that the simplification by neglecting the nearfield terms is further justified.

$$p_+(L-l_j) = A_i e^{-jk_0(L-l_j)} + B_r e^{jk_0(L-l_j)} = 0, \tag{E.3.3}$$

$$p_-(-l_j) = C_i e^{-jk_0 l_j} + D_r e^{jk_0 l_j} = 0, \tag{E.3.4}$$

where $p(L-l_j)$ denotes the pressure at the end of the duct to the right from the input, whereas $p(-l_j)$ is the pressure at the duct's end to the left from the position of the input. Thus

$$B_r = -A_i e^{-2jk_0(L-l_j)}, \tag{E.3.5}$$

$$D_r = -C_i e^{-2jk_0 l_j}, \tag{E.3.6}$$

so that

$$R_1 = \frac{B_r}{A_i} = -e^{-2jk_0(L-l_j)}, \tag{E.3.7}$$

$$R_2 = \frac{D_r}{C_i} = -e^{-2jk_0 l_j}, \tag{E.3.8}$$

and we denote R_1 as the reflection coefficient for the reflected wave travelling in the right-hand side region from the input, and R_2 for the reflected wave travelling in the left-hand side region from the input. Hence, using Eqs.E.2.9-E.2.10, the plate displacement in a duct of a finite length can be expressed as

$$w_+(y) = A_+(e^{-jk_0 y} + R_1 e^{jk_0 y}), \tag{E.3.9}$$

$$w_-(y) = A_-(e^{jk_0 y} + R_2 e^{-jk_0 y}), \tag{E.3.10}$$

where the nearfield components were neglected and A_+ and A_- are the amplitudes of the waves travelling in the positive and negative direction from the input source. Furthermore, there cannot be any discontinuity of the plate displacement at the point of excitation, which we choose to be at y=0, and we can assume that $w_+(0)$=$w_-(0)$. Therefore, Eqs.E.3.9-E.3.10 give

$$w_+(0) = A_+(1+R_1), \tag{E.3.11}$$

$$w_-(0) = A_-(1+R_2), \tag{E.3.12}$$

and hence

$$A_- = A_+ \left(\frac{1 + R_1}{1 + R_2} \right). \tag{E.3.13}$$

Assuming that the input force is acting at the positions of the OHC1-3 (Fig.6.1), i.e. l_1=30 μm, l_2=50 μm and l_2=70 μm from the IHC position, which also define the origin of the coordinate system within the duct, we calculate the plate displacements in a finite duct according to Eq.E.3.9-E.3.10, where R_1 and R_2 are defined in Eqs.E.3.7-E.3.8 for different positions of the OHC input. The magnitude and phase of A_+ are set to 1 and 0, respectively, and A_- is defined in Eq.E.3.13. The length of the duct L is equal to 80 μm and the parameters used for calculating the wavenumber are gathered in Table 6.1. The real and imaginary part of the plate displacement due to the excitation at the position of the first OHC along the subtectorial duct, are shown in Fig.E.4, whereas the plate displacements due to the excitations at the second and third OHC along the subtectorial duct, are shown in Fig.E.5.

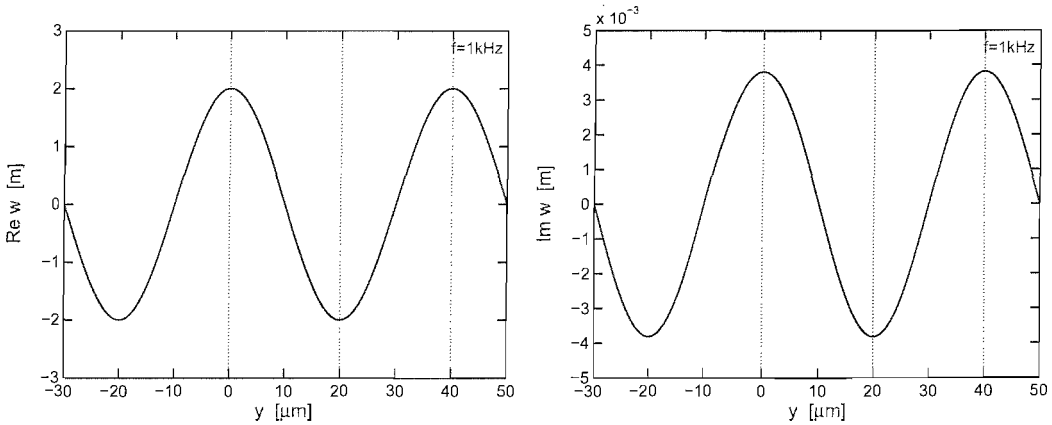

(a) (b)

Figure E.4: Real (a) and imaginary (b) part of the vertical plate displacement, $w(y)$, at 1 kHz propagating in a finite plate due to the excitation at the first outer hair cell, as a function of radial position in the subtectorial duct. Relative positions of the outer hair cells are indicated by the vertical lines.

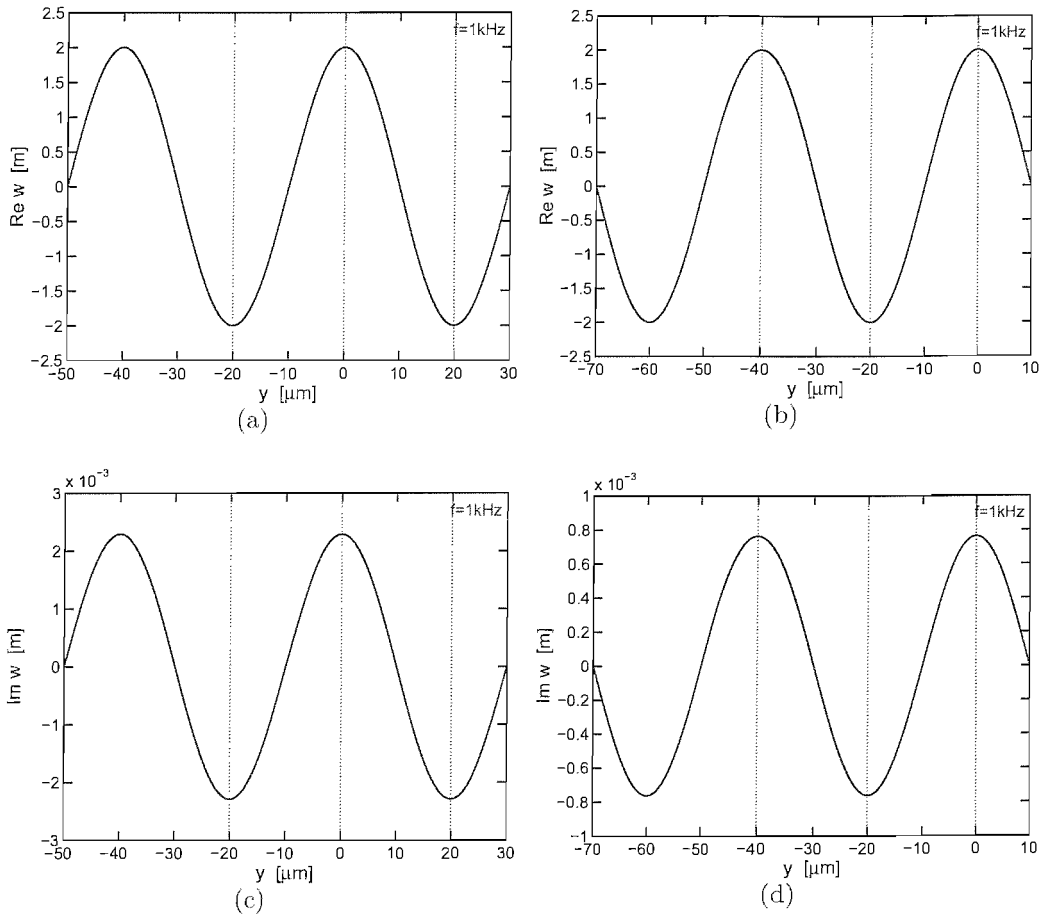

Figure E.5: Real and imaginary part of the vertical plate displacement, $w(y)$, at 1 kHz propagating in a finite plate due to the excitation at the second (a, c) and the third (b, d) outer hair cell, as a function of radial position in the subtectorial duct. Relative positions of the outer hair cells are indicated by the vertical lines.

Using Eq.E.2.18 and Eqs.E.3.9-E.3.10, the fluid particle displacement in a finite duct can be derived as

$$u_+(y) = \frac{2}{d}\int w_+(y)dy = \frac{2A_+}{d}\left(\int e^{-jk_0y}dy + R_1\int e^{jk_0y}dy\right), \quad \text{(E.3.14)}$$

$$u_-(y) = \frac{2}{d}\int w_-(y)dy = \frac{2A_-}{d}\left(\int e^{jk_0y}dy + R_2\int e^{-jk_0y}dy\right), \quad \text{(E.3.15)}$$

for the positive- and negative-going waves. The solutions of the integrals in the above equations are given in Eq.E.2.20 and E.2.25, so that

$$u_+(y) = \frac{j2A_+}{k_0d}(e^{-jk_0y} - R_1e^{jk_0y}), \quad \text{(E.3.16)}$$

$$u_-(y) = -\frac{j2A_-}{k_0d}(e^{jk_0y} - R_2e^{-jk_0y}), \quad \text{(E.3.17)}$$

hence given the position of the excitation in the finite duct, the resulting fluid displacement can be calculated.

The fluid particle displacements in a finite duct were calculated according to the above equations where all conditions and parameters used for the calculations are the same as for the calculation of the plate displacements. The real and imaginary part of the fluid displacement due to the excitation at the position of the first OHC along the subtectorial duct, are shown in Fig.E.6, whereas the plate displacements due to the excitations at the second and third OHC along the subtectorial duct, are shown in Fig.E.7.

E.4 Viscous 'squirting' waves

In the following section we derive the wave equation for the 'squirting' waves with the viscosity of the subtectorial fluid taken into account. For a viscous fluid an additional term due to the resistive forces acting against the propagation of the fluid, appears in the wave equation. These forces depend on the thickness of the viscous boundary layer, i.e.

$$\delta = \left(\frac{2\eta}{\rho\omega}\right)^{\frac{1}{2}}, \quad \text{(E.4.1)}$$

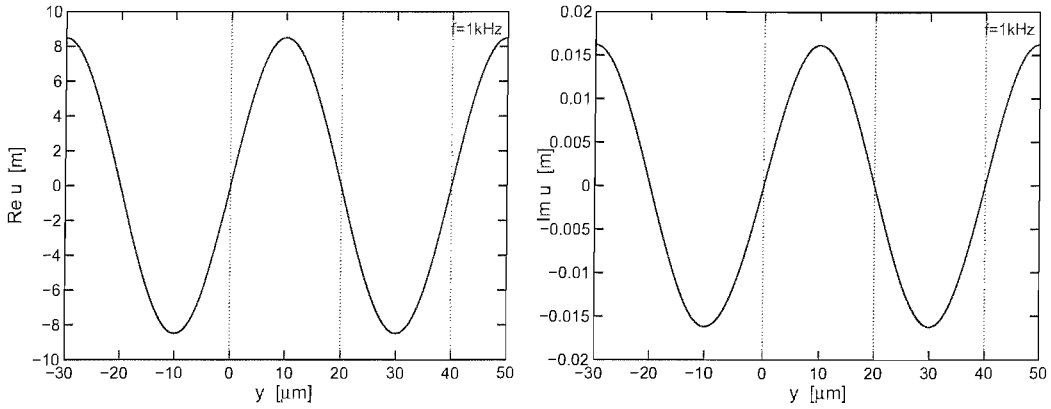

(a) (b)

Figure E.6: Real (a) and imaginary (b) part of the fluid particle displacement, $u(y)$, at 1 kHz in a finite duct due to the excitation at the first row of the outer hair cell, as a function of radial position in the subtectorial duct. Relative positions of the outer hair cells are indicated by the vertical lines.

where η is the coefficient of viscosity, ρ is the density of fluid, and ω is the angular frequency [48, 81]. The force, F, required to overcome the resistive forces due to the fluid's viscosity is proportional to the fluid layer thickness, d_2, through a coefficient of resistance $16\eta/d_2^2$ [54], such that

$$F(y,t) = \frac{16\eta}{d_2^2}\frac{\partial u(y,t)}{\partial t}. \tag{E.4.2}$$

Incorporating the above equation into the fluid force equation defined in Eq.E.1.5, we have

$$\rho\frac{\partial^2 u(y,t)}{\partial t^2} + \frac{16\eta}{d_2^2}\frac{\partial u(y,t)}{\partial t} = -\frac{\partial p(y,t)}{\partial y}, \tag{E.4.3}$$

where u is now interpreted as the mean particle displacement over a section of the duct [54].

As for the derivation in Section E.1, we differentiate Eq.E.1.4 with respect to

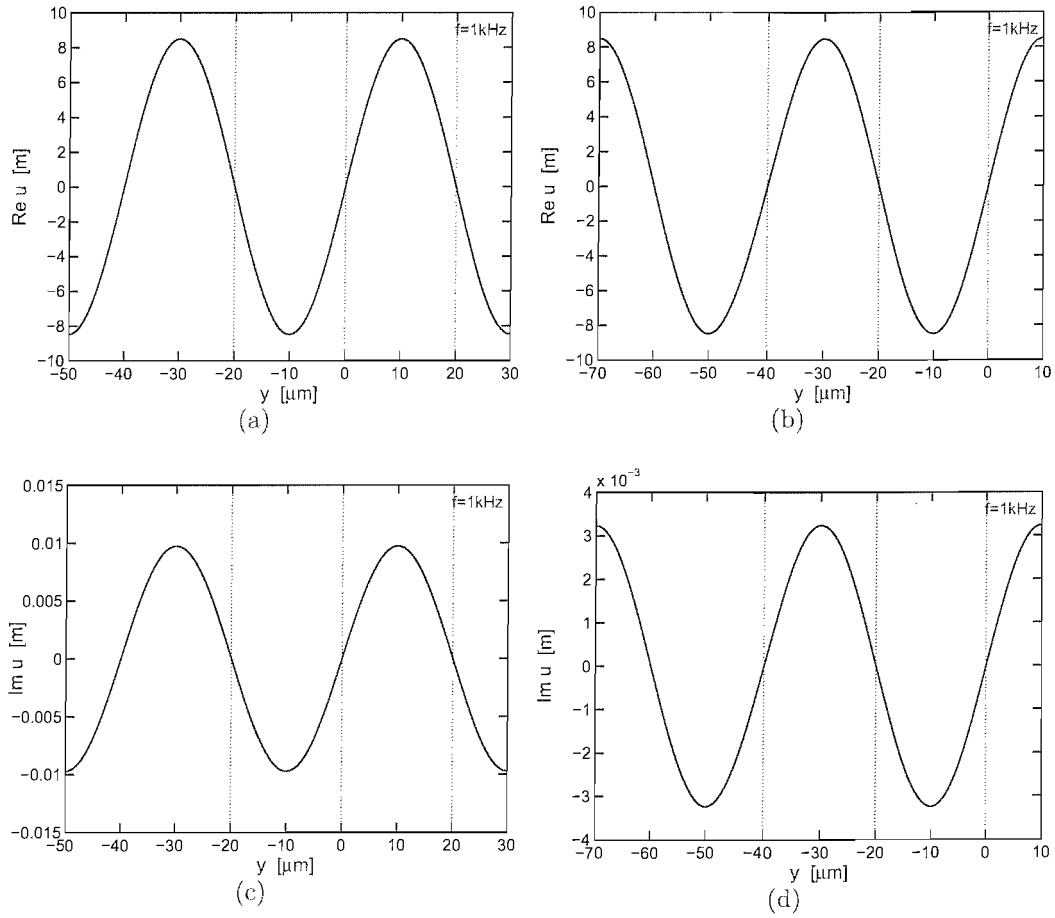

Figure E.7: Real and imaginary part of the fluid particle displacement, $u(y)$, at 1 kHz in a finite duct due to the excitation at the second (a, c) and the third (b, d) outer hair cell, as a function of radial position in the subtectorial duct. Relative positions of the outer hair cells are indicated by the vertical lines.

y and substitute for $\partial p(y,t)/\partial y$ in Eq.E.4.3, so that

$$\rho \frac{\partial^2 u(y,t)}{\partial t^2} + \frac{16\eta}{d_2^2} \frac{\partial u(y,t)}{\partial t} = EI \frac{\partial^5 w(y,t)}{\partial y^5}, \tag{E.4.4}$$

and after differentiating the above equation with respect to y and substituting for $\partial^3 u(y,t)/\partial y \partial t^2$ from Eq.E.1.8, we have

$$\frac{2\rho}{d_2} \frac{\partial^2 w(y,t)}{\partial t^2} + \frac{16\eta}{d_2^2} \frac{\partial^2 u(y,t)}{\partial y \partial t} = EI \frac{\partial^6 w(y,t)}{\partial y^6}, \tag{E.4.5}$$

or

$$\rho \frac{\partial^2 w(y,t)}{\partial t^2} + \frac{8\eta}{d_2} \frac{\partial^2 u(y,t)}{\partial y \partial t} = \frac{EId_2}{2} \frac{\partial^6 w(y,t)}{\partial y^6}. \tag{E.4.6}$$

Finally, differentiating the continuity equation for the incompressible fluid defined in Eq.E.1.6 with respect to time gives

$$\frac{\partial w(y,t)}{\partial t} = \frac{d_2}{2} \frac{\partial^2 u(y,t)}{\partial y \partial t}, \tag{E.4.7}$$

which after substitution for $\partial^2 u(y,t)/\partial y \partial t$ in Eq.E.4.6, leads to the formulation of the wave equation for the viscous 'squirting' waves, i.e.

$$\rho \frac{\partial^2 w(y,t)}{\partial t^2} + \frac{16\eta}{d_2^2} \frac{\partial w(y,t)}{\partial t} - \frac{EId_2}{2} \frac{\partial^6 w(y,t)}{\partial y^6} = 0. \tag{E.4.8}$$

Assuming the plate displacement, w, in Eq.E.4.8 is complex and harmonic, i.e. $w(y,t)=Ae^{j(\omega t - ky)}$, we write

$$\frac{EId_2}{2} k_v^6 = \rho\omega^2 - \frac{j16\eta\omega}{d_2^2}, \tag{E.4.9}$$

where k_v denotes the wavenumber of the viscous 'squirting' wave, and the dispersion relationship for the 'squirting' waves with viscosity takes the form

$$k_v = \left(\frac{2\rho\omega^2}{EId_2} - j\frac{32\eta\omega}{EId_2^3} \right)^{\frac{1}{6}}. \tag{E.4.10}$$

Note that the fluid force equation in Eq.E.4.3 is defined for the model with the fluid layer of thickness d_2, confined between two elastic plates of thickness h_s. Thus, we rewrite the expressions for the wave equation and the wavenumber as

for the viscous 'squirting' waves in the fluid layer of thickness d=$d_2/2$ confined between a rigid surface and a plate of thickness h=$2h_s$. Replacing d_2 by $2d$ in Eq.E.4.8 we have

$$\rho \frac{\partial^2 w(y,t)}{\partial t^2} + \frac{4\eta}{d^2} \frac{\partial w(y,t)}{\partial t} - EId \frac{\partial^6 w(y,t)}{\partial y^6} = 0, \tag{E.4.11}$$

and the corresponding wavenumber will take the form

$$k_v = \left(\frac{\rho\omega^2}{EId} - j\frac{4\eta\omega}{EId^3} \right)^{\frac{1}{6}}, \tag{E.4.12}$$

where the moment of inertia, I, is defined in Eq.E.1.15.

It should be noted that again there are six distinctive roots, k_{a-f}, of the dispersion relation that form a hexagon in the complex plane of k_v, as shown in Fig.E.8 for k_v at 1 kHz, evaluated for the set of parameters in Table 6.1 and fluid's viscosity η=6.6×10^{-4} kgm^{-1}s^{-1}. However, now also two wavenumber components corresponding to the waves travelling along the duct, k_a and k_d, have imaginary parts and so the travelling waves are decaying with the distance from the source. The remaining four roots of the above equation, $k_{b,c,e,f}$, form the standing nearfield in an infinite duct and are predicted to decay even faster than in the case without viscosity. Therefore, the nearfield components will be neglected in the analysis of the wave motion so that we consider only the wavenumber solutions for the travelling waves, which we denote as k_{v0} and $-k_{v0}$ for the positive- and negative-going direction, respectively. Also note that setting η to zero in Eq.E.4.10 reduces the wavenumber to its real part, which is equal to the wavenumber derived for the lossless 'squirting' waves, and hence k_{v0} becomes equal to k_0.

Note that the hexagon lying on a circle of radius k_a [51], is rotated clockwise with regard to the hexagon obtained for the lossless case. Since

$$k_v = |k_v| e^{j\phi/6}$$

where ϕ is the phase of the wavenumber k_v equal to $\tan^{-1}(Im\{k_v\}/Re\{k_v\})$, as $Re\{k_v\}$ decreases ϕ approaches $\pi/2$ so that the maximum angle of rotation of the first vertex k_{v0}, and hence the hexagon, amounts to $\pi/12$=15° according to the above expression.

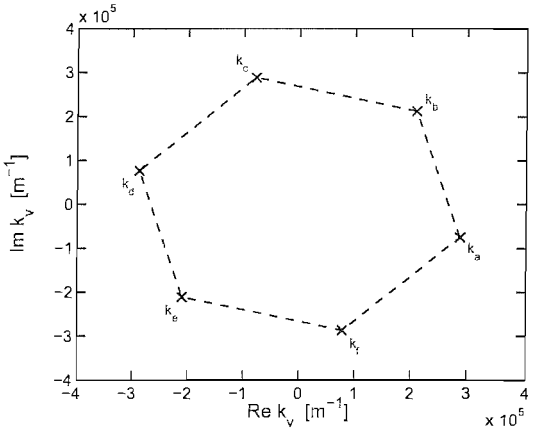

Figure E.8: The roots, k_{a-f} (crosses '$\times$'), of the wavenumber of the viscous 'squirting' wave, k_v, at 1 kHz.

The travelling transverse displacement of the finite plates will take the same from as for the case with no viscosity, Eqs.E.3.9 and E.3.10, where we replace k_0 by k_{v0}

$$w_{v+}(y) = A_+(e^{-jk_{v0}y} + R_1 e^{jk_{v0}y}), \tag{E.4.13}$$

$$w_{v-}(y) = A_-(e^{jk_{v0}y} + R_2 e^{-jk_{v0}y}), \tag{E.4.14}$$

where the index 'v' refers to the 'viscous case' of wave propagation, and R_1 and R_2 are now defined as (compare Eqs.E.3.7-E.3.8)

$$R_1 = -e^{-2jk_{v0}(L-l_j)}, \tag{E.4.15}$$

$$R_2 = -e^{-2jk_{v0}l_j}. \tag{E.4.16}$$

Analogously, the fluid particle displacement in a finite duct takes the form

$$u_{v+}(y) = \frac{j2A_+}{k_{v0}d}(e^{-jk_{v0}y} - R_1 e^{jk_{v0}y}), \tag{E.4.17}$$

$$u_{v-}(y) = -\frac{j2A_-}{k_{v0}d}(e^{jk_{v0}y} - R_2 e^{-jk_{v0}y}), \tag{E.4.18}$$

according to Eqs.E.3.16 and E.3.17.

The real and imaginary parts of the vertical plate displacement, $w_v(y)$, and the fluid particle displacement, $u_v(y)$, due to the excitation from the OHC1-3 at 1 kHz in a finite subtectorial duct of the 'squirting' wave model with viscosity taken into account, are shown as a function of position in the duct in Fig.E.9-E.11, respectively. The model was solved for the parameters in Table 6.1 and viscosity of η=6.6×10^{-4} kgm^{-1}s^{-1}.

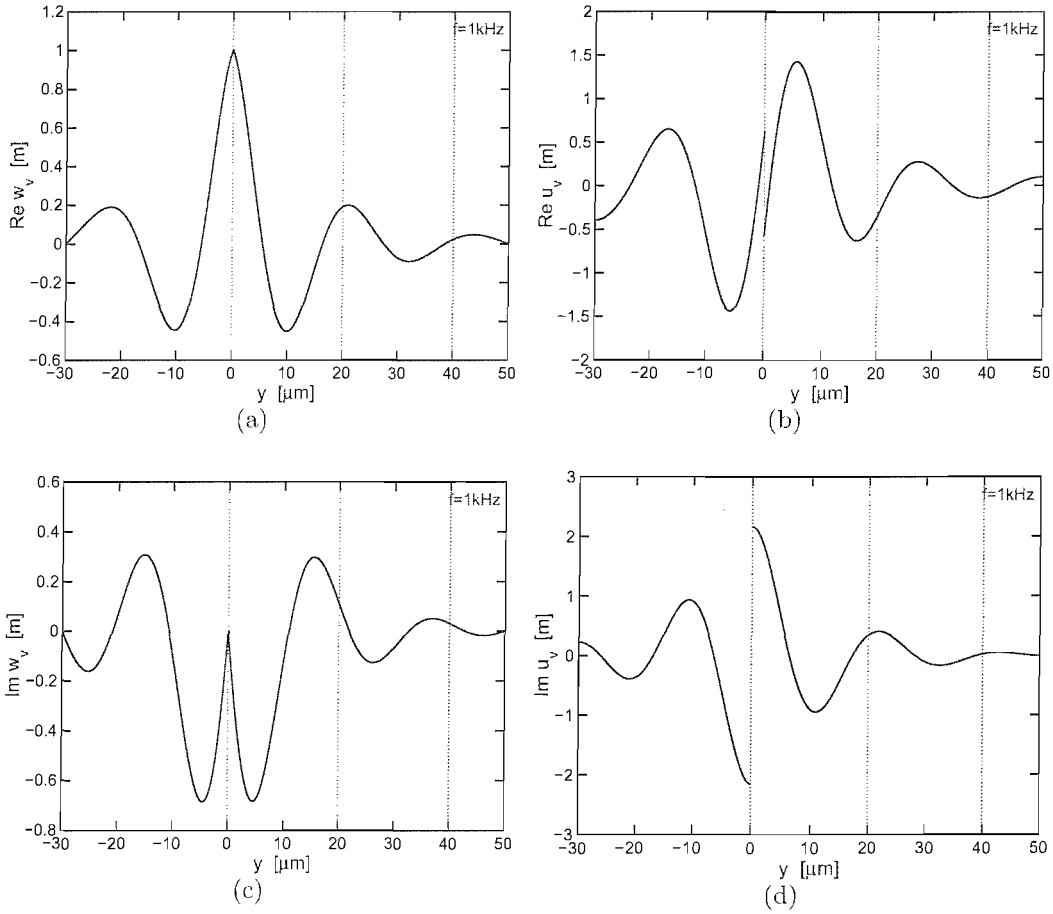

Figure E.9: Real and imaginary part of the vertical plate displacement, $w_v(y)$ (a, c), and the fluid particle displacement, $u_v(y)$ (b, d), at 1 kHz due to the excitation at the first outer hair cell, as a function of radial position in a finite subtectorial duct of the 'squirting' wave model with viscosity. Relative positions of the outer hair cells are indicated by the vertical lines.

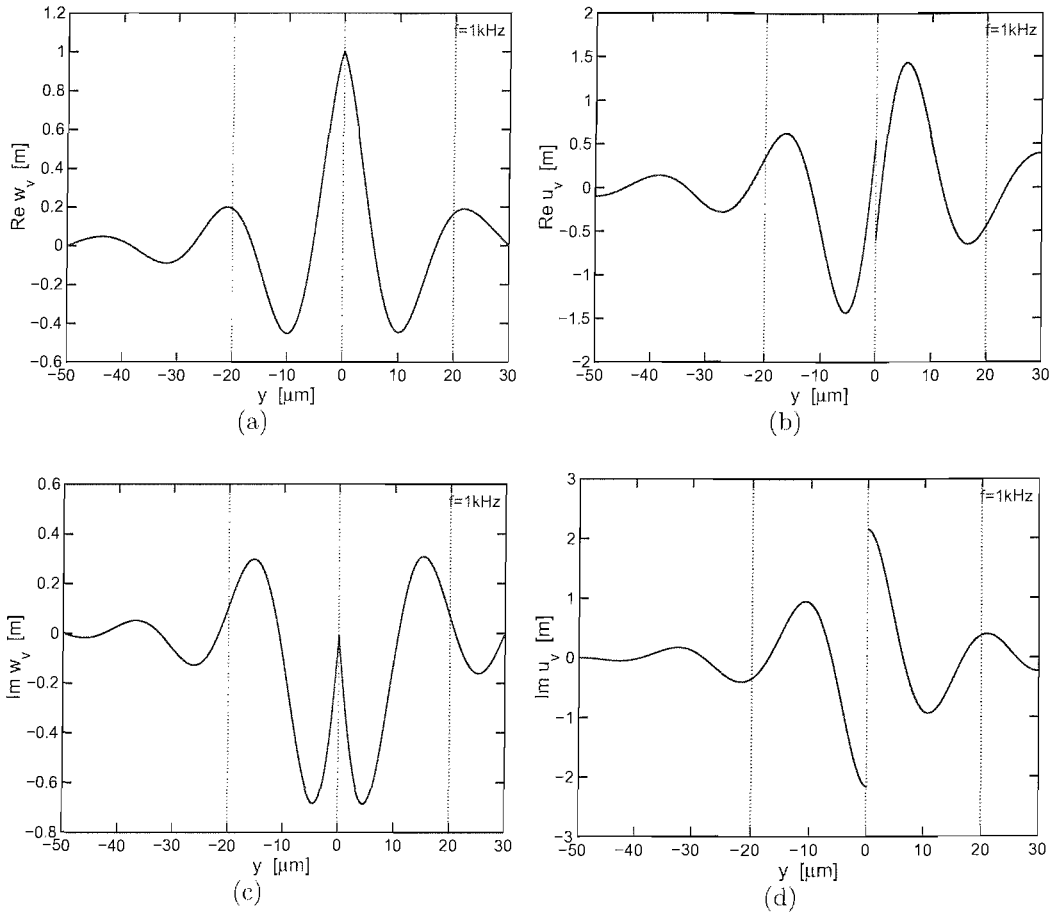

Figure E.10: Real and imaginary part of the vertical plate displacement, $w_v(y)$ (a, c), and the fluid particle displacement, $u_v(y)$ (b, d), at 1 kHz due to the excitation at the second outer hair cell, as a function of radial position in a finite subtectorial duct of the 'squirting' wave model with viscosity. Relative positions of the outer hair cells are indicated by the vertical lines.

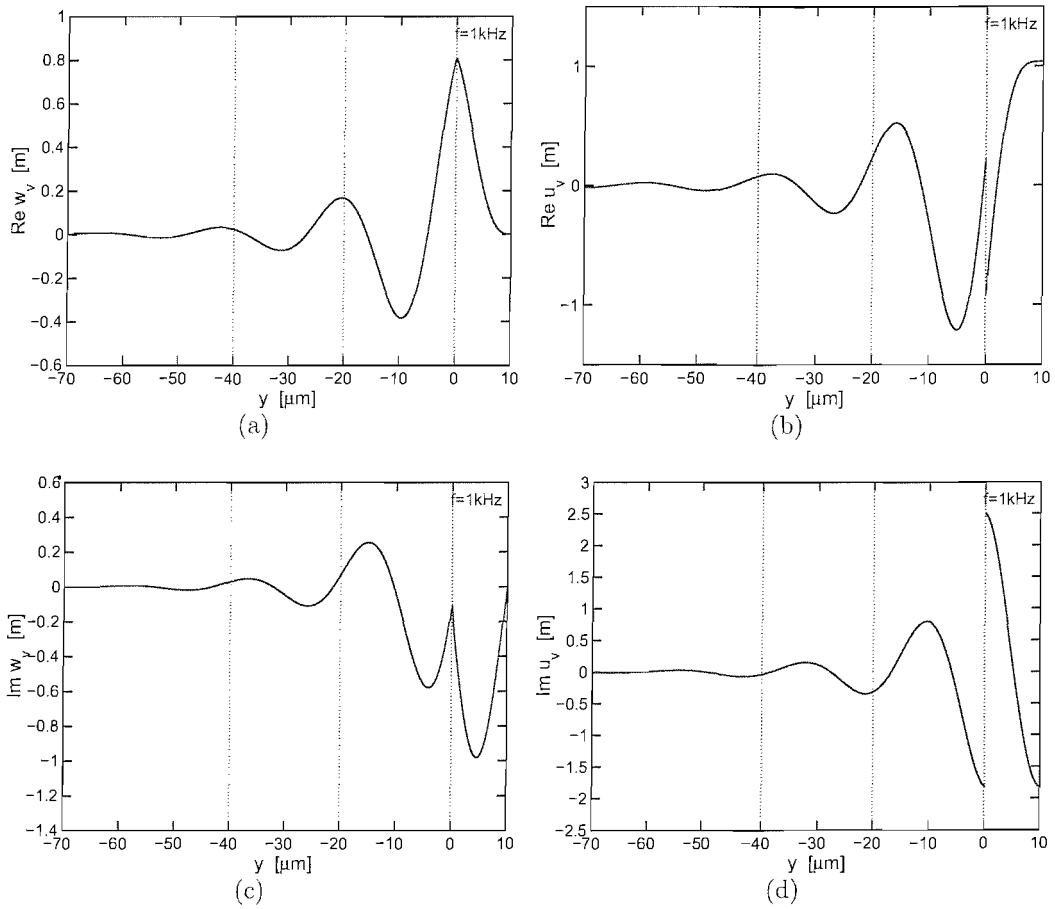

Figure E.11: Real and imaginary part of the vertical plate displacement, $w_v(y)$ (a, c), and the fluid particle displacement, $u_v(y)$ (b, d), at 1 kHz due to the excitation at the third outer hair cell, as a function of radial position in a finite subtectorial duct of the 'squirting' wave model with viscosity. Relative positions of the outer hair cells are indicated by the vertical lines.

E.5 Calculation of the individual responses

In the present section we define the constitutive responses of the feedback controller model shown in Fig.6.7. According to Fig.6.7 we have four individual types of responses that have to be calculated to derive the overall response of the active 'squirting' wave model. These include two external responses due to the external pressure in scala media, the fluid particle displacement at the IHC end of the duct and the plate displacement at the OHCs positions, G_{up} (duct response) and G_{wp}, respectively. Also, there are two internal responses, i.e. the fluid particle displacement at the location of the IHC and the plate displacements at locations above the OHC rows, both caused by the OHCs electromotile force excitation and referred to as G_{uf} and G_{wf}, respectively.

E.5.1 The duct response G_{up}

To begin with we define the fluid particle displacement at the IHC end of the duct in response to the external pressure excitation at the scala media end of the duct. Choosing y=0 at the scala media end of the duct (position of the input), the IHC end is located at y=$-L$, where L is the length of the duct, as shown in Fig.E.12. Thus, at the IHC the fluid particle displacement will be denoted by $u(-L)$, while the driving pressure at the scala media end by $p(0)$=p_{ext}, and we can write

$$G_{up} = \frac{u(-L)}{p(0)} = \frac{u(-L)}{p_{ext}}. \tag{E.5.1}$$

Furthermore, we assume that $p(-L)$=0, due to the pressure release condition. Note that the pressure wave is propagating in the left-hand side region of the duct from y=0. Therefore, using the relationship between the pressure load and the plate displacement in Eq.E.1.4 and Eq.E.4.14 for the damped plate displacement in a finite duct, we derive the expression for the pressure wave propagating in the left hand-side region of the duct

$$p_{v-}(y) = -EIk_{v0}^4 A_-(e^{jk_{v0}y} + R_2 e^{-jk_{v0}y}), \tag{E.5.2}$$

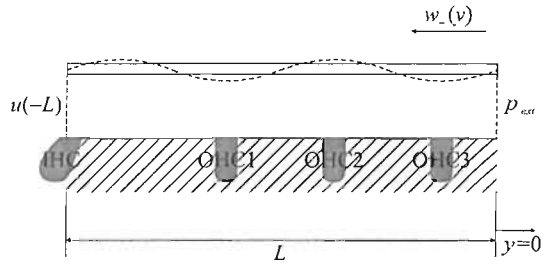

Figure E.12: Schematic of the subtectorial duct for the calculation of the duct response G_{up}. The origin of the coordinate system is chosen at the scala media end of the duct of length L, where the external pressure p_{ext} is exciting the subtectorial fluid particle displacement, which is measured at the inner hair cell (IHC) end of the duct, i.e. $u(-L)$. The three rows of the outer hair cells, OHC1-3, are also shown.

so that at y=0

$$p_{v-}(0) = -EIk_{v0}^4 A_-(1 + R_2), \tag{E.5.3}$$

where R_2 is equal to $-e^{-2jk_{v0}L}$ according to Eq.E.3.8, since the pressure wave travels along the length of the duct before it is reflected at the IHC end boundary. Hence

$$p_{v-}(0) = -EIk_{v0}^4 A_-(1 - e^{-2jk_{v0}L}). \tag{E.5.4}$$

The fluid particle displacement for the lossy 'squirting' waves propagating in a finite duct is given in Eq.E.4.18, hence at y=$-L$ it will take the form

$$u_{v-}(-L) = -\frac{j2A_-}{k_{v0}d}(e^{-jk_{v0}L} - R_2 e^{jk_{v0}L}), \tag{E.5.5}$$

where R_2 is again $-e^{-2jk_{v0}L}$, and

$$u_{v-}(-L) = -\frac{j2A_-}{k_{v0}d}(e^{-jk_{v0}L} + e^{-2jk_{v0}L}e^{jk_{v0}L}) = -\frac{j2A_-}{k_{v0}d}(e^{-jk_{v0}L} + e^{-jk_{v0}L}) =$$

$$= -\frac{j4A_-}{k_{v0}d}e^{-jk_{v0}L}. \tag{E.5.6}$$

Therefore, after rearrangement and knowing that

$$e^{j\theta} - e^{-j\theta} = 2j\sin\theta, \tag{E.5.7}$$

the response of the duct, G_{up}, will be defined by

$$G_{up} = \frac{u_{v-}(-L)}{p_{v-}(0)} = -\frac{j4A_-}{k_{v0}d(-EIk_{v0}^4A_-)}\frac{e^{-jk_{v0}L}}{1-e^{-2jk_{v0}L}} =$$

$$= \frac{j4}{EIk_{v0}^5 d}\frac{e^{-jk_{v0}L}}{e^{-jk_{v0}L}(e^{jk_{v0}L}-e^{-jk_{v0}L})} = \frac{j4}{EIk_{v0}^5 d}\frac{1}{2j\sin k_{v0}L} =$$

$$= \frac{2}{EIk_{v0}^5 d}\frac{1}{\sin k_{v0}L}. \tag{E.5.8}$$

The magnitude and phase of the response G_{up} calculated for the parameters in Table 6.1 and viscosity of η=6.6×10^{-4} kgm^{-1}s^{-1}, are shown in Fig.E.13.

E.5.2 The G_{uf} response

We have defined the ratio of the fluid displacement at the IHC end of the subtectorial space, and the internal force due to the motility of the OHC, as the response G_{uf}. Note that since there are three rows of OHCs, i.e. three inputs, and only one output, the general expression for the response G_{uf} according to the schematic in Fig.E.14, will take the form

$$G_{uf_j} = \frac{u(-l_j)}{f_j(0)}, \tag{E.5.9}$$

where the index j denotes the number of the input, i.e. number of the OHC row counting from the position of the IHC as shown in Fig.6.1, and thus $G_{uf_{1-3}}$ is a 1×3 row vector. Also note that $f_j(0)$ is a line force, since the geometry assumes uniform displacement in the x (longitudinal) direction, with dimensions [Nm^{-1}]. It was also assumed that y=0 is located at the site of the input force (OHC row), so that the position of the IHC, is denoted by $-l_j$, where l_j was defined as the length of the duct from the IHC end to the location of the input.

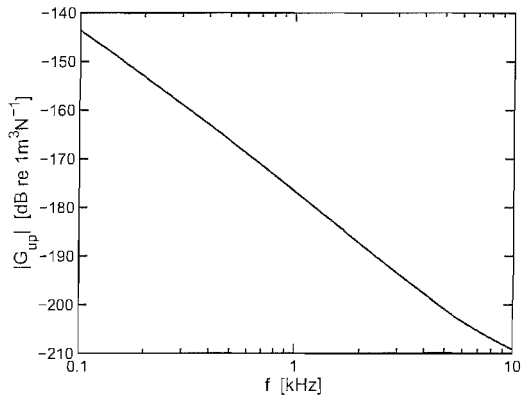

(a)

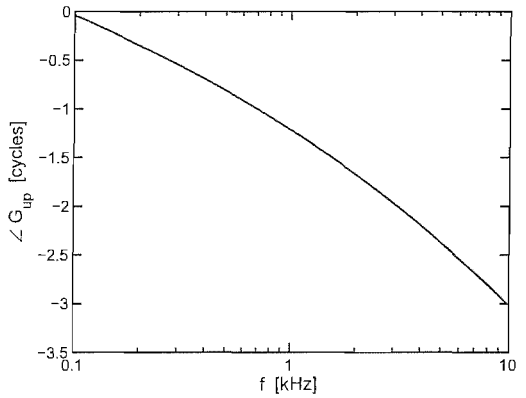

(b)

Figure E.13: Magnitude (a) and phase (b) of the response, G_{up}, as a function of frequency.

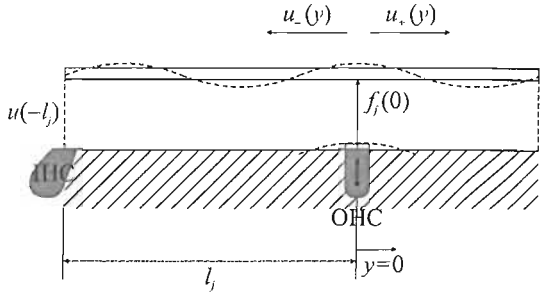

Figure E.14: The idealisation of the response G_{uf_j} within the subtectorial duct. The outer hair cell (OHC) electromotile force located at a distance l_j from the inner hair cell (IHC), causes an upward displacement of the plate and travelling waves of the fluid. The origin of the coordinate system, y=0, is chosen at the position of the outer hair cell excitation, thus the fluid particle displacement measured at the inner hair cell position is $u(-l_j)$.

Since for each of the $G_{uf_{1-3}}$ responses the input is considered at y=0, we begin with the derivation of the forces from the OHCs. We assume that a segment of the upper plate is displaced upwards due to the elongation of the OHC body. We also assume that the elongation of the hair cell body displaces the rigid surface of the RL only locally, so that it could be still considered as rigid outside the positions of the OHCs.

The forces acting on the left- and right-hand side of the plate's segment are opposite, so that the net force at y=0 will be equal to

$$f(0) = EI\left(\frac{\partial^3 w_{v+}(0)}{\partial y^3} - \frac{\partial^3 w_{v-}(0)}{\partial y^3}\right), \tag{E.5.10}$$

according to Eq.E.1.3, and since

$$\frac{\partial^3 w_{v+}}{\partial y^3}(y) = jk_{v0}^3 A_+(e^{-jk_{v0}y} - R_1 e^{jk_{v0}y}), \tag{E.5.11}$$

$$\frac{\partial^3 w_{v-}}{\partial y^3}(y) = -jk_{v0}^3 A_-(e^{jk_{v0}y} - R_2 e^{-jk_{v0}y}), \tag{E.5.12}$$

according to Eqs.E.4.13-E.4.14, where R_1 and R_2 are defined in Eqs.E.4.15-E.4.16, so that

$$\frac{\partial^3 w_{v+}}{\partial y^3}(0) = jk_{v0}^3 A_+(1-R_1), \tag{E.5.13}$$

$$\frac{\partial^3 w_{v-}}{\partial y^3}(0) = -jk_{v0}^3 A_-(1-R_2), \tag{E.5.14}$$

and therefore

$$f(0) = jEIk_{v0}^3[A_+(1-R_1) + A_-(1-R_2)], \tag{E.5.15}$$

Solving the relationship between A_+ and A_- in Eq.E.3.13 for A_+ in terms of A_-, because the fluid waves are propagating in the negative direction towards $-l_j$, and substituting into Eq.E.5.15 gives

$$f(0) = jEIk_{v0}^3 A_- \left[\frac{(1-R_1)(1+R_2)}{(1+R_1)} + (1-R_2)\right], \tag{E.5.16}$$

The expression for fluid particle displacement at the IHC end of the duct, $u(-l_j)$, can be found using Eq.E.4.18 for the waves propagating in the negative y direction, and takes the form

$$u_{v-}(-l_j) = -\frac{j2A_-}{k_{v0}d}(e^{-jk_{v0}l_j} - R_2 e^{jk_{v0}l_j}), \tag{E.5.17}$$

where R_2 is defined in Eq.E.4.16. Thus, according to Eq.E.5.9, the response G_{uf_j} can be written as

$$G_{uf_j} = -\frac{j2A_-}{k_{v0}d(jEIk_{v0}^3 A_-)}(e^{-jk_{v0}l_j} - R_2 e^{jk_{v0}l_j}) \cdot$$

$$\cdot \left[\frac{(1-R_1)(1+R_2)}{(1+R_1)} + (1-R_2)\right]^{-1} =$$

$$= -\frac{2}{EIk_{v0}^4 d}(e^{-jk_{v0}l_j} - R_2 e^{jk_{v0}l_j}) \left[\frac{(1-R_1)(1+R_2)}{(1+R_1)} + (1-R_2)\right]^{-1}. \tag{E.5.18}$$

Substituting for R_1 and R_2 and simplifying the bracketed expressions on the right-hand side of the above equation, gives

$$(e^{-jk_{v0}l_j} - R_2 e^{jk_{v0}l_j}) \left[\frac{(1-R_1)(1+R_2)}{(1+R_1)} + (1-R_2)\right]^{-1} =$$

$$= (e^{-jk_{v0}l_j} + e^{-2jk_{v0}l_j} e^{jk_{v0}l_j}) \left[\frac{(1-R_1)(1+R_2) + (1+R_1)(1-R_2)}{(1+R_1)}\right]^{-1} =$$

$$= 2e^{-jk_{v0}l_j} \left[\frac{1+R_1}{1+R_2-R_1-R_1R_2+(1-R_2+R_1-R_1R_2)}\right] =$$

$$= 2e^{-jk_{v0}l_j} \frac{(1+R_1)}{2(1-R_1R_2)} = e^{-jk_{v0}l_j} \frac{1-e^{-2jk_{v0}(L-l_j)}}{1-e^{-2jk_{v0}(L-l_j)}e^{-2jk_{v0}l_j}} =$$

$$= e^{-jk_{v0}l_j} \frac{e^{-jk_{v0}(L-l_j)}[e^{jk_{v0}(L-l_j)} - e^{-jk_{v0}(L-l_j)}]}{1-e^{-2jk_{v0}L}} = \frac{e^{-jk_{v0}L} 2j \sin k_{v0}(L-l_j)}{e^{-jk_{v0}L}(e^{jk_{v0}L} - e^{-jk_{v0}L})} =$$

$$= \frac{2j \sin k_{v0}(L-l_j)}{2j \sin k_{v0}L} = \frac{\sin k_{v0}(L-l_j)}{\sin k_{v0}L},$$

hence

$$G_{uf_j} = -\frac{2}{EIk_{v0}^4 d} \frac{\sin k_{v0}(L-l_j)}{\sin k_{v0}L}, \tag{E.5.19}$$

or explicitly

$$G_{uf_1} = -\frac{2}{EIk_{v0}^4 d} \frac{\sin k_{v0}(L-l_1)}{\sin k_{v0}L}, \tag{E.5.20}$$

$$G_{uf_2} = -\frac{2}{EIk_{v0}^4 d} \frac{\sin k_{v0}(L-l_2)}{\sin k_{v0}L}, \tag{E.5.21}$$

$$G_{uf_3} = -\frac{2}{EIk_{v0}^4 d} \frac{\sin k_{v0}(L-l_3)}{\sin k_{v0}L}, \tag{E.5.22}$$

for the corresponding positions of the OHC1-3, i.e. l_1, l_2 and l_3 equal to $30\,\mu m$, $50\,\mu m$ and $70\,\mu m$, respectively.

Figure E.15 shows the magnitude and phase of the response G_{uf_j} due to the excitation force at the position of the first (G_{uf_1}), second (G_{uf_2}) and third (G_{uf_3}) OHC, located at a distance of l_1=30 μm, l_2=50 μm and l_3=70 μm from the IHC, respectively. The responses were calculated for the parameters in Table 6.1 and viscosity of η=6.6×10^{-4} kgm^{-1}s^{-1}.

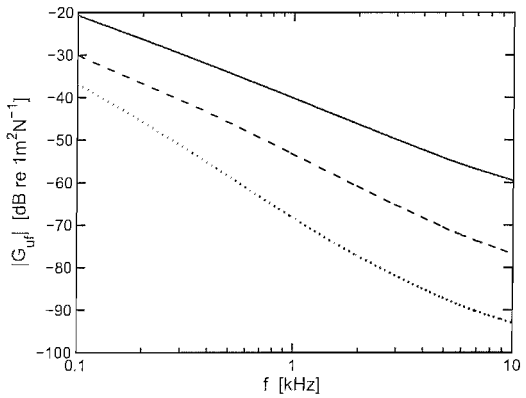

(a)

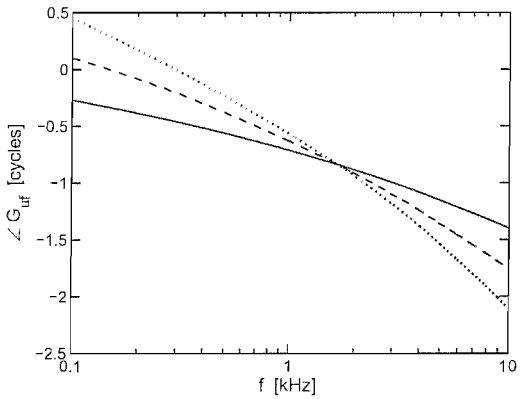

(b)

Figure E.15: Magnitude (a) and phase (b) of the response, G_{uf_j}, as a function of frequency. Response G_{uf_1} (solid), G_{uf_2} (dashed) and G_{uf_3} (dotted) due to excitation at the first, second and third outer hair cell, respectively.

E.5.3 The G_{wp} response

In the following section we derive the G_{wp} responses, being the ratio of the upper plate displacement w at positions of the OHC rows, to the external pressure, p_{ext}, excitation at the scala media end of the duct. Note that in this case there are three outputs at positions l_i away from the IHC and just a single input, and we choose the origin of the coordinate system at the right-hand side end of the duct as shown in Fig.E.16, so that the positions at which the displacement output is 'sensed' are $-(L-l_i)=l_i-L$ (for the OHC1-3). Thereby

$$G_{w_ip} = \frac{w(l_i - L)}{p(0)} = \frac{w(l_i - L)}{p_{ext}}, \tag{E.5.23}$$

where i=1, 2 and 3 and thus G_{w_ip} is a 3×1 column vector.

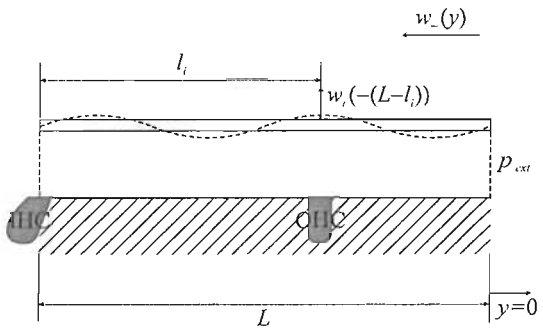

Figure E.16: The G_{w_ip} response, i.e. the plate displacement $w(-(L-l_i))=w(l_i - L)$, where L is the duct length and l_i is the distance from the inner hair cell (IHC), as a result of the external pressure excitation, p_{ext}, at y=0. OHC denotes the outer hair cell.

The plate displacement for a viscous 'squirting' wave travelling in a finite duct in the negative direction from y=0, is defined in Eq.E.4.14, and at $y=(l_i - L)$ it will take the form

$$w_{v-}(l_i - L) = A_-(e^{jk_{v0}(l_i-L)} + R_2 e^{-jk_{v0}(l_i-L)}), \tag{E.5.24}$$

where, since the duct length from the position of the input to the position of the wave reflection at the IHC end is equal to L, R_2 is equal to $-e^{-2jk_{v0}L}$ according to definition in Eq.E.4.16.

Hence, using the expression for $p_{v-}(0)$ in Eq.E.5.4, we have

$$G_{w_ip} = \frac{w_{v-}(l_i - L)}{p_{v-}(0)} = \frac{A_-(e^{jk_{v0}(l_i-L)} + R_2 e^{-jk_{v0}(l_i-L)})}{-EIk_{v0}^4 A_-(1 - e^{-2jk_{v0}L})} =$$

$$= -\frac{1}{EIk_{v0}^4} \frac{e^{jk_{v0}(l_i-L)} - e^{-2jk_{v0}L} e^{-jk_{v0}(l_i-L)}}{e^{-jk_{v0}L}(e^{jk_{v0}L} - e^{-jk_{v0}L})} =$$

$$= -\frac{1}{EIk_{v0}^4} \frac{e^{-jk_{v0}L}[e^{jk_{v0}L} e^{jk_{v0}(l_i-L)} - e^{-jk_{v0}L} e^{-jk_{v0}(l_i-L)}]}{e^{-jk_{v0}L}\, 2j \sin k_{v0}L} =$$

$$= -\frac{1}{EIk_{v0}^4} \frac{e^{jk_{v0}l_i} - e^{-jk_{v0}l_i}}{2j \sin k_{v0}L} = -\frac{1}{EIk_{v0}^4} \frac{2j \sin k_{v0}l_i}{2j \sin k_{v0}L} = -\frac{1}{EIk_{v0}^4} \frac{\sin k_{v0}l_i}{\sin k_{v0}L}. \tag{E.5.25}$$

Thus, the responses G_{w_ip} 'sensed' at the positions of the OHC1-3 rows, i.e. l_{1-3}, will be formulated by

$$G_{w_1p} = -\frac{1}{EIk_{v0}^4} \frac{\sin k_{v0}l_1}{\sin k_{v0}L}, \tag{E.5.26}$$

$$G_{w_2p} = -\frac{1}{EIk_{v0}^4} \frac{\sin k_{v0}l_2}{\sin k_{v0}L}, \tag{E.5.27}$$

$$G_{w_3p} = -\frac{1}{EIk_{v0}^4} \frac{\sin k_{v0}l_3}{\sin k_{v0}L}, \tag{E.5.28}$$

where l_1, l_2 and l_3 are equal to $30\,\mu m$, $50\,\mu m$ and $70\,\mu m$, respectively.

Figure E.17 shows the magnitude and phase of the response G_{w_ip} due to the external pressure p at positions of the first (G_{w_1p}), second (G_{w_2p}) and third (G_{w_3p}) OHC, located at a distance of l_1=30 μm, l_2=50 μm and l_3=70 μm from the IHC, respectively. The responses were calculated for the parameters in Table 6.1 and viscosity of η=6.6×10^{-4} kgm^{-1}s^{-1}.

E.5.4 The forced response G_{wf}

In the last section we derive the forced responses of the duct, $G_{w_if_j}$, where the input forces, f_j, are exerted on the upper plate by the electromotile OHC1-3,

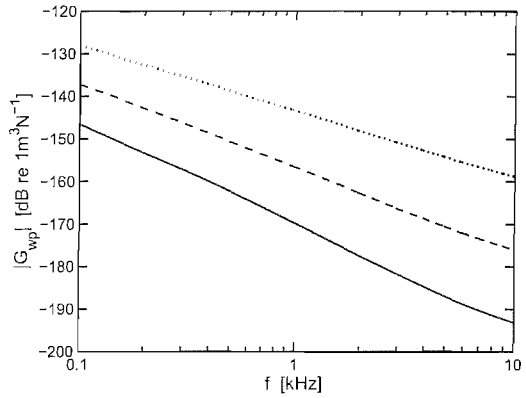

(a)

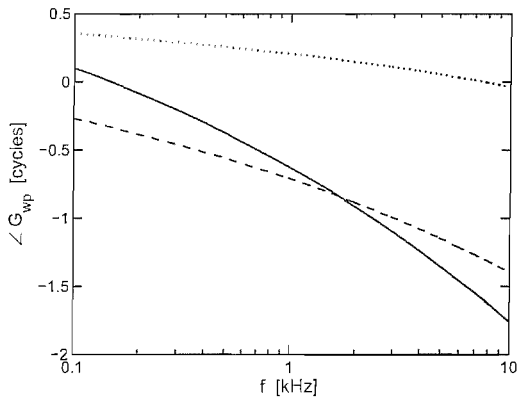

(b)

Figure E.17: Magnitude (a) and phase (b) of the response, G_{w_ip}, due to the external pressure excitation, as a function of frequency. Response G_{w_1p} (solid), G_{w_2p} (dashed) and G_{w_3p} (dotted) at positions of the first, second and third outer hair cell, respectively.

respectively, causing an upward displacement of the plate w_i, where i=1, 2 and 3 corresponds to the sites above the respective OHC rows. $G_{w_i f_j}$ will be defined by

$$G_{w_i f_j} = \frac{w(l_i)}{f(0)}, \tag{E.5.29}$$

where by such definition we assume that the input force is always located at the origin of the coordinate system, i.e. at y=0. Note that $G_{w_i f_j}$ is a 3×3 matrix where the diagonal terms correspond to the point receptances of the system, since i=j, which dominate the overall response, and for $i \neq j$ we have the transfer receptances of the system. To begin with we derive the expressions for the point receptances of the forced response, i.e. $G_{w_j f_j}$, according to the schematic in Fig.E.18.

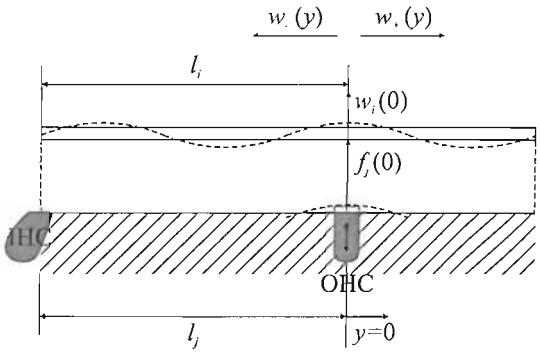

Figure E.18: Schematic for the internal point response $G_{w_i f_j}$ where i=j. The local outer hair cell (OHC) force, f, at l_j distance from the inner hair cell (IHC) causes an upward displacement, w, of the plate above and l_i away from the inner hair cell position. Note that both the force and the displacement are chosen to be located at the origin of the coordinate system and l_i=l_j in this case.

Knowing that $f(0)$ is defined in Eq.E.5.16 using the amplitude of the negative-going wave, A_-, and at y=0 $w_{v+}(0)$=$w_{v-}(0)$, we use also the expressions for the plate displacement of the wave propagating in the negative direction defined in Eq.E.4.14, i.e.

$$w_{v-}(0) = A_-(1 + R_2), \tag{E.5.30}$$

where R_2 is defined in Eq.E.4.16.

In such a case the forced response will be expressed as

$$G_{w_j f_j} = \frac{w_{v-}(0)}{f(0)} = \frac{A_-(1+R_2)}{jEIk_{v0}^3 A_-}\left[\frac{(1-R_1)(1+R_2)}{(1+R_1)} + (1-R_2)\right]^{-1} =$$

$$= -\frac{j(1+R_2)}{EIk_{v0}^3}\left[\frac{(1-R_1)(1+R_2)}{(1+R_1)} + (1-R_2)\right]^{-1}. \qquad \text{(E.5.31)}$$

According to the derivation for Eq.E.5.18 we can rewrite the above equation as

$$G_{w_j f_j} = -\frac{j}{EIk_{v0}^3}\frac{(1+R_1)(1+R_2)}{2(1-R_1R_2)}, \qquad \text{(E.5.32)}$$

so that substituting for R_1=$-e^{-2jk_{v0}(L-l_j)}$ and R_2=$-e^{-2jk_{v0}l_j}$ from Eqs.E.4.15-E.4.16, we have

$$G_{w_j f_j} = -\frac{j}{2EIk_{v0}^3}\frac{[1-e^{-2jk_{v0}(L-l_j)}][1-e^{-2jk_{v0}l_j}]}{1-e^{-2jk_{v0}(L-l_j)}e^{-2jk_{v0}l_j}} =$$

$$= -\frac{j}{2EIk_{v0}^3}\frac{e^{-jk_{v0}(L-l_j)}[e^{jk_{v0}(L-l_j)} - e^{-jk_{v0}(L-l_j)}]e^{-jk_{v0}l_j}[e^{jk_{v0}l_j} - e^{-jk_{v0}l_j}]}{1-e^{-2jk_{v0}L}} =$$

$$= -\frac{j}{2EIk_{v0}^3}\frac{e^{-jk_{v0}(L-l_j)}e^{-jk_{v0}l_j}[e^{jk_{v0}(L-l_j)} - e^{-jk_{v0}(L-l_j)}][e^{jk_{v0}l_j} - e^{-jk_{v0}l_j}]}{e^{-jk_{v0}L}(e^{jk_{v0}L} - e^{-jk_{v0}L})}, \qquad \text{(E.5.33)}$$

which using trigonometric relationship in Eq.E.5.7, can be written as

$$G_{w_j f_j} = -\frac{j}{2EIk_{v0}^3}\frac{e^{-jk_{v0}L}[2j\sin k_{v0}(L-l_j)2j\sin k_{v0}l_j]}{e^{-jk_{v0}L}[2j\sin k_{v0}L]} =$$

$$= \frac{1}{EIk_{v0}^3}\frac{\sin k_{v0}(L-l_j)\sin k_{v0}l_j}{\sin k_{v0}L}. \qquad \text{(E.5.34)}$$

Hence, the point receptances of the plate due to the outer hair cell electromotile forces will take the form

$$G_{w_1 f_1} = \frac{1}{EIk_{v0}^3} \frac{\sin k_{v0}(L-l_1)\sin k_{v0}l_1}{\sin k_{v0}L}, \tag{E.5.35}$$

$$G_{w_2 f_2} = \frac{1}{EIk_{v0}^3} \frac{\sin k_{v0}(L-l_2)\sin k_{v0}l_2}{\sin k_{v0}L}, \tag{E.5.36}$$

$$G_{w_3 f_3} = \frac{1}{EIk_{v0}^3} \frac{\sin k_{v0}(L-l_3)\sin k_{v0}l_3}{\sin k_{v0}L}, \tag{E.5.37}$$

where l_1=30 μm, l_2=50 μm and l_3=70 μm denote again the position of the OHC row along the duct measuring from the IHC location.

Figure E.19 shows the magnitude and phase of the point responses $G_{w_j f_j}$ at positions of the first ($G_{w_1 f_1}$), second ($G_{w_2 f_2}$) and third ($G_{w_3 f_3}$) OHC, located at a distance of l_1=30 μm, l_2=50 μm and l_3=70 μm from the IHC, respectively, due to the excitation of each OHC at the same corresponding positions. The responses were calculated for the parameters in Table 6.1 and viscosity of η=6.6×10^{-4} kgm^{-1}s^{-1}. Note that after substituting for l_1 and l_2 into Eqs.E.5.35 and E.5.36, the responses $G_{w_1 f_1}$ and $G_{w_2 f_2}$ are equal and the corresponding lines in the figure cover each other.

The transfer receptances of $G_{w_i f_j}$, i.e. for $i \neq j$, of the duct system with multichannel feedback can be divided into two groups. The first group of the transfer responses will be defined for the case where the input force from the OHC is located at l_j (measured from the IHC site) and to the left from the output displacements of the TM plate. Furthermore, we will refer to the plate displacement at the neighbouring OHCs positions as to l_i (measured from the IHC site) and hence $i>j$ in this case. This is shown schematically in Fig.E.20.

Assuming that the input force is at y=0, for $G_{w_i f_j}$ where $i>j$, the plate displacement will be defined as for the positive-going waves, so that

$$G_{w_i f_j} = \frac{w_{v+}(l_i - l_j)}{f(0)}, \qquad \text{for } i > j, \tag{E.5.38}$$

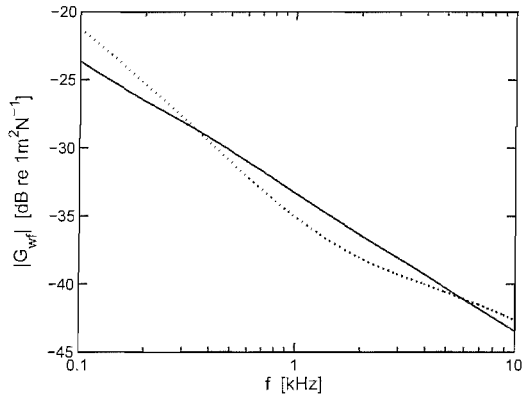

(a)

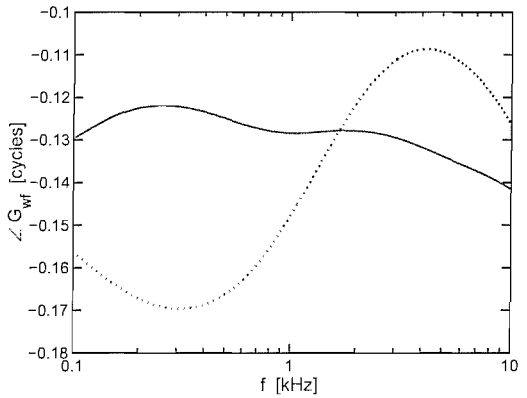

(b)

Figure E.19: Magnitude (a) and phase (b) of the point responses, $G_{w_j f_j}$, as a function of frequency. Response $G_{w_1 f_1}$ (solid), $G_{w_2 f_2}$ (dashed) and $G_{w_3 f_3}$ (dotted) at positions of the first, second and third outer hair cell, respectively. **NB** $G_{w_1 f_1}$ and $G_{w_2 f_2}$ are equal.

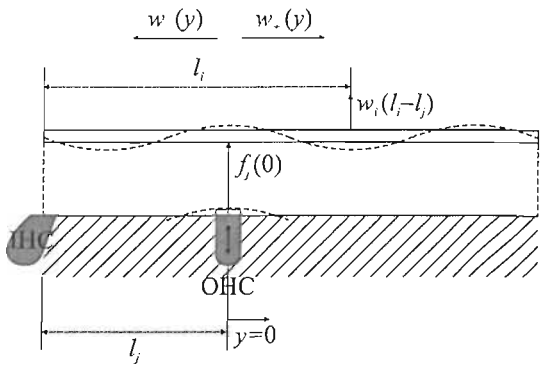

Figure E.20: Schematic of the internal response $G_{w_i f_j}$ for which $i>j$, i.e. the plate displacement, w, measured at the distance l_i from the inner hair cell (IHC), is located to the right of the input force from the outer hair cell (OHC), f. The input force is assumed to be located at y=0, and l_j away from the inner hair cell position. Thus the output displacement is measured at $l_i - l_j$.

where w_{v+} and $f(0)$ are defined in Eqs.E.4.13 and E.5.16, respectively. Therefore

$$G_{w_i f_j} = \frac{A_+(e^{-jk_{v0}(l_i-l_j)} + R_1 e^{jk_{v0}(l_i-l_j)})}{jEIk_{v0}^3 A_-} \left[\frac{(1-R_1)(1+R_2)}{(1+R_1)} + (1-R_2)\right]^{-1} \tag{E.5.39}$$

and $R_{1,2}$ are defined in Eqs.E.4.15-E.4.16. Knowing the relationship between A_+ and A_- from Eq.E.3.13, we rewrite the above equation as

$$G_{w_i f_j} = \frac{A_-(e^{-jk_{v0}(l_i-l_j)} + R_1 e^{jk_{v0}(l_i-l_j)})}{jEIk_{v0}^3 A_-} \frac{(1+R_2)}{(1+R_1)} \cdot$$

$$\cdot \left[\frac{(1+R_1)}{(1-R_1)(1+R_2)+(1+R_1)(1-R_2)}\right] =$$

$$= \frac{e^{-jk_{v0}(l_i-l_j)} + R_1 e^{jk_{v0}(l_i-l_j)}}{jEIk_{v0}^3} \frac{(1+R_2)}{2(1-R_1R_2)}. \tag{E.5.40}$$

Thus,

$$G_{w_i f_j} = \frac{e^{-jk_{v0}(l_i-l_j)} - e^{-2jk_{v0}(L-l_j)}e^{jk_{v0}(l_i-l_j)}}{2jEIk_{v0}^3} \frac{1-e^{-2jk_{v0}l_j}}{1-e^{-2jk_{v0}(L-l_j)}e^{-2jk_{v0}l_j}} =$$

$$= \frac{e^{-jk_{v0}(L-l_j)}\left[e^{jk_{v0}(L-l_j)}e^{-jk_{v0}(l_i-l_j)} - e^{-jk_{v0}(L-l_j)}e^{jk_{v0}(l_i-l_j)}\right]}{2jEIk_{v0}^3} \frac{1-e^{-2jk_{v0}l_j}}{1-e^{-2jk_{v0}L}} =$$

$$= \frac{e^{-jk_{v0}(L-l_j)}\left[e^{jk_{v0}(L-l_i)} - e^{-jk_{v0}(L-l_i)}\right]}{2jEIk_{v0}^3} \frac{e^{-jk_{v0}l_j}\left[e^{jk_{v0}l_j} - e^{-jk_{v0}l_j}\right]}{e^{-jk_{v0}L}\left[e^{jk_{v0}L} - e^{-jk_{v0}L}\right]} =$$

$$= \frac{e^{-jk_{v0}(L-l_j)}2j\sin k_{v0}(L-l_i)}{2jEIk_{v0}^3} \frac{e^{jk_{v0}(L-l_j)}2j\sin k_{v0}l_j}{e^{jk_{v0}L} - e^{-jk_{v0}L}} =$$

$$= \frac{2j\sin k_{v0}(L-l_i)}{EIk_{v0}^3} \frac{\sin k_{v0}l_j}{2j\sin k_{v0}L} = \frac{1}{EIk_{v0}^3} \frac{\sin k_{v0}(L-l_i)\sin k_{v0}l_j}{\sin k_{v0}L}. \quad \text{(E.5.41)}$$

Thus, for $i>j$, the transfer responses will take the form

$$G_{w_2 f_1} = \frac{1}{EIk_{v0}^3} \frac{\sin k_{v0}(L-l_2)\sin k_{v0}l_1}{\sin k_{v0}L}, \quad \text{(E.5.42)}$$

$$G_{w_3 f_1} = \frac{1}{EIk_{v0}^3} \frac{\sin k_{v0}(L-l_3)\sin k_{v0}l_1}{\sin k_{v0}L}, \quad \text{(E.5.43)}$$

$$G_{w_3 f_2} = \frac{1}{EIk_{v0}^3} \frac{\sin k_{v0}(L-l_3)\sin k_{v0}l_2}{\sin k_{v0}L}, \quad \text{(E.5.44)}$$

where l_1=30 μm, l_2=50 μm and l_3=70 μm.

The magnitude and phase of the transfer responses $G_{w_i f_j}$ for the case where i is greater than j, i.e. at l_2=50 μm and l_3=70 μm from the IHC due to the OHC force located at a distance of l_1=30 μm: $G_{w_2 f_1}$ and $G_{w_3 f_1}$, respectively, and at l_3=70 μm from the IHC due to the OHC force located at a distance of l_2=50 μm: $G_{w_3 f_2}$, are shown in Fig.E.21. The responses were calculated for the parameters in Table 6.1 and viscosity of η=6.6×10^{-4} kgm^{-1}s^{-1}.

The second group of the transfer responses $G_{w_i f_j}$ will be derived for $i<j$, that is for the situation when the plate displacement is 'measured' on the left-hand side from the input, as shown in Fig.E.22.

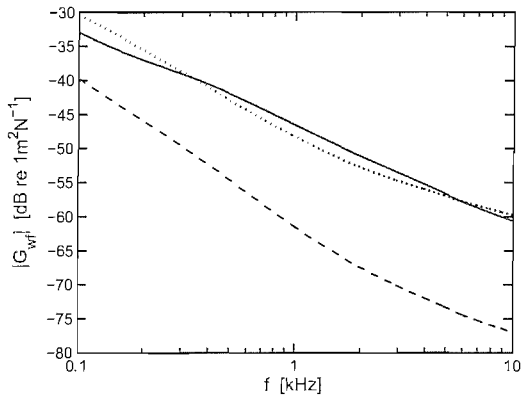

(a)

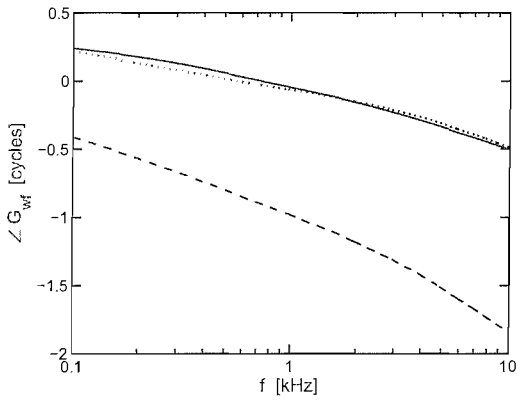

(b)

Figure E.21: Magnitude (a) and phase (b) of the point responses, $G_{w_i f_j}$ for $i>j$, as a function of frequency. Response $G_{w_2 f_1}$ (solid), $G_{w_3 f_1}$ (dashed) at positions of the second and third outer hair cell due to the force at the first outer hair cell, and at the third outer hair cell due to the force at the second outer hair cell, $G_{w_3 f_2}$.

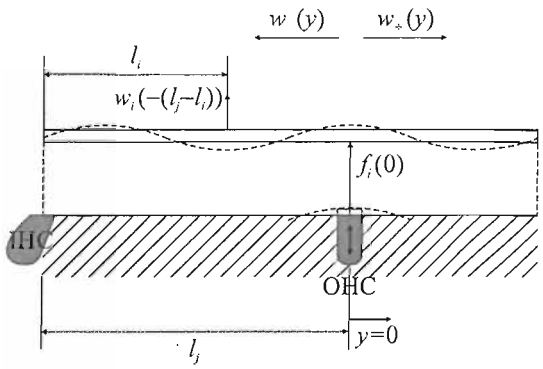

Figure E.22: Illustration of the $G_{w_i f_j}$ response within the duct, where $i<j$. The outer hair cell (OHC) force, f, acting locally at y=0, is at a distance l_j from the inner hair cell (IHC). The output plate displacement located to the left from the input force and at a distance l_i away from the inner hair cell, and hence the relative distance between the input and the output is equal to $-(l_j-l_i)=l_i-l_j$ in this case.

We assume again that the excitation is located at y=0, so that the plate displacement waves travelling in the negative direction, i.e. w_{v-}, are taken into account. Hence

$$G_{w_i f_j} = \frac{w_{v-}(l_i - l_j)}{f(0)}, \qquad \text{for } i < j. \tag{E.5.45}$$

Using Eq.E.4.14 for w_{v-} at l_i-l_j and Eq.E.5.16 for $f(0)$, we can write

$$G_{w_i f_j} = \frac{A_-(e^{jk_{v0}(l_i-l_j)} + R_2 e^{-jk_{v0}(l_i-l_j)})}{jEIk_{v0}^3 A_-} \frac{(1+R_1)}{2(1-R_1R_2)}, \tag{E.5.46}$$

where R_1 and R_2 are defined in Eqs.E.4.15-E.4.16.

Thus

$$G_{w_i f_j} = \frac{e^{jk_{v0}(l_i-l_j)} - e^{-2jk_{v0}l_j}e^{-jk_{v0}(l_i-l_j)}}{2jEIk_{v0}^3} \frac{1-e^{-2jk_{v0}(L-l_j)}}{1-e^{-2jk_{v0}(L-l_j)}e^{-2jk_{v0}l_j}} =$$

$$= \frac{e^{-jk_{v0}l_j}\left[e^{jk_{v0}(l_i-l_j)}e^{jk_{v0}l_j} - e^{-jk_{v0}(l_i-l_j)}e^{-jk_{v0}l_j}\right]}{2jEIk_{v0}^3} \frac{1-e^{-2jk_{v0}(L-l_j)}}{1-e^{-2jk_{v0}L}} =$$

$$= \frac{e^{-jk_{v0}l_j}\left(e^{jk_{v0}l_i} - e^{-jk_{v0}l_i}\right)}{2jEIk_{v0}^3} \frac{e^{-jk_{v0}(L-l_j)}\left[e^{jk_{v0}(L-l_j)} - e^{-jk_{v0}(L-l_j)}\right]}{e^{-jk_{v0}L}\left[e^{jk_{v0}L} - e^{-jk_{v0}L}\right]} =$$

$$= \frac{2j\sin k_{v0}l_i}{2jEIk_{v0}^3} \frac{e^{-jk_{v0}L}2j\sin k_{v0}(L-l_j)}{e^{-jk_{v0}L}2j\sin k_{v0}L} = \frac{1}{EIk_{v0}^3} \frac{\sin k_{v0}(L-l_j)\sin k_{v0}l_i}{\sin k_{v0}L}. \tag{E.5.47}$$

Using the above result, we can define the transfer responses for $i<j$ as follows

$$G_{w_1 f_2} = \frac{1}{EIk_{v0}^3} \frac{\sin k_{v0}(L-l_2)\sin k_{v0}l_1}{\sin k_{v0}L}, \tag{E.5.48}$$

$$G_{w_1 f_3} = \frac{1}{EIk_{v0}^3} \frac{\sin k_{v0}(L-l_3)\sin k_{v0}l_1}{\sin k_{v0}L}, \tag{E.5.49}$$

$$G_{w_2 f_3} = \frac{1}{EIk_{v0}^3} \frac{\sin k_{v0}(L-l_3)\sin k_{v0}l_2}{\sin k_{v0}L}, \tag{E.5.50}$$

where again l_1, l_2 and l_3 are equal to $30\,\mu m$, $50\,\mu m$ and $70\,\mu m$, respectively.

Note that $G_{w_1 f_2}$, $G_{w_1 f_3}$ and $G_{w_2 f_3}$ are equal to $G_{w_2 f_1}$, $G_{w_3 f_1}$ and $G_{w_3 f_2}$, respectively, so that the matrix $\mathbf{G}_{wf}$ is diagonally symmetric and the responses for $i<j$ are the same as the corresponding responses for $i>j$ shown in Fig.E.21.

We gather the expressions for all the constitutive responses of the feedback controller model in Fig.6.7 in Table E.1.

RESPONSE	EXPRESSION
G_{up} $[\mathrm{m}^3\mathrm{N}^{-1}]$	$\frac{2}{EIk_{v0}^5 d}\ \frac{1}{\sin k_{v0}L}$
G_{uf_j} $[\mathrm{m}^2\mathrm{N}^{-1}]$	$-\frac{2}{EIk_{v0}^4 d}\ \frac{\sin k_{v0}(L-l_j)}{\sin k_{v0}L}$
$G_{w_i p}$ $[\mathrm{m}^3\mathrm{N}^{-1}]$	$-\frac{1}{EIk_{v0}^4}\ \frac{\sin k_{v0}l_j}{\sin k_{v0}L}$
$G_{w_i f_j}$ $[\mathrm{m}^2\mathrm{N}^{-1}]$	$\frac{1}{EIk_{v0}^3}\ \frac{\sin k_{v0}(L-l_j)\sin k_{v0}l_j}{\sin k_{v0}L}$ for $i=j$ $\frac{1}{EIk_{v0}^3}\ \frac{\sin k_{v0}(L-l_i)\sin k_{v0}l_j}{\sin k_{v0}L}$ for $i>j$ $\frac{1}{EIk_{v0}^3}\ \frac{\sin k_{v0}(L-l_j)\sin k_{v0}l_i}{\sin k_{v0}L}$ for $i<j$

Table E.1: Constitutive responses of the feedback controller proposed for the active 'squirting' wave model.

Appendix F

Derivation of the expressions for the wavenumber of the lossy fluid-elastic waves

To derive the explicit expressions for real, β, and imaginary, α, parts of the wavenumber, k, we take Eq.7.3.8

$$k^2 Re\{k\} = \underbrace{\frac{\rho\omega^2(1+\nu)}{E_0(1+j\mu)d}}_{A} - j\underbrace{\frac{16\eta\omega(1+\nu)}{E_0(1+j\mu)d^3}}_{B}, \tag{F.1}$$

and group the real and imaginary components, so that

$$A = \underbrace{\frac{\rho\omega^2(1+\nu)}{E_0 d}}_{C}\left(\frac{1}{1+j\mu}\,\frac{1-j\mu}{1-j\mu}\right) = C\,\frac{1-j\mu}{(1+\mu^2)} = \frac{C}{(1+\mu^2)} - j\frac{C\mu}{(1+\mu^2)} =$$

$$= \underbrace{\frac{\rho\omega^2(1+\nu)}{E_0(1+\mu^2)d}}_{Re\{A\}} + j\underbrace{\left[-\frac{\rho\omega^2(1+\nu)\mu}{E_0(1+\mu^2)d}\right]}_{Im\{A\}},$$

and similarly

$$B = \underbrace{\frac{16\eta\omega(1+\nu)}{E_0 d^3}}_{D}\left(\frac{1}{1+j\mu}\frac{1-j\mu}{1-j\mu}\right) = D\frac{1-j\mu}{(1+\mu^2)} = \frac{D}{(1+\mu^2)} - j\frac{D\mu}{(1+\mu^2)} =$$

$$= \underbrace{\frac{16\eta\omega(1+\nu)}{E_0(1+\mu^2)d^3}}_{Re\{B\}} + j\underbrace{\left[-\frac{16\eta\omega(1+\nu)\mu}{E_0(1+\mu^2)d^3}\right]}_{Im\{B\}}.$$

Therefore,

$$k^2 Re\{k\} = A - jB = (Re\{A\} + jIm\{A\}) - j(Re\{B\} + jIm\{B\}) =$$

$$= \underbrace{(Re\{A\} + Im\{B\})}_{R} + j\underbrace{(Im\{A\} - Re\{B\})}_{X},$$

hence

$$k^2 Re\{k\} = \underbrace{\frac{\rho\omega^2(1+\nu)}{E_0(1+\mu^2)d} - \frac{16\eta\omega(1+\nu)\mu}{E_0(1+\mu^2)d^3}}_{R} + j\underbrace{\left[-\frac{\rho\omega^2(1+\nu)\mu}{E_0(1+\mu^2)d} - \frac{16\eta\omega(1+\nu)}{E_0(1+\mu^2)d^3}\right]}_{X},$$

which can be simplified to give

$$k^2 Re\{k\} = \underbrace{\frac{\omega(\rho\omega d^2 - 16\eta\mu)(1+\nu)}{E_0(1+\mu^2)d^3}}_{R} + j\underbrace{\left[-\frac{\omega(\mu\rho\omega d^2 + 16\eta)(1+\nu)}{E_0(1+\mu^2)d^3}\right]}_{X}. \qquad \text{(F.2)}$$

Setting $k=\beta-j\alpha$ to solve the above equation, where β corresponds to the real part of the wavenumber, thus to the propagating component of the wave, and α, being the imaginary part of k, to the wave's attenuation coefficient, and the right-hand side of Eq.F.2 to $R+jX$ gives

$$(\beta - j\alpha)^2\beta = R + jX, \qquad \text{(F.3)}$$

and hence equating the real and imaginary parts of the above equation gives

$$\beta^3 - \alpha^2\beta = R, \tag{F.4}$$

and

$$2\alpha\beta^2 = -X. \tag{F.5}$$

Thus, the attenuation coefficient will be equal to

$$\alpha = -\frac{X}{2\beta^2}, \tag{F.6}$$

which after substituting to Eq.F.4 leads to a quadratic in β^3

$$\beta^6 - R\beta^3 - \frac{X^2}{4} = 0. \tag{F.7}$$

Solving Eqs.F.6 and F.7 gives the expressions for β and α, so that the waves propagating and decaying in two directions can be calculated since $k{=}{\pm}(\beta{-}j\alpha)$.

Let

$$\beta^3 = \Omega \ \therefore \ \beta = \Omega^{\frac{1}{3}},$$

so that Eq.F.7 takes the form

$$\Omega^2 - R\Omega - \frac{X^2}{4} = 0, \tag{F.8}$$

thus

$$\Omega_{1,2} = \frac{R \pm \sqrt{R^2 + X^2}}{2}, \tag{F.9}$$

and hence

$$\beta_{1,2} = \left(\frac{R \pm \sqrt{R^2 + X^2}}{2}\right)^{\frac{1}{3}}, \tag{F.10}$$

and, according to Eq.F.6,

$$\alpha_{1,2} = -\frac{X}{2\beta_{1,2}^2} = -\frac{X}{2}\left(\frac{R \pm \sqrt{R^2 + X^2}}{2}\right)^{-\frac{2}{3}}. \tag{F.11}$$

Therefore $k_{1,2}=\beta_{1,2}-j\alpha_{1,2}$, and

$$c_{1,2} = \frac{\omega}{\beta_{1,2}}. \tag{F.12}$$

Four conditions for the fluid-elastic waves in the subtectorial space of the organ of Corti are considered here:

1) η=0 [Pa s], μ=0; no losses,

2) η=0 [Pa s], μ=0.5; losses only in the elastic half-space,

3) η=6.6×10^{-4} [Pa s], μ=0; losses only in the fluid,

4) η=6.6×10^{-4} [Pa s], μ=0.5; losses in both elastic half-space and the fluid.

Thus, it can be seen that for condition 1) the imaginary part of Eq.F.2 is equal to zero and hence Ω_2=0, β_2=0, and c_2=∞, i.e.

$$\Omega_2^1 = \frac{R - \sqrt{R^2 + X^2}}{2} = 0, \qquad \text{for} \qquad \eta = \mu = 0 \;\Rightarrow\; X = 0 \tag{F.13}$$

where the upper index denotes the loss condition. On the other hand for conditions 2), 3) and 4) the root Ω_2 is always negative and thus β_2 is complex, i.e.

$$\Omega_2^{2,3,4} = \frac{R - \sqrt{R^2 + X^2}}{2} = -const., \qquad \text{for all} \qquad R, X \;\Leftrightarrow\; X \neq 0 \tag{F.14}$$

Therefore we reject Ω_2 taking only Ω_1 solution for simulations.

Appendix G

Derivation of the responses in the fluid-elastic model

G.1 The subtectorial fluid pressure, elastic half-space and fluid displacements due to the external pressure excitation p_{ext}

In the first instance waves in the duct, due to the external pressure at y=L, p_{ext}=$p(L)$, producing the fluid displacement u at position y=0 as shown in Fig.G.1, will be considered and described in a way similar to that of Nelson and Elliott [69] for compressional waves and fluctuating volume flow. However, for the fluid-elastic waves in the subtectorial duct the characteristic impedance will take a different form than the $\rho_0 c_0$ for compressional waves. Therefore, the relations between the pressure, $p(y,t)$ and the fluid displacement, $u(y,t)$ must be formulated.

We assume that the subtectorial fluid pressure and the wall and fluid displacements are of the form $p(y,t)$=$p(\omega,k)e^{j(\omega t-ky)}$, $w(y,t)$=$w(\omega,k)e^{j(\omega t-ky)}$ and $u(y,t)$=$u(\omega,k)e^{j(\omega t-ky)}$, respectively. The lossy version of the relationship between the complex pressure and the wall displacement is given in Eq.7.3.6 and is inversely proportional to the wavelength [22].

Taking the wave equation for the fluid-elastic waves with losses (fluid force

equation, Eq.7.3.1), and solving for the complex harmonic fluid pressure and displacement in an infinite duct, gives

$$-jkp(\omega,k) = \rho\omega^2 u(\omega,k) - j\frac{16\eta\omega}{d^2}\, u(\omega,k), \tag{G.1.1}$$

so that the ratio $p(\omega,k)/u(\omega,k)$ for a single wave takes the form

$$\frac{p(\omega,k)}{u(\omega,k)} = \frac{j\rho\omega^2}{k} + \frac{16\eta\omega}{kd^2} = S_{wave}. \tag{G.1.2}$$

The above equation defines the 'dynamic wave stiffness', which relates the fluid pressure to its displacement for the fluid-elastic waves, analogously to the characteristic impedance for the compressional waves, $\rho_0 c_0$. Specifically, for the particle velocity, $j\omega u$, the characteristic impedance, in the absence of viscosity, i.e. η=0, and for k=ω/c, can be defined according to Eq.G.1.2 as

$$Z_0 = \frac{p(\omega,k)}{j\omega u(\omega,k)_{|_{\eta=0}}} = \rho c. \tag{G.1.3}$$

It should be noted, however, that c=$\sqrt{S_{wall}d/\rho}$ (Eq.7.2.12) for the lossless case, where the wall stiffness S_{wall} is defined in Eq.7.2.10, and not $\sqrt{\gamma P_0/\rho_0}$ as for the sound waves in fluids, where γ is the ratio of specific heats, and P_0 and ρ_0 are the ambient pressure and density of the fluid, respectively [48].

The subtectorial duct shown in Fig.G.1, is driven by the external pressure, p_{ext}, at its right-hand side end, i.e. y=L, which produces elastic half-space displacement, w, at the positions of the OHCs (second row of OHCs at l_2 shown in figure), as well as the fluid particle displacement, u, at the left-hand side end of the duct, i.e. y=0. Furthermore, the boundary conditions, $p(0)$=0 and $p(L)$=p_{ext}, are indicated in the figure, together with an area displacement s, which is modelled by a loudspeaker, and idealised by a plane acoustic monopole. The monopole shown in Fig.G.1, can be represented by two massless pistons vibrating apart due to the displacement s between them and producing plane waves in the downstream and upstream directions in the duct [69].

Assuming the boundary conditions for the duct excited at y=L by p_{ext} to be

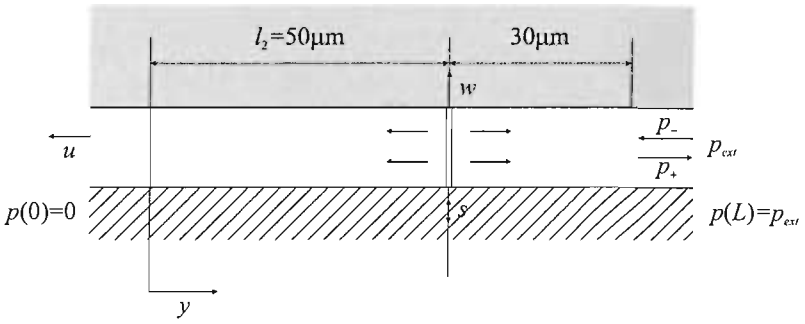

Figure G.1: The subtectorial duct in which the fluid displacement at the inner hair cell end of the duct, u, and the elastic half-space displacement, w, occur due to the external pressure in the scala media, p_{ext}. The dimensions of the duct of the subtectorial space are shown for comparison with Fig.7.4 along with the indication of the boundary conditions at the ends of the duct. An idealised plane monopole source, s, due to the action of the outer hair cells is depicted at the position of the second row of these cells.

$$p(0) = 0,$$
$$p(L) = p_{ext},$$

and complex harmonic pressures and fluid particle displacements, at t=0, of the form

$$\begin{aligned} p(y) &= p_+ e^{-jky} + p_- e^{jky}, \\ u(y) &= u_+ e^{-jky} + u_- e^{jky}, \end{aligned} \tag{G.1.4}$$

where the '+' and '−' indices refer to the amplitudes of the positive- and negative-going pressure and fluid displacement waves, so that

$$\begin{aligned} p(0) &= 0 = p_+ + p_-, \\ p_- &= -p_+, \end{aligned} \tag{G.1.5}$$

and

$$p(L) = p_{ext} = p_+ e^{-jkL} + p_- e^{jkL} = p_+(e^{-jkL} - e^{jkL}),$$

$$p_+ = \frac{p_{ext}}{(e^{-jkL} - e^{jkL})} = \frac{jp_{ext}}{2\sin kL}. \tag{G.1.6}$$

The pressure at any position in the duct will be equal, according to Eq.G.1.4 and Eq.G.1.6, to

$$p(y) = p_+ e^{-jky} + p_- e^{jky} = p_+(e^{-jky} - e^{jky}),$$

thus, since $e^{-jky} - e^{jky} = -2j\sin ky$,

$$p(y) = \frac{jp_{ext}}{2\sin kL}(-2j\sin ky) = \frac{p_{ext}}{\sin kL}\sin ky. \tag{G.1.7}$$

The dynamic wave stiffness, S_{wave} (Eq.G.1.2), is defined for positive- and negative-going waves as

$$\frac{p_+}{u_+} = -\frac{p_-}{u_-} = S_{wave}, \tag{G.1.8}$$

thus, according to Eq.G.1.8 and knowing that $p_- = -p_+$ (Eq.G.1.5),

$$u_+ = \frac{p_+}{S_{wave}},$$

$$u_- = -\frac{p_-}{S_{wave}} = \frac{p_+}{S_{wave}}. \tag{G.1.9}$$

According to Eqs.G.1.4 and G.1.9, the expression for the fluid displacement $u(y)$ will take the form

$$u(y) = u_+ e^{-jky} + u_- e^{jky} = \frac{p_+}{S_{wave}}(e^{-jky} + e^{jky}), \tag{G.1.10}$$

hence using G.1.6, and since $e^{-jky} + e^{jky} = 2\cos ky$,

$$u(y) = \frac{jp_{ext}}{2S_{wave}\sin kL} 2\cos ky = \frac{jp_{ext}}{S_{wave}\sin kL}\cos ky. \tag{G.1.11}$$

Figure G.2 depict the distribution along the duct of the magnitude an phase of the pressure, $p(y)$, and fluid particle displacement, $u(y)$, formulated in Eqs.G.1.7 and G.1.11, at 1 kHz due to the external pressure driving at the right-hand side end of the duct, p_{ext}. The external pressure from the scala media was set to p_{ext}=2×10^{-5} Pa and the length of the duct was assumed to be equal to L=80 μm. All the remaining parameters are listed in Table 7.1.

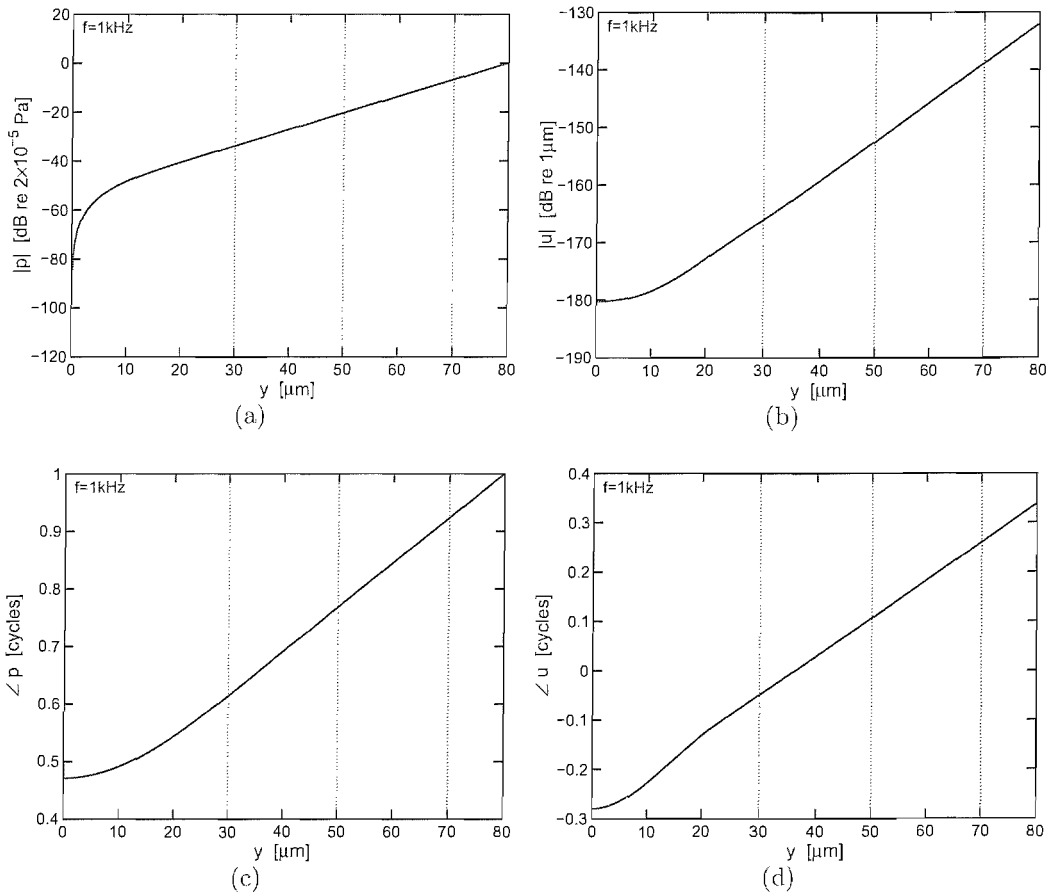

Figure G.2: The magnitude and phase of the pressure p (a, c) and the fluid particle displacement u (b, d) at 1 kHz due to the external pressure in the scala media, p_{ext}=2×10^{-5} Pa, as a function of position along the duct, y. Horizontal lines indicate the positions of the outer hair cell rows.

Knowing that the elastic half-space displacement, $w(y)$, is related to the com-

plex pressure $p(y)$ by the lossy version of the wall stiffness S_{wall} defined in Eq.7.3.6, i.e.

$$w(y) = \frac{1}{S_{wall}} p(y) = \frac{(1+\nu)}{Re\{k\}E_0(1+j\mu)} p(y), \tag{G.1.12}$$

thus taking the expression for the subtectorial fluid pressure in Eq.G.1.7, the wall displacement due to the external pressure, p_{ext}, will be formulated by

$$w(y) = \frac{p_{ext}}{S_{wall} \sin kL} \sin ky, \tag{G.1.13}$$

where S_{wall} is again defined in Eq.7.3.6.

G.2 The subtectorial fluid pressure, elastic half-space and fluid displacements due to the area displacement of the outer hair cell s_i

To calculate the internal responses of the feedback controller system, the pressure within the duct $p(y)$, fluid displacement $u(y)$ at the inner hair cell end of the duct and the elastic half-space wall displacement, $w(y)$ in response to the area displacement source modelled as an acoustic plane monopole, shown schematically in Fig.G.3, will be derived in this section.

In this case we assume pressure release boundary conditions at the ends of the duct, namely

$$p(0) = 0,$$
$$p(L) = 0,$$

thus the complex pressure and particle displacement of the fluid in the finite duct shown in Fig.G.3 can be formulated by

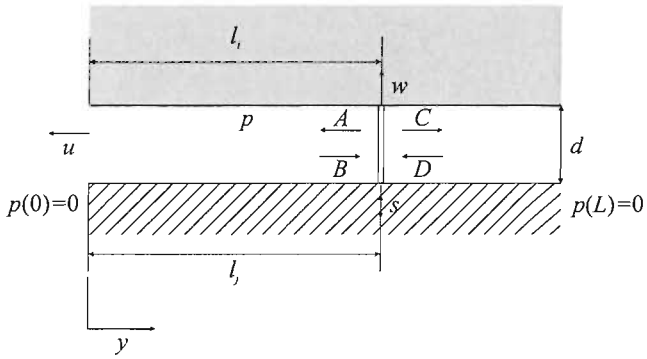

Figure G.3: Schematic of the subtectorial duct for the calculation of the wall, $w(l_i)$, and fluid displacement, $u(0)$, responses due to the internal area displacement excitation at the position of the outer hair cell, $s(l_j)$. The boundary conditions at the ends of the duct are also indicated.

$$p_L(y) = Ae^{-jky} + Be^{jky},$$
$$0 \leq y \leq l_i \qquad \text{(G.2.1)}$$
$$u_L(y) = \frac{A}{S_{wave}} e^{-jky} - \frac{B}{S_{wave}} e^{jky},$$

for the waves propagating in the left-hand side region from the source, and

$$p_R(y) = Ce^{-jky} + De^{jky},$$
$$l_i \leq y \leq L \qquad \text{(G.2.2)}$$
$$u_R(y) = \frac{C}{S_{wave}} e^{-jky} - \frac{D}{S_{wave}} e^{jky},$$

for the waves in the right-hand side region from the source, where S_{wave} is the dynamic wave stiffness defined in Eq.G.1.2, and l_i denotes the position in the duct at which the pressure or the particle displacement is measured.

For the assumed pressure release conditions at the ends of the duct from Eq.G.2.1 we have

$$p_L(0) = 0 = A + B, \qquad \text{(G.2.3)}$$

and from Eq.G.2.2

$$p_R(L) = 0 = Ce^{-jkL} + De^{jkL}, \tag{G.2.4}$$

therefore

$$\begin{aligned} B &= -A, \\ D &= -Ce^{-2jkL}. \end{aligned} \tag{G.2.5}$$

Since the pressure across the source must be continuous, and the difference in the particle displacement of the massless pistons at their positions, l_j, equals to the source strength, s/d (**NB** because we consider a 2D problem, the source is linear and corresponds to an area displacement divided by the height of the duct, d) [69], thus from Eqs.G.2.1 and G.2.2, we have

$$\begin{aligned} p(l_j) = p_L(l_j) = p_R(l_j) = Ae^{-jkl_j} + Be^{jkl_j} = Ce^{-jkl_j} + De^{jkl_j}, \\ \frac{s(l_j)}{d} = u_R(l_j) - u_L(l_j) = \\ = \frac{C}{S_{wave}} e^{-jkl_j} - \frac{D}{S_{wave}} e^{jkl_j} - \left(\frac{A}{S_{wave}} e^{-jkl_j} - \frac{B}{S_{wave}} e^{jkl_j} \right), \end{aligned} \tag{G.2.6}$$

hence, taking into account expressions in Eq.G.2.5,

$$\begin{aligned} p(l_j) = A\left(e^{-jkl_j} - e^{jkl_j}\right) = Ce^{-jkL}\left(e^{-jk(l_j-L)} - e^{jk(l_j-L)}\right), \\ \frac{s(l_j)}{d} = \frac{C}{S_{wave}} e^{-jkL}\left(e^{-jk(l_j-L)} + e^{jk(l_j-L)}\right) - \frac{A}{S_{wave}}\left(e^{-jkl_j} + e^{jkl_j}\right). \end{aligned} \tag{G.2.7}$$

Note that the position of the source in the duct was denoted as l_j, so that the constitutive responses of the feedback controller model in Fig.7.5 can be expressed in a generalised form of the ratio of the output at position l_i to the input source at position l_j, similarly as for the responses of the 'squirting' wave model derived in Appendix E.5. Specifically, when i=j then a point response is specified, that

is the output is located at the same position as the input along the subtectorial duct.

The constants A and C can be derived using the equations in G.2.7, so that

$$C = A \frac{e^{-jkl_j} - e^{jkl_j}}{e^{-jkL}\left(e^{-jk(l_j-L)} - e^{jk(l_j-L)}\right)}, \tag{G.2.8}$$

which after substituting to the second expression in Eq.G.2.7, gives

$$\frac{S_{wave}s(l_j)}{d} = A \frac{e^{-jkl_j} - e^{jkl_j}}{e^{-jkL}\left(e^{-jk(l_j-L)} - e^{jk(l_j-L)}\right)} e^{-jkL}\left(e^{-jk(l_j-L)} + e^{jk(l_j-L)}\right) -$$

$$- A(e^{-jkl_j} + e^{jkl_j}) =$$

$$= A\left[\frac{\left(e^{-jkl_j} - e^{jkl_j}\right)\left(e^{-jk(l_j-L)} + e^{jk(l_j-L)}\right)}{e^{-jk(l_j-L)} - e^{jk(l_j-L)}} - \left(e^{-jkl_j} + e^{jkl_j}\right)\right] =$$

$$= A\left[\frac{\left(e^{-jkl_j} - e^{jkl_j}\right)\left(e^{-jk(l_j-L)} + e^{jk(l_j-L)}\right)}{e^{-jk(l_j-L)} - e^{jk(l_j-L)}} -\right.$$

$$\left. - \frac{\left(e^{-jkl_j} + e^{jkl_j}\right)\left(e^{-jk(l_j-L)} - e^{jk(l_j-L)}\right)}{e^{-jk(l_j-L)} - e^{jk(l_j-L)}}\right] =$$

$$= A\left[\frac{e^{-2jkl_j}e^{jkL} + e^{-jkL} - e^{jkL} - e^{2jkl_j}e^{-jkL}}{e^{-jk(l_j-L)} - e^{jk(l_j-L)}} -\right.$$

$$\left. - \frac{e^{-2jkl_j}e^{jkL} - e^{-jkL} + e^{jkL} - e^{2jkl_j}e^{-jkL}}{e^{-jk(l_j-L)} - e^{jk(l_j-L)}}\right] =$$

$$= A \frac{2(e^{-jkL} - e^{jkL})}{e^{-jk(l_j-L)} - e^{jk(l_j-L)}},$$

and knowing that

$$e^{-j\theta} + e^{j\theta} = 2\cos\theta,$$
$$e^{-j\theta} - e^{j\theta} = -2j\sin\theta,$$

we can write

$$\frac{S_{wave}s(l_j)}{d} = 2A\,\frac{-2j\sin kL}{-2j\sin k(l_j - L)} = 2A\,\frac{\sin kL}{\sin k(l_j - L)}. \tag{G.2.9}$$

From the above relationship the constant A can be obtained and is equal to

$$A = \frac{S_{wave}s(l_j)}{2d\sin kL}\sin k(l_j - L), \tag{G.2.10}$$

so that, according to Eq.G.2.8,

$$C = \frac{S_{wave}s(l_j)}{2d\sin kL}\sin k(l_j - L)\,\frac{e^{-jkl_j} - e^{jkl_j}}{e^{-jkL}\left(e^{-jk(l_j-L)} - e^{jk(l_j-L)}\right)} =$$

$$= \frac{S_{wave}s(l_j)}{2d\sin kL}\sin k(l_j - L)\,\frac{-2j\sin kl_j}{e^{-jkL}[-2j\sin k(l_j - L)]},$$

thus the constant C is equal to

$$C = \frac{S_{wave}s(l_j)}{2d\sin kL}\,\frac{\sin kl_j}{\cos kL - j\sin kL}. \tag{G.2.11}$$

Using the expression in Eq.G.2.1, and knowing that $B{=}{-}A$ according to Eq.G.2.5, where A is given in Eq.G.2.10, the complex acoustic pressure wave propagating in the left-hand side region from the source, i.e. $0{\leq}y{\leq}\,l_i$, takes the form

$$p_L(y) = Ae^{-jky} + Be^{jky} = A\left(e^{-jky} - e^{jky}\right) = \frac{S_{wave}s(l_j)}{2d\sin kL}\sin k(l_j - L)(-2j\sin ky)$$

$$= -\frac{jS_{wave}s(l_j)}{d\sin kL}\sin k(l_j - L)\sin ky = \frac{jS_{wave}s(l_j)}{d\sin kL}\sin k(L - l_j)\sin ky,$$

and using Eqs.G.2.2, G.2.5 and G.2.11 for $p_R(y)$, D and C, respectively, for the right-hand side region, i.e. $l_i \leq y \leq L$, we have

$$p_R(y) = Ce^{-jky} + De^{jky} = Ce^{-jkL}\left(e^{-jk(y-L)} - e^{jk(y-L)}\right) =$$

$$= \frac{S_{wave}s(l_j)}{2d\sin kL}\,\frac{\sin kl_j}{\cos kL - j\sin kL}[\cos kL - j\sin kL][-2j\sin k(y-L)] =$$

$$= -\frac{jS_{wave}s(l_j)}{d\sin kL}\sin kl_j \sin k(y-L) = \frac{jS_{wave}s(l_j)}{d\sin kL}\sin kl_j \sin k(L-y),$$

and hence

$$p_L(y) = \frac{jS_{wave}s(l_j)}{d\sin kL}\sin k(L-l_j)\sin ky, \qquad 0 \leq y \leq l_i, \tag{G.2.12}$$

$$p_R(y) = \frac{jS_{wave}s(l_j)}{d\sin kL}\sin kl_j \sin k(L-y), \qquad l_i \leq y \leq L. \tag{G.2.13}$$

Combining Eq.G.1.12 with Eqs.G.2.12 and G.2.13 gives the relations between the wall displacement $w(y)$ and the pressures in two regions away from the OHC, i.e. $p_L(y)$ and $p_R(y)$, so that taking

$$\begin{aligned} w_L(y) &= \frac{1}{S_{wall}}\,p_L(y), \\ w_R(y) &= \frac{1}{S_{wall}}\,p_R(y), \end{aligned} \tag{G.2.14}$$

we have

$$w_L(y) = \frac{jS_{wave}s(l_j)}{S_{wall}d\sin kL}\sin k(L-l_j)\sin ky, \qquad 0 \leq y \leq l_i, \tag{G.2.15}$$

$$w_R(y) = \frac{jS_{wave}s(l_j)}{S_{wall}d\sin kL}\sin kl_j \sin k(L-y), \qquad l_i \leq y \leq L. \tag{G.2.16}$$

It is interesting to note that the ratio of the dynamic wave stiffness and the lossy version of the dynamic wall stiffness can be written, according to Eqs.7.3.6 and G.1.2, as

$$\frac{S_{wave}}{S_{wall}} = \left(\frac{j\rho\omega^2}{k} + \frac{16\eta\omega}{kd^2}\right) \frac{(1+\nu)}{Re\{k\}E_0(1+j\mu)} =$$

$$= \frac{j}{kRe\{k\}} \left(\frac{\rho\omega^2(1+\nu)}{E_0(1+j\mu)} - j\,\frac{16\eta\omega(1+\nu)}{E_0(1+j\mu)d^2}\right) =$$

$$= \frac{jd}{kRe\{k\}} \left(\frac{\rho\omega^2(1+\nu)}{E_0(1+j\mu)d} - j\,\frac{16\eta\omega(1+\nu)}{E_0(1+j\mu)d^3}\right),$$

but the term in brackets on the right-hand side of the above equation is equal to Eq.7.3.8, i.e.

$$k^2Re\{k\} = \frac{\rho\omega^2(1+\nu)}{E_0(1+j\mu)d} - j\,\frac{16\eta\omega(1+\nu)}{E_0(1+j\mu)d^3}, \tag{G.2.17}$$

hence

$$\frac{S_{wave}}{S_{wall}} = \frac{jd}{kRe\{k\}}\, k^2Re\{k\} = jkd. \tag{G.2.18}$$

Thus, substituting the above ratio into Eqs.G.2.15-G.2.16 gives

$$w_L(y) = -\frac{ks(l_j)}{\sin kL} \sin k(L-l_j) \sin ky, \qquad 0 \le y \le l_i, \tag{G.2.19}$$

$$w_R(y) = -\frac{ks(l_j)}{\sin kL} \sin kl_j \sin k(L-y), \qquad l_i \le y \le L. \tag{G.2.20}$$

Furthermore, using the relationships for the fluid particle displacement given in Eqs.G.2.1 and G.2.2, and substituting for A, B, C and D (Eqs.G.2.5, G.2.10 and G.2.11) we have

$$u_L(y) = \frac{A}{S_{wave}} e^{-jky} - \frac{B}{S_{wave}} e^{jky} = \frac{A}{S_{wave}} \left(e^{-jky} + e^{jky}\right) =$$

$$= \frac{S_{wave} s(l_j)}{S_{wave} 2d \sin kL} [\sin k(l_j - L)][2 \cos ky] = -\frac{s(l_j)}{d \sin kL} \sin k(L - l_j) \cos ky,$$

for the waves travelling in the left-hand side region from the source, i.e. $0 \leq y \leq l_i$, and

$$u_R(y) = \frac{C}{S_{wave}} e^{-jky} - \frac{D}{S_{wave}} e^{jky} = \frac{C}{S_{wave}} e^{-jky} + \frac{C}{S_{wave}} e^{-2jkL} e^{jky} =$$

$$= \frac{C}{S_{wave}} e^{-jkL} \left(e^{-jk(y-L)} + e^{jk(y-L)}\right) =$$

$$= \frac{S_{wave} s(l_j)}{S_{wave} 2d \sin kL} \frac{\sin kl_j}{\cos kL - j \sin kL} [\cos kL - j \sin kL][2 \cos k(y - L)] =$$

$$= \frac{s(l_j)}{d \sin kL} \sin kl_j \cos k(y - L) = \frac{s(l_j)}{d \sin kL} \sin kl_j \cos k(L - y),$$

for the waves propagating in the right-hand side region, i.e. $l_i \leq y \leq L$, so that

$$u_L(y) = -\frac{s(l_j)}{d \sin kL} \sin k(L - l_j) \cos ky, \qquad 0 \leq y \leq l_i, \tag{G.2.21}$$

$$u_R(y) = \frac{s(l_j)}{d \sin kL} \sin kl_j \cos k(L - y), \qquad l_i \leq y \leq L. \tag{G.2.22}$$

Distribution of the magnitude and phase of the pressure, $p(y)$, and fluid particle displacement, $u(y)$, along the subtectorial duct at 1kHz, due to the fluctuating unit area displacement at the position of the first, second and third OHC, s_1, s_2 and s_3, respectively, was calculated using Eqs.G.2.12-G.2.13 and G.2.21-G.2.22 and shown in Fig.G.4. The length of the duct was assumed to be equal to L=80 μm and the position of the first, second and third OHC to l_1=30 μm,

l_2=50 μm and l_3=70 μm, respectively. The remaining parameters are presented in Table 7.1.

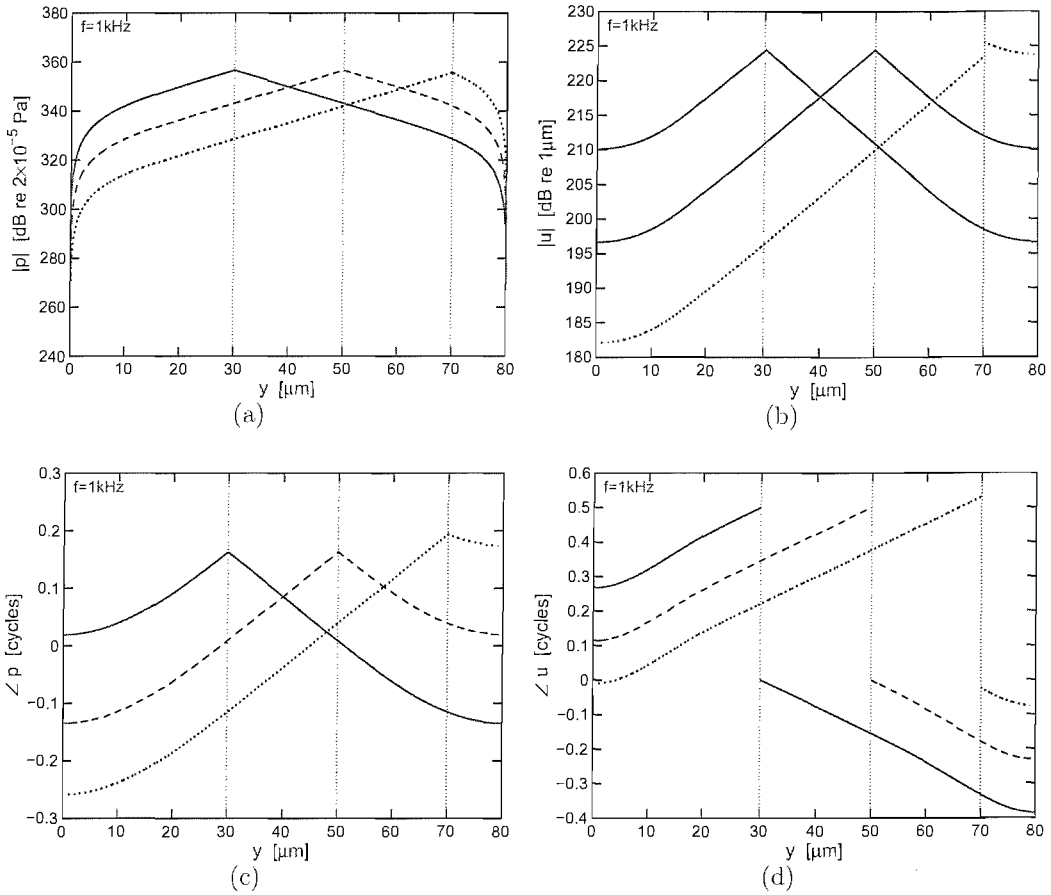

Figure G.4: The magnitude and phase of the pressure, p (a, c), and fluid particle displacement, u (b, d), at 1 kHz due to the unit area displacement from the outer hair cell source, s_1, solid; s_2, dashed and s_3, dotted; as a function of position in the duct, y. Horizontal lines indicate the positions of the outer hair cell rows.

G.3 External and internal responses of the feedback controller model

Having formulated the expressions for the pressure (Eq.G.1.7), fluid particle displacement (Eq.G.1.11), and elastic half-space displacement (Eq.G.1.13) due to the external pressure, p_{ext}, as well as the pressure (Eqs.G.2.12, G.2.13), elastic half-space (Eqs.G.2.19, G.2.20) and fluid particle displacements (Eqs.G.2.21, G.2.22) due to the action of the OHC, we will derive the external and internal responses of the feedback controller model shown in Fig.7.5(b) in a way similar to that presented in Appendix E.

Because the feedback controller in Fig.7.5(b) is a multichannel system since there are three internal inputs and outputs, each of the constitutive responses, excluding the duct response G_{up}, forms again a vector or matrix. The rows of the vector/matrix elements will correspond to the output of each transfer function and will be indexed by i, whereas the columns will be denoted by index j and will correspond to the inputs of these functions.

The duct response, G_{up}, which relates the fluid displacement output at the site of the IHC, i.e. y=0, due to the external pressure input p_{ext} at y=L, is a scalar, and according to Eq.G.1.11 takes the form

$$G_{up} = \frac{u(0)}{p(L)} = \frac{jp_{ext}}{S_{wave}\sin kL}\frac{1}{p_{ext}} = \frac{j}{S_{wave}\sin kL}. \tag{G.3.1}$$

The elastic half-space displacement at the site of the OHC, $w(l_i)$ (Eq.G.1.13), due to the external pressure excitation, p_{ext}, at y=L defined in Eq.G.1.7, will be formulated

$$G_{w_ip} = \frac{w(l_i)}{p(L)} = \frac{p_{ext}\sin kl_i}{S_{wall}\sin kL}\frac{1}{p_{ext}} = \frac{\sin kl_i}{S_{wall}\sin kL}, \tag{G.3.2}$$

where index i corresponds to the position at which the response is to be evaluated. Thus, at a single frequency, $\mathbf{G}_{wp}$ will be a [3×1] column vector such that

$$\left\{\begin{array}{c} w_1 \\ w_2 \\ w_3 \end{array}\right\} = \left\{\begin{array}{c} G_{w_1p} \\ G_{w_2p} \\ G_{w_3p} \end{array}\right\} p, \tag{G.3.3}$$

where

$$G_{w_1p} = \frac{\sin kl_1}{S_{wall} \sin kL}, \tag{G.3.4}$$

$$G_{w_2p} = \frac{\sin kl_2}{S_{wall} \sin kL}, \tag{G.3.5}$$

$$G_{w_3p} = \frac{\sin kl_3}{S_{wall} \sin kL}. \tag{G.3.6}$$

Figure G.5 shows the magnitude and phase of the responses due to external pressure excitation, p_{ext}, i.e. G_{up} at the position of the IHC (left panels), and G_{w_1p}, G_{w_2p} and G_{w_3p} at the position of the first, l_1=30 μm, second, l_2=50 μm, and third, l_3=70 μm, row of the OHCs (right panels), as a function of frequency. The parameters used in simulations are shown in Table 7.1.

The internal response G_{us_j}, relating the fluid particle displacement at the IHC site, $u(0)$, to the area displacement s at position of the OHC (Fig.G.3), l_j, can be evaluated using the expression for the fluid particle displacement for the waves propagating in the left-hand side region of the duct from the source, $u_L(0)$, according to Eq.G.2.21, so that

$$G_{us_j} = \frac{u(0)}{s(l_j)} = -\frac{s(l_j)}{d \sin kL} \sin k(L - l_j) \frac{1}{s(l_j)} = -\frac{\sin k(L - l_j)}{d \sin kL}, \tag{G.3.7}$$

where index j corresponds to the position of the source, that is the OHC position along the duct, and while there is only a single position of the output, i.e. $u(0)$ (position of the IHC), the response $\mathbf{G}_{us}$ is a [1×3] row vector. Therefore, at a single frequency

$$u = \left\{ \; G_{us_1}, G_{us_2}, G_{us_3} \; \right\} \left\{ \begin{array}{c} s_1 \\ s_2 \\ s_3 \end{array} \right\}, \tag{G.3.8}$$

where

$$G_{us_1} = -\frac{\sin k(L - l_1)}{d \sin kL}, \tag{G.3.9}$$

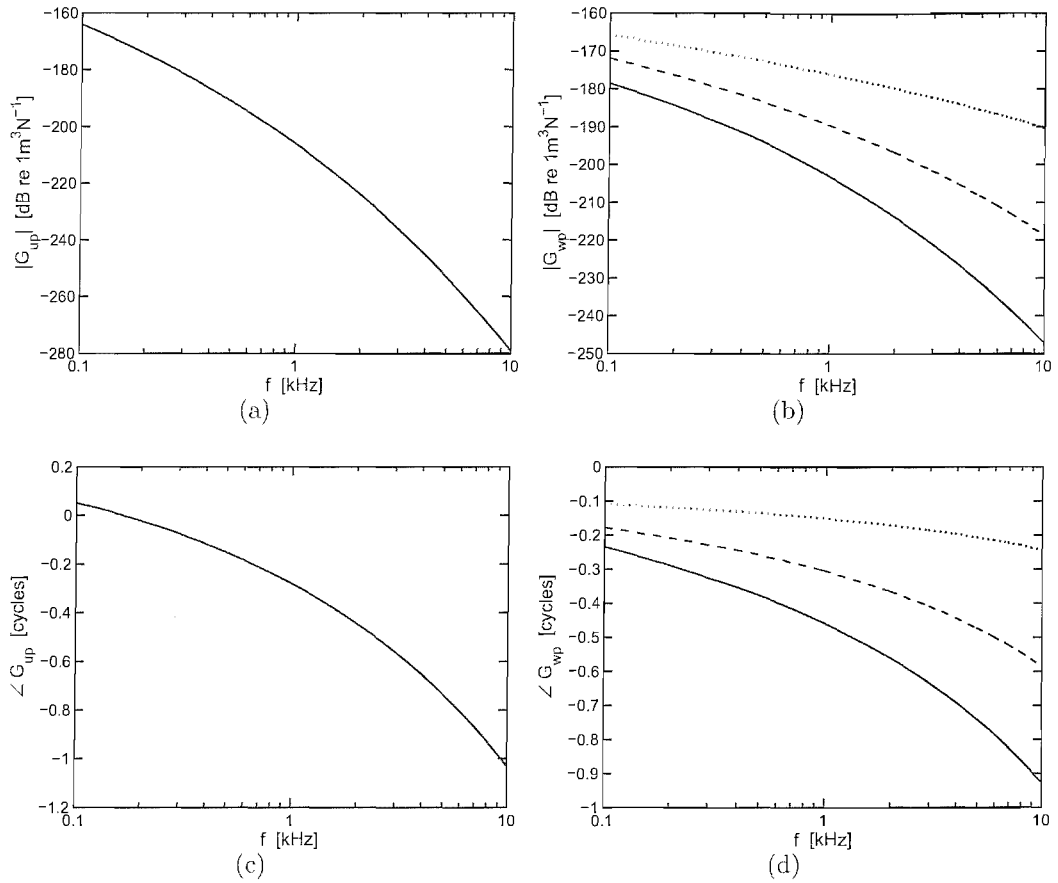

Figure G.5: The magnitude and phase of the fluid-elastic model responses due to external pressure excitation, p_{ext}, as a function of frequency. G_{up} (a, c) and G_{w_1p}, solid; G_{w_2p}, dashed; G_{w_3p}, dotted (b, d), at the first, second and third outer hair cell row.

$$G_{us_2} = -\frac{\sin k(L-l_2)}{d\sin kL}, \tag{G.3.10}$$

$$G_{us_3} = -\frac{\sin k(L-l_3)}{d\sin kL}. \tag{G.3.11}$$

Finally, we will derive the responses $G_{w_i s_j}$, being the ratio of the elastic half-space displacement, w_i, due to the OHC source input, s_j,

$$G_{w_i s_j} = \frac{w(l_i)}{s(l_j)}, \tag{G.3.12}$$

where index i corresponds to the position of the output, i.e. w_{1-3}, whereas the second index, j, to the position of the source, s_{1-3}, so that the response $\mathbf{G}_{ws}$ will be a [3×3] matrix, such that

$$\begin{Bmatrix} w_1 \\ w_2 \\ w_3 \end{Bmatrix} = \begin{bmatrix} G_{u_1 s_1} & G_{u_1 s_2} & G_{u_1 s_3} \\ G_{u_2 s_1} & G_{u_2 s_2} & G_{u_2 s_3} \\ G_{u_3 s_1} & G_{u_3 s_2} & G_{u_3 s_3} \end{bmatrix} \begin{Bmatrix} s_1 \\ s_2 \\ s_3 \end{Bmatrix}, \tag{G.3.13}$$

Note that the components on the diagonal of $\mathbf{G}_{ws}$, correspond to the point responses, i.e. i=j, and the position of the resulting displacement of the elastic half-space coincides with the position of the input area displacement from the OHC. In such a case y=l_i in Eqs.G.2.19-G.2.20, and l_i=l_j so that w_L=w_R, hence[1]

$$w(l_i) = w(l_j) = -\frac{ks(l_j)}{\sin kL}\sin k(L-l_j)\sin kl_j, \tag{G.3.14}$$

and $G_{w_i s_i}$=$w(l_i)/s(l_i)$=$G_{w_j s_j}$=$w(l_j)/s(l_j)$, therefore

$$G_{w_1 s_1} = -\frac{k}{\sin kL}\sin k(L-l_1)\sin kl_1, \tag{G.3.15}$$

$$G_{w_2 s_2} = -\frac{k}{\sin kL}\sin k(L-l_2)\sin kl_2, \tag{G.3.16}$$

$$G_{w_3 s_3} = -\frac{k}{\sin kL}\sin k(L-l_3)\sin kl_3. \tag{G.3.17}$$

[1]The pressure at the position of the source is continuous, so that $p_L(l_j)$=$p_R(l_j)$, and thus the elastic half-space displacement, being proportional to the pressure (Eq.G.2.14), is also continuous, i.e. $w_L(l_j)$=$w_R(l_j)$.

For the remaining components of the matrix $\mathbf{G}_{ws}$, $i \neq j$, and therefore these correspond to transfer responses where the displacement of the elastic-half space is due to the area displacement from the neighbouring OHCs. Note that the appropriate expression for $w(l_i)$ has to be used, i.e. $w_L(l_i)$ (Eq.G.2.19) or $w_R(l_i)$ (Eq.G.2.20), depending on whether the output wall displacement is located in the left- or right-hand side region from the source, respectively. Thus, the remaining responses of the $\mathbf{G}_{ws}$ matrix will take the form

$$G_{w_1 s_2} = \frac{w(l_1)}{s(l_2)} = \frac{w_L(l_1)}{s(l_2)} = -\frac{k}{\sin kL} \sin k(L - l_2) \sin kl_1, \tag{G.3.18}$$

$$G_{w_1 s_3} = \frac{w(l_1)}{s(l_3)} = \frac{w_L(l_1)}{s(l_3)} = -\frac{k}{\sin kL} \sin k(L - l_3) \sin kl_1, \tag{G.3.19}$$

$$G_{w_2 s_3} = \frac{w(l_2)}{s(l_3)} = \frac{w_L(l_2)}{s(l_3)} = -\frac{k}{\sin kL} \sin k(L - l_3) \sin kl_2, \tag{G.3.20}$$

$$G_{w_2 s_1} = \frac{w(l_2)}{s(l_1)} = \frac{w_R(l_2)}{s(l_1)} = -\frac{k}{\sin kL} \sin kl_1 \sin k(L - l_2), \tag{G.3.21}$$

$$G_{w_3 s_1} = \frac{w(l_3)}{s(l_1)} = \frac{w_R(l_3)}{s(l_1)} = -\frac{k}{\sin kL} \sin kl_1 \sin k(L - l_3), \tag{G.3.22}$$

$$G_{w_3 s_2} = \frac{w(l_3)}{s(l_2)} = \frac{w_R(l_3)}{s(l_2)} = -\frac{k}{\sin kL} \sin kl_2 \sin k(L - l_3), \tag{G.3.23}$$

It can be seen from the above expressions that $G_{w_i s_j}$=$G_{w_j s_i}$, and hence the matrix $\mathbf{G}_{ws}$ is symmetric. We gather all the constitutive responses of the feedback controller model, proposed for the fluid-elastic wave model, in Table G.1.

Figure G.6 depicts the magnitude and phase of the frequency responses to internal area displacement, s_{1-3} (y=30 μm, 50 μm and 70 μm, respectively), i.e. G_{us_1}, G_{us_2} and G_{us_3} at the IHC (left panel), as well as the point responses $G_{w_1 s_1}$, $G_{w_2 s_2}$ and $G_{w_3 s_3}$ at the corresponding OHC positions, calculated for the parameters in Table 7.1. Note that after substituting for l_1=30 μm and l_2=50 μm in Eqs.G.3.15-G.3.16, $G_{w_1 s_1}$ is equal to $G_{w_2 s_2}$, which can be seen in Fig.G.6(b).

The magnitude and phase of the transfer responses $G_{w_i s_j}$ for i>j, i.e. $G_{w_2 s_1}$, $G_{w_3 s_1}$ and $G_{w_3 s_2}$ are shown in Fig.G.7. Note that due to the symmetry of the

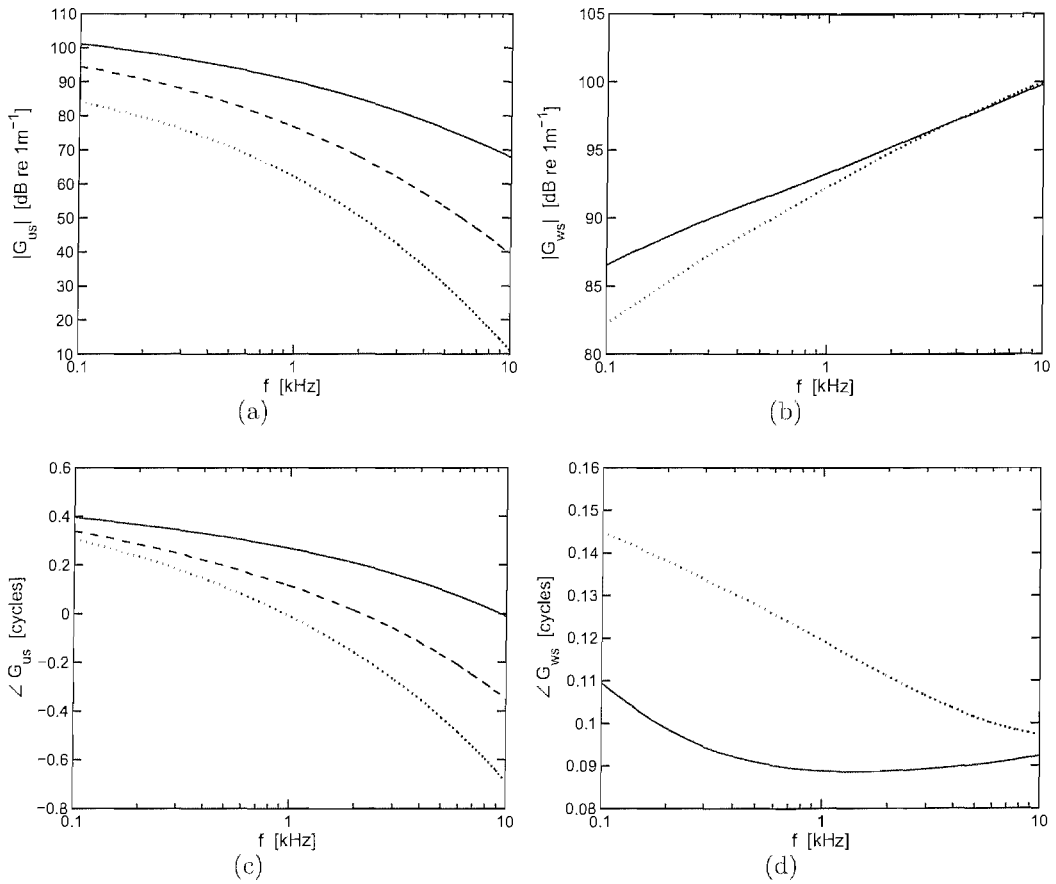

Figure G.6: The magnitude and phase of the frequency response of the fluid particle displacements, $G_{us_{1-3}}$ (a, c) due to the area displacement input at the first (solid), second (dashed) and the third (dotted) outer hair cell; and the point responses $G_{w_1s_1}$ (solid), $G_{w_2s_2}$ (dashed) and $G_{w_3s_3}$ (dotted) at the first, second and third outer hair cell position, respectively (b, d). **NB** $G_{w_1s_1}$ is equal to $G_{w_2s_2}$.

$\mathbf{G}_{ws}$ matrix, $G_{w_1s_2}$, $G_{w_1s_3}$ and $G_{w_2s_3}$ are equal to $G_{w_2s_1}$, $G_{w_3s_1}$ and $G_{w_3s_2}$, respectively, and have the same characteristics as the corresponding responses shown in Fig.G.7.

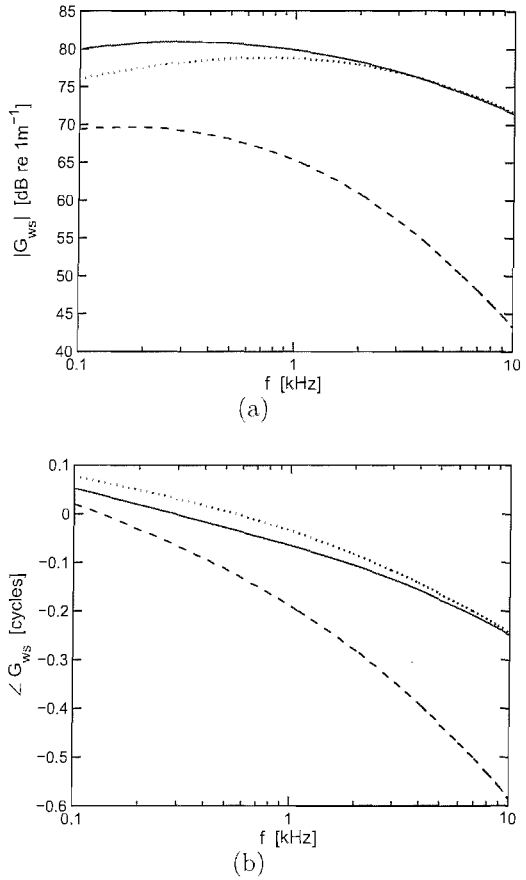

Figure G.7: The magnitude and phase of the transfer frequency responses $G_{w_2s_1}$, $G_{w_3s_1}$ due to the area displacement at the first outer hair cell and $G_{w_3s_2}$ due to the area displacement at the second outer hair cell.

RESPONSE	EXPRESSION
G_{up} $[\mathrm{m}^3\mathrm{N}^{-1}]$	$\frac{j}{S_{wave}} \frac{1}{\sin kL}$
G_{us_j} $[\mathrm{m}^{-1}]$	$-\frac{1}{d} \frac{\sin k(L-l_j)}{\sin kL}$
$G_{w_i p}$ $[\mathrm{m}^3\mathrm{N}^{-1}]$	$\frac{1}{S_{wall}} \frac{\sin kl_i}{\sin kL}$
$G_{w_i s_j}$ $[\mathrm{m}^{-1}]$	$-k \frac{\sin k(L-l_j) \sin kl_j}{\sin kL}$ for $i = j$
	$-k \frac{\sin k(L-l_i) \sin kl_j}{\sin kL}$ for $i > j$
	$-k \frac{\sin k(L-l_j) \sin kl_i}{\sin kL}$ for $i < j$

Table G.1: Constitutive responses of the feedback controller proposed for the active fluid-elastic wave model.

References

[1] Allen, J. B. (**1980**). "Cochlear micromechanics-A physical model of transduction," J. Acoust. Soc. Am. **68**, 1660-1670.

[2] Andoh, M. and Wada, H. (**2003**). "Dynamic characteristics of the force generated by the outer hair cell motility in the organ of Corti (Theoretical consideration)," JSME International Journal, Series C, **46**, 1256-1265.

[3] Andoh, M., Nakajima, C. and Wada, H. (**2005**). "Phase of neural excitation relative to basilar membrane motion in the organ of Corti: Theoretical considerations," J. Acoust. Soc. Am. **118**, 1554-1565.

[4] Ashmore, J. and Gale, J. (**2000**). "The Cochlea," Curr. Biol. **10**, 325-327.

[5] Ashmore, J. and Gale, J. (**2004**). "The cochlear amplifier," Curr. Biol. **14**, 403-404.

[6] Ashmore, J. and Géléoc, G. S. G. (**1999**). "Cochlear function: Hearing in the fast lane," Curr. Biol. **9**, 572-574.

[7] Baumann, O. N. and Elliott, S. J. (**2007**) "The stability of decentralized multichannel velocity feedback controllers using inertial actuators," J. Acoust. Soc. Am. **121**, 188-196.

[8] Békésy von, G. (**1960**). *Experiments in Hearing* (McGraw-Hill, New York).

[9] Bell, A. and Fletcher, N. H. (**2004**) "The cochlear amplifier as a standing wave: 'Squirting' waves between rows of outer hair cells?," J. Acoust. Soc. Am. **116**, 1016-1024.

[10] Cooper, N. P. and Rhode, W. S. (**1996**). "Fast travelling waves, slow travelling waves and their interactions in experimental studies of apical cochlear mechanics," Aud. Neurosci. **2**, 289-299.

[11] Dallos, P. (**1996**). "Overview: Cochlear Neurobiology," in *The Cochlea* edited by P. Dallos, A. N. Popper and R. R. Fay (Springer, New York), pp.1-43.

[12] Davis, H. (**1962**). "Advances in the neurophysiology and neuroanatomy of the cochlea," J. Acoust. Soc. Am. **34**, 1377-1385.

[13] Davis, H. (**1983**). "An active process in cochlear mechanics," Hear. Res. **9**, 79-90.

[14] de Boer, E. (**1991**). "Auditory Physics. Physical principles in hearing theory. III," Phys. Rep. **203**, 125-231.

[15] de Boer, E. (**1995a**). "The 'inverse problem' solved for a three-dimensional model of the cochlea. II. Application to experimental data sets," J. Acoust. Soc. Am. **98**, 904-910.

[16] de Boer, E. (**1995b**). "On equivalence of locally active models of the cochlea," J. Acoust. Soc. Am. **98**, 1400-1409.

[17] de Boer, E. (**1996**). "Mechanics of the Cochlea: Modeling Efforts," in *The Cochlea* edited by P. Dallos, A. N. Popper and R. R. Fay (Springer, New York), pp.258-317.

[18] Dong, W. and Cooper, N. P. (**2006**). "An experimental study into the acousto-mechanical effects of invading the cochlea," Journal of the Royal Society, Interface **3**, 561-571.

[19] Dorf, R. C. and Bishop, R. H. (**2005**). *Modern Control Systems*, Tenth Edition, (Pearson Prentice Hall).

[20] Elliott, S. J. (**2005**). "Fluid-elastic waves between the tectorial membrane and the organ of Corti." Technical memorandum No.952, Institute of Sound and Vibration Research, University of Southampton, UK.

[21] Elliott, S. J. (**2006**). "Global vibration control through local feedback," in *Adaptive Structures: Engineering Applications*, Proc. of Adaptive Structures 2006, (John Wiley and Sons Ltd).

[22] Elliott, S. J. (**2007**). "Wave propagation in a constrained fluid layer bounded by an elastic half-space and its relevance in cochlear micromechanics," J. Sound Vib. **305**, 918-924.

[23] Elliott, S. J. and Harte, J. M. (**2003**). "Models for compressive nonlinearities in the cochlea." Technical memorandum No.913, Institute of Sound and Vibration Research, University of Southampton, UK.

[24] Elliott, S. J., Pierzycki, R. and Lineton, B. (**2006**). "Lumped-parameter models for cochlear micromechanics." Technical memorandum No.967, Institute of Sound and Vibration Research, University of Southampton, UK.

[25] Emadi, G., Richter, C.-P. and Dallos, P. (**2004**). "Stiffness of the gerbil basilar membrane: Radial and longitudinal variations," J. Neurophysiol. **91**, 474-488.

[26] Evans, M. G., Guha, U., Mahendrasingam, S., Dallender, S., Furness, D. N. and Hackney, C. M. (**2005**). "An investigation of the properties of stereociliary rootlets," Proc. of the British Society of Audiology Short Papers Meeting on Experimental Studies of Hearing and Deafness, Cardiff.

[27] Fahy, F. J. (**1985**). *Sound and Structural Vibration: Radiation, Transmission and Response*, (Academic Press, London).

[28] Fettiplace, R. and Ricci, A. J. (**2003**). "Adaptation in auditory hair cells," Curr. Opin. Neurobiol. **13**, 446-451.

[29] Frank, G., Hemmert, W. and Gummer, A. W. (**1999**). "Limiting dynamics of high-frequency electromechanical transduction of outer hair cells," Proc. Natl. Acad. Sci. U.S.A. **96**, 4420-4425.

[30] Freeman, D. M., Abnet, C. C., Hemmert, W., Tsai, B. S., and Weiss, T. F. (**2003**). "Dynamic material properties of the tectorial membrane: a summary," Hear. Res. **180**, 1-10.

[31] Fridberger, A. and de Monvel, J. B. (**2003**). "Sound-induced differential motion within the hearing organ," Nat. Neurosci. **6**, 446-448.

[32] Fukazawa, T. (**1997**). "A model of cochlear micromechanics," Hear. Res. **113**, 182-190.

[33] Furness, D. N. and Hackney, C. M. (**2005**). "The ultrastructure of stereociliary rootlets," Proc. of the British Society of Audiology Short Papers Meeting on Experimental Studies of Hearing and Deafness, Cardiff.

[34] Geisler, C. D. (**1993**). "A realizable cochlear model using feedback from motile outer hair cells," Hear. Res. **68**, 253-262.

[35] Gelfand, S. A. (**2004**). *Hearing: An Introduction to Psychological and Physiological Acoustics*, Fourth Edition (Marcel Dekker, New York).

[36] Glueckert, R., Pfaller, K., Kinnefors, A., Rask-Andersen, H. and Schrott-Fischer, A. (**2005**). "Ultrastructure of the normal human organ of Corti. New anatomical findings in surgical specimens," Acta Otolaryngol. **125**, 534-539.

[37] Gold, T. (**1948**). "Hearing. II. The physical basis of the action of the cochlea," Proc. R. Soc. Lond., B, Biol. Sci. **135**, 492-498.

[38] Graff, K. F. (**1991**). *Wave motion in elastic solids*, Dover Edition (Dover Publications, Inc., New York).

[39] Greenwood, D. D. (**1990**). "A cochlear frequency-position function for several species-29 years later," J. Acoust. Soc. Am. **87**, 2592-2605.

[40] Gummer, A. W., Hemmert, W. and Zenner, H.-P. (**1996**). "Resonant tectorial membrane motion in the inner ear: Its crucial role in frequency tuning," Proc. Natl. Acad. Sci. U.S.A. **93**, 8727-8732.

[41] Hassan, W. and Nagy, P. B. (**1997**). "On the low-frequency oscillation of a fluid layer between two elastic plates," J. Acoust. Soc. Am. **102**, 3343-3348.

[42] Hemmert, W., Zenner, H.-P. and Gummer, A. W. (**2000a**). "Characteristics of the travelling wave in the low-frequency region of a temporal-bone preparation of the guinea-pig cochlea," Hear. Res. **142**, 184-202.

[43] Hemmert, W., Zenner, H.-P. and Gummer, A. W. (**2000b**). "Three-dimensional motion of the organ of Corti," Biophys. J. **78**, 2285-2297.

[44] Hudspeth, A. J. and Jacobs, R. (**1979**). "Stereocilia mediate transduction in vertebrate hair cells," Proc. Natl. Acad. Sci. U.S.A. **76**, 1506-1509.

[45] Hudspeth, A. J. (**1997**). "Mechanical amplification of stimuli by hair cells," Curr. Opin. Neurobiol. **7**, 480-486.

[46] Johnstone, B. M., Patuzzi, R. and Yates, G. K. (**1986**). "Basilar membrane measurements and the travelling wave," Hear. Res. **22**, 147-153.

[47] Kanis, L. J. and de Boer, E. (**1993**). "Self-suppression in a locally active nonlinear model of the cochlea: A quasilinear approach," J. Acoust. Soc. Am. **94**, 3199-3206.

[48] Kinsler, L. E., Frey, A. R., Coppens, A. B. and Sanders, J. V. (**2000**). *Fundamentals of Acoustics*, Fourth Edition, (John Wiley and Sons, Inc., New York).

[49] Kolston, P. J. and Ashmore, J. F. (**1996**). "Finite element micromechanical modeling of the cochlea in three dimensions," J. Acoust. Soc. Am. **99**, 455-467.

[50] Kolston, P. J. (**1999**). "Comparing in vitro, in situ, and in vivo experimental data in a three-dimensional model of mammalian cochlear mechanics," Proc. Natl. Acad. Sci. U.S.A. **96**, 3676-3681.

[51] Kreyszig, E. (**1993**). *Advanced Engineering Mathematics*, Seventh Edition, (John Wiley and Sons, Inc., Singapore).

[52] Kros, C. (**2005**). "Hearing: Aid from hair force," Nature **433**, 810-811.

[53] Krstić, R. V. (**1991**). *Human Microscopic Anatomy: An Atlas for Students of Medicine and Biology*, (Springer-Verlag Berlin Heidelberg).

[54] Lamb, H. (**1960**). *The Dynamical Theory of Sound*, Second Edition, (Dover Publications, Inc., New York).

[55] Le Henaff, B., Elliott, S. J. and Maury, C. (**2003**). "Modelling wave propagation in the cochlea." Technical Memorandum No.925, Institute of Sound and Vibration Research, University of Southampton, UK.

[56] Liberman, M. C. (**1982**). "The cochlear frequency map for the cat: Labeling auditory-nerve fibers of known characteristic frequency," J. Acoust. Soc. Am. **72**, 1441-1449.

[57] Lim, D. J. (**1980**). "Cochlear anatomy related to cochlear micromechanics. A review," J. Acoust. Soc. Am. **67**, 1686-1695.

[58] Lim, D. J. (**1986**). "Functional structure of the organ of Corti: a review," Hear. Res. **22**, 117-146.

[59] Lineton, B. (**2001**). "Testing a model of stimulus frequency otoacoustic emissions in humans," PhD Thesis, Institute of Sound and Vibration Research, University of Southampton, UK.

[60] Lloyd, P. and Redwood M. (**1965**). "Wave propagation in a layered plate composed of two solids with perfect contact, slip, or a fluid layer at their interface," Acustica **16**, 224-232.

[61] Lukashkin, A. N., Russell, I. J. (**2003**). "A second, low-frequency mode of vibration in the intact mammalian cochlea," J. Acoust. Soc. Am. **113**, 1544-1550.

[62] Moore, B. C. J. (**1995**). "Frequency Analysis and Masking," in *Hearing* edited by B. C. J. Moore, Second Edition (Academic Press, San Diego), pp.161-206.

[63] Naidu, R. C. and Mountain, D. C. (**2001**). "Longitudinal coupling in the basilar membrane," J. Assoc. Res. Otolaryngol. **2**, 257-267.

[64] Neely, S. T. (**1981**). "Finite difference solution of a two-dimensional mathematical model of the cochlea," J. Acoust. Soc. Am. **69**, 1386-1393.

[65] Neely, S. T. (**1985**). "Mathematical modeling of cochlear mechanics," J. Acoust. Soc. Am. **78**, 345-352.

[66] Neely, S. T. (**1993**). "A model of cochlear mechanics with outer hair cell motility," J. Acoust. Soc. Am. **94**, 137-146.

[67] Neely, S. T. and Kim, D. O. (**1983**). "An active cochlear model showing sharp tuning and high sensitivity," Hear. Res. **9**, 123-130.

[68] Neely, S. T. and Kim D. O. (**1986**). "A model for active elements in cochlear biomechanics," J. Acoust. Soc. Am. **79**, 1472-1480.

[69] Nelson, P. A. and Elliott, S. J. (**1992**). *Active Control of Sound* (Academic Press, London).

[70] Newland, D. E. (**1989**). *Mechanical vibration analysis and computation* (Longman Scientific and Technical, Essex).

[71] Nilsen, K. E. and Russell, I. J. (**1999**). "Timing of cochlear feedback: spatial and temporal representation of a tone across the basilar membrane," Nat. Neurosci. **2**, 642-648.

[72] Nilsen, K. E. and Russell, I. J. (**2000**). "The spatial and temporal representation of a tone on the guinea pig basilar membrane," Proc. Natl. Acad. Sci. U.S.A. **97**, 11751-11758.

[73] Nobili, R., Mammano, F. and Ashmore, J. (**1998**). "How well do we understand the cochlea?," Trends Neurosci. **21**, 159-167.

[74] Nowotny, M. and Gummer, A. W. (**2006**). "Nanomechanics of the subtectorial space caused by electromechanics of cochlear outer hair cells," Proc. Natl. Acad. Sci. U.S.A. **103**, 2120-2125.

[75] Olson, E. S. and Mountain, D. C. (**1994**). "Mapping the cochlear partition's stiffness to its cellular architecture," J. Acoust. Soc. Am. **95**, 395-400.

[76] Oppenheim, A. V., Willsky, A. S. and Nawab, S. H. (**2002**). *Signals and Systems*, Second Edition, (Electronics Industry Publishing House, Beijing).

[77] Osborne, M. P., Comis, S. D. and Pickles, J. O. (**1988**). "Further observations on the fine structure of tip links between stereocilia of the guinea pig cochlea," Hear. Res. **35**, 99-108.

[78] Patuzzi, R. (**1996**). "Cochlear Micromechanics and Macromechanics," in *The Cochlea* edited by P. Dallos, A. N. Popper and R. R. Fay (Springer, New York), pp.186-257.

[79] Pickles, J. O. (**1988**). *An Introduction to the Physiology of Hearing* (Academic Press, London).

[80] Pickles, J. O., Comis, S. D. and Osborne, M. P. (**1984**). "Cross-links between stereocilia in the guinea pig organ of Corti, and their possible relation to sensory transduction," Hear. Res. **15**, 103-112.

[81] Pierce, A. D. (**1981**). *Acoustics: An Introduction to Its Physical Principles and Applications*, (McGraw-Hill, Inc., New York).

[82] Pierzycki, R. H. and Elliott, S. J. (**2004**). "Comparison of two locally active models of the cochlea." Technical Memorandum No.938, Institute of Sound and Vibration Research, University of Southampton, UK.

[83] Raftenberg, M. N. (**1990**). "Flow of endolymph in the inner spiral sulcus and the subtectorial space," J. Acoust. Soc. Am. **87**, 2606-2620.

[84] Reuter, G. and Zenner H.-P. (**1990**). "Active radial and transverse motile responses of outer hair cells in the organ of Corti," Hear. Res. **43**, 219-230.

[85] Rhode, W. S. (**1971**). "Observations of the vibration of the basilar membrane in squirrel monkeys using the Mössbauer technique," J. Acoust. Soc. Am. **49**, 1218-1231.

[86] Rhode, W. S. (**1978**). "Some observations on cochlear mechanics," J. Acoust. Soc. Am. **64**, 158-176.

[87] Robles, L., Ruggero, M. A. (**2001**). "Mechanics of the mammalian cochlea," Physiol. Rev. **81**, 1305-1352.

[88] Scherer, M. P. and Gummer, A. W. (**2004**). "Impedance analysis of the organ of Corti with magnetically actuated probes," Biophys. J. **87**, 1378-1391.

[89] Shoelson, B., Dimitriadis, E. K., Cai, H., Kachar, B. and Chadwick, R. S. (**2004**). "Evidence and implications of inhomogeneity in tectorial membrane elasticity," Biophys. J. **87**, 2768-2777.

[90] Slepecky, N. B. (**1996**). "Structure of the Mammalian Cochlea," in *The Cochlea* edited by P. Dallos, A. N. Popper and R. R. Fay (Springer, New York), pp.44-129.

[91] Strelioff, D. and Flock, A. (**1984**). "Stiffness of sensory-cell hair bundles in the isolated guinea pig cochlea," Hear. Res. **15**, 19-28.

[92] Talmadge, C. L., Tubis, A., Long, G. R. and Piskorski, P. (**1998**). "Modeling otoacoustic emission and hearing threshold fine structures," J. Acoust. Soc. Am. **104**, 1517-1543.

[93] Temkin, S. (**1981**). *Elements of Acoustics*, (John Wiley and Sons, Inc., New York).

[94] Tse, F. S., Morse, I. E., Hinkle, R. T. (**2001**). *Mechanical Vibrations: Theory and Applications*, Second Edition (Allyn and Bacon, Boston).

[95] Voldřich, L. (**1978**). "Mechanical properties of basilar membrane," Acta Otolaryngol. **86**, 331-335.

[96] Wangemann, P. and Schacht, J. (**1996**). "Homeostatic Mechanisms in the Cochlea," in *The Cochlea* edited by P. Dallos, A. N. Popper and R. R. Fay (Springer, New York), pp.130-185.

[97] Withnell, R. H., Shaffer, L. A. and Lilly, D. J. (**2002**). "What drives mechanical amplification in the mammalian cochlea?," Ear Hear. **23**, 49-57.

[98] Wright, A. (**1984**). "Dimensions of the cochlear stereocilia in man and the guinea pig," Hear. Res. **13**, 89-98.

[99] Yates, G. K. (**1990a**). "The Basilar Membrane Nonlinear Input-Output Function," in *Mechanics and Biophysics of Hearing* edited by P. Dallos, C. D. Geisler, J. W. Matthews, M. A. Ruggero and C. Steele (Springer-Verlag, New York), pp.106-113.

[100] Yates, G. K. (**1990b**). "Basilar membrane nonlinearity and its influence on auditory nerve rate-intensity functions," Hear. Res. **50**, 145-162.

[101] Yates, G. K. (**1995**). "Cochlear Structure and Function," in *Hearing* edited by B. C. J. Moore, Second Edition (Academic Press, London), pp.41-74.

[102] Zhao, H.-B. and Santos-Sacchi, J. (**1999**). "Auditory collusion and a coupled couple of outer hair cells," Nature **399**, 359-362.

[103] Zweig, G. (**1991**). "Finding the impedance of the organ of Corti," J. Acoust. Soc. Am. **89**, 1229-1254.

[104] Zwislocki, J. J. and Kletsky, E. J. (**1979**). "Tectorial membrane: a possible effect on frequency analysis in the cochlea," Science **204**, 639-641.

[105] Zwislocki, J. J. and Cefaratti, L. K. (**1989**). "Tectorial membrane II: Stiffness measurements in vivo," Hear. Res. **42**, 211-227.